Persistent Currents in Bose-Einstein Condensates

Stuart Moulder

Trinity College
University of Cambridge

This dissertation is submitted for the degree of
Doctor of Philosophy

September 2, 2013

UNIVERSITY OF
CAMBRIDGE

To my parents Kevin and
Christine, and my sister Carren.

I declare that this thesis is my own work and is not substantially the same as any that I have submitted or am currently submitting for a degree, diploma or any other qualification at any other university. No part of this thesis has already been or is being concurrently submitted for any such degree, diploma or any other qualification. This thesis does not exceed the word limit of sixty thousand words, including tables, footnotes, bibliography and appendices, set out by the Faculty of Physics and Chemistry.

Abstract

Persistent Currents in Bose-Einstein Condensates

Stuart Moulder

This thesis describes a set of experiments which probe the superfluid nature of both single and two component Bose-Einstein condensates of ^{87}Rb in a multiply connected toroidal geometry.

The first part of this thesis describes the preparation and detection of persistent currents in a toroidal Bose-Einstein condensate (BEC). The apparatus and procedure for cooling of a dilute vapour of ^{87}Rb atoms to degeneracy is briefly outlined. We then explain how the condensate is transferred to a purely optical ring trap, formed at the intersection of a horizontal sheet beam to confine against gravity, and a vertical tube beam which produces the multiply connected geometry required for persistent flow. Multiply charged superfluid flow is induced using a two photon transfer, and the final angular momentum is detected kinematically in time of flight.

We study the metastability and decay of multiply charged superflow in a ring-shaped BEC. High-charge superflow persisting for over a minute is observed, and we clearly resolve a cascade of quantised steps in its decay. These stochastic decay events, associated with vortex-induced 2π phase slips, correspond to collective jumps of atoms between discrete angular momentum states. By numerical calculation of the excitation spectrum and superflow velocity, we show the supercurrent decays rapidly if the flow velocity approaches a critical velocity in agreement with the local sound speed. For superflow below this limit, stochastic phase slips are also observed to occur at a much slower rate.

This work is extended to study the stability of supercurrents in a toroidal two-component spinor gas consisting of ^{87}Rb atoms in two different spin states. We show that for a large spin-population imbalance we recover the long-lived metastable behaviour of the single component case, with superflow limited only by atom-number decay. However we find that the supercurrent is unstable for spin polarisations below a well defined critical value. The role of phase coherence between the two spin components is investigated, and it is shown that only the magnitude of the spin-polarisation

vector, rather than its orientation in spin space, is relevant for supercurrent stability.

By continuously coupling the magnetic levels of the ground state we generate an azimuthal vector potential, corresponding to a non-zero magnetic flux threading the ring. By varying this effective magnetic field we demonstrate the creation of a limited subset of dressed states with coupled angular motion and spin composition. Application of such a setup is presented by explaining a proposed superfluid fraction measurement. With a view to future work, the technical limitations of our current setup are then discussed.

Acknowledgements

I owe a huge debt of thanks to all the people who have helped and supported me through this PhD. Those that know me well will attest to the fact that I've never been particularly forthcoming with gratitude, reserving it for truly landmark occasions. Since such an occasion has come, I sincerely hope that my brandishing the stick of sarcastic cynicism for the last three and a half years, has made the carrot of humble gratitude all the sweeter. The biggest thanks must go to my supervisor Zoran Hadizibabic, whose endless drive and enthusiasm for his work first won me over to the field of degenerate ultracold gases, and have been a continuing source of inspiration and motivation ever since. In particular, conversations with Zoran always seem to conclude with feverish nodding of heads and adamant belief in our revised plan to 'get famous' and 'conquer the world'; and while we seem to have differing ideas of what constitutes famous, I was always instilled with a renewed sense of excitement and conviction for my work.

A huge thanks must go to Scott Beattie who was the Tango to my Cash, the Goose to my Maverick, and without whom I would often have been left floundering. For three years we enjoyed an unnatural amount of time together, and though tempers occasionally frayed, Scott must take a large portion of the credit for making my time in Cambridge so enjoyable. A great friend both in and out of the lab, and ever willing partner in too many sports to mention[1], I wish him and Erin all the best back in their homeland of Canada.

This work would never have been possible without the help of the three original founding members of this lab, Naaman Tammuz, Robbie Campbell, and Rob Smith, whose tireless efforts built the system which I used in this thesis. I must thank them for making the lab such a welcoming and friendly place, and for readily passing on so much wisdom which they themselves learnt through hard graft. One must particularly applaud the efforts of Naaman to introduce a sense of culture to the lab, and forgive Robbie his efforts to introduce musical theatre to the lab. Special thanks go to Rob whose wealth of experience and knowledge have made him an invaluable asset upon which the entire fate of the lab hinges...

I would also like to thank the newer members of the group for their assistance, the so called A-team: Toby (explosives), Igor (the muscles), Alex (gadgets), and Rich (effort?). In particular the enthusiasm of Alex and Rich to get involved and bring new ideas to the table revitalised our studies on persistent currents, and I leave knowing the lab has a promising future. Thanks are also in order to Nigel Cooper, Stefan Baur, and

[1] football, tennis, squash, table tennis, badminton, Robot Unicorn Attack

Jean Dalibard for numerous insightful and helpful discussions along the way. A special mention has to go to Pam Hadder, who seamlessly dealt with every administrative problem, half completed claims form, and misguided order I was able to muster.

Outside of the lab there are a few people who offered more support and guidance than I could ever have deserved. Flying in the face of the dreaded thesis acknowledgement curse I simply have to thank Marion for being an absolute rock and an endless source of compassion and understanding. Finally, and surpassing all others, I thank my family for their endless support and belief.

Contents

Chapter 1

Introduction

The theory of quantum mechanics has underpinned many of the greatest scientific and technological advances in the last century. Nevertheless, for much of the time we prefer to understand the world through classical mechanics, a high temperature approximation, where the wave-like nature of particles can be neglected. Occasionally however, the quantum nature of the world refuses to be ignored, and in order to progress we are forced out of our comfort zone. Superfluidity and superconductivity offer two particularly striking examples where classical physics falls short. Superfluidity, the phenomena of mass currents without viscosity, and superconductivity, the phenomena of charge currents without resistance, are fundamentally related and arise as a consequence of the existence of a macroscopic wavefunction describing the system.

Such a wavefunction was first postulated by Einstein in 1924 [1] following the work of Bose on blackbody radiation [2]. Einstein showed the existence of a phase transition for a gas of non-interacting bosons at low temperatures, arising purely from the quantum statistics of the particles involved. As the temperature is lowered, a critical threshold is reached where the interatomic distance is on the order of the coherence length of the matter waves, and the classical viewpoint breaks down. At this point a Bose-Einstein condensate (BEC) forms, containing a macroscopic number of particles all occupying the same quantum state. These particles are thus described by the same macroscopic wavefunction and the system constitutes a quantum fluid. The properties of such a quantum fluid were shown to be vastly different from those of a classical fluid, providing an explanation for the unfamiliar behaviour observed in superfluid and superconducting systems.

At this point, the first such quantum fluid had already been observed, with the discovery of superconductivity in 1911, when Onnes [3] found the resistance of solid mercury dropped to zero at temperatures below 4 K. The connection between superconductivity and BEC wasn't fully made however until later, ultimately leading to the formulation of the landmark BCS theory in 1957 [4], which describes superconductivity as a microscopic effect caused by the condensation of Cooper pairs of electrons in a boson-like state. Instead, Einstein's prediction of a macroscopically occupied condensed state remained unproved experimentally until the discovery of superfluidity in liquid

helium in 1938 [5, 6], when it was found that the viscosity of liquid helium vanishes suddenly below 2.17 K. In spite of the fact that liquid helium is strongly interacting, it was soon argued by F. London that this transition was an example of Bose-Einstein condensation [7].

With this insight, superflow could now be understood as an adiabatic transformation of the condensed state brought about by changes in the macroscopic boundary conditions. Such motion would not require the presence of intermediate excited states, and therefore could occur without energy dissipation. This interpretation lead directly to the two-fluid model for liquid helium [8, 9], which succeeded in explaining and predicting many of the physical phenomena of superfluid helium. Fundamentally however, a full theoretical understanding of superfluid helium is difficult due to the strength of the atomic interactions present in the liquid phase which exclude the possibility of a perturbative expansion from the non-interacting Bose gas considered by Einstein.

The realisation of Bose-Einstein condensation in dilute atomic gases in 1995 represented a breakthrough in the history of quantum fluids. This scientific milestone was first achieved by the groups of E. Cornell and C. Wieman at Boulder [10], and a few months later by W. Ketterle at MIT [11]. The significance of this achievement, together with the decades of work on laser-cooling and manipulation of atoms which preceded it, were recognised by the Physics Nobel prizes of 1997, 2001, and 2005. Such systems provide the ideal test beds for simulating and understanding the broad array of many-body quantum phenomena observed in condensed matter physics. In part this is due to the ever expanding arsenal of experimental tools which have now been developed to allow one to effectively construct a desired Hamiltonian. Additionally, due to the low densities required to prevent the gas transitioning to a solid, the inter-atomic interactions present in these systems are often sufficiently weak to permit an accurate perturbative treatment. This is in stark contrast to the superfluid experiments of Helium, where the macroscopic condensed state accounts for less than 10% of the total density [12].

The combination of a clean and controllable environment together with a tractable theoretical framework, mean experiments on atomic condensates offer an excellent playground for probing superfluidity, and by extension, superconductivity. From this, it's hoped that progress can be made in outstanding problems such as high temperature superconductors, the connection between superfluidity and dimensionality, and the precise connection between superfluidity and BEC. The specific questions tackled in this thesis relate to understanding the metastability and decay of persistent currents in superfluids.

1.1 Persistent currents

The significance of persistent currents can be seen in an alternate definition of superfluidity and superconductivity, which is given by the response of the system to rotation, or equivalently an external magnetic field[1]. Such a definition is explained in [13], where the author considers liquid helium in a multiply-connected annular geometry. Starting above the transition temperature to superfluidity, T_λ, the annulus is set into rapid rotation, causing the helium in its normal state to come into rotation with the container. The liquid is then cooled through T_λ and the container is brought to a stop. The liquid helium, which is now in its superfluid state, will continue to rotate indefinitely, forming a persistent mass current. For a stationary container, this rotating state cannot be the thermodynamic equilibrium, and so is an example of an extremely long-lived metastable state. Such behaviour is characteristic of the superfluid state only, where angular momentum is conserved.

The equivalent phenomena in superconducting systems is the conservation of magnetic flux. Starting with a cylindrical superconductor above the transition temperature T_c, an external magnetic field is applied along the axis of symmetry. The sample is then cooled below T_c and the field removed. The analogous effect in superconductors is now observed, where a persistent surface charge current forms, generating a magnetic field such that the flux penetrating the sample remains unchanged. In both cases, the systems remain in an excited metastable state due to the presence of a free energy barrier to decay, the origin of which is the presence of a macroscopically occupied quantum state.

The stability and eventual decay of such supercurrents have been studied for decades in both helium and superconductors, however the decay mechanism is still not fully understood. Persistent currents in dilute atomic BECs therefore offer an ideal platform with which to make further progress, and in addition, to explore the relationship between condensation and superfluidity.

1.2 Thesis outline

This thesis details our work on the stability and decay of persistent currents in dilute annular BECs confined to a toroidal geometry. The remainder of this thesis is structured as follows:

- Chapter 2 provides a theoretical background to the phenomena of Bose-Einstein condensation and superfluidity.
- Chapter 3 covers the experimental methods necessary for producing condensates of ^{87}Rb, as well as the physical principles relevant to preparing and studying

[1] One can show that the Hamiltonian for a neutral atom in a rotating frame of reference is equivalent to that of a charged particle in a magnetic field

persistent currents.

- Chapter 4 describes our experimental setup for creating an all-optical ring trap and preparing a state of definite rotation using a two-photon transition to imprint an azimuthal phase winding onto the condensate wavefunction. The method for kinematic detection of rotation by time-of-flight expansion is also presented. The significance of a multiply-connected geometry for long-lived supercurrents is illustrated by studying the rapid loss of angular momentum through vortex dynamics in a simply-connected rotating condensate.

- Chapter 5 presents our first results on the metastability and decay of persistent currents, which are published in [14]. We demonstrate the extreme metastability of multiply-charged superflow persisting for over a minute. The persistent current is found to decay in a cascade of quantised decay steps which unambiguously confirms that 2π phase slips are the supercurrent decay mechanism. The dynamics of these phase slips is shown to be stochastic, with a probability which increases as the flow velocity approaches a critical velocity set by the local sound speed.

- Chapter 6 extends our studies to a two-component spinor condensate, the results of which are published in [15]. We identify a regime at large population imbalances where the two-component supercurrent is fundamentally stable and exhibits the long-lived metastability observed in the single-component case. Below a well defined critical population imbalance however, we show the presence of both components means the supercurrent is fundamentally unstable.

- Chapter 7 discusses our current progress towards creating an azimuthal vector potential, analogous to generating a rotating frame of reference. We present some preliminary experimental results, and describe the technical hurdles which remain.

- Finally, in chapter 8 we summarise our results and mention possible directions for future work.

Chapter 2

Theory of Bose-Einstein condensation and superfluidity

This chapter presents some of the theory behind Bose-Einstein condensation (BEC) and attempts to illuminate the intrinsic connection between the phenomena of condensation and superfluidity. We start by discussing how the BEC phase transition arises in the ideal Bose gas purely as a result of the quantum statistics of the particles. The role of interactions is then introduced and the excitation spectrum of the weakly interacting Bose gas is calculated. From this we show the concept of superfluid flow as adiabatic motion of the condensate leads directly to the ideas of a critical velocity and quantised vortex states.

2.1 Condensation of an ideal Bose gas

For non-interacting bosons in thermodynamic equilibrium, the mean occupancy of a single-particle state of energy ϵ at temperature T is given by the Bose-Einstein distribution

$$f(\epsilon) = \frac{1}{\exp\left[(\epsilon - \mu)/k_B T\right] - 1}, \tag{2.1}$$

where k_B is the Boltzmann constant and μ is the chemical potential. The chemical potential is determined as a function of both the total atom number N and temperature T, such that particle number is conserved. The total atom number is then given by the product of the mean occupancy $f(\epsilon)$ with the density of states $g(\epsilon)$ summed over all available energy levels. Assuming that the confining potential is such that the energy level spacing is much less than $k_B T$, we can replace the sum with an integral. Consequently, the system can be described by a continuum of excited states plus the discrete ground state which must be explicitly retained [16, 17]:

$$N = N_0 + N_{\text{ex}} = N_0 + \int_{\epsilon_{\min}}^{\infty} d\epsilon f(\epsilon) g(\epsilon), \tag{2.2}$$

where N_0 is the number of particles in the ground state, and N_{ex} the number in the excited states of the system. As the temperature is lowered the chemical potential rises

and the mean occupancy of the allowed states changes. For the distribution $f(\epsilon)$ to be positive for all states, the chemical potential is limited by $\mu < \epsilon_{\min}$, and as a result, while the occupation of the ground state can be arbitrarily large, the occupation number of any excited state ν is constrained to be less than $1/(\exp[(\epsilon_\nu - \epsilon_{\min})/k_B T] - 1)$. If the total number of atoms in the excited states, $N_{\rm ex}$, is less than the total atom number, N, the remaining atoms are accommodated in the ground state and form a condensate of N_0 atoms. We therefore quantify the phase transition to BEC as occurring at a critical atom number N_c for a given T, or equivalently, at a critical temperature T_c for a given N:

$$N_c = N_{\rm ex}(T, \mu = \epsilon_{\min}) = \int_{\epsilon_{\min}}^{\infty} d\epsilon g(\epsilon) \frac{1}{\exp\left[(\epsilon - \epsilon_{\min})/k_B T\right] - 1}. \tag{2.3}$$

Within the semi-classical approximation we can define a local distribution function, where $f_{\mathbf{p}}(\mathbf{r}) d\mathbf{p} d\mathbf{r}/(2\pi\hbar)^3$ denotes the mean number of particles in the phase space volume $d\mathbf{p}d\mathbf{r}$:

$$f_{\mathbf{p}}(\mathbf{r}) = \frac{1}{\exp\left[(\epsilon_{\mathbf{p}}(\mathbf{r}) - \mu)/k_B T\right] - 1} \tag{2.4}$$

The particle energies are those of a free particle at point $\mathbf{r}$

$$\epsilon_{\mathbf{p}}(\mathbf{r}) = \frac{p^2}{2m} + V(\mathbf{r}), \tag{2.5}$$

where $V(\mathbf{r})$ is the external potential. With this definition we calculate the density of particles occupying the excited states of the system as

$$\begin{aligned} n_{\rm ex}(\mathbf{r}) &= \int \frac{d\mathbf{p}}{(2\pi\hbar)^3} \frac{1}{\exp\left[(\epsilon_{\mathbf{p}}(\mathbf{r}) - \mu)/k_B T\right] - 1} \\ &= \frac{g_{3/2}(z(\mathbf{r}))}{\lambda_T^3}, \end{aligned} \tag{2.6}$$

where λ_T is the thermal de Broglie wavelength associated with the finite extent of each particle wave packet

$$\lambda_T = \sqrt{\frac{2\pi\hbar^2}{m k_B T}}, \tag{2.7}$$

$z(\mathbf{r}) = \exp\left(\mu - V(\mathbf{r})\right)/k_B T$ is the fugacity, and $g_{3/2}$ is the polylogarithm function defined by

$$g_\gamma(z) = \sum_{n=1}^{\infty} \frac{z^n}{n^\gamma}. \tag{2.8}$$

2.1.1 Uniform trapping potential

In a uniform system the three dimensional free particle density of states is given by

$$g(\epsilon) = \frac{V m^{3/2}}{2^{1/2}\pi^2\hbar^3} \epsilon^{1/2}, \tag{2.9}$$

where V is the volume of the system. Inserting equation (2.9) into (2.2), gives the result (2.6), with an external potential $V(\mathbf{r}) = 0$, as expected. For a uniform ideal gas $\mu \leq 0$, and as μ approaches zero the fugacity $z(\mathbf{r})$ approaches unity, and hence $g_{3/2}(z(\mathbf{r}))$ tends to $g_{3/2}(1) = 2.612$. This gives an upper bound on the density of particles in the excited states and gives the criteria for Bose condensation as

$$n\lambda_T^3 > \max(n_{\text{ex}}\lambda_T^3) = 2.612, \tag{2.10}$$

where n is the total particle density. This equation illustrates that condensation occurs when the inter-particle spacing, $n^{-1/3}$, becomes smaller than the wavelength associated with each particle, λ_T.

The critical temperature at which condensation occurs is given by (2.6) with $z(\mathbf{r}) = 1$ and $n_{\text{ex}} = n$,

$$T_c = \frac{2\pi\hbar^2}{mk_B}\left(\frac{n}{g_{3/2}(1)}\right)^{2/3}. \tag{2.11}$$

This gives the temperature at which condensation first occurs; combining (2.6) with (2.11) gives the functional form of the condensate fraction for $T \leq T_c$

$$\frac{N_0}{N} = 1 - \left(\frac{T}{T_c}\right)^{3/2}. \tag{2.12}$$

2.1.2 Harmonic trapping potential

To first order we can expand any trap in three dimensions around the minimum and approximate it to a harmonic trap with confining potential

$$V(\mathbf{r}) = \frac{m}{2}(\omega_x^2 x^2 + \omega_y^2 y^2 + \omega_z^2 z^2). \tag{2.13}$$

This yields a quantised energy spectrum of single-particle energies that are labeled by the non-negative quantum numbers n_x, n_y, n_z,

$$\epsilon_{n_x,n_y,n_z} = \hbar(n_x\omega_x + n_y\omega_y + n_z\omega_z) + \epsilon_0, \tag{2.14}$$

where ϵ_0 is the zero-point energy $\hbar(\omega_x + \omega_y + \omega_z)/2$. The onset of condensation in a harmonic trap therefore occurs at $\mu = \epsilon_0$. Using the harmonic oscillator quantum numbers, equation (2.2) can be written as

$$N = N_0 + \int_0^\infty \frac{dn_x dn_y dn_z}{\exp\left[\hbar(\omega_x n_x + \omega_y n_y + \omega_z n_z)/k_B T\right] - 1}, \tag{2.15}$$

where again we approximate the sum to an integral, assuming $k_B T \gg \hbar\omega_0$, where $\omega_0 = (\omega_x\omega_y\omega_z)^{1/3}$ is the geometric mean of the trapping frequencies. This integral can

be performed by changing variables $\hbar\omega_i n_i/k_B T = \tilde{n}_i$ to give

$$N = N_0 + g_3(1)\left(\frac{k_B T}{\hbar\omega_0}\right)^3. \tag{2.16}$$

With the condition $N_0 = 0$, we rearrange this expression to find the critical temperature

$$T_c = \frac{\hbar\omega_0}{k_B}\left(\frac{N}{g_3(1)}\right)^{1/3}, \tag{2.17}$$

and the functional form of the condensate fraction for $T \leq T_c$

$$\frac{N_0}{N} = 1 - \left(\frac{T}{T_c}\right)^3. \tag{2.18}$$

For an ideal gas in the absence of interactions, the density distribution of the condensate will reflect the ground state wavefunction $\psi_0(\mathbf{r})$, which for a harmonic trap is given by

$$n_0(\mathbf{r}) = N_0|\psi_0(\mathbf{r})|^2 = N_0\left(\frac{m\omega_0}{\pi\hbar}\right)^{3/2}\exp\left[-\left(\frac{x}{a_x}\right)^2 - \left(\frac{y}{a_y}\right)^2 - \left(\frac{z}{a_z}\right)^2\right], \tag{2.19}$$

where $a_i = \sqrt{\frac{\hbar}{m\omega_i}}$ is the oscillator length. Neglecting the zero point energy, ϵ_0, the density distribution of the excited states for $T < T_c$ is given by (2.6) with $\mu = 0$

$$n_{\rm ex}(\mathbf{r}) = \frac{g_{3/2}(e^{-V(\mathbf{r})/k_B T})}{\lambda_T^3} = \frac{g_{3/2}(\exp\left[-m(\omega_x x^2 + \omega_y y^2 + \omega_z z^2)/2k_B T\right])}{\lambda_T^3}. \tag{2.20}$$

For typical experimental parameters, the condensate width is much narrower than the width of the thermal distribution. As a result, in harmonically trapped gases, condensation occurs both in momentum space, with the macroscopic occupation of the ground state, and in real space, with the condensate appearing as a sharp peak in the central region of the density distribution.

2.2 Weakly interacting Bose gas

So far we have considered the ideal Bose gas, which even in the absence of interactions exhibits a purely quantum-statistical phase transition to BEC. In reality particles will always interact, and even in the weakly interacting limit a real Bose gas behaves qualitatively differently from an ideal Bose gas. Interactions between atoms will modify the equilibrium shape and dynamics of the condensate, and play an essential role in the superfluid properties studied in this thesis.

2.2.1 Basic scattering theory

Here we outline the basic scattering theory in the context of ultracold gases, which has been extensively covered in textbooks and lectures [18–20]. We consider a collision

process between two particles, 1 and 2, of mass m, interacting through the spherically symmetric potential $V(\mathbf{r}_1 - \mathbf{r}_2)$. Defining the relative coordinates $\mathbf{r} = \mathbf{r}_1 - \mathbf{r}_2$ and $\mathbf{p} = (\mathbf{p}_1 - \mathbf{p}_2)/2$, the Hamiltonian for the relative motion is given by

$$\left(\frac{\hat{p}^2}{2m_r} + V(\hat{\mathbf{r}})\right)\psi_{\mathbf{k}}(\mathbf{r}) = E_{\mathbf{k}}\psi_{\mathbf{k}}(\mathbf{r}), \tag{2.21}$$

where $m_r = m/2$ is the reduced mass, and $E_{\mathbf{k}} = \hbar^2 k^2/2m_r$ is the incident energy. Assuming $V(\mathbf{r}) \to 0$ at large distances we look for solutions at $|\mathbf{r}| \to \infty$ with the asymptotic form:

$$\psi_{\mathbf{k}}(\mathbf{r}) \simeq e^{i\mathbf{k}\cdot\mathbf{r}} + f(\theta)\frac{e^{ikr}}{r}, \tag{2.22}$$

where θ is the angle between the incoming and outgoing waves. The physical meaning of this collision state is the superposition of an incident plane wave with momentum $\mathbf{k}$, and a scattered wave function. The form of the scattering potential, $V(\mathbf{r})$, determines the scattering amplitude $f(\theta)$. At the very low energies considered in ultracold gases experiments, only partial waves with zero angular momentum ($l = 0$) will contribute to the outgoing wavefunction. In this s-wave scattering limit the scattering amplitude has no angular dependence and approaches a constant, denoted by $-a$. Therefore in the low energy, $k \to 0$, limit, the wavefunction becomes

$$\psi(\mathbf{r}) = 1 - \frac{a}{r}. \tag{2.23}$$

The constant a is the scattering length, and gives the intercept of the asymptotic wavefunction with the r axis. To relate the scattering length and the interatomic potential $V(\mathbf{r})$, we must solve (2.21) and take the same low energy limit. Rewriting (2.21) as

$$(\nabla^2 + k^2)\psi_{\mathbf{k}}(\mathbf{r}) = U(\mathbf{r})\psi_{\mathbf{k}}(\mathbf{r}), \tag{2.24}$$

where $U(\mathbf{r}) = 2m_r V(\mathbf{r})/\hbar^2$, the general solution can be written as

$$\psi_{\mathbf{k}}(\mathbf{r}) = \phi_{\mathbf{k}}(\mathbf{r}) + \int d^3\mathbf{r}' G_0(\mathbf{r} - \mathbf{r}')U(\mathbf{r}')\psi_{\mathbf{k}}(\mathbf{r}'), \tag{2.25}$$

where $\phi_{\mathbf{k}}(\mathbf{r}) = e^{i\mathbf{k}.\mathbf{r}}$ is the solution to the free particle Hamiltonian, $(\nabla^2 + k^2)\phi_{\mathbf{k}}(\mathbf{r}) = 0$, and $G_0(\mathbf{r})$ is a Green's function of the Laplace operator

$$(\nabla^2 + k^2)G_0(\mathbf{r}) = \delta^3(\mathbf{r}) \qquad \Longrightarrow \qquad G_0(\mathbf{r}) = -\frac{1}{4\pi}\frac{e^{ikr}}{r}. \tag{2.26}$$

To compare to (2.22), we take the far field limit where r is much greater than the range of the interaction.

$$|\mathbf{r} - \mathbf{r}'| \simeq r - \frac{\mathbf{r}\cdot\mathbf{r}'}{r} \qquad \Longrightarrow \qquad \frac{e^{ik|\mathbf{r}-\mathbf{r}'|}}{|\mathbf{r} - \mathbf{r}'|} \simeq \frac{e^{ikr}}{r}e^{-i\mathbf{k}'\cdot\mathbf{r}'}, \tag{2.27}$$

where the vector $\mathbf{k}' = k\hat{\mathbf{r}}$ is orientated along the direction of the scattered particle. Within this approximation we obtain the far field form of (2.25),

$$\begin{aligned}\psi_{\mathbf{k}}(\mathbf{r}) &= \phi_{\mathbf{k}}(\mathbf{r}) - \frac{e^{ikr}}{4\pi r}\int d^3\mathbf{r}' e^{-i\mathbf{k}'\cdot\mathbf{r}'}U(\mathbf{r}')\psi_{\mathbf{k}}(\mathbf{r}') \\ &= \phi_{\mathbf{k}}(\mathbf{r}) - \frac{e^{ikr}}{4\pi r}\left\langle\phi_{\mathbf{k}'}\right| U(\mathbf{r}')\left|\psi_{\mathbf{k}}\right\rangle, \end{aligned} \tag{2.28}$$

and by direct comparison with (2.22), we identify $f(\theta)$ as

$$f(\theta) = -\frac{1}{4\pi}\left\langle\phi_{\mathbf{k}'}\right| U(\mathbf{r}')\left|\psi_{\mathbf{k}}\right\rangle \equiv -\frac{1}{4\pi}\int d^3\mathbf{r}' e^{-i\mathbf{k}'\cdot\mathbf{r}'}U(\mathbf{r}')\psi_{\mathbf{k}}(\mathbf{r}'). \tag{2.29}$$

In the low energy limit $|\mathbf{k}'.\mathbf{r}'| \ll 1$, and we can replace $e^{i\mathbf{k}'.\mathbf{r}'}$ by 1, removing the angular dependence in the scattering amplitude. Equation (2.25) is an iterative equation, however making the first Born approximation by inserting the incoming wave on the right hand side gives $f_{\text{Born}}(\theta) = \left\langle\phi'_{\mathbf{k}}\right| U(\mathbf{r}')\left|\phi_{\mathbf{k}}\right\rangle/4\pi$. Taking the $k \to 0$ limit we obtain an expression for the s-wave scattering length,

$$a = \frac{m}{4\pi\hbar^2}\int d^3\mathbf{r} V(\mathbf{r}). \tag{2.30}$$

We therefore see that in the low energy limit the details of the interaction potential are integrated out and can be replaced by an effective potential,

$$V(\mathbf{r} - \mathbf{r}') = g\delta(\mathbf{r} - \mathbf{r}'), \tag{2.31}$$

where the coupling constant, g, and the s-wave scattering length, a, are related by

$$g = \frac{4\pi\hbar^2 a}{m}. \tag{2.32}$$

Low energy collisions are therefore characterised by a single parameter, the s-wave scattering length, independent of the details of the two-body potential.

2.2.2 Gross-Pitaevskii equation

The many-body Hamiltonian describing N interacting bosons confined in an external potential $V_{\text{ext}}(\mathbf{r})$ is given by [16],

$$\begin{aligned}\hat{H} = &\int d\mathbf{r}\hat{\Psi}^\dagger(\mathbf{r})\left[-\frac{\hbar^2}{2m}\nabla^2 + V_{\text{ext}}(\mathbf{r})\right]\hat{\Psi}(\mathbf{r}) \\ &+ \frac{1}{2}\int d\mathbf{r}d\mathbf{r}'\hat{\Psi}^\dagger(\mathbf{r})\hat{\Psi}^\dagger(\mathbf{r}')V(\mathbf{r}-\mathbf{r}')\hat{\Psi}(\mathbf{r}')\hat{\Psi}(\mathbf{r}),\end{aligned} \tag{2.33}$$

where $\hat{\Psi}^\dagger(\mathbf{r})$ and $\hat{\Psi}(\mathbf{r})$ are the creation and annihilation operators for a boson at position $\mathbf{r}$, and $V(\mathbf{r} - \mathbf{r}')$ is the two-body interatomic potential. The operators $\hat{\Psi}(\mathbf{r})$ and $\hat{\Psi}^\dagger(\mathbf{r})$

obey the usual Bose commutation relations:

$$[\hat{\Psi}(\mathbf{r}), \hat{\Psi}^\dagger(\mathbf{r}')] = \delta(\mathbf{r}-\mathbf{r}'), \quad [\hat{\Psi}(\mathbf{r}), \hat{\Psi}(\mathbf{r}')] = 0, \quad \text{and} \quad [\hat{\Psi}^\dagger(\mathbf{r}), \hat{\Psi}^\dagger(\mathbf{r}')] = 0. \tag{2.34}$$

The time evolution of the field operator is given by the Heisenberg equation with the many-body Hamiltonian:

$$\begin{aligned} i\hbar\frac{\partial}{\partial t}\hat{\Psi}(\mathbf{r},t) &= [\hat{\Psi}, \hat{H}] \\ &= \left[-\frac{\hbar^2\nabla^2}{2m} + V_{\text{ext}}(\mathbf{r}) + \int d\mathbf{r}'\hat{\Psi}^\dagger(\mathbf{r}',t)V(\mathbf{r}'-\mathbf{r})\hat{\Psi}(\mathbf{r}',t)\right]\hat{\Psi}(\mathbf{r},t). \end{aligned} \tag{2.35}$$

For $T \ll T_c$, when the ground state is macroscopically occupied, we may use the Bogoliubov mean-field description [21] and replace the field operator by

$$\hat{\Psi}(\mathbf{r},t) = \Phi(\mathbf{r},t) + \delta\hat{\Psi}(\mathbf{r},t), \tag{2.36}$$

where $\Phi(\mathbf{r},t) = \langle\hat{\Psi}(\mathbf{r},t)\rangle$ is a complex function defined as the expectation value of the field operator, and $\delta\hat{\Psi}(\mathbf{r},t)$ is a small perturbation due to atoms not in the condensate. The function $\Phi(\mathbf{r},t)$ is an order parameter and is referred to as the wavefunction of the condensate. For the mean of the field operator, $\langle\hat{\Psi}(\mathbf{r},t)\rangle$, to be non-zero, a well defined phase relation must be enforced, otherwise the average over all phases of the wavefunction would result in zero. From this, a generalised criterion for Bose condensation can be formed as a constraint on the first order spatial coherence function $G^{(1)}(\mathbf{r},\mathbf{r}') = \langle\hat{\Psi}^\dagger(\mathbf{r})\hat{\Psi}(\mathbf{r}')\rangle$ [22, 23],

$$\lim_{|\mathbf{r}-\mathbf{r}'|\to\infty}\langle\hat{\Psi}^\dagger(\mathbf{r})\hat{\Psi}(\mathbf{r}')\rangle = \Phi^*(\mathbf{r})\Phi(\mathbf{r}') \neq 0. \tag{2.37}$$

Condensation can therefore be viewed as the onset of long-range off-diagonal order.

To zeroth order, the excited state perturbation can be ignored, and the field operator is simply replaced by the condensate wavefunction. At low energies where s-wave collisions dominate, the interatomic potential, $V(\mathbf{r}'-\mathbf{r})$, can be replaced by the effective potential (2.31). Using these two approximations we obtain the time dependent Gross-Pitaevski equation (GPE)

$$i\hbar\frac{\partial}{\partial t}\Phi(\mathbf{r},t) = \left(-\frac{\hbar^2\nabla^2}{2m} + V_{\text{ext}}(\mathbf{r}) + g|\Phi(\mathbf{r},t)|^2\right)\Phi(\mathbf{r},t). \tag{2.38}$$

The condensate density and number are then given by

$$n_0(\mathbf{r},t) = |\Phi(\mathbf{r},t)|^2 \qquad \Longrightarrow \qquad N_0 = \int d\mathbf{r}|\Phi(\mathbf{r},t)|^2. \tag{2.39}$$

Separating out the time dependence of the condensate wave function [24], $\Phi(\mathbf{r},t) = \Phi(\mathbf{r})e^{-i\mu t/\hbar}$, where μ is the chemical potential, we obtain the time-independent GPE

$$\left(-\frac{\hbar^2\nabla^2}{2m} + V_{\text{ext}}(\mathbf{r}) + g|\Phi(\mathbf{r})|^2\right)\Phi(\mathbf{r}) = \mu\Phi(\mathbf{r}). \tag{2.40}$$

This has the form of a nonlinear Schrödinger equation, where the effect of interactions is to add a mean field potential, proportional to the condensate density.

2.2.3 The Thomas-Fermi regime

For most experimental parameters where N_0 is sufficiently large, the kinetic energy term is much smaller than the interaction energy term and can be neglected [19]. In this regime the GPE simplifies to

$$\left[V_{\text{ext}}(\mathbf{r}) + g|\Phi(\mathbf{r})|^2\right]\Phi(\mathbf{r}) = \mu\Phi(\mathbf{r}), \tag{2.41}$$

and the condensate density to

$$\begin{aligned} n_0(\mathbf{r}) = |\Phi(\mathbf{r})|^2 &= \frac{\mu - V_{\text{ext}}(\mathbf{r})}{g} \quad \text{for} \quad \mu > V_{\text{ext}}(\mathbf{r}) \\ &= 0 \qquad\qquad\quad \text{for} \quad \mu < V_{\text{ext}}(\mathbf{r}). \end{aligned} \tag{2.42}$$

For the case of a harmonic trap the condensate density profile is parabolic

$$n_0(\mathbf{r}) = \frac{\mu}{g}\left(1 - \frac{x^2}{R_x^2} - \frac{y^2}{R_y^2} - \frac{z^2}{R_z^2}\right), \tag{2.43}$$

where $R_i = \sqrt{2\mu/m\omega_i^2}$ is the Thomas-Fermi radius. The chemical potential, μ, is found from normalising the condensate wavefunction according to (2.39)

$$\mu = \frac{\hbar\omega_0}{2}\left(\frac{15N_0a}{a_0}\right)^{2/5}, \tag{2.44}$$

where $a_0 = \sqrt{\hbar/m\omega_0}$ is the harmonic oscillator length associated with the mean trapping frequency. In reality the condensate wavefunction will deviate from this inverted parabola at the surface, otherwise the kinetic energy associated with the discontinuity at the Thomas-Fermi radius diverges.

2.3 Excitation spectrum

In deriving the GPE we made use of the zeroth order Bogoliubov approximation by treating the wavefunction of the condensate as a classical field. To take into account fluctuations about the condensed state, we now retain the first order perturbation in (2.36), $\delta\hat{\Psi}(\mathbf{r},t)$, which is assumed to be small. To conserve particle number on average, the appropriate operator to consider is $\hat{K} = \hat{H} - \mu\hat{N}$, where the Hamiltonian, $\hat{H}$, is the

same as (2.33). To second order in the fluctuations

$$\begin{aligned}\hat{K} = \hat{H} - \mu\hat{N} =& E_0 - \mu N_0 + \int d\mathbf{r}\Bigg(-\delta\hat{\Psi}^\dagger(\mathbf{r},t)\frac{\hbar^2}{2m}\nabla^2\delta\hat{\Psi}(\mathbf{r},t) \\ &+ [V_{\text{ext}}(\mathbf{r}) + 2g|\Phi(\mathbf{r},t)|^2 - \mu]\delta\hat{\Psi}^\dagger(\mathbf{r},t)\delta\hat{\Psi}(\mathbf{r},t) \\ &+ \frac{g}{2}\left(\Phi(\mathbf{r},t)^2[\delta\hat{\Psi}^\dagger(\mathbf{r},t)]^2 + \Phi^*(\mathbf{r},t)^2[\delta\hat{\Psi}(\mathbf{r},t)]^2\right)\Bigg),\end{aligned} \tag{2.45}$$

where E_0 is the energy of the condensate wavefunction only. The equations of motion for the operators $\delta\hat{\Psi}$ and $\delta\hat{\Psi}^\dagger$ are given by

$$i\hbar\frac{\partial\delta\hat{\Psi}}{\partial t} = [\delta\hat{\Psi}, K] \qquad \text{and} \qquad i\hbar\frac{\partial\delta\hat{\Psi}^\dagger}{\partial t} = [\delta\hat{\Psi}^\dagger, K]. \tag{2.46}$$

This gives the two coupled equations:

$$i\hbar\frac{\partial\delta\hat{\Psi}}{\partial t} = \left[-\frac{\hbar^2}{2m}\nabla^2 + V_{\text{ext}}(\mathbf{r}) + 2n_0(\mathbf{r})g - \mu\right]\delta\hat{\Psi} + g\Phi(\mathbf{r})^2\delta\hat{\Psi}^\dagger \tag{2.47}$$

$$-i\hbar\frac{\partial\delta\hat{\Psi}^\dagger}{\partial t} = \left[-\frac{\hbar^2}{2m}\nabla^2 + V_{\text{ext}}(\mathbf{r}) + 2n_0(\mathbf{r})g - \mu\right]\delta\hat{\Psi}^\dagger + g\Phi^*(\mathbf{r})^2\delta\hat{\Psi} \tag{2.48}$$

To solve these equations we look for solutions which are periodic in time, of the form

$$\delta\hat{\Psi}(\mathbf{r},t) = \sum_i [u_i(\mathbf{r})\alpha_i e^{-i\epsilon_i t/\hbar} - v_i^*(\mathbf{r})\alpha_i^\dagger e^{i\epsilon_i t/\hbar}], \tag{2.49}$$

where the operators $\alpha_i^\dagger$ and α_i create and destroy bosons in the i^{th} excited state. The requirement that $\alpha_i^\dagger$ and α_i satisfy the Bose commutation relations leads to the condition

$$\int d\mathbf{r}[|u_i(\mathbf{r})|^2 - |v_i(\mathbf{r})|^2] = 1. \tag{2.50}$$

Noting that the condensate wavefunction is real, we obtain the Bogoliubov equations:

$$\left[-\frac{\hbar^2}{2m}\nabla^2 + V_{\text{ext}}(\mathbf{r}) + 2n_0(\mathbf{r})g - \mu - \epsilon_i\right]u_i(\mathbf{r}) - n_0(\mathbf{r})gv_i(\mathbf{r}) = 0 \tag{2.51}$$

$$\left[-\frac{\hbar^2}{2m}\nabla^2 + V_{\text{ext}}(\mathbf{r}) + 2n_0(\mathbf{r})g - \mu + \epsilon_i\right]v_i(\mathbf{r}) - n_0(\mathbf{r})gu_i(\mathbf{r}) = 0 \tag{2.52}$$

Solving to find the eigenvalues ϵ_i, the operator $\hat{K}$ can then be expressed in the form $\hat{K} = \sum_i \alpha_i^\dagger\alpha_i + \text{constant}$, which simply has the form of the excitation energy times the number of excitations. This is most easily solved in the case of a uniform system where the excitations have the form of plane waves.

2.3.1 Excitations in a uniform Bose gas

For a uniform Bose gas, $V_{\text{ext}}(\mathbf{r}) = 0$, and from (2.42) the chemical potential $\mu = n_0 g$. From the translational invariance of the system the solutions to (2.51) and (2.52) can

be written in the from

$$u_i(\mathbf{r}) = u_q \frac{e^{i\mathbf{q}\cdot\mathbf{r}}}{\sqrt{V}} \qquad \text{and} \qquad v_i(\mathbf{r}) = v_q \frac{e^{i\mathbf{q}\cdot\mathbf{r}}}{\sqrt{V}}, \tag{2.53}$$

where V is the volume of the system. Substituting these solutions into the Bogoliubov equations gives

$$\left(\epsilon_q^0 + n_0 g - \epsilon_q\right) u_q - n_0 g v_q = 0 \tag{2.54}$$

$$\left(\epsilon_q^0 + n_0 g + \epsilon_q\right) v_q - n_0 g u_q = 0, \tag{2.55}$$

where $\epsilon_q^0 = \hbar^2 q^2/2m$ is the free particle energy. This equation can be solved by the requirement that the determinant of the coefficients of u_q and v_q equals zero, leading to the excitation energy

$$\epsilon_q = \sqrt{\left(\epsilon_q^0 + n_0 g\right)^2 - (n_0 g)^2}, \tag{2.56}$$

and using the normalisation condition (2.50), we find that

$$u_q^2 = \frac{1}{2}\left(\frac{\epsilon_q^0 + n_0 g}{\epsilon_q} + 1\right) \tag{2.57}$$

$$v_q^2 = \frac{1}{2}\left(\frac{\epsilon_q^0 + n_0 g}{\epsilon_q} - 1\right), \tag{2.58}$$

where the phase freedom of the solution permits us to choose u_q and v_q to be real and positive. Having found the excitation spectrum for the uniform system, we use the expressions for u_q and v_q in the first order perturbation operator

$$\delta\hat{\Psi}(\mathbf{r}, t) = \sum_{q\neq 0}\left[u_q \frac{e^{i\mathbf{q}\cdot\mathbf{r}}}{\sqrt{V}}\alpha_q e^{-i\epsilon_q t/\hbar} - v_q \frac{e^{-i\mathbf{q}\cdot\mathbf{r}}}{\sqrt{V}}\alpha_q^\dagger e^{i\epsilon_q t/\hbar}\right], \tag{2.59}$$

to express the number conserving Hamiltonian (2.45) in terms of the operators α_q and $\alpha_q^\dagger$:

$$\hat{K} = E_0 - \mu N_0 + \sum_{q\neq 0}\epsilon_q \alpha_q^\dagger \alpha_q - \frac{1}{2}\sum_{q\neq 0}\left(\epsilon_q^0 + g n_0 - \epsilon_q\right). \tag{2.60}$$

It can now be seen that the system behaves as a collection of non-interacting bosons with an energy given by the Bogoliubov spectrum (2.56). In the long wavelength limit ($q^2 \ll 2mgn_0/\hbar^2$) the dispersion relation reduces to a linear function of q,

$$\epsilon_q \simeq c\hbar q, \tag{2.61}$$

and the spectrum is sound like. Excitations are phonons and the speed of sound is given by

$$c = \sqrt{\frac{\mu}{m}}. \tag{2.62}$$

In the short wavelength limit ($q^2 \gg 2mgn_0/\hbar^2$) the spectrum reduces to that of a free particle in the mean field potential of the other atoms

$$\epsilon_q \simeq \epsilon_q^0 + gn_0. \tag{2.63}$$

The transition from phonon to free particle excitation occurs when the wavelength of the excitation $\sim \hbar/\sqrt{2mn_0g}$. This length scale is termed the healing length ξ, and denotes the shortest distance over which the wavefunction tends to its bulk value when subject to a local perturbation. If we consider the density varying from 0 to n over a length scale ξ, then the competing kinetic and potential terms will balance when

$$\frac{\hbar^2}{2m\xi^2} = ng \qquad \Longrightarrow \qquad \xi^2 = \frac{1}{8\pi na}. \tag{2.64}$$

We can therefore understand that on length scales larger than ξ, the atoms are able to move collectively as phonons, whereas on shorter scales they will behave as free particles.

Thermal component

We now consider the depletion of the condensate due to excitations. The total particle number is given by

$$\hat{N} = N_0 + \int d\mathbf{r}\delta\Psi^\dagger(\mathbf{r})\delta\Psi(\mathbf{r}). \tag{2.65}$$

Using the form of the perturbation wavefunction in terms of plane waves, this takes the form

$$\hat{N} = N_0 + \sum_{q\neq 0} v_q^2 + \sum_{q\neq 0}(v_q^2 + u_q^2)\alpha_q^\dagger\alpha_q, \tag{2.66}$$

where we have made use of the Bose commutation relations for α_q. This expression shows that the condensate is depleted due to interactions, even at $T = 0$ when no real excitations are present. The two-body interaction mixes the ground state components with higher energy states, and hence the ground state of the interacting gas does not have all atoms occupying the zero momentum state. The zero temperature depletion of the condensate is then given by

$$\frac{n_{\rm ex}}{n} = \frac{8}{3\sqrt{\pi}}\sqrt{na^3}, \tag{2.67}$$

which for most experimental parameters is less than a percent.

When a real excitation is added to the system, keeping the total number fixed, the condensate is depleted by an amount

$$\nu_q = u_q^2 + v_q^2 = \frac{\epsilon_q^0 + gn_0}{\epsilon_q}. \tag{2.68}$$

For large momenta, when the excitations behave as free particles, this value tends towards unity as expected. For non-zero temperatures we can calculate the thermal distribution of such excitations using the Bose-Einstein distribution function, f_q (2.1). Since the addition of an excitation does not change the total particle number, the chemical potential is set to zero. From this, we get the thermal depletion of the condensate density as

$$n_{\text{ex}}(T) = n_{\text{ex}}(T=0) + \int \frac{d\mathbf{q}}{(2\pi)^3} \frac{\epsilon_q^0 + gn_0}{\epsilon_q} \frac{1}{\exp(\epsilon_q/k_BT) - 1}. \tag{2.69}$$

In deriving this expression we have used the Bogoliubov approximation, which assumes the system is close to its ground state, and excitations are independent of one another. As a result this expression is only valid at low temperatures; for temperatures closer to the transition temperatures we must include higher order terms corresponding to interactions between excitations. Such extensions are used in the Hartree-Fock and Popov approximations, as explained in [16, 19].

2.4 Bose-Einstein condensation and superfluidity

The phenomena of superfluidity is fundamentally linked with the existence of a condensate; a single macroscopically occupied quantum state. In 1938, London published the idea that superfluidity could be understood intuitively as an experimental manifestation of BEC [7]. Superfluid motion, viewed as the motion of the condensed particles as a whole, is therefore a collective phenomenon in which particles move together to preserve the macroscopic occupation of a single state. Modification of the entire condensate wavefunction would have a macroscopic energy cost, therefore superfluid flow can only be altered by depletion of the condensate as a result of the creation of excitations. Below a certain critical velocity the energy to create such excitations is not available, and the superfluid is able to flow unperturbed by its environment, and hence without viscosity.

2.4.1 The Landau criterion

In the previous section we calculated the excitation spectrum for the interacting Bose gas. Landau showed that if the excitation spectrum satisfies certain criteria, the motion of the fluid does not cause energy dissipation [25]. To see this, consider the motion of a uniform condensate, flowing at velocity $\mathbf{v}_s$. In the frame of reference stationary with respect to the condensate, the excitation spectrum is the same as that found before in equation (2.56). To find the Hamiltonian in the frame of the observer we use a Galilean

transformation to obtain

$$\begin{aligned} H' &= \sum_i \frac{(\mathbf{p}_i + m\mathbf{v}_s)^2}{2m} + \frac{1}{2}\sum_{i\neq j} V(\mathbf{r}_i - \mathbf{r}_j) \\ &= \sum_i \frac{(\mathbf{p}_i)^2}{2m} + \frac{1}{2}\sum_{i\neq j} V(\mathbf{r}_i - \mathbf{r}_j) + \mathbf{p}\cdot\mathbf{v}_s + \frac{Nmv_s^2}{2}, \end{aligned} \tag{2.70}$$

where $\mathbf{p} = \sum_i \mathbf{p}_i$ is the net momentum of the particles in the condensate frame. For the fluid in its ground state ($E = E_0$, the energy of the pure condensate, and $\mathbf{p} = 0$) the energy of the system in the frame of the observer is

$$E_0' = E_0 + \frac{Nmv_s^2}{2}. \tag{2.71}$$

If we now add a single excitation to the ground state of energy ϵ_p and momentum $\mathbf{p}$ as measured in the condensate frame, the new system energy in the observer frame is

$$E_1' = E_0 + \frac{Nmv_s^2}{2} + \epsilon_p + \mathbf{p}\cdot\mathbf{v}_s = E_0' + \epsilon_p + \mathbf{p}\cdot\mathbf{v}_s. \tag{2.72}$$

It therefore follows that an excitation cannot be created provided

$$\epsilon_p + \mathbf{p}\cdot\mathbf{v}_s > 0. \tag{2.73}$$

This is the Landau criterion, and for flow without viscosity it needs to hold across the entire spectrum for all $\mathbf{p}$. If the Landau criterion is violated, the relevant excitation will have negative energy in the observer frame, and therefore will grow exponentially with time. Energy and momentum from the coherent motion of the condensate will be transferred to incoherent quasi-particles, and the motion of the superfluid will become unstable. This criterion is more commonly presented as a critical velocity

$$v_c = \min\left[\frac{\epsilon_p}{p}\right], \tag{2.74}$$

where for $v_s < v_c$, there is no mechanism for transfer of superfluid flow to heat, and the fluid flows without viscosity. The ground state of any system is clearly for the condensate to be stationary with respect to the laboratory frame. Superfluid flow is therefore a long-lived metastable state, protected from decay to the true ground state by the lack of low energy excitation states.

Taking the excitation spectrum for an interacting uniform condensate, (2.56), plotted in figure 2.1, we see that the critical velocity is the speed of sound, corresponding to exciting long wavelength phonons. Therefore a uniform BEC has a non-zero critical velocity, and at low flow velocities will behave as a superfluid. The concepts of superfluidity and Bose-Einstein condensation are therefore fundamentally connected, with the Landau criterion linking the onset of viscosity in a superfluid to the creation of excitations in a condensate. For the case of a non-interacting gas, the spectrum is

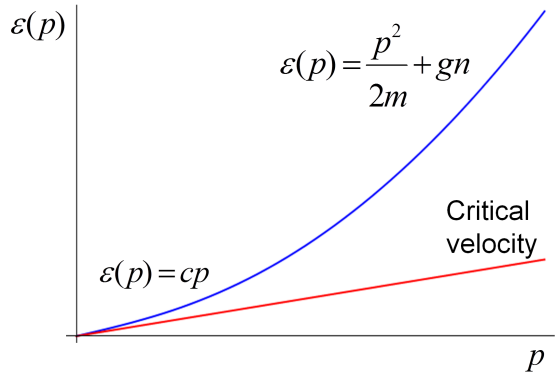

Figure 2.1: Excitation spectrum for the uniform weakly interacting Bose gas: This illustrates that the Landau critical velocity is equal to the speed of sound, and viscosity is therefore brought about by the excitation of long wavelength phonon modes.

simply that of a free particle $\epsilon(p) = p^2/2m$, and hence the critical velocity disappears. Interparticle interactions are therefore essential for the existence of superfluidity, and intuitively we would then expect that decreasing the strength of interactions must decrease the critical velocity.

In reality the Landau criterion is actually only a necessary, but not sufficient condition for superfluid flow without viscosity, with many systems exhibiting lower energy excitations involving vortex like motion of the superfluid leading to superfluid turbulence and unstable flow. In the classic experiments on strongly interacting He II flowing through narrow channels, it was found that the critical velocities were typically around two orders of magnitude lower than those expected from the Landau criterion, which in this case corresponds to roton excitations. As discussed in Section 2.4.3, this is due to low energy vortex states which involve a macroscopic transformation of the condensate wavefunction, and therefore were not initially predicted by the perturbative method used by Bogoliubov. As first predicted by Feynman, vortices nucleate inside the channel and carry energy away from the superfluid via the phase-slip mechanism [26, 27]. The critical velocity for such a process is still set by equation (2.74), only now the relevant energy and momentum are those of the vortex state.

2.4.2 Superfluid component

In describing the theory of BEC we used a two-component picture of the particle density, where the cloud could be considered to be composed of a condensed component and a thermal component. Superfluids are also described by a two-component model where the superfluid is made up of two interpenetrating fluids: the normal fluid associated with excitations, and the superfluid which is associated with the condensate. Since particles are converted between the two components the two fluids are not physically distinct, and one cannot separate the fluid into two such parts. More accurately we can say that a quantum fluid can execute two motions at once, each with its own effective mass. One of these motions is normal (ie. has the same properties as an ordinary viscous fluid), but the other is the motion of a superfluid. This concept is referred to as the two-fluid model of superfluids and is used to successfully explain many observed

phenomena in liquid helium experiments, as well as predict the phenomenon of second sound.

In many ultracold gas experiments it is common to simply equate the condensed fraction and the superfluid fraction, however in general these two quantities take very different values. Although superfluidity and condensation are strongly related, the definition of superfluidity as dissipationless flow and the definition of condensation as the macroscopic occupation of the ground state are clearly distinct. For low temperature ^{4}He experiments the condensed and superfluid fractions are believed to be approximately 10% and 100% respectively [12], while in two-dimensions the superfluid fraction can be non-zero even if the condensate vanishes [28]. To formulate a strict expression for the superfluid and normal component we consider a gas at rest and calculate the momentum density carried by the excitations of the system

$$\mathbf{j}_{\text{ex}} = \int \frac{d\mathbf{p}}{(2\pi\hbar)^3} \mathbf{p} f_{\mathbf{p}}, \tag{2.75}$$

where, as in (2.69), we have used the Bose-Einstein function to find the distribution of thermal states. Transforming to a frame moving with a velocity $-\mathbf{v}_s$, in which the condensate is now moving with velocity $\mathbf{v}_s$, the total momentum density in this new frame is given by

$$\mathbf{j} = \rho \mathbf{v}_s + \mathbf{j}_{\text{ex}}, \tag{2.76}$$

where $\rho = nm$ is the total mass density. Using (2.72), the energy of an excitation in this moving frame is given by $\epsilon_p - \mathbf{p}.(\mathbf{v}_n - \mathbf{v}_s)$, where $\mathbf{v}_n$ is the velocity of the excitation in the original frame. As a result this transformed excitation energy enters the Bose-Einstein function and the momentum density of the excitation spectrum is given by

$$\mathbf{j}_{\text{ex}} = \rho_n(|\mathbf{v}_n - \mathbf{v}_s|)(\mathbf{v}_n - \mathbf{v}_s), \tag{2.77}$$

where

$$\rho_n(v) = \int \frac{d\mathbf{p}}{(2\pi\hbar)^3} \frac{\mathbf{p}\cdot\mathbf{v}}{v^2} \frac{1}{\exp\left[(\epsilon_p - \mathbf{p}\cdot\mathbf{v})/k_B T\right] - 1}. \tag{2.78}$$

Substituting this into the expression for the total momentum density (2.76), we obtain

$$\mathbf{j} = \rho_n(\mathbf{v}_n - \mathbf{v}_s) + \rho \mathbf{v}_s. \tag{2.79}$$

If we define the superfluid density as the difference between the total and normal densities, $\rho_s = \rho - \rho_n$, the total momentum density can be written in the form

$$\mathbf{j} = \rho_s \mathbf{v}_s + \rho_n \mathbf{v}_n. \tag{2.80}$$

This clearly takes the form of two interpenetrating fluids, and we can now compare the normal fluid fraction (2.78) to the thermal fraction derived earlier (2.69). We note in general that the normal fluid and thermal component are not equivalent, and we

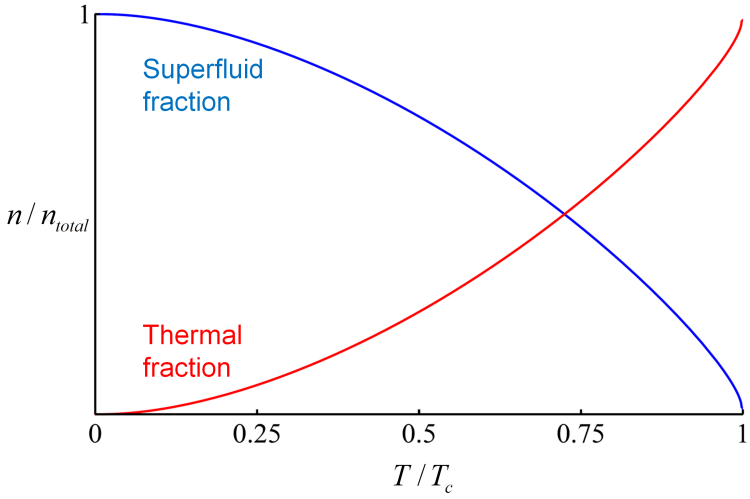

Figure 2.2: Superfluid fraction and thermal fraction of a weakly interacting uniform Bose gas as a function of temperature: The thermal fraction in red is calculated using the Hartree-Fock version of (2.69), whereas the superfluid fraction in blue is calculated using (2.78).

also find that the superfluid fraction is velocity dependent. The superfluid fraction of a uniform weakly interacting Bose gas can be calculated using the excitation spectrum calculated earlier (2.56) and is shown in figure 2.2 as a function of temperature. The corresponding thermal fraction is also shown. This is calculated using the Hartree-Fock form of (2.69), which is more accurate at higher temperatures. For this situation the condensed fraction and superfluid fraction closely track one another, and to first order can be considered equal.

To confirm this, we consider the case of small relative velocities where we can expand the distribution function to first order as

$$\rho_n \simeq \int \frac{d\mathbf{p}}{(2\pi\hbar)^3} (\mathbf{p}\cdot\hat{\mathbf{v}})^2 \left(-\frac{\partial f_p^0}{\partial \epsilon_p}\right) \tag{2.81}$$

$$\simeq \int \frac{d\mathbf{p}}{(2\pi\hbar)^3} \frac{p^2}{3} \left(-\frac{\partial f_p^0}{\partial \epsilon_p}\right), \tag{2.82}$$

where $f_p^0 = [\exp(\epsilon_p/k_B T) - 1]^{-1}$ is the zero velocity distribution function. Integrating this by parts we obtain

$$\rho_n \simeq \int \frac{4\pi dp}{(2\pi\hbar)^3} \frac{\partial}{\partial p} \left(\frac{p^4}{3} \frac{\partial p}{\partial \epsilon_p}\right) f_p^0. \tag{2.83}$$

For temperatures $T \gg T^* = nU_0/k_B$ the dominant contribution comes from high momentum states, where the energy of an excitation is approximately equal to that of a free particle $\epsilon_p \simeq p^2/2m$. Equation (2.83) then simplifies to

$$\rho_n \simeq \int \frac{d\mathbf{p}}{(2\pi\hbar)^3} m f_p^0 \tag{2.84}$$

$$\simeq m n_{\text{ex}}, \tag{2.85}$$

where we have used the $T \gg T^*$ form of the thermal particle density in (2.69), neglecting the zero-temperature quantum depletion. We therefore see that the thermal component and normal component are only equal at high temperatures, where excitations behave as free particles and contribute precisely one particle to the thermal component and particle mass m to the normal component. At lower temperatures excitations are collective and this relation is no longer valid.

2.4.3 Vorticity and irrotational flow

In this section we show that the connection between superfluid flow and condensate motion constrains superfluid flow to be irrotational. This leads to quantised circulation of the entire condensate, and the existence of quantised vortices; lines of zero density about which the phase of the condensate wavefunction must wrap around an integer multiple of 2π. One can show that the condensate in a rotating frame is analogous to the physics of a charged particle in a magnetic field, and hence the irrotational nature of the condensate maps onto the Meissner effect in superconductors [29].

Quantised circulation

Starting from the time dependent GPE (2.38) we derive the equation,

$$\frac{\partial|\Phi|^2}{\partial t} + \nabla \cdot \left[\frac{\hbar}{2mi}(\Phi^*\nabla\Phi - \Phi\nabla\Phi^*)\right] = 0. \tag{2.86}$$

Identifying the condensate density $n_0 = |\Phi|^2$, this takes the form of the continuity equation for particle density,

$$\frac{\partial n_0}{\partial t} + \nabla \cdot (n_0\mathbf{v}) = 0, \tag{2.87}$$

where we distinguish the velocity of the condensate as

$$\mathbf{v} = \frac{\hbar}{2mi}\frac{(\Phi^*\nabla\Phi - \Phi\nabla\Phi^*)}{|\Phi|^2}. \tag{2.88}$$

Splitting the condensate wavefunction into its amplitude and phase, $\Phi = fe^{i\phi}$, the velocity is then simply the gradient of the phase

$$\mathbf{v} = \frac{\hbar}{m}\nabla\phi. \tag{2.89}$$

From this it then follows that the condensate velocity is irrotational,

$$\nabla \times \mathbf{v} = 0, \tag{2.90}$$

and hence the motion of the condensate is more restricted than that of a classical fluid.

Calculating the circulation, Γ, around a closed path we find

$$\begin{aligned}\Gamma &= \oint \mathbf{v} \cdot d\mathbf{l} \\ &= \frac{\hbar}{m} \oint \nabla\phi \cdot d\mathbf{l} = \frac{\hbar}{m} 2\pi\ell,\end{aligned} \tag{2.91}$$

where from the single-valuedness of the wavefunction, the phase of the wavefunction must change by an integer multiple of 2π around a closed loop. This immediately leads to the quantisation of circulation of the BEC. However, to create such a state we have created a phase singularity within the closed loop, about which the phase winds and the wavefunction is many-valued. Such a state can therefore only exist in a multiply-connected geometry, where the condensate density vanishes at this phase singularity. Such a multiply-connected geometry can be created either by the external trapping potential, or by the formation of vortices; lines of zero density about which the condensate phase winds. Using Stoke's theorem the general form of (2.90), allowing for such phase singularities, is

$$\nabla \times \mathbf{v} = \hat{\mathbf{z}} \frac{\ell h}{m} \delta^2(\mathbf{r} - \mathbf{r}_0), \tag{2.92}$$

where ℓ is referred to as the charge of the singularity, δ^2 is a two-dimensional delta function in the xy plane, and $\mathbf{r}_0$ is the location of the singularity. This tells us that a condensate can rotate, but at the expense of producing such phase singularities. Such phase singularities have been experimentally observed in BECs in several experiments including as density singularities in [30–32] and as phase singularities in [33, 34].

Quantised vortices

If we consider purely azimuthal flow of a condensate in a system with rotational symmetry about the z axis, from (2.91) the flow velocity is given by

$$v_\theta = \ell \frac{\hbar}{mr}, \tag{2.93}$$

where r is the radial distance from the trap axis, and the condensate wavefunction must vary as $e^{il\theta}$, where θ is the azimuthal angle. This velocity profile is that of a vortex line, and for the kinetic energy to remain finite the condensate density must vanish along the axis of the trap ($r = 0$). Such quantised vortices were first proposed by Onsager [35] and Feynman [36] in the context of liquid helium experiments, and were first experimentally verified by measuring the attenuation of second sound propagating perpendicular to the axis of rotation, due to scattering of the normal fluid by vortex lines [37]. Since the experimental realisation of BEC, several experiments have been able to generate and study both a single vortex [30], and vortex arrays [31, 32] in rotating condensates.

An important distinction to note is that although the circulation of a condensate is quantised for all flow configurations, the angular momentum per particle of the condensate need not be. To demonstrate this we now consider a cylindrically symmetric trap of radius R rotating about its axis z. The angular momentum about the axis of the trap is equal to

$$L_z = n_{2D} m \int r dr d\theta v_\theta r, \tag{2.94}$$

where n_{2D} is the columnar particle density integrated along the axis of rotation, which is assumed constant. The angular integral can be written in terms of the circulation

$$\int d\theta v_\theta r = \oint \mathbf{v} \cdot d\mathbf{l}, \tag{2.95}$$

which is equal to $\ell h/m$ if the contour contains the vortex line, and zero otherwise. For a system with a vortex along the axis of symmetry this simply evaluates to $L_z = N\ell\hbar$, and therefore the angular momentum per particle is also quantised. If the vortex is now displaced a distance d from the axis, the total angular momentum is given by

$$L_z = nh \int_d^R r dr = N\ell\hbar \left(1 - \frac{d^2}{R^2}\right), \tag{2.96}$$

and the angular momentum per particle need not be quantised.

Energy of a single vortex

The creation of vortex states is clearly of significance as it allows the bulk condensate to rotate by the formation of phase singularities where the irrotational condition is allowed to break down. To find whether such vortices form, we first calculate the energy per unit length of a single vortex of charge ℓ on axis in a uniform condensate of density n, and radius R. This can be found approximately by simply integrating the kinetic energy associated with the flow,

$$\begin{aligned} E &= \frac{nm}{2} \int_0^{2\pi} \int_0^R v_s^2 r dr d\theta = \frac{\pi N}{m} \ell^2 \hbar^2 \int_0^R \frac{dr}{r} \\ &= \frac{\pi n}{m} \ell^2 \hbar^2 \ln \frac{R}{r_c}. \end{aligned} \tag{2.97}$$

The integral diverges for $r = 0$, hence a cutoff r_c is introduced, below which the expression for the velocity breaks down. This cutoff is typically taken to be the healing length, ξ in (2.64), however more accurate variational calculations give $r_c = \xi/1.46$ [19]. In principle, the potential energy due to the density profile of the vortex should also be included, however this can be shown to be a small contribution and is typically included in the uncertainty of r_c. Because the energy of a vortex scales as ℓ^2, the lowest energy configuration is for the multiply charged vortex to break up into an array of ℓ, singly-charged vortices. The vortices will attempt to form a regular hexagonal array to maximise their separation and minimise the total energy.

We now consider the response of the condensate in a frame rotating with angular velocity Ω about the axis. The energy of the vortex in the rotating frame is given by

$$E' = E - \Omega L_z, \tag{2.98}$$

where L_z is the angular momentum of the condensate in the laboratory frame. For the case considered of a singly charged vortex on axis, the angular momentum is simply $L_z = N\hbar$, where the total atom number $N = n\pi R^2$. The condition for the vortex solution to become energetically favourable is then when the rotation velocity exceeds a critical value given by

$$\Omega_c = \frac{E}{L_z} = \frac{\hbar}{mR^2} \ln\left(\frac{R}{\xi}\right). \tag{2.99}$$

Therefore, for $\Omega < \Omega_c$, the superfluid will remain at rest while the normal component will be brought into rotation. As Ω is increased above Ω_c it will become energetically favourable for the condensate to rotate and form a vortex, and at even higher Ω additional vortices will enter the system and a vortex array will form. Such an experiment was performed in [38], where the angular momentum of the condensate was measured as the stirring rate of an auxiliary laser beam was increased. For a large range of stirring frequencies L_z remains zero, corresponding to stirring below the critical frequency. At $\Omega \simeq \Omega_c$ an abrupt jump in L_z was observed corresponding to the nucleation of a vortex at the condensate surface which quickly moves to the central axis, giving $L_z/N = \hbar$. As Ω is increased further L_z is found to increase continuously, which is facilitated by nucleation of a secondary vortex at the surface and the motion of the first vortex off axis due to mutual interactions between the vortices. At even higher Ω additional vortices enter the system and L_z, determined in a non-trivial manner from their arrangement, increases continuously. Above a certain Ω the vortex array breaks apart and the formation of a turbulent state is observed where L_z no longer increases monotonically with Ω.

From this we see that the counter situation of a rotating condensate in a stationary frame is an excited state, and that the ground state is the non-rotating vortex-free state. While it's simple to understand the ground state of such systems, the mechanism by which a condensate gains or loses vorticity is far from trivial, and still an active area of research. If the appropriate excitation for the system to acquire or dissipate vorticity is not energetically accessible, then the metastable state is protected from decay to the true ground state.

Feynman critical velocity

We now switch to a different flow geometry, relevant to our studies on persistent currents in annular condensates and studied extensively in superfluid helium experiments. Here we consider superfluid flow through a long narrow channel of radius R (figure 2.3). In such a flow channel it was found that the measured critical velocity was significantly

lower than that predicted by the Landau criterion, and was also dependent on the channel geometry. It was Feynman who first suggested that these low critical velocities could be due to the formation of vortices produced by friction with the walls [39]. The mechanism by which such vortices are created then determines the critical velocity, and the fate of these vortices determines the nature of the supercritical flow. We can envisage two possibilities for nucleated vortices:

1. For velocities larger than v_c, vortices nucleate as small vortex rings attached to the container wall, which then interact with the normal fluid through mutual friction. This allows the vortex energy to dissipate into heat and the vortex ring shrinks steadily until reaching atomic size and decaying into quasiparticles. Such a scenario converts superfluid kinetic energy into heat and therefore appears as viscosity, identical to that considered by Landau.

2. Alternately, the vortex ring may grow and enter into the fluid, creating a complicated tangle of vortex lines which are characteristic of a turbulent state. Such superfluid turbulence will act to damp the superfluid flow, but via a different mechanism to that in scenario 1.

Numerical calculations suggest that for a weakly interacting BEC the first scenario applies [40]. Experimental evidence indicates that the superfluid flow of liquid helium above v_c is a superfluid turbulent state, corresponding to the second scenario. Understanding turbulent flow is a notoriously difficult problem, and as a result there are still many open questions [41]. The mechanism by which vortices nucleate off the walls, enter into the bulk of the fluid, and how turbulence damps the superfluid flow are all still not fully understood. Nevertheless we can formulate a crude model outlined in [39, 42] to obtain an order of magnitude estimate of the critical velocity for both scenarios.

To estimate the critical velocity we simply ask at what flow velocity is it energetically favourable to place a vortex structure into the flow channel. It turns out that the lowest energy structure to consider is a vortex ring, illustrated in figure 2.3. For a vortex ring of radius r, the energy E_r and momentum $\mathbf{P}_r$ are given by [43]

$$E_r = 2\pi^2 r \frac{n\hbar^2}{m} \ln \frac{r}{\xi} \tag{2.100}$$

$$\mathbf{P}_r = 2\pi^2 n\hbar r^2 \hat{\mathbf{z}}, \tag{2.101}$$

where $\hat{\mathbf{z}}$ is the unit vector normal to the plane of the vortex ring. Using (2.72) the energy of a vortex ring in the plane perpendicular to a background flow of velocity $\mathbf{v}_s$ is given by

$$E_r' = E_r + \mathbf{P}_r \cdot \mathbf{v}_s = 2\pi^2 r^2 n\hbar \left(\frac{\hbar}{mr} \ln \left(\frac{r}{\xi} \right) \pm v_s \right), \tag{2.102}$$

where the sign characterises the sense of rotation of the vortex ring. This expression is minimised by letting r attain its largest value, which is R, the radius of the container.

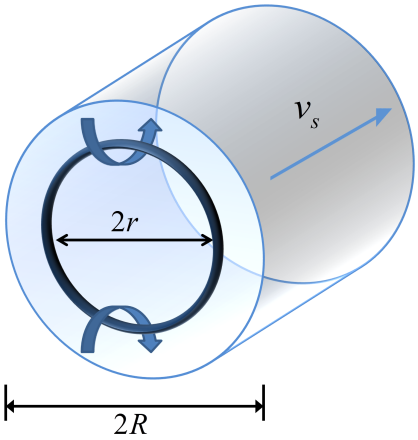

Figure 2.3: Formation of a vortex ring in a flow channel: The vortex ring is a single vortex connected back onto itself, and therefore at distances far from the ring the velocity tends to zero. As a result, unlike a single vortex, a vortex ring has a finite energy dependent on its size and not the size of the container it is in.

For $v_s > v_c$ this energy will be negative, and hence we obtain the Feynman estimate of the critical velocity,

$$v_c^F = \frac{\hbar}{mR} \ln \frac{R}{\xi}. \tag{2.103}$$

We note that this is only an estimate as it neglects interactions of the vortex with the walls, the energy barrier present to actually reaching such a state, and any density modification due to the vortex and edge effects. Nevertheless (2.103) gives the correct order of magnitude of critical velocity for liquid helium experiments, and gives the observed scaling of v_c with pipe radius R. Although here we considered the case of a vortex ring, the same expression is obtained for the case of a vortex-antivortex pair, separated by a distance $2R$. For the case of $r \gg \xi$ the curvature of the vortex can be neglected, and hence a vortex ring of radius r maps onto a vortex-antivortex pair of length πr.

2.5 Conclusion

In conclusion we have introduced some of the theory of BEC and superfluidity relevant for discussing persistent currents. Of particular importance is the concept of superflow as the translation of an interacting condensate which permits flow without viscosity below a critical velocity. The value of this critical velocity is set by the allowed excitations of the system, and in particular by the formation of vortex states. This is discussed further in Chapter 5 for the case of a ring BEC, where the role of quantised vortices is found to be essential in explaining the stability and eventual decay of superflow.

Chapter 3

Experimental methods and BEC production

This chapter covers the experimental methods and parts of the experiment used for the production of ^{87}Rb BECs. Most of the work in designing and building the system for achieving both ^{87}Rb and ^{39}K condensates was carried out by students before me, so I will attempt to only briefly cover the aspects relevant for cooling to quantum degeneracy. For a more detailed and exhaustive explanation of this part of the experiment refer to [44–46]. The specific sections relevant to studying persistent currents I will cover in greater depth. This includes (i) the theory of atom-light interactions (relevant for the production of an optical ring trap and transfer of angular momentum to the condensate), (ii) the interaction of atoms with an external magnetic field (relevant for defining the basis of states used in transfers and multi-component studies), and (iii) absorption imaging (relevant for the quantitative analysis of persistent current stability).

The experimental setup used in this work was primarily designed for the production of ^{39}K condensates via sympathetic cooling with ^{87}Rb. The broad Feshbach resonance present in ^{39}K allows us to tune the interparticle interactions across a wide range. This has been used in several studies performed on this system, to study the thermodynamics of ultracold Bose gases [47–49] as well as condensates out of equilibrium [50, 51]. The work presented here only made use of ^{87}Rb condensates, however due to the significance of the ^{39}K experiments, the system remained optimised for ^{39}K condensate production for much of my time.

The structure of this chapter will be as follows. The first section will outline the experimental sequence and techniques used in cooling a room temperature vapour of ^{87}Rb to degeneracy. The sections that follow explain some of the physics and technical details behind these stages, with additional information provided for those stages relevant to studying persistent currents. The ordering of these sections will try and reflect the order in which they appear in the experimental sequence.

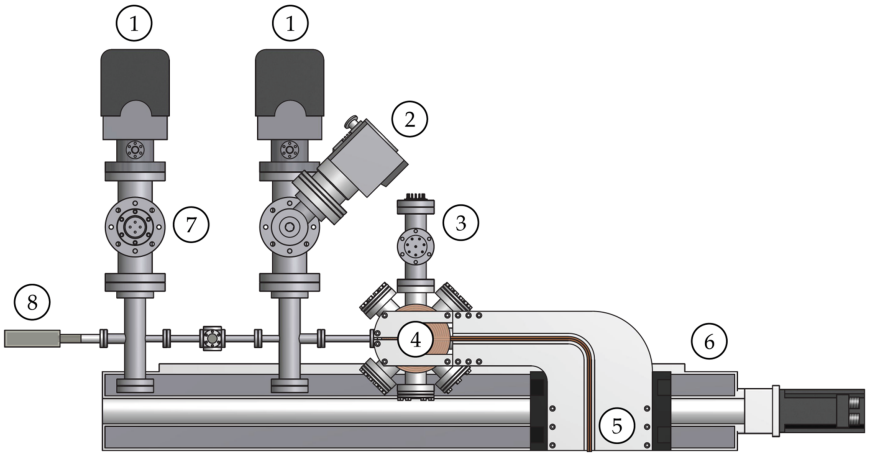

Figure 3.1: Diagram of the vacuum system, translation stage and quadrupole coil support. Components labeled include (1) ion pumps, (2) turbo pump, (3) atom source module, (4) MOT cell and quadrupole coils, (5) quadrupole coil mounting arm, (6) translation stage, (7) Ti-Sub pump, and (8) science cell.

3.1 Sequence overview

The experiment is performed in an ultra-high vacuum chamber which is illustrated in figure 3.1 [46]. ^{87}Rb vapour is released into the Magneto-Optical Trap (MOT) chamber (4) by heating getters fitted in (3). Following laser cooling, the atoms are magnetically trapped and transported to the science cell (8) where they are cooled to degeneracy. This dual-chamber setup is beneficial for two reasons. Firstly, the MOT chamber requires sufficiently high ^{87}Rb vapor pressure, on the order of 10^{-9}mbar, for rapid loading of the MOT, whereas the science cell requires very low background pressure, in the region of 10^{-11}mbar, to ensure the long lifetime of the atoms required for efficient evaporative cooling and long BEC lifetime. This is achieved by splitting the system into two regions, connected by a low-conduction section. The second advantage of this design is to increase optical access to the BEC, which is required for imaging, trapping, and manipulation of the condensate.

The ground state of the atoms is the $5^2S_{1/2}$ state, which is split into the $F = 2$ and $F = 1$ hyperfine levels, with the final BEC produced in the $|F = 2, m_F = 2\rangle$ state. For studies on persistent currents we then transfer the BEC to the $|F = 1, m_F = 1\rangle$ state using a microwave transfer. The sequence outline is as follows:

1. ^{87}Rb vapour is loaded into the MOT (4) and Doppler cooled (Section 3.3.2)

2. The quadrupole field is removed and the molasses stage cools the atoms further, maximising phase space density (Section 3.3.3)

3. The atoms are then optically pumped into the $|F = 2, m_F = 2\rangle$ magnetically trappable state (Section 3.4)

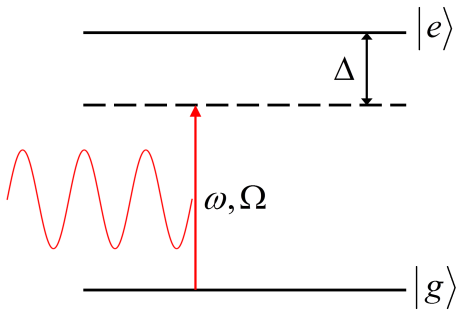

Figure 3.2: The two-level atom: The two energy levels are separated by a transition with frequency ω_{eg} and the atom is driven by a monochromatic plane wave of frequency ω. The variable parameters are the detuning of the light field from resonance $\Delta = \omega - \omega_{eg}$, and the strength of the atom-field coupling Ω.

4. The atoms are transferred to a magnetic quadrupole trap and transported to the low pressure science cell (8) (Section 3.5.1)

5. The quadrupole trap is transformed to a QUIC trap and the gas is evaporatively cooled (Section 3.6)

6. The atoms are loaded into an optical dipole trap and the depth is gradually lowered to cool the gas to BEC (Section 3.7)

7. (Optional) An adiabatic microwave sweep transfers the atoms from $|F = 2, m_F = 2\rangle \rightarrow |F = 1, m_F = 1\rangle$ (Section 3.8)

8. All optical and magnetic fields are removed and the cloud is absorption imaged after a variable time of flight (Section 3.9)

All subsequent experiments on persistent currents follow the same steps (1-7) to prepare the initial BEC.

3.2 Atom-light interactions

The interaction of light and atoms is of great significance in the field of ultracold gases. When an atom is placed in a light field the oscillating electric field induces an electric dipole moment in the atom which then couples to the field. The effect of this is typically divided into two process which are used extensively in the field of laser cooling and trapping. Firstly the light may induce transitions between atomic states involving the absorption and emission of photons. Secondly this coupling will modify the atomic eigenstates, creating new dressed states with different eigenenergies. To understand these processes we consider a simple two-level model of the atom.

3.2.1 Two-level atom

The two-level atom we consider is shown in figure 3.2, where the atom is simply composed of a ground state $|g\rangle$ and an excited state $|e\rangle$ separated by a transition of frequency ω_{eg}. Incident on the atom is a time varying electric field $\mathbf{E} = \hat{\mathbf{e}} E_0 \cos(\omega t)$. The dipole

moment of the atom, $\mathbf{d} = -e\mathbf{r}$, couples to the electric field producing a perturbation

$$H' = -\mathbf{d} \cdot \hat{\mathbf{e}} \frac{E_0}{2} (e^{i\omega t} + e^{-i\omega t}). \tag{3.1}$$

The atomic wavefunction at any time can be written as a superposition of the unperturbed ground and excited states,

$$\Psi(\mathbf{r}, t) = c_g(t) \left|g\right\rangle + c_e(t) \left|e\right\rangle e^{-i\omega_{eg} t}. \tag{3.2}$$

Substituting this into the time-dependent Schrödinger equation with the Hamiltonian $H = H_0 + H'$, where H_0 is the unperturbed Hamiltonian, gives the coupled equations

$$i\hbar \frac{dc_g(t)}{dt} = c_e \hbar \frac{\Omega^*}{2} \left(e^{i(\omega - \omega_{eg})t} + e^{-i(\omega + \omega_{eg})t} \right) \tag{3.3}$$

$$i\hbar \frac{dc_e(t)}{dt} = c_g \hbar \frac{\Omega}{2} \left(e^{i(\omega + \omega_{eg})t} + e^{-i(\omega - \omega_{eg})t} \right), \tag{3.4}$$

where we have defined the Rabi frequency

$$\Omega = \frac{E_0}{\hbar} \left\langle e \right| \mathbf{d} \cdot \hat{\mathbf{e}} \left| g \right\rangle, \tag{3.5}$$

which describes the strength of the coupling between the atom and the electric field. If we assume the field is close to resonance we can make the rotating wave approximation (RWA) by neglecting terms which oscillate at twice the driving frequency since their time dependence will average out to zero compared to the much slower evolution of c_e and c_g. In this regime the equations simplify to

$$i\hbar \frac{dc_g(t)}{dt} = c_e \hbar \Omega^* \frac{e^{i\Delta t}}{2} \tag{3.6}$$

$$i\hbar \frac{dc_e(t)}{dt} = c_g \hbar \Omega \frac{e^{-i\Delta t}}{2}, \tag{3.7}$$

where we have introduced the detuning from resonance $\Delta = \omega - \omega_{eg}$.

Rabi oscillations

To obtain the time dependence of c_e and c_g we solve the coupled equations by differentiating (3.6) and (3.7) in time to obtain the uncoupled second order equations

$$\frac{d^2 c_g}{dt^2} - i\Delta \frac{dc_g}{dt} + \frac{\Omega^2}{4} c_g = 0 \tag{3.8}$$

$$\frac{d^2 c_e}{dt^2} + i\Delta \frac{dc_e}{dt} + \frac{\Omega^2}{4} c_e = 0. \tag{3.9}$$

Such equations are simply solved, and assuming only the ground state is populated at $t = 0$ when the field is turned on, the population of the excited state at time t is given

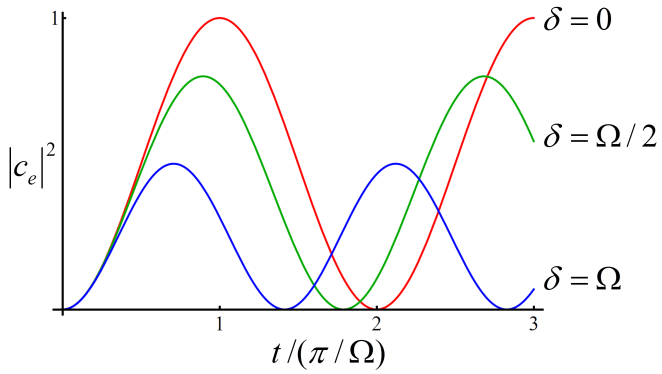

Figure 3.3: Rabi Oscillations: This figure shows the time dependent oscillations of the excited state population for different detunings. As the detuning increases the frequency increases and the maximum population transferred decreases.

by

$$|c_e(t)|^2 = \frac{\Omega^2}{W^2} \sin^2\left(\frac{Wt}{2}\right), \tag{3.10}$$

where we define the effective Rabi frequency

$$W = \sqrt{\Omega^2 + \Delta^2}. \tag{3.11}$$

The population of the excited state therefore undergoes Rabi oscillations at the frequency W. The efficiency of transfer to the excited state depends on the detuning Δ, with complete transfer to the excited state only possible on resonance. If we apply the light field on resonance for duration $T = \pi/\Omega$ the atom undergoes a π pulse whereby the state is flipped completely from pure $|g\rangle$ to pure $|e\rangle$. Likewise for a light pulse of half the duration, the atom undergoes a $\pi/2$ pulse and is left in an equal superposition of ground state and excited state $(|e\rangle \pm |g\rangle)/\sqrt{2}$. Such operations are used extensively in this work.

AC Stark shift

In addition to affecting populations, the perturbing radiation also changes the energy levels of the states. We show this by defining the new coefficients $\tilde{c}_g = c_g e^{-i\Delta t/2}$ and $\tilde{c}_e = c_e e^{i\Delta t/2}$ which removes the time dependence from (3.6) and (3.7). The equations of motion then take the form

$$i\frac{d\tilde{c}_g}{dt} = \frac{\Omega}{2}\tilde{c}_e + \frac{\Delta}{2}\tilde{c}_g \tag{3.12}$$

$$i\frac{d\tilde{c}_e}{dt} = \frac{\Omega}{2}\tilde{c}_g - \frac{\Delta}{2}\tilde{c}_e, \tag{3.13}$$

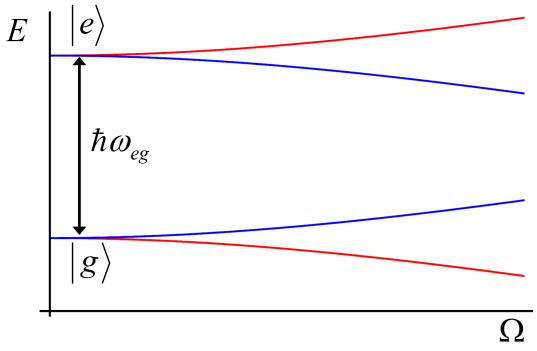

Figure 3.4: Light shift of a two-level atom interacting with an external electric field: The energy shift of the ground and excited state are shown as a function of increasing Rabi frequency. The red line is for negative detuning, and the blue line is positive detuning. In the limit of zero coupling the energy levels revert back to their unperturbed levels. The effect shown here is exaggerated for clarity.

and the Hamiltonian is written as

$$\hat{H} = \frac{\hbar}{2}\begin{bmatrix} \Delta & \Omega \\ \Omega & -\Delta \end{bmatrix} \tag{3.14}$$

Diagonalising this Hamiltonian, the eigenvalues are

$$\lambda = \pm\frac{\hbar}{2}\sqrt{\Omega^2 + \Delta^2}, \tag{3.15}$$

and the new eigenvectors can be written as

$$\left|e'\right\rangle = \cos\theta\left|g\right\rangle - \sin\theta\left|e\right\rangle \qquad , \qquad \left|g'\right\rangle = \sin\theta\left|g\right\rangle + \cos\theta\left|e\right\rangle, \tag{3.16}$$

where $\tan 2\theta = -\Omega/\Delta$. These new states are the dressed states of the excited state and the ground state plus a photon. At $\Delta = 0$ there is an avoided crossing and the dressed states are split by $\hbar\Omega$. The composition of the dressed states varies as a function of detuning and on resonance the dressed states are an equal superposition of the original ground and excited states. For far detuned light, $\Delta \to \pm\infty$, the dressed states revert to the pure unperturbed states, $|g\rangle$ and $|e\rangle$. Reversing the various coefficient transformations we have done until this point, the energies of the excited and ground state in the original basis are then given by

$$E_e = \hbar\omega_{eg} + \frac{\hbar\Delta}{2} \pm \frac{\hbar}{2}\sqrt{\Omega^2 + \Delta^2} \tag{3.17}$$

$$E_g = -\frac{\hbar\Delta}{2} \mp \frac{\hbar}{2}\sqrt{\Omega^2 + \Delta^2}, \tag{3.18}$$

where the top sign choice is for negative detuning ($\Delta < 0$ corresponding to red detuning) and the bottom sign choice is for positive detuning ($\Delta > 0$ corresponding to blue detuning) to give the correct unperturbed energies in the limit $\Omega \to 0$. The perturbed states experience a shift which is dependent on the strength and detuning of the light field, and the overall sign of the shift depends on the sign of the detuning. This is illustrated in figure 3.4 where the light shift is plotted as a function of increasing electric field strength. This is known as the AC Stark shift and is used to optically

trap atoms by spatially varying the energy of the ground state to create a trapping potential.

3.2.2 Optical Bloch equations

In the discussion so far, an atom in a light field undergoes oscillations between the ground and excited states, with conservation of energy requiring that the energy is transferred coherently to and from the external field by absorption and stimulated emission. To include the process of spontaneous emission which limits the lifetime of the excited state, we use the density matrix representation of the atom to account for the loss of energy to a background field. The density operator is defined for our two state atom as

$$\hat{\rho} = |\Psi\rangle \langle\Psi| = \begin{pmatrix} \rho_{gg} & \rho_{ge} \\ \rho_{eg} & \rho_{ee} \end{pmatrix} = \begin{pmatrix} c_g c_g^* & c_g c_e^* \\ c_e c_g^* & c_e c_e^* \end{pmatrix}. \tag{3.19}$$

Diagonal elements give populations, while off diagonal elements are coherences. If a state has non-zero coherences then there exist observables whose value depends on the relative phase between the states $|g\rangle$ and $|e\rangle$. The time evolution of the density matrix is given by von Neumann's equation

$$\frac{d\rho}{dt} = \frac{i}{\hbar}\left[\hat{\rho}, \hat{H}\right]. \tag{3.20}$$

The advantage of this formalism is that we can now include the effect of spontaneous emission into the time evolution of the density operator. If the lifetime of the excited state $|e\rangle$ is $1/\Gamma$, it can be shown that the complete equation of motion for the density matrix is given by [52]

$$\frac{d\rho}{dt} = \frac{i}{\hbar}\left[\hat{\rho}, \hat{H}\right] - \begin{pmatrix} -\Gamma\rho_{ee} & \frac{\Gamma}{2}\rho_{ge} \\ \frac{\Gamma}{2}\rho_{eg} & \Gamma\rho_{ee} \end{pmatrix}. \tag{3.21}$$

Using the Hamiltonian derived in (3.14) we obtain the coupled differential equations

$$\begin{aligned} \dot{\rho}_{gg} =& \frac{i\Omega}{2}(\tilde{\rho}_{ge} - \tilde{\rho}_{eg}) + \Gamma\rho_{ee} \\ \dot{\rho}_{ee} =& -\frac{i\Omega}{2}(\tilde{\rho}_{ge} - \tilde{\rho}_{eg}) - \Gamma\rho_{ee} \\ \dot{\tilde{\rho}}_{ge} =& -\frac{i\Omega}{2}(\rho_{ee} - \rho_{gg}) - i\Delta\tilde{\rho}_{ge} - \frac{\Gamma}{2}\tilde{\rho}_{ge} \\ \dot{\tilde{\rho}}_{eg} =& \frac{i\Omega}{2}(\rho_{ee} - \rho_{gg}) + i\Delta\tilde{\rho}_{ge} - \frac{\Gamma}{2}\tilde{\rho}_{eg}. \end{aligned} \tag{3.22}$$

These equations are further constrained by the sum of the populations totalling one ($\rho_{ee} + \rho_{gg} = 1$), and the fact that the coherences are complex conjugates of each other ($\tilde{\rho}_{ge} = \tilde{\rho}_{eg}^*$), reducing the number of independent variables to three. These are usually

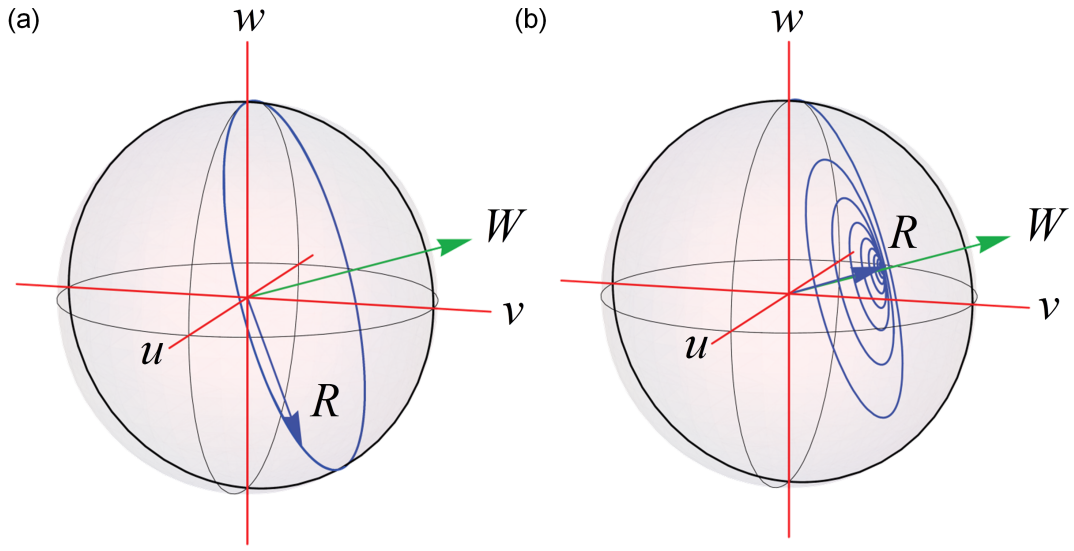

Figure 3.5: Evolution of the Bloch vector: (a) Evolution of the Bloch vector for the parameters $\Omega = 1$, $\Delta = 0.3$, and $\Gamma = 0$. In the absence of decay the Bloch vector is of unit length and the atom remains in a fully coherent state. (b) Evolution of the Bloch vector for the parameters $\Omega = 1$, $\Delta = 0.3$, and $\Gamma = 0.1$. The inclusion of spontaneous emission causes the Bloch vector to shorten and the system to decohere to a statistical mixture.

formulated as the components of the Bloch vector $\mathbf{R} = (u, v, w)$:

$$u = (\tilde{\rho}_{ge} + \tilde{\rho}_{eg}), \qquad v = i(\tilde{\rho}_{eg} - \tilde{\rho}_{ge}), \qquad w = (\rho_{gg} - \rho_{ee}). \tag{3.23}$$

The equation of motion of the Bloch vector is found from (3.22), to give the standard form of the optical Bloch equations

$$\begin{aligned} \dot{u} =& \Delta v - \frac{\Gamma}{2} u \\ \dot{v} =& \Delta u + \Omega w - \frac{\Gamma}{2} v \\ \dot{w} =& -\Omega v - \Gamma(w - 1). \end{aligned} \tag{3.24}$$

In the absence of spontaneous decay ($\Gamma = 0$), the evolution of the Bloch vector can be expressed in the more intuitive form

$$\dot{\mathbf{R}} = \mathbf{R} \times \mathbf{W}, \tag{3.25}$$

where we define the vector $\mathbf{W} = (\Omega, 0, \Delta)$. From this it follows that $\dot{\mathbf{R}} \cdot \mathbf{R} = 0$ and $\dot{\mathbf{R}} \cdot \mathbf{W} = 0$ and hence the Bloch vector $\mathbf{R}$ precesses about $\mathbf{W}$ at a fixed angle at a frequency equal to $|\mathbf{W}|$. This time evolution is shown in figure 3.5(a) for non-zero detuning. This offers an intuitive method for visualising Rabi oscillations and the sequential application of π and $\pi/2$ pulses. In figure 3.5(b) we show the effect of spontaneous emission on the evolution of the Bloch vector. The Bloch vector spirals in

towards **W** and the Bloch sphere collapses down such that the Bloch vector no longer has unit length. This can be viewed as the decoherence of the initial pure state with $|\mathbf{R}| = 1$ towards an incoherent mixture with $|\mathbf{R}| < 1$.

Steady state solutions

The inclusion of spontaneous emission means that at long times ($t \gg \Gamma^{-1}$), the atoms will no longer undergo Rabi oscillations but will reach steady state populations. Setting the time derivatives in (3.24) to zero gives the steady state solutions

$$\begin{pmatrix} u \\ v \\ w \end{pmatrix} = \frac{1}{\Delta^2 + \Omega^2/2 + \Gamma^2/4} \begin{pmatrix} \Omega\Delta \\ \Omega\Gamma/2 \\ \Delta^2 + \Gamma^2/4 \end{pmatrix}. \tag{3.26}$$

From this we find the steady state population of the excited state is given by

$$\rho_{ee} = \frac{1-w}{2} = \frac{1}{2}\frac{s}{1 + s + 4\Delta^2/\Gamma^2}, \tag{3.27}$$

where we have defined the on-resonant saturation parameter $s = I/I_{\text{sat}} = 2(\Omega/\Gamma)^2$. Here the intensity of the light field is given by $I = \frac{1}{2}c\epsilon_0 E_0^2$, where ϵ_0 is the permittivity of free space and c is the speed of light. The saturation intensity, I_{sat}, describes the strength of the transition and is given in terms of the dipole moment as

$$I_{\text{sat}} = \frac{\epsilon_0 c \Gamma^2 \hbar^2}{4|\hat{\epsilon} \cdot \mathbf{d}|^2}. \tag{3.28}$$

We therefore see that in the limit of high intensity, the population of the excited state saturates at 1/2. Using the steady state excited population (3.27), the total photon scattering rate over all directions and frequencies is then given by $\Gamma\rho_{ee}$, which equals

$$R_{\text{sc}} = \frac{\Gamma}{2}\frac{s}{1 + s + 4\Delta^2/\Gamma^2}. \tag{3.29}$$

We note that the scattering rate has a Lorentz lineshape with width $\Gamma' = \Gamma\sqrt{1+s}$, hence at higher intensities the width increases and the line is said to be power broadened.

3.2.3 Two photon processes

A Raman transition is a two-photon process involving simultaneous absorption and stimulated emission by an atom. Figure 3.6 illustrates the coherent Raman transition of an atom addressed by two lasers between the levels $|g\rangle$ and $|e\rangle$. The atom is excited from the ground state $|g\rangle$ to an intermediate state $|i\rangle$, far detuned from the single photon transition, by the absorption of light of frequency ω_1 from one beam. Simultaneously the atom emits a photon of frequency ω_2 into the second beam by stimulated emission

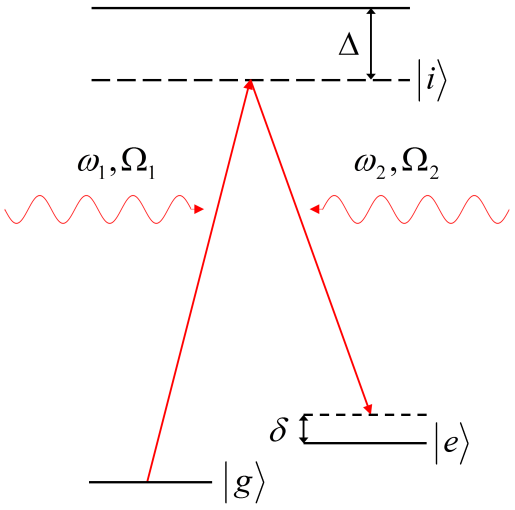

Figure 3.6: A Raman transition between levels $|g\rangle$ and $|e\rangle$ driven by two laser beams via an intermediate state $|i\rangle$. Provided the detuning Δ of the virtual state is large, single photon excitation is negligible and the atom is coherently transferred from $|g\rangle$ to $|e\rangle$.

and ends in the excited state, $|e\rangle$. Raman transitions are extensively used in ultracold gases with applications including Raman cooling [53] and electromagnetically induced transparency [54]. This work uses two-photon Raman transitions to coherently transfer the BEC between two rotational states without imparting linear momentum to the system (See Section 4.3).

To calculate the effect of both laser beams on the atom we extend the two-level discussion and show that for large detuning of the intermediate state $|i\rangle$, the system behaves simply as a two-level atom with coherent Rabi oscillations between $|g\rangle$ and $|e\rangle$ and negligible occupation of the intermediate state, $|i\rangle$. Unfortunately for the situations we consider, $\Delta \gg \Gamma$, the dynamics of the intermediate population are very fast and can be difficult to calculate numerically. From arguments presented in [55], one can show that in the limit $\Delta \gg \delta$, the interaction of the atom with both lasers yields an effective Rabi frequency, Ω_{eff}, which depends on the individual Rabi frequencies of each beam, Ω_{gi1} and Ω_{ei2}, as well as the detuning from single-photon resonance, Δ:

$$\Omega_{\text{eff}} = \frac{\Omega_{gi1}\Omega_{ei2}}{2\Delta}. \tag{3.30}$$

The Raman coupling gives rise to coherent Rabi oscillations between $|g\rangle$ and $|e\rangle$ of the form in (3.10), with Ω replaced by Ω_{eff}, and the relevant detuning being the two-photon detuning δ, illustrated in figure 3.6.

The significance of the Raman transfer comes from the fact that the transfer efficiency depends on the two-photon detuning, δ, while the rate of spontaneously emitted photons depends on the single photon detuning, Δ. For $\delta = 0$ the duration of a π-pulse is $t_\pi = \pi/\Omega_{\text{eff}}$. The rate of incoherent photon scattering is the sum of the scattering

rates for each beam, given by (3.29). For large detunings ($\Delta \gg \Gamma$) the total number of photons scattered in a single π-pulse is then found to be

$$\begin{aligned} R_{\mathrm{sc}} t_\pi &= \frac{\Gamma}{4\Delta^2}(\Omega_{gi1}^2 + \Omega_{ei2}^2)\frac{2\pi\Delta}{\Omega_{gi1}\Omega_{ei2}} \\ &= \frac{\Gamma\pi}{2}\frac{\Omega_{gi1}^2 + \Omega_{ei2}^2}{\Omega_{gi1}\Omega_{ei2}}\frac{1}{\Delta}. \end{aligned} \tag{3.31}$$

Therefore we can almost eliminate spontaneous emission events and maintain coherence for many Rabi oscillations by detuning both beams far from the single-photon resonance. Unfortunately this comes at the cost of reduced effective Rabi frequency, which scales as $1/\Delta^2$.

3.2.4 Adiabatic rapid passage

The task of coherently transferring a BEC from an occupied state to an empty one can be achieved by applying a π-pulse to exactly flip the state vector. This requires a pulse of radiation whose duration, power and frequency with respect to the atomic transition need to be closely controlled for efficient transfer. Another method is to use an adiabatic rapid passage (ARP), where the radiation is tuned above or below the resonance frequency, and the radiation or level itself is swept through resonance. Provided the process is performed adiabatically the atoms will remain in a single dressed eigenstate and the dressed state itself, which is a function of the detuning, will transform from the initial state to the final state. When the coupling between the states is by a Raman transfer this process is referred to as stimulated Raman adiabatic passage (STIRAP)[56]. ARP transfer schemes tend to be more robust and able to achieve higher transfer efficiencies.

This process is illustrated in figure 3.7. If one starts in the ground state $|g\rangle$ and applies a coupling field with frequency far below resonance, this effectively loads the condensate into the lowest band. Sweeping the frequency across resonance the system remains in the lowest band, and the composition of the lowest dressed state changes to pure $|e\rangle$ for detuning far above resonance. Rapidly removing the coupling field projects the dressed state into the original bare states. If one sweeps the frequency in the other directions the same state transfer is observed, but this is achieved by loading into the upper band.

The possibility of adiabatic crossing of energy levels was first considered by Landau and Zener. They showed that for a system of two coupled states of the form

$$H\phi_1 = \epsilon_1\phi_1 + \epsilon_{12}\phi_2 \tag{3.32}$$

$$H\phi_2 = \epsilon_{12}\phi_1 + \epsilon_2\phi_2, \tag{3.33}$$

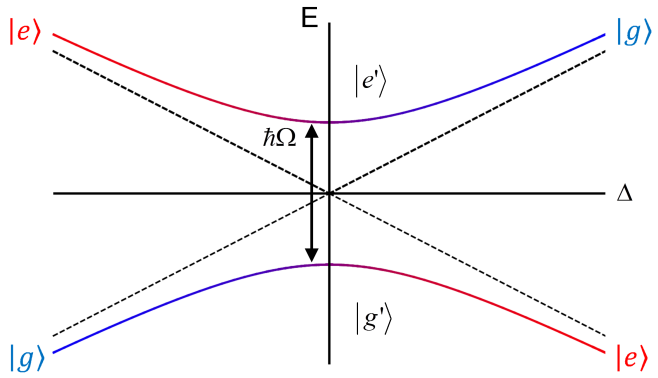

Figure 3.7: Dressed states energy bands and decomposition: The energy levels of the dressed bands as a function of detuning are obtained from diagonalising (3.14). The color of the band indicates the relative decomposition of the dressed states in terms of the bare states, with blue being pure $|g\rangle$, and red pure $|e\rangle$. In the limit of far detuning the dressed states tend toward the corresponding labeled bare states.

the probability of adiabatically crossing from one state to the other is given by [57]

$$P = 1 - e^{-2\pi\gamma}, \qquad \gamma = \frac{2\pi}{\hbar}\frac{\epsilon_{12}^2}{\left|\frac{d}{dt}(\epsilon_1 - \epsilon_2)\right|}. \tag{3.34}$$

Identifying the terms $\epsilon_1 = \hbar\Delta/2$, $\epsilon_2 = -\hbar\Delta/2$, and $\epsilon_{12} = \hbar\Omega/2$, the adiabatic criterion is given as

$$\Omega^2 \gg \frac{1}{\pi^2}\left|\frac{d\Delta}{dt}\right|. \tag{3.35}$$

Sweeping faster than this will cause admixture of the other dressed state and imperfect state transfer.

3.2.5 Optical forces

So far we have derived the AC Stark shift which exerts an optical dipole force used for optical trapping, and we have derived the scattering rate which exerts a scattering force used in Doppler cooling. To connect these two forces and include the effect of spontaneous emission in our discussion of the optical dipole potential, we now derive the complex polarizability and show that the real and imaginary parts correspond to the dipole and scattering force respectively. This also elucidates the imaging of atomic clouds, which behave as an object with complex refractive index.

The electric field we have considered so far has the form $\mathbf{E}(\mathbf{r},t) = \hat{\mathbf{e}}(E_0(\mathbf{r})/2)e^{i\omega t} + c.c.$ This induces a time-varying dipole moment of the form $\mathbf{d}(\mathbf{r},t) = \hat{\mathbf{e}}(d_0(\mathbf{r})/2)e^{i\omega t} + c.c.$, where the the dipole moment amplitude, d_0, and the field amplitude E_0, are related by the complex polarizability

$$d_0 = \alpha(\omega)E_0. \tag{3.36}$$

Here we have assumed we are dealing with linear optics and that α is simply a scalar. The dipole potential and scattering rate are then related to α by [58]:

$$U_{\text{dip}}(\mathbf{r}) = -\frac{1}{2}\langle \mathbf{d}\cdot\mathbf{E}\rangle = -\frac{1}{2\epsilon_0 c}\text{Re}(\alpha)I(\mathbf{r}), \tag{3.37}$$

$$R_{\text{sc}}(\mathbf{r}) = \frac{\langle \dot{\mathbf{d}}\mathbf{E}\rangle}{\hbar\omega} = \frac{1}{\hbar\epsilon_0 c}\text{Im}(\alpha)I(\mathbf{r}). \tag{3.38}$$

The energy level shift therefore results from the in-phase interaction between the electric field and the induced dipole, while the out of phase interaction is responsible for absorption. The expectation value of the dipole moment is given by $\langle d\rangle = \langle\Psi|\,\mathbf{d}\cdot\hat{\mathbf{e}}\,|\Psi\rangle$, where the wavefunction Ψ is given by (3.2). Substituting in this expression for the wavefunction gives

$$\begin{aligned}\langle d\rangle &= d_{eg}\rho_{eg}e^{i\omega_{eg}t} + c.c.\\ &= d_{eg}\tilde{\rho}_{eg}e^{i\omega t} + c.c.\\ &= d_{eg}\frac{(u-iv)}{2}e^{i\omega t} + c.c.,\end{aligned} \tag{3.39}$$

where we define $d_{eg} = \langle e|\,\mathbf{d}\cdot\hat{\mathbf{e}}\,|g\rangle = \hbar\Omega/E_0$. By comparison with (3.36) we can then identify

$$\begin{aligned}\langle d\rangle &= \frac{1}{2}E_0(\alpha e^{i\omega t} + \alpha^* e^{-i\omega t})\\ &= \frac{1}{2}(d_{eg}(u-iv)e^{i\omega t} + d_{ge}(u+iv)e^{-i\omega t})\\ \Rightarrow \alpha &= \frac{d_{eg}}{E_0}(u-iv).\end{aligned} \tag{3.40}$$

Using the steady state solutions of the Bloch vector (3.26) this directly gives the polarizability as

$$\alpha = -\frac{\hbar c\epsilon_0}{I_{\text{sat}}}\frac{1}{1+I/I_{\text{sat}}+(2\Delta/\Gamma)^2}\left[\Delta - \frac{i\Gamma}{2}\right], \tag{3.41}$$

and from this we obtain

$$U_{\text{dip}}(\mathbf{r}) = \hbar\frac{\Delta}{2}\frac{I/I_{\text{sat}}}{1+I/I_{\text{sat}}+(2\Delta/\Gamma)^2} \xrightarrow{\Delta\gg\Gamma} \frac{\hbar\Omega^2}{4\Delta}, \tag{3.42}$$

$$R_{\text{sc}}(\mathbf{r}) = \frac{\Gamma}{2}\frac{I/I_{\text{sat}}}{1+I/I_{\text{sat}}+(2\Delta/\Gamma)^2} \xrightarrow{\Delta\gg\Gamma} \frac{\Gamma\Omega^2}{4\Delta^2}, \tag{3.43}$$

where the expressions are also given in the limit of large detuning, $\Delta \gg \Gamma$. The expression (3.43) is the same result as (3.29) derived earlier. We note that these results were derived using the RWA approximation, and as a result for very large detunings from resonance one needs to include a small correction due to the co-rotating term of order $(\omega-\omega_{eg})/(\omega+\omega_{eg})$.

The optical dipole force is simply obtained from the gradient of the potential, and for the common case of large detunings used in traps ($|\Delta| \gg \Gamma$), the dipole force reduces

to the expression

$$\mathbf{F}_{\text{dip}} = -\nabla U_{\text{dip}} \simeq -\nabla \left(\frac{\hbar \Omega^2}{4\Delta} \right). \tag{3.44}$$

This approximate expression is also obtained by taking the large detuning limit of the AC Stark energy shift derived in (3.15). In a field with spatially varying intensity or detuning, the atom will experience a net force, the direction of which depends on the sign of the detuning. In this work red-detuned traps ($\Delta < 0$) are used, where the atom is attracted to regions of high intensity. The scattering force is simply obtained from the product of the scattering rate, R_{sc}, with the momentum per photon, $\hbar\mathbf{k}$,

$$\mathbf{F}_{\text{sc}} = \hbar \mathbf{k} \frac{\Gamma}{2} \frac{s}{1 + s + (2\Delta/\Gamma)^2}. \tag{3.45}$$

3.3 Laser cooling and trapping

Having covered the interaction of light with atoms, we are now in a position to describe the experimental techniques used to slow and spatially constrain atoms. The first of these is the magneto-optical trap which uses the scattering component of the radiative force to cool atoms down to the Doppler limit. The second technique is the optical molasses stage, which employs Sisyphus cooling. To relate these techniques directly to the experiment we first consider the ^{87}Rb D_2 transition hyperfine structure.

3.3.1 ^{87}Rb hyperfine structure

So far we have considered a simple two-level atom, however real atoms possess a far more complicated electronic level structure with multiple ground and excited states and several decay paths. Applying the principles of laser cooling to real atoms therefore seems like a daunting task. Thankfully alkali atoms, which have a single valence electron, permit a perturbative and accurate calculation of their electronic level structure. In ^{87}Rb suitable transitions are found in the D_2 transition between the $5^2S_{1/2}$ ground state and $5^2P_{3/2}$ excited state.

The hyperfine structure of these states is illustrated in figure 3.8, along with the transitions used in the production of a BEC. The nuclear spin for ^{87}Rb is $I = 3/2$, hence the ground state $|L = 0, J = 1/2\rangle$ is split by the hyperfine interaction into the $F = I + J = 1, 2$ levels. Similarly the excited state $|L = 1, J = 3/2\rangle$ is split into the $F' = 0, 1, 2, 3$ levels. For the MOT and Molasses stages described in Section 3.3.2 the cooling transition is the cycling $|F = 2\rangle \rightarrow |F' = 3\rangle$ transition. To prevent pumping to the $|F = 1\rangle$ dark state, repump light is added to continuously transfer the $|F = 1\rangle$ population to the $|F' = 2\rangle$ state. For the pumping stage described in Section 3.4, the $|F = 2\rangle \rightarrow |F' = 2\rangle$ transition is used to cycle the atoms over to a magnetically trappable state. The microwave transition between the two ground state hyperfine levels $|F = 1\rangle \rightarrow |F = 2\rangle$ is also indicated by the green arrow. This transition is used for

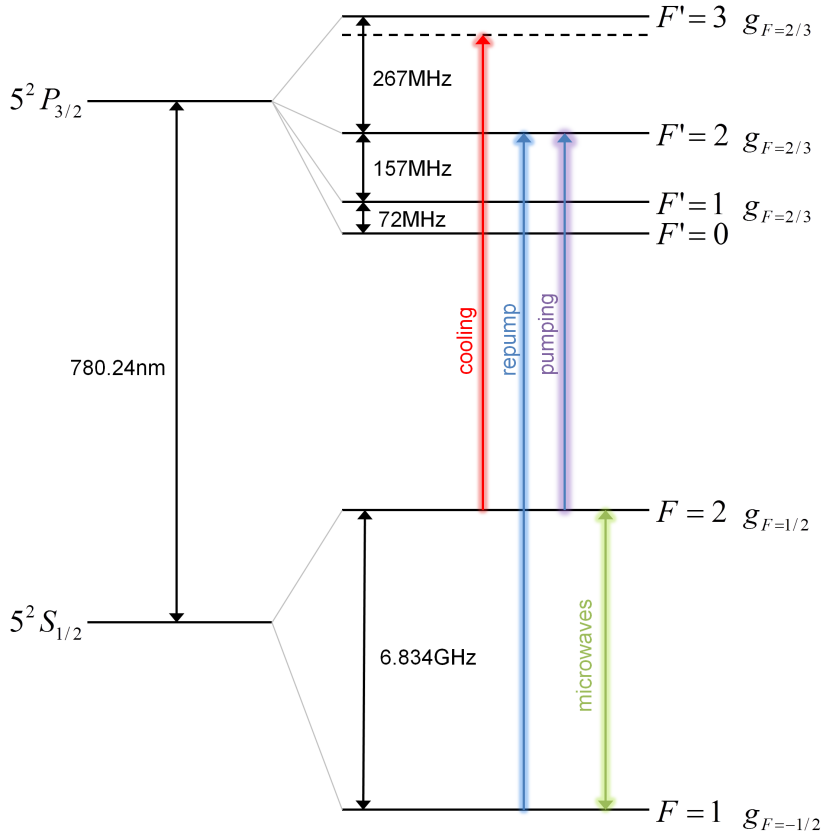

Figure 3.8: ^{87}Rb D_2 hyperfine structure: Levels are labeled by their total angular momentum, F, and the approximate Landé g-factor, g_F. The appropriate cooling and repump transitions used in the MOT and molasses stage are indicated by the red and blue arrows respectively. The transition for optical pumping before magnetic trapping is indicated by the purple arrow. The microwave transition used in both evaporative cooling and the final state transfer is shown by the green arrow.

evaporative cooling described in Section 3.6 and in the final state transfer explained in Section 3.8. Absorption imaging makes use of the same $|F = 2\rangle \rightarrow |F' = 3\rangle$ transition used for laser cooling.

The laser setup used to generate the cooling, repump, pumping, and imaging light is described in detail in [45, 46]. The lasers used are two temperature controlled commercial external cavity diode lasers (ECDL). Both are locked using saturated-absorption spectroscopy, with the cooling laser locked to the $|F = 2\rangle \rightarrow |F' = 2, 3\rangle$ crossover peak, and the repump laser locked to the $|F = 1\rangle \rightarrow |F' = 1, 2\rangle$ crossover peak. The precise frequencies required are then obtained using acousto-optic modulators (AOM) to shift the laser frequencies. Sufficient cooling power is achieved by using the cooling laser to seed an integrated master-oscillator-power-amplifier which provides several hundred mW of cooling light used in the MOT beams.

3.3.2 Magneto-optical trap (MOT)

A MOT is a combination of light and magnetic fields used to both cool and spatially confine atoms, and was first demonstrated in [59]. The ability of the MOT to capture and cool a room temperature atom vapour down to a few hundred μK means that it has become the starting point for most experiments on ultracold gases. A MOT is formed by three pairs of counter-propagating red-detuned laser beams, overlayed with a magnetic quadrupole field, such that the magnetic field strength increases along all directions from the origin. This is illustrated in figure 3.9 for one dimension for the example of cooling the $F = 0$ state using the $F = 0 \rightarrow F' = 1$ transition. If one initially neglects the magnetic gradient there is no shift of the Zeeman levels and the lasers are red-detuned of resonance for all z. However, the one-dimensional velocity of the atom along the direction of the beams, v, causes a Doppler shift of $\pm kv$ of the observed frequency of the laser light. As a result the motion of an atom towards one of the beams causes it to Doppler-shift into resonance and the resultant scattering force due to absorption slows the atom, creating a viscous damping force. This effect is called Doppler cooling and is used to cool the atoms in a technique called optical molasses. To spatially confine as well as cool the atoms a magnetic gradient must be included, creating a MOT.

As described in Section 3.5, the quadrupole field has a magnetic zero at the origin, and the magnitude of the field increases linearly with distance. The effect of this gradient is to cause the energy levels of the three sub-levels of the $F = 1$ level to vary linearly with the atom's position. In a MOT the polarisation of the pair of beams with respect to a fixed direction in space is chosen to be opposite: σ^+ and σ^-. The effect of this is that when an atom is displaced from $z = 0$, the selection rules mean that absorption from the beam that will push the atom back towards $z = 0$ will dominate over absorption from the opposite beam. This imbalance of radiative force caused by the Zeeman effect creates a position dependent force, confining atoms at the origin.

Using the scattering force derived in (3.45), we can write the overall scattering force in the MOT configuration as

$$F_{\mathrm{MOT}} = F_{\mathrm{sc}}^{\sigma^+}\left(\Delta - kv - \frac{\mu B'}{\hbar}z\right) - F_{\mathrm{sc}}^{\sigma^-}\left(\Delta + kv + \frac{\mu B'}{\hbar}z\right) \tag{3.46}$$

$$= -2\frac{\partial F_{\mathrm{sc}}}{\partial \Delta}\left(kv + \frac{\mu B'}{\hbar}z\right), \tag{3.47}$$

where μ is the dipole moment of the atom, and B' is the magnetic field gradient. By expanding the expression to first order we see that the motion of an atom in the MOT is equivalent to damped simple harmonic motion. The MOT configuration has a high capture velocity and therefore is able to trap and cool room temperature atom vapour. The limit to which an atom cloud can be cooled in a MOT is given by the Doppler limit. This limit arises due to the recoil energy associated with random fluctuations

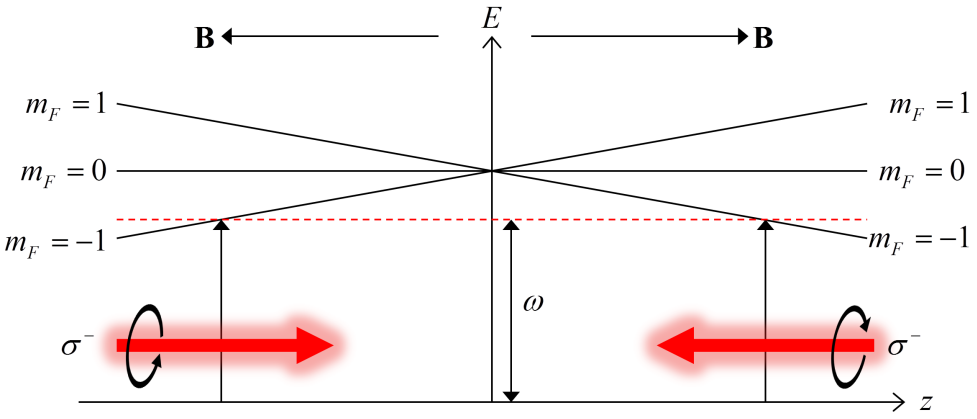

Figure 3.9: Mechanism for a 1D magneto-optical trap illustrated for the $F = 0$ to $F = 1$ transition. Two counter-propagating circularly polarised beams, red-detuned of the zero field transition, are overlayed with a magnetic field gradient. The handedness of the beams is the same with respect to their direction of propagation, but opposite with respect to the field axis. The magnetic gradient adds spatial confinement, bringing atoms far from the origin into resonance with the appropriately polarised beam.

about the mean number of photons absorbed and spontaneously emitted [55]. This gives rise to the Doppler cooling limit

$$T > T_D = \frac{\hbar\Gamma}{2k_B}, \tag{3.48}$$

which for the case of ^{87}Rb gives a temperature of 146 μK.

As mentioned in Section 3.3.1 the cooling transition used is the $|F = 2\rangle \rightarrow |F' = 3\rangle$ transition. Because the laser polarisation with respect to the field direction is σ^-, the precise transition is the $|F = 2, m_F = -2\rangle \rightarrow |F' = 3, m_{F'} = -3\rangle$ transition, which is a closed cycling transition since $|F' = 3, m_{F'} = -3\rangle$ should only decay back to $|F = 2, m_F = -2\rangle$. Due to the continuous absorption and emission of photons, off resonant excitation to the $|F' = 2\rangle$ state can occur, which can then decay to the $|F = 1\rangle$ ground state which is optically dark to the cooling light. To prevent all the atoms accumulating in this state, repump light which is resonant with the $|F = 1\rangle \rightarrow |F' = 2\rangle$ transition is also present in the MOT stage and clears out this dark state.

For our MOT we typically use 130 mW of cooling light, red-detuned 3.1Γ below resonance, where $\Gamma \approx 6$ MHz is the linewidth of the excited state. The $1/e^2$ beam diameter of our MOT beams is ≈ 3 cm. Overlapped with the cooling beams is 10 mW of resonant repump light. The magnetic gradient is 6.4 G cm^{-1} along the vertical direction and 3.2 G cm^{-1} in the horizontal plane. Typical MOT loading time is about 15 seconds and the atom number saturates at $\approx 5 \times 10^9$.

3.3.3 Sub-Doppler cooling

Sub-Doppler cooling was first achieved using the standard molasses technique described above [60]. This unexpected effect arises due to the fact that real atoms have a ground state with degenerate magnetic sublevels which were neglected in the previous discussion. The first explanation of temperatures observed below the Doppler cooling limit was provided by the mechanism of Sisyphus cooling [61], which can be used to explain many of the sub-Doppler cooling techniques which have been developed. To briefly explain the process, we consider a simplified system consisting of a $J = 1/2$ ground state (with degenerate $m_J = \pm 1/2$ magnetic sublevels) and a $J' = 3/2$ excited state (with degenerate $m_J = \pm 3/2, \pm 1/2$ magnetic sublevels). This atom is dressed in zero magnetic field with two counter-propagating red-detuned laser beams, linearly polarised orthogonal to one another [1].

The interference of the two beams creates a polarisation standing wave, where the polarisation varies from σ^+ to π to σ^- with a period of $\lambda/2$. If the ground state has degenerate magnetic sublevels, the light shift experienced by each sublevel will be polarisation dependent, and the degeneracy will be lifted. For the case of $m_J = +1/2$, the electric dipole transition for the σ^+ transition to $m_{J'} = 3/2$ is stronger than the π transition to $m_{J'} = 1/2$ and stronger still than the σ^- transition to $m_{J'} = -1/2$, with the ratio $3 : 2 : 1$. This relates directly to the Rabi frequency, Ω, hence the light shift will vary spatially along with the polarisation, being largest where the light is pure σ^+ and smallest where it's pure σ^-. For the $m_J = -1/2$ ground state the ordering of the ratios is flipped and the light shift will also vary spatially, but π out of phase with respect to that of the $m_J = +1/2$ state. This effect is illustrated in figure 3.10.

The other effect of the polarisation standing wave is spatially selective pumping of the ground states. In regions of pure σ^+ polarisation the $m_J = +1/2$ state can only transition to $m_{J'} = 3/2$, where it spontaneously decays back to its original state. Conversely the $m_J = -1/2$ is pumped to the $m_J = +1/2$ ground state since it can only transition to the $m_{J'} = +1/2$ excited state, where there is a possible decay path to the $m_J = +1/2$ ground state. We therefore see that in regions of σ^+ polarisation the atoms are pumped towards the lower energy $m_J = +1/2$ ground state, and similarly in regions of σ^- polarisation the atoms are pumped towards the lower energy $m_J = -1/2$ ground state. This is illustrated in figure 3.10, where we see that an atom moving in this potential will repeatedly climb the potential barrier of one state and then be pumped to the potential minima of the other state, thus giving up its kinetic energy to the background field. The limit of such a cooling method is the recoil energy associated with spontaneous emission which provides a lower threshold for the temperature called the recoil limit:

$$T > T_{\text{rec}} = \frac{\hbar^2 k^2}{k_B m}. \tag{3.49}$$

[1] This is the textbook lin $\perp$ lin configuration, but the effect is also present for two circularly polarised beams of opposite handedness

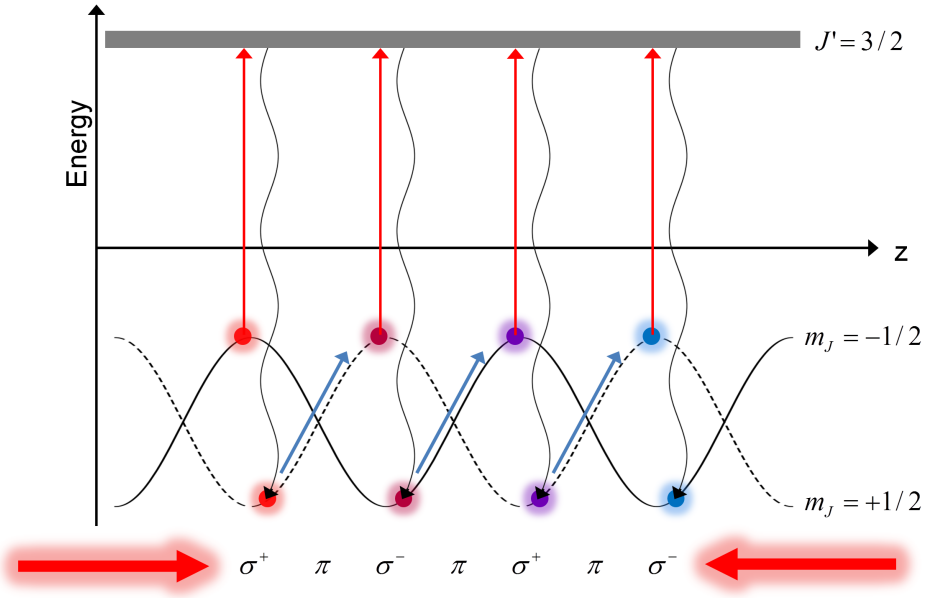

Figure 3.10: Sisyphus cooling mechanism in the lin ⊥ lin configuration: The counter propagating beams create a polarisation standing wave, where the polarisation varies between σ^+, π, and σ^- with period $\lambda/2$. Due to the different electric dipole transitions of the different magnetic sublevels this creates a periodic shift in the ground state energies. The polarisation standing wave preferentially pumps atoms from the upper ground state to the lower, hence as an atom moves it climbs a potential barrier and is then pumped to a potential minima. This removes the kinetic energy of the atoms, cooling the cloud.

For the case of ^{87}Rb this gives a recoil temperature of 180 nK, well below the limits of Doppler cooling.

The typical experimental sequence used in our optical molasses involves removing the magnetic field gradient and further detuning the MOT beams to -4.1Γ. The power of the cooling light is also reduced to about 60 mW. The molasses stage typically only lasts about 6ms, after which the ^{87}Rb atoms reach ≈ 50 μK. Our molasses stage is optimised to maximise phase space density, rather than actually achieve cooling to T_{rec}.

3.4 Optical pumping

At the end of the MOT and molasses stages the atoms are distributed between the various m_F states of the $F = 2$ manifold. As explained in Section 3.5, only states with $m_F = 2, 1$ are magnetically trappable, hence to avoid losing over half the atoms the cloud is optically pumped to the $|F = 2, m_F = 2\rangle$ state before the quadrupole field is ramped up. Transferring the atoms to the stretched state is also beneficial for two other reasons. Firstly the increased magnetic dipole moment of the $m_F = 2$ state provides tighter magnetic confinement. This improves efficiency of transport to the science cell, and increases the elastic collision rate which is important for efficient

evaporative cooling. Secondly, the presence of other spin states allows inelastic spin-exchange collisions which can lead to additional heating and losses. While this effect is only modest in the case of ^{87}Rb, removal of atoms in the $|F = 2, m_F = 1\rangle$ state significantly improves the sympathetic cooling of ^{39}K.

The pumping sequence starts after molasses by removing the cooling beams but retaining the repump light, allowing the atoms to fall under gravity. A guide field of several Gauss is ramped up over 800 μs to provide a quantisation axis for the atoms, defining the polarisation of the pumping light. The pumping light is then flashed on for approximately 80 μs with an intensity of about the saturation intensity. The pumping light is resonant with the $|F = 2\rangle \rightarrow |F' = 2\rangle$ transition, as illustrated in figure 3.8. The pumping light is chosen to be σ^+ polarised, exciting transitions of the type $|F = 2, m_F\rangle \rightarrow |F' = 2, m_F + 1\rangle$. While the excited $F' = 2$ state can spontaneously decay back to the $F = 2$ state via any $\Delta m_F = 0, \pm 1$ transition, the polarisation of the pumping light ensures the atoms migrate towards the $|F = 2, m_F = 2\rangle$ state. Once in the $|F = 2, m_F = 2\rangle$ state, the atoms are dark to the light since there is no $\Delta m_F = +1$ transition, therefore for perfect σ^+ polarisation the atoms accumulate in the stretched state, where they are then transparent to the pumping light. The repump light is present to transfer any atoms which decay to the $F = 1$ state back into the pumping cycle.

To test the efficiency of the pumping stage we load the atoms into the magnetic trap and then back into the MOT. Only those atoms pumped into a magnetically trappable state will remain, causing the MOT to load from a non-zero population. With pumping this starting population can reach $\approx 80\%$ of the saturated MOT population, compared to only 40% without pumping. We can test the correct sign of the pumping polarisation by reversing the direction of the guide field and observing anti-pumping to the $|F = 2, m_F = -2\rangle$ state, and a much lower starting MOT value.

3.5 Atoms in an external magnetic field

The Zeeman Hamiltonian describing the interaction of an atom with a static external magnetic field $\mathbf{B}$ is given by

$$H_B = \frac{\mu_B}{\hbar} \left(g_S \mathbf{S} + g_L \mathbf{L} + g_I \mathbf{I} \right) \cdot \mathbf{B}, \tag{3.50}$$

where $\mathbf{S}$ is the total electronic spin operator, $\mathbf{L}$ is the total electronic orbital angular momentum operator, $\mathbf{I}$ is the internal nuclear spin operator, and g_S, g_L, and g_I are the corresponding Landé g factors. The interaction of the electron spin with the effective magnetic field of the nucleus leads to the spin-orbit coupling term in the atomic Hamiltonian which couples $\mathbf{S}$ and $\mathbf{L}$ into the total angular momentum $\mathbf{J} = \mathbf{L} + \mathbf{S}$. With $\mathbf{J}$ as

a good quantum number, the magnetic Hamiltonian now takes the form

$$H_B = \frac{\mu_B}{\hbar}\left(g_J\mathbf{J} + g_I\mathbf{I}\right)\cdot\mathbf{B}, \tag{3.51}$$

where g_J is given in terms of g_S and g_L [55]. If we now include the hyperfine term in the atomic Hamiltonian, arising due to the interaction of the nuclear spin with the effective magnetic field of the electron, the relevant Hamiltonian to diagonalise is

$$H = A\mathbf{I}\cdot\mathbf{J} + \frac{\mu_B}{\hbar}\left(g_J\mathbf{J} + g_I\mathbf{I}\right)\cdot\mathbf{B}, \tag{3.52}$$

where A is the hyperfine structure constant, and is equal to $A = h \times 3.417$ GHz for ^{87}Rb. This can be easily solved in the two limiting cases of low and high field. In both cases we neglect the nuclear Zeeman term since the coefficient g_I is smaller than g_J by about three orders of magnitude.

Low field: When the energy shift due to the field is much smaller than the hyperfine term, the coupling between **I** and **J** dominates over that with the magnetic field and we may define $\mathbf{F} = \mathbf{I} + \mathbf{J}$, where F and m_F are good quantum numbers. The Zeeman terms now act as perturbations to the states labeled by $|F, m_F\rangle$ and the energy levels are

$$E_{AZ} = \frac{1}{2}A[F(F+1) - I(I+1) - J(J+1)] + g_F m_F \mu_B B_z, \tag{3.53}$$

and the corresponding g_F is given in terms of g_J [55]. The first term is the usual hyperfine splitting, while the second term gives the field dependence. Different m_F states split linearly with magnetic field according to

$$\Delta E_{|F,m_F\rangle} = \mu_B g_F m_F B_z, \tag{3.54}$$

and hence the energy spacing $E_{|F,m_F\rangle} - E_{|F,m_F\pm1\rangle}$ is equal for all m_F in a given F manifold.

High field: When the energy shift due to the field is much larger than the hyperfine term, **I** and **J** will couple strongly to **B** and hence the states will be labeled by $|m_J, m_I\rangle$. The energy levels are then given by

$$E_{PB} = Am_J m_I + g_J m_J \mu_B B_z, \tag{3.55}$$

and now m_J determines the scaling of the energy with magnetic field.

For intermediate field strengths the full Hamiltonian (3.52) must be diagonalised. This can be done by expanding the hyperfine term into raising and lowering operators using the identity

$$\mathbf{I}.\mathbf{J} = I_z J_z + \frac{1}{2}(I_+ J_- + I_- J_+). \tag{3.56}$$

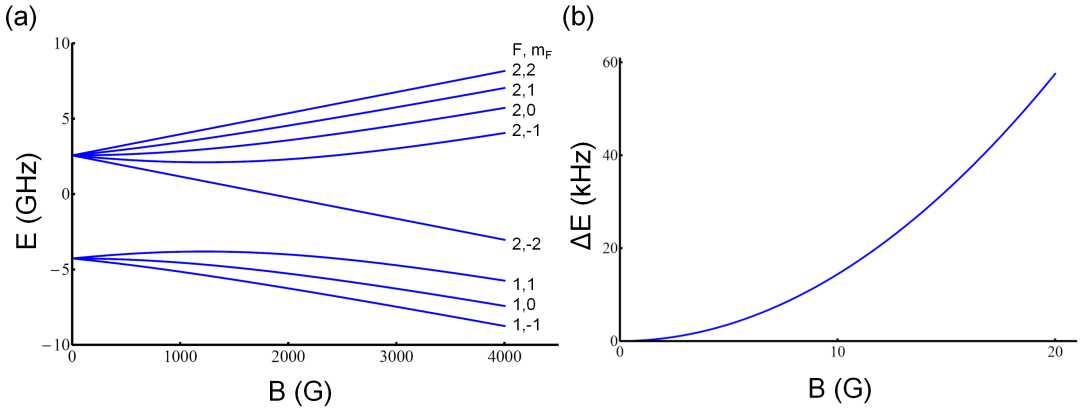

Figure 3.11: Energy shift in a magnetic field: (a) Hyperfine structure of the $5^2S_{1/2}$ ground state of ^{87}Rb in an external magnetic field. States are labeled with their low field quantum number $|F, m_F\rangle$. (b) The energy difference $\Delta E = E(|F = 1, m_F = 0\rangle \rightarrow |F = 1, m_F = 1\rangle) - E(|F = 1, m_F = -1\rangle \rightarrow |F = 1, m_F = 0\rangle)$.

For the state we care about, which is the ground state of the D line transition with $I = 3/2$ and $J = 1/2$, there exists an analytical form of the solution called the Breit-Rabi formula [62]:

$$E_{|J=1/2,m_J,I,m_I\rangle} = -\frac{\Delta E_{\text{hfs}}}{2(2I+1)} + g_I \mu_B m B \pm \frac{\Delta E_{\text{hfs}}}{2}\left(1 + \frac{4mx}{2I+1} + x^2\right)^{1/2}, \quad (3.57)$$

where $\Delta E_{\text{hfs}} = A(I+1/2)$ is the zero field hyperfine splitting, $m = m_I \pm m_J = m_I \pm 1/2$, and

$$x = \frac{(g_J - g_I)\mu_B B}{\Delta E_{\text{hfs}}}. \quad (3.58)$$

This is plotted in figure 3.11(a) for the ground state of ^{87}Rb, $5^2S_{1/2}$. We see that the energy splitting is approximately linear up to about 500 G, and therefore the low field approximation for the energy splitting (3.53) can be used for most experimental parameters. We note however in figure 3.11(b) that the energy differences $E_{|F=1,m_F=1\rangle} - E_{|F=1,m_F=0\rangle}$ and $E_{|F=1,m_F=0\rangle} - E_{|F=1,m_F=-1\rangle}$ differ by several kHz even at a modest field of a few Gauss. This has strong implications when coupling the $F = 1$ manifold. If the Rabi frequency of the coupling field is less than this difference, the coupling can only be resonant for one of the energy splittings at any one time, and hence the three level system $m_F = +1, 0, -1$ is reduced to a two level system.

3.5.1 Magnetic trapping

In our experiments we can assume the linear form of the Zeeman energy

$$U(\mathbf{r})_{|F,m_F\rangle} = \mu_B g_F m_F B(\mathbf{r}), \quad (3.59)$$

where we have replaced B_z by $B = |\mathbf{B}|$, since for sufficiently large magnetic fields the dipole of the atom will adiabatically follow the field direction. If we allow the magnetic field to vary spatially the atom will experience a force

$$\mathbf{F}(\mathbf{r}) = -\nabla U(\mathbf{r}) = -\mu_B g_F m_F \nabla B. \tag{3.60}$$

From (3.59) it follows that a local field minimum would act as a trap for low-field seeking states with $g_F m_F > 0$. For ^{87}Rb, the Landé factors for the ground state are $g_{F=1} = -1/2$ and $g_{F=2} = 1/2$, and hence the magnetically trappable states are $|F, m_F\rangle = |1, -1\rangle, |2, 2\rangle$, and $|2, 1\rangle$.

Once in a magnetic trap it is possible to cool the gas down to degeneracy using microwave or RF fields to selectively transfer the most energetic atoms to untrapped states. The advantage of using magnetic traps is that firstly they can be very deep, allowing them to efficiently collect the atoms at the end of the laser cooling stage. Secondly the lifetime in such traps can be extremely long, limited only by collisions with the residual background gas. This is particularly useful in our setup when we need to sympathetically cool ^{39}K with ^{87}Rb, which has a long thermalisation time due to the small inter-species scattering length, a_{K-Rb}. Finally evaporative cooling in a magnetic trap can be state and species selective, which again is utilised in the sympathetic cooling of ^{39}K to only remove ^{87}Rb atoms and maximise the phase space density of ^{39}K.

Quadrupole trap

In our experiment, following laser cooling in the MOT and molasses stages, the atoms are transferred to a quadrupole trap produced by a pair of opposed Helmholtz coils as shown in figure 3.12(a). Defining the axis of symmetry as the z direction, using the Maxwell relation $\nabla \cdot \mathbf{B} = 0$, the magnetic field near the origin is given by

$$\mathbf{B} = B'(x, y, -2z). \tag{3.61}$$

The strength of the field varies linearly with distance from the origin, and due to the symmetry of the trap the gradient is twice as strong along the vertical direction than along the radial. The full field calculation is shown in figure 3.12(b), and shows that the trap is only a local minimum with the trap depth given by the difference between the minimum field at the origin and the maximum field along the radial direction. The field lines shown in figure 3.12(a) illustrate that the field direction is the same as that required for the MOT stage, hence we use the same coils for both roles.

In this experiment, the quadrupole coils are a pair of water-cooled copper coils in anti-Helmholtz configuration mounted on a track mount, which is used to translate them between the MOT chamber and the science cell. Following optical pumping, the trap is loaded by jumping the field to 40 G/cm along the strong axis, and then ramping the field over 50 ms to its maximum value of 160 G/cm. This tightly confines the

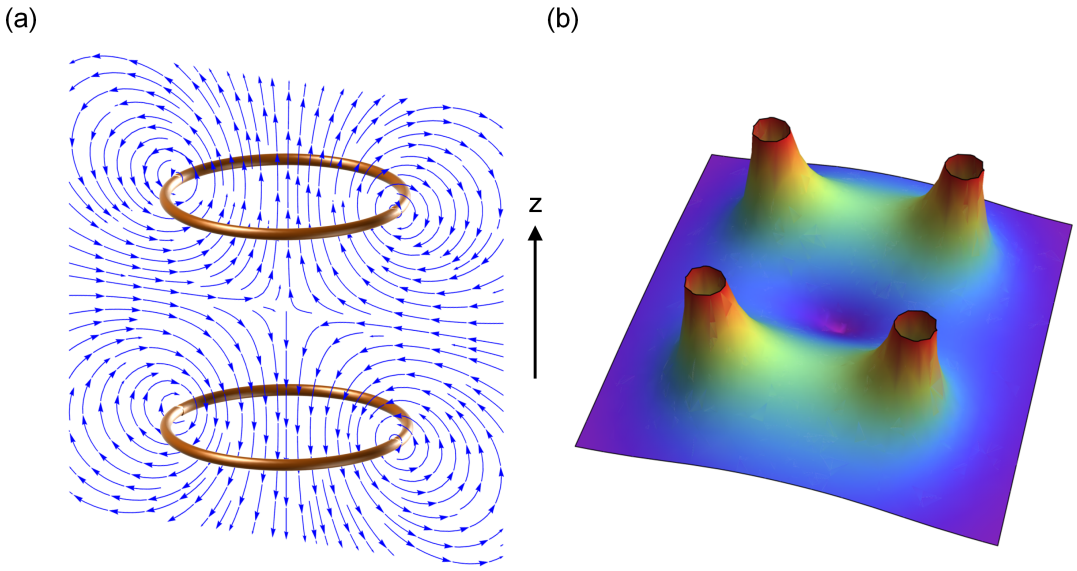

Figure 3.12: Quadrupole trap: (a) Direction of the magnetic field in the xz plane created by a pair of coils in Anti-Helmholtz configuration. The vertical spacing between the coils is chosen equal to the diameter of the coils. (b) Potential created in the xz plane by the quadrupole trap.

atoms, allowing the track to move the coils to the science cell, carrying the atom cloud with it down the narrow channel and into the lower pressure environment.

The main disadvantage of the quadrupole trap is that the magnetic field vanishes at the origin. In this region of very low field, states with different m_F become degenerate and the magnetic field no longer defines the quantisation axis for the atoms to adiabatically follow. This allows non-adiabatic transfers between different m_F states to occur, and if these new states are not magnetically trapped they are lost from the system, reducing the cloud lifetime. Such spin flips are called Majorana spin flips [63] and cause trap losses and heating. Ultimately this process dictates that cooling to quantum degeneracy in a quadrupole trap alone is not possible [64]. Several solutions to this problem have been found, however the solution used in our experiment is to transform the quadrupole trap into a QUIC (Quadrupole-Ioffe configuration) trap where the magnetic minimum is offset from zero.

QUIC trap

To overcome the problem of Majorana spin flips several solutions were implemented in our system and used to cool to degeneracy. These include:

Optically plugged quadrupole The magnetic zero in the quadrupole trap is overlapped with a blue-detuned repulsive optical potential which acts to "plug" the hole. This method was first used successfully at MIT in 1995 [11].

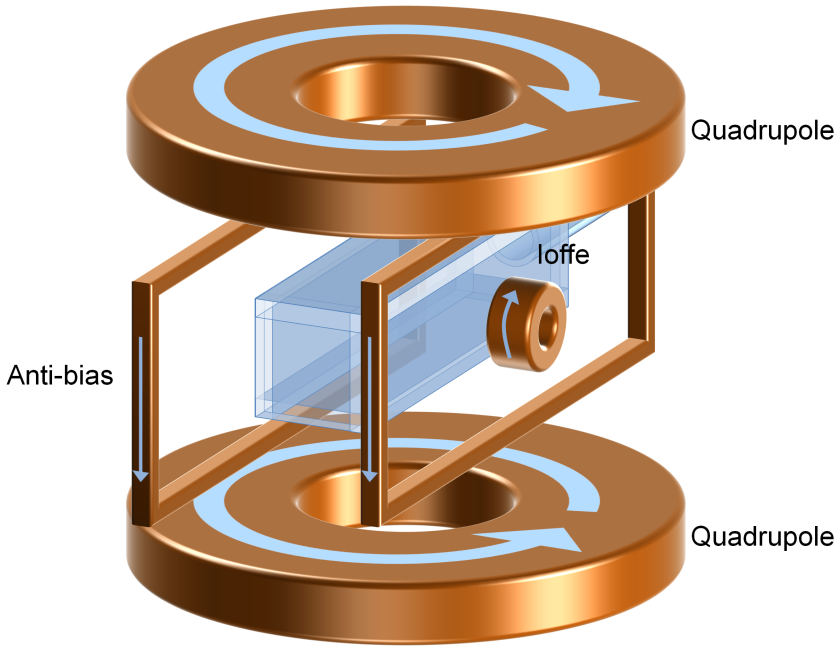

Figure 3.13: QUIC trap: This illustrates the configuration of the quadrupole, Ioffe and anti-bias coils in the QUIC trap relative to the science cell. The arrows on the coils indicate the direction of current.

Time-averaged orbiting potential (TOP) trap The quadrupole field is superimposed with a rotating, spatially uniform magnetic field which causes the magnetic zero to move out from the original origin and orbit about it. If the frequency of the rotation is chosen to be slow enough for adiabatic following to prevent transitions between m_F states, but faster than the motion of the atoms, the atoms move in the effective time-averaged potential of the instantaneous potential: a harmonic trap with non-zero field everywhere [10, 65].

Optical dimple hybrid trap A red-detuned attractive optical potential is positioned approximately a beam waist from the quadrupole magnetic zero. At very low temperatures close to degeneracy the optical "dimple" dominates over the magnetic field minimum and the coldest atoms are held away from the magnetic zero, and therefore protected from spin flips [66].

Of these three the optical dimple trap was the optimal method for ^{87}Rb, producing condensates of 5×10^5 atoms with less than 10 s of evaporation. Unfortunately for much of the time during this work it was necessary to optimise the experiment for production of ^{39}K condensates, which requires very long evaporation sweeps due to the relatively small K-Rb interspecies scattering length of $a_{K-Rb} \simeq 28a_0$ [67], compared to $a_{Rb} \simeq 99a_0$ [68] for ^{87}Rb. The solution which worked best for sympathetic cooling of ^{39}K was found to be to evaporate in a QUIC trap, and as a result the same method is

used to produce ^{87}Rb BECs.

The QUIC trap is a relatively simple Ioffe-Pritchard type trap first implemented in [69], where the quadrupole field is modified to offset the trap minimum to a positive value of magnetic field, and convert the trapping potential from linear to harmonic. This QUIC trap is formed by adding the field from a single coil, known as the Ioffe coil, orientated perpendicular to the quadrupole coils, which produces the offset harmonic potential. An additional uniform field known as the anti-bias field opposes the field generated by the Ioffe coil and provides greater control in the position of the magnetic field minimum along the direction of the Ioffe coil. The orientation of these coils is illustrated in figure 3.13. For full details of the setup, potential, and loading procedure of our QUIC trap see [45, 46]. The main disadvantage of the QUIC trap is that the confinement along the direction of the Ioffe coil is quite weak, and as a result evaporation sweeps must be slow to allow thermalisation.

3.6 Evaporative cooling

The phase space densities achieved at the end of laser cooling are still typically many orders of magnitude below unity and hence degeneracy. As a result, evaporative cooling is a necessary stage of nearly all ultracold experiments, and allows one to achieve arbitrarily low temperatures. The basic principle of evaporative cooling is to selectively remove only the highest energy atoms in a cloud and then allow the remaining sample to rethermalise at a lower equilibrium temperature. By repeatedly truncating the thermal distribution in this way the temperature can be lowered indefinitely, limited only by the discrete particle number. Provided the evaporation is efficient in removing only the most energetic atoms and background loses and heating are limited, the atom loss and temperature reduction result in a net increase in phase space density.

The first evaporative cooling stage is done in a magnetic trap once the atoms have been transported to the science cell. This itself is split into two steps: an initial evaporative sweep in the quadrupole trap, followed by a slower sweep in the QUIC trap. The principles for both steps are the same. The energy levels of the $F = 1$ and $F = 2$ magnetic sublevels are shown in figure 3.14 as a function of field strength which, for a quadrupole trap, is proportional to distance from the magnetic zero. We apply a microwave (MW) field of a frequency Δ_{MW} greater than the hyperfine splitting, ω_{HF}, indicated by the green arrow. For an atom to move into resonance with the MW field it must move away from the origin to a region of higher field. If we choose Δ_{MW} to be sufficiently large, only the most energetic atoms will reach this region, at which point they will undergo a magnetic dipole transition to the untrapped $|1, 1\rangle$ state and are lost.

We therefore have a method for selectively ejecting the high energy atoms from the trap, hence by gradually sweeping the MW frequency downwards we can evaporatively

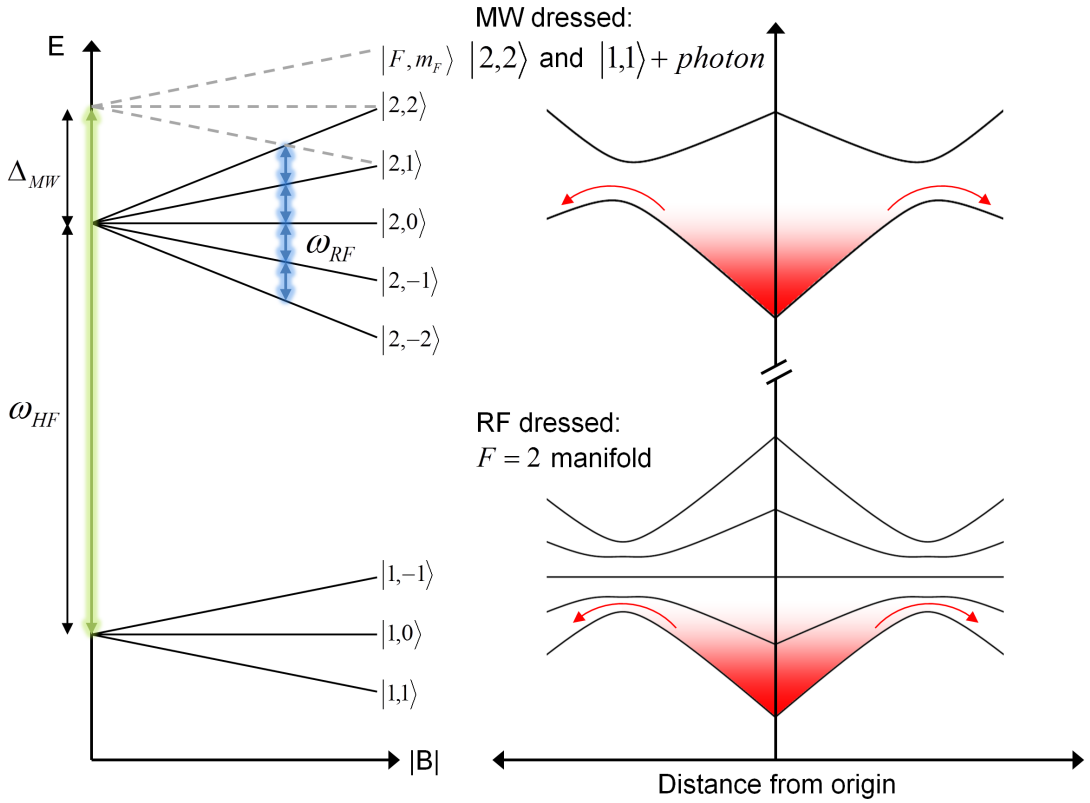

Figure 3.14: Evaporation in a magnetic trap: The left figure shows the hyperfine energy levels as a function of magnetic field. The $F = 1$ and $F = 2$ manifolds are coupled by a microwave field (green arrow) detuned Δ_{MW} above the zero-field hyperfine splitting, ω_{HF}. The grey lines indicate the $F = 1$ manifold shifted by the microwave photon energy, hence we see the first states coupled are $|2, 2\rangle$ and $|1, 1\rangle$ plus a photon. The microwave dressed states are shown in the upper right panel. The $F = 2$ magnetic sublevels are coupled by an RF field (blue arrow) of frequency ω_{RF}. Here we assume the field is low and the states are all equally spaced such that the RF couples all five sublevels at once. The RF dressed version of the $F = 2$ manifold is shown in the bottom right.

cool the cloud, with the final temperature set by the final MW frequency. The same effect can be achieved by applying a radio-frequency (RF) field of frequency ω_{RF}. This drives $\Delta m_F = 1$ transitions between the different m_F levels of the $F = 2$ manifold until ultimately the atoms transfer to the untrapped $m_F = 0$, and the anti-trapped $m_F = -1, -2$ states and are lost from the trap. To create an equivalent trap depth to the case of MW, the RF frequency is given by $\omega_{RF} = \Delta_{MW}/3$. The main advantage of using microwaves is that it allows selective cooling of ^{87}Rb only, which is used to sympathetically cool ^{39}K.

A more informative picture can be obtained using the dressed state formalism developed in Section 3.2.1 [70]. If we label states as $|F, m_F; n\rangle$, which is the $|F, m_F\rangle$ state plus n photons, the $|1, m_F; 1\rangle$ manifold is indicated by the grey levels in figure 3.14. We therefore see that the evaporation point is set by where microwaves first couple the $|2, 2\rangle$ and $|1, 1; 1\rangle$ states. At higher fields it is clear that additional couplings will

occur, which can lead to production of atoms in the $|2,1\rangle$ state. The Hamiltonian of the coupled $|2,2\rangle$ and $|1,1;1\rangle$ states in a magnetic field is an intuitive modification of that in (3.14):

$$\hat{H} = \frac{\hbar}{2}\begin{bmatrix} \Delta_{MW} - \mu_B B(\mathbf{r}) & \Omega \\ \Omega & -\Delta_{MW} + 2\mu_B B(\mathbf{r}) \end{bmatrix}, \tag{3.62}$$

where we have used that $g_F = 1/2$ $(-1/2)$ for the $F = 2$ $(F = 1)$ states. This is diagonalised to obtain the dressed state eigenvalues which are plotted in figure 3.14 as a function of distance from the trap zero. The ground state forms a trap, whose depth can be reduced by reducing the MW frequency, or increasing the field gradient. Provided the atoms cross the edge sufficiently slowly they remain in the dressed ground state and are transferred to the $|1,1\rangle$ state and are lost. Atoms which cross the boundary too quickly can be transferred to the upper band, and can then be trapped at the cloud's edge. To prevent this, the coupling strength between the states, Ω, must be sufficient for the adiabatic crossing criteria (3.35) to apply. We identify the detuning as $\Delta = (3\mu_B B' x/2\hbar)$, where B' is the field gradient and x is the position in the trap. Estimating the typical atom velocity as $v = \sqrt{k_B T/m}$ the adiabatic condition is given as

$$\Omega \gg \Omega_0 = \sqrt{\frac{3\mu_B B'}{2\pi^2\hbar}}\left(\frac{k_B T}{m}\right)^{1/4}. \tag{3.63}$$

For typical parameters at the start of the quadrupole evaporation, this gives a value of $\Omega_0 \sim 7$ kHz. If this is satisfied, atoms crossing the resonance point will leave the trap. If one evaporates with insufficient power, hot atoms can oscillate past the resonance point several times before being ejected, causing heating of the remaining cloud and inefficient evaporation. This process is extended to calculate the RF dressed $F = 2$ manifold which is also shown in figure 3.14. The relevant states coupled are the $|2,2\rangle, |2,1;1\rangle, |2,0;2\rangle, |2,-1;3\rangle$ and $|2,-2;4\rangle$. An atom adiabatically following the lowest band transitions from the trapped $|2,2\rangle$ state to the anti-trapped $|2,-2\rangle$ state. Because this is a higher order process, the necessary RF power for adiabatic following is higher than that required for MW, however we note that atoms transferring to the second and third band will still be lost from the trap. The requirement for higher power follows somewhat intuitively from observing the reduced level spacing present in the RF dressed states for the same Ω.

Following magnetic transport to the low pressure science cell we use a linear 2 s MW forced evaporation sweep in the quadrupole trap. The trap is then transformed into the QUIC trap and we then employ a 32 s forced evaporation using an exponential frequency sweep. Once this concludes we typically have about 4×10^7 atoms at a temperature of about 3 μK [44]. This is sufficiently cold to be loaded into an all optical dipole trap, where the final evaporation is done to achieve condensation. We now briefly describe the microwave and RF systems used in the experiment, since these are used extensively to perform state transfers which are integral to studying persistent currents.

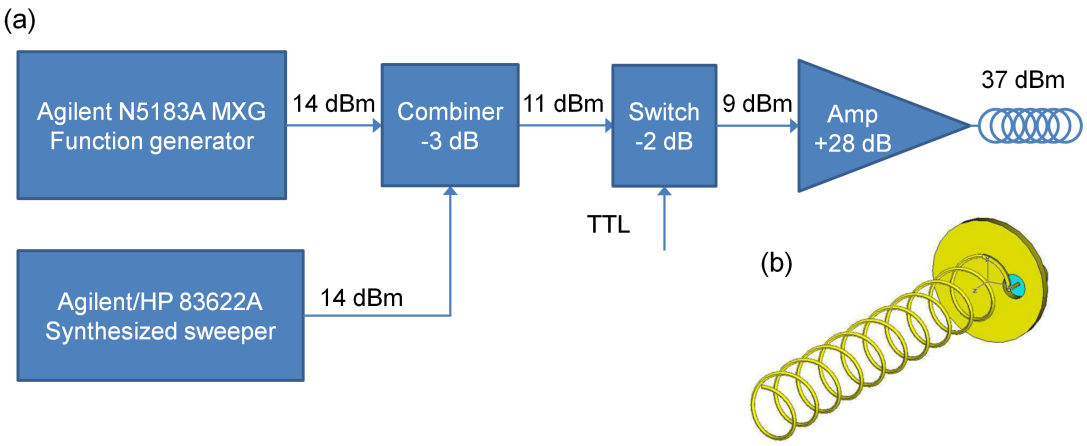

Figure 3.15: Microwave system: (a) The generator used for forced evaporation is the Agilent N5183A MXG function generator. The secondary generator (Agilent/HP 83622A) is used for $|2,1\rangle$ clean up and state manipulation. Both can output a maximum of 14 dBm and are combined using a power combiner. This is then passed through an RF switch and a custom made 28 dB amplifier before going to the microwave antenna. (b) Custom made helix antenna designed by I. Gotlibovych [71].

3.6.1 Microwave system

The microwave setup was designed by Igor Gotlibovych for a master's project and is detailed in [71]. Figure 3.15 (a) illustrates the basic configuration. The system is optimised to radiate the maximum power at a frequency equal to that of the hyperfine splitting, 6.8 GHz. The signal for forced evaporative cooling is derived from a function generator[1] which is then passed through a custom made amplifier built by Microwave Amplifiers Ltd. to give a maximum output power at the antenna of 37 dBm= 5 W. A secondary synthesizer[2] is power coupled[3] to this transmission line and provides the option to perform $|2,1\rangle$ clean up sweeps during evaporation, and is used to perform state manipulations of the BEC. The output of both generators is controlled by an external TTL-controlled RF switch[4] which provides timing resolution of 1 μs, limited by the resolution of our sequence control software.

The antenna is illustrated in figure 3.15 (b) and uses a helix design to try and increase directionality of the radiated power. The first 1/4 of the helix turn closest to the ground plate is deformed to impedance match the antenna with the cable and reduce reflections. The antenna radiates circularly polarised light, with a directionality, $D = 4.5$. The directionality is defined as the maximum intensity over the average

[1] Agilent N5183A MXG
[2] Agilent/HP 83622A
[3] Mini-Circuits ZX10-2-71-S+
[4] Mini-Circuits ZYSWA-2-50-DR

intensity,

$$I(r,\theta,\phi) = \frac{P}{4\pi r^2} G(\theta,\phi) \tag{3.64}$$

$$D = \max_{\theta,\phi} G(\theta,\phi), \tag{3.65}$$

where P is the total power, and r is the distance from the antenna. From this the maximum possible Rabi frequency can be calculated.

Electric dipole transitions between $|F, m_F\rangle$ states are forbidden, so the relevant matrix elements are magnetic dipole transitions. The coupling is given by

$$\hbar\Omega_{ij} = \langle\Psi_i| \mu \cdot \mathbf{B} |\Psi_j\rangle \tag{3.66}$$

with

$$\mu = \mu_B(g_I\hat{\mathbf{I}} + g_L\hat{\mathbf{L}} + g_S\hat{\mathbf{S}}). \tag{3.67}$$

Using $L = 0$ and $g_I \ll g_S$, we simply need to compute matrix elements of the spin operator. Using Clebsch-Gordan coefficients we can decompose the hyperfine states into eigenstates of the spin operator

$$|F, m_F\rangle = \sum_{m_I, m_S} C_{m_I,m_S} |I, m_I; S, m_S\rangle , \tag{3.68}$$

where C_{m_I,m_s} are the Clebsch-Gordan coefficients. We define the spin operator as $\hat{\mathbf{S}} = (\hat{\sigma}_x, \hat{\sigma}_y, \hat{\sigma}_z)/2$, where $\sigma_{x,y,z}$ are the appropriate Pauli spin matrices. The magnetic dipole moment between two states, (1) and (2), is then given by

$$\left\langle F^{(1)}, m_{F^{(1)}} \middle| \mu \middle| F^{(2)}, m_{F^{(2)}} \right\rangle = g_S\mu_B \sum \delta_{m_{I^{(1)}}, m_{I^{(2)}}} C^{(1)}C^{(2)} \left\langle S^{(1)}, m_{S^{(1)}} \middle| \hat{\mathbf{S}} \middle| S^{(2)}, m_{S^{(2)}} \right\rangle \tag{3.69}$$

Relevant non-zero magnetic dipole matrix elements are listed below

Element	Value
$\langle 2,2\| \mu \|2,1\rangle$	$\frac{1}{2}\mu_B(1,-i,0)^T$
$\langle 2,1\| \mu \|2,0\rangle$	$\frac{\sqrt{6}}{4}\mu_B(1,-i,0)^T$
$\langle 2,2\| \mu \|1,1\rangle$	$\frac{\sqrt{3}}{2}\mu_B(1,-i,0)^T$
$\langle 1,1\| \mu \|1,0\rangle$	$-\frac{1}{2\sqrt{2}}\mu_B(1,-i,0)^T$

Using the relation between intensity and magnetic field, $I = B^2c/2\mu_0$, the maximum Rabi frequency for the $|2,2\rangle \to |1,1\rangle$ transition is then given by

$$\hbar\Omega_{|2,2\rangle\to|1,1\rangle} = \frac{\sqrt{3}}{2}\mu_B\sqrt{\frac{\mu_0 PD}{2\pi r^2 c}} \approx 14 \text{ kHz}, \tag{3.70}$$

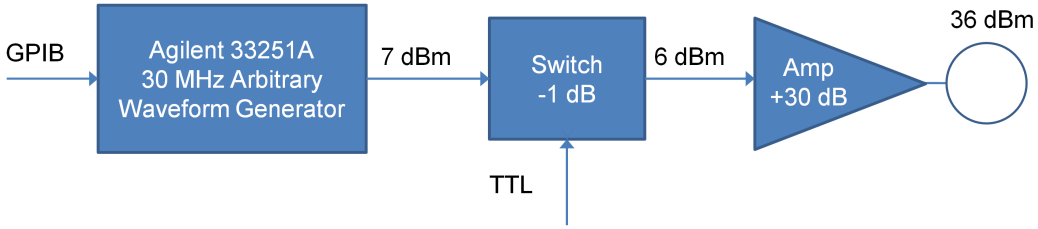

Figure 3.16: RF system: The waveform generator used to produce the RF signal can output frequencies up to 30 MHz with a power of up to 24 dBm. The usable power is restricted to 7 dBm so as to prevent damaging the amplifier. The output state is controlled by a switch which provides time control of pulse times required for Rabi flopping. The RF signal is boosted by 30 dB by an amplifier before going to a single loop antenna, giving a maximum power of 36 dBm (4 W).

where we assume a distance $r = 10$ cm. This is an upper limit on the attainable Rabi frequency since we have neglected reflections at the antenna due to unmatched impedances which will reduce the useable power. Comparison with (3.65) suggests this Rabi frequency is sufficient for evaporative cooling.

3.6.2 RF system

The RF system is no longer used for evaporation, but is still used to perform state transfers between magnetic sublevels. The RF setup is illustrated in figure 3.16. The waveform is produced by a 30 MHz waveform generator[1]. To achieve short bursts (~ 100 μs) required for Rabi flopping, the output of the generator is controlled by an external TTL-controlled RF switch[2] which provides timing resolution of 1 μs, limited by the resolution of our sequence control software. This signal is amplified by 30 dBm using a broadband RF amplifier[3] and then sent to the antenna. The maximum power is limited to 36 dBm (4 W) due to the threshold of the amplifier.

The antenna is a single copper wire loop of radius $r = 18$ mm with wire radius $a = 0.5$ mm, mounted horizontally less than $z = 20$ mm directly above the atoms. To estimate the magnetic field at the atoms and hence the Rabi frequency we first calculate the impedance of the coil. Magnetic state transfers are typically done in a field of 10 G, corresponding to an RF frequency of about 7 MHz. At this frequency the wavelength of the radiation is large compared to the dimensions of the experiment, justifying the use of magneto-static methods to calculate the field. The current distribution across the wire is mostly confined to the surface with a skin depth of

$$\delta = \sqrt{\frac{2\rho}{\omega\mu_0}}, \tag{3.71}$$

[1] Agilent, 33521A
[2] Mini-Circuits ZYSWA-2-50-DR
[3] Delta RF Technology, LA2-1-525-30

where ρ is the conductivity, which for copper is $\rho = 1.68 \times 10^{-8}$ Ωm. This gives a typical skin depth of $\delta = 24$ μm. The Ohmic resistance, R, can be easily calculated, and the inductance of the coil, L, can be found using standard formulae [72]

$$R = \frac{r\rho}{a\delta} \tag{3.72}$$

$$L = \mu_0 r \left[\ln\left(\frac{8r}{a}\right) - 2 \right]. \tag{3.73}$$

For our RF coil and typical operating frequency we obtain $Z_R = R = 0.025$ Ω and $|Z_L| = |i\omega L| = 3.64$ Ω, giving a total impedance of $Z_{\text{loop}} = Z_R + Z_L$. The antenna is connected to a coaxial cable of impedance $Z_0 = 50$ Ω. If the waveguide carries a signal of peak voltage V_{in} towards the antenna, the impedance mismatch will cause reflections and therefore the transmitted voltage is given by

$$V_{\text{loop}} = \frac{2Z_{\text{loop}}}{Z_{\text{loop}} + Z_0} V_{\text{in}} \tag{3.74}$$

giving a current in the antenna of

$$I_{\text{loop}} = \frac{V_{\text{loop}}}{Z_{\text{loop}}} = \frac{2V_{\text{in}}}{Z_{\text{loop}} + Z_0}. \tag{3.75}$$

The amplitude of the magnetic field at the atoms can be found using the standard formula for the on axis field from a current loop

$$B = \mu_0 |I_{\text{loop}}| \frac{r^2}{(r^2 + z^2)^{3/2}}. \tag{3.76}$$

Using the relation $V_{\text{in}} = \sqrt{2P_{\text{in}}Z_0}$, the relevant Rabi frequencies at 7 MHz are

$$\hbar\Omega_{|2,2\rangle\rightarrow|2,1\rangle} = \frac{1}{2}\mu_B B \approx 58 \text{ kHz}\sqrt{\frac{P_{\text{in}}}{1 \text{ W}}}, \tag{3.77}$$

$$\hbar\Omega_{|1,1\rangle\rightarrow|1,0\rangle} = \frac{1}{2\sqrt{2}}\mu_B B \approx 41 \text{ kHz}\sqrt{\frac{P_{\text{in}}}{1 \text{ W}}}. \tag{3.78}$$

At such low frequencies the inductive impedance of the coil is sufficiently low that very high Rabi frequencies are possible. Typically we run the waveform generator well below its maximum power, producing a Rabi frequency of approximately 5 kHz, corresponding to an input power at the antenna of approximately 12 dBm (16 mW). For higher frequency applications, where the inductance of the loop becomes significant, the output power can be enhanced by insertion of a capacitor in series. By tuning the value of this capacitor such that $(\omega C)^{-1} = \omega L_{\text{loop}}$, the reactance of the loop can be canceled to increase the power output. Due to its significance in MRI experiments, extensive literature exists on RF coil design for both transmission and pick-up [73].

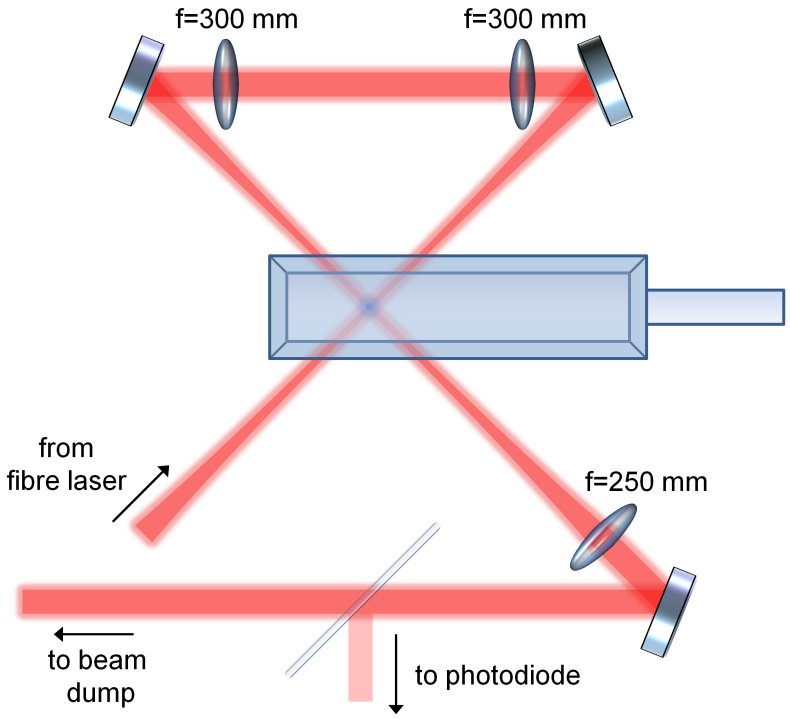

Figure 3.17: Crossed optical dipole trap: 1070 nm laser light from a fibre laser is passed through an AOM and focused down onto the atoms. The light is recycled in a bow-tie configuration and a second beam is focused onto the atoms, orthogonal to the first beam, producing a crossed dipole trap which confines the atoms in all three dimensions. The power of the trap is stabilised by picking off a weak reflection towards a photodiode, providing input for a PID which controls the AOM efficiency to attain the desired trap power.

3.7 Optical dipole trap

Following evaporative cooling in the QUIC trap, the atoms are transferred to an all optical dipole trap (ODT) illustrated in figure 3.17. The trap is formed using red-detuned 1070 nm laser light from a 10 W linearly polarised ytterbium fibre laser[1]. The linewidth of the laser is 1.2 nm, corresponding to a coherence length of only $\Delta x \approx \lambda^2/\Delta\lambda \approx 0.8$ mm. This short coherence length ensures no interference effects which could modify the trapping potential. The crossed trap is constructed using a bow-tie configuration, where the light is focused onto the atoms and then recycled to form a second, focused, orthogonal beam. This provides additional trap depth and confinement along the direction of propagation of the first beam.

It is important to stabilise the beam power to prevent long-term drifts in trap depth and high frequency modulations which can cause additional heating. To achieve this the beam is passed through an AOM[2] and the first diffraction order is used to form the

[1]IPG Photonics YLM-10-LP-SC
[2]Crystal Technology 3110-197

trap. Following the bow-tie configuration the laser is sent to a beam dump, but before this a glass slide picks off a weak reflection towards a monitor photodiode. The voltage signal obtained from the photodiode is compared with a set voltage generated by the control software using a PID controller (Proportional-Integral-Derivative controller). The PID outputs an error signal which suitably attenuates the AOM driving signal to increase or decrease the AOM efficiency to achieve the desired trap power. This AOM-PID setup is used on several more occasions in this experiment to stabilise beam powers.

For such far-detuned trapping light the expressions for the dipole potential and scattering rate derived in (3.42) and (3.43) respectively using the rotating-wave-approximation are no longer accurate. Instead, a weakly perturbative method can be used to derive the following expressions, relevant in the case of large detunings and negligible saturation [58]:

$$U_{\text{dip}}(\mathbf{r}) = -\frac{3\pi c^2}{2\omega_{eg}^3}\left(\frac{\Gamma}{\omega_{eg}-\omega}+\frac{\Gamma}{\omega_{eg}+\omega}\right) I(\mathbf{r}), \tag{3.79}$$

$$R_{\text{sc}}(\mathbf{r}) = \frac{3\pi c^2}{2\hbar\omega_{eg}^3}\left(\frac{\omega}{\omega_{eg}}\right)^3\left(\frac{\Gamma}{\omega_{eg}-\omega}+\frac{\Gamma}{\omega_{eg}+\omega}\right)^2 I(\mathbf{r}). \tag{3.80}$$

In the limit of large detuning the optical dipole force dominates over the scattering force. While U_{dip} scales as I/Δ, R_{sc} scales as I/Δ^2, hence far detuned optical traps benefit from reduced scattering rates and heating.

The ODT is loaded by linearly ramping the beam power up to 6.8 W, corresponding to a trap depth of ~ 35 μK. The QUIC trap is then overlapped with the ODT and abruptly switched off, achieving transfer efficiency of $\sim 60\%$ with a temperature of ≈ 6 μK. The antibias field remains on at a fixed field of approximately 3 G. The final evaporative cooling to degeneracy is performed in the ODT by gradually reducing the beam power and trap depth over 6 s. The final temperature and condensate fraction are controlled by choosing the PID voltage and correspondingly the beam power. With this protocol pure BECs of ^{87}Rb can be achieved with up to 8×10^5 atoms, however when the system is optimised for production of ^{39}K BECs, the ^{87}Rb BEC atom number is typically about half this value.

3.8 $|F = 1, m_F = 1\rangle$ state preparation

After cooling to BEC in the $|F = 2, m_F = 2\rangle$ state we transfer the atoms to the $|F = 1, m_F = 1\rangle$ state while holding in the ODT. The original purpose of this was to reduce the number of magnetic sublevels from five to three, and hence simplify the system for coupling the different m_F states. Another advantage of changing states is an observed increase in the BEC lifetime. Due to a reduced three-body recombination rate the lifetime of the $|1, 1\rangle$ state is found to be slightly longer than that of the $|2, 2\rangle$

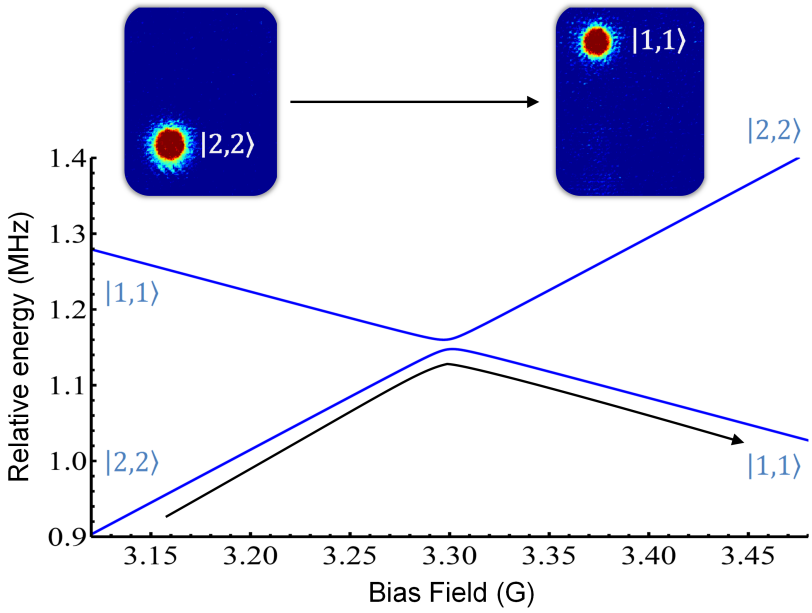

Figure 3.18: Adiabatic state transfer $|2, 2\rangle \rightarrow |1, 1\rangle$: Plotted are the dressed state energy levels as a function of external bias field. The bias field is swept from 3.12 G$\rightarrow$ 3.48 G in 100 ms in the presence of a microwave field of $\Omega \approx 13$ kHz which causes adiabatic following of the lowest band. This transfers the atoms from the initial $|2, 2\rangle$ state to the $|1, 1\rangle$ state with 95% efficiency. The upper insets show 18 ms time-of-flight absorption images of the BEC in the presence of a vertical Stern-Gerlach gradient to spatially separate the different magnetic sublevels.

state. For the three $F = 1$ sublevels, the lifetimes are found to be approximately equal, while conversely the lifetime of the $|2, 1\rangle$ state is observed to be considerably shorter than that of $|2, 2\rangle$, and the $|2, 0\rangle$ state lives shorter still. While the extended lifetime of the stretched state can be understood as the absence of spin-changing collisions, the discrepancy between $F = 2$ and $F = 1$ states is less clear. Although not understood, nevertheless we use this feature to our advantage by operating in the $F = 1$ manifold which provides a long-lived basis of states.

This state transfer is achieved using an adiabatic Landau-Zeener sweep illustrated in figure 3.18. With the antibias field providing a uniform field of 3.12 G, an off-resonant microwave field is applied at fixed frequency 6841.98 MHz and Rabi frequency 13 kHz. The antibias field is then swept across resonance by 0.36 G in 100 ms before removing the microwave field. The efficiency of this transfer is detected by spatially splitting the two states in time-of-flight by applying a vertical magnetic gradient. Typical transfer efficiency is about 95%. The remaining atoms in the $|2, 2\rangle$ state are removed by a short (10 μs) resonant pulse of imaging light which scatters the $|2, 2\rangle$ atoms out of the trap, but is far detuned for the $|1, 1\rangle$ state.

3.9 Absorption imaging

Our experiment uses absorption imaging to extract information about the density profile, atom number, and temperature of our atoms. Absorption imaging simply relies on illuminating the atoms with a laser pulse and measuring the spatial attenuation of the beam profile, which relates directly to the density profile of the atom cloud. This is done by imaging the shadow cast by the atoms onto a CCD camera.

To calculate the change in laser light due to the atom cloud, we use the relationship between the refractive index, n_{ref}, and the complex polarizability, α

$$n_{\text{ref}} = \sqrt{1 + n\alpha/\epsilon_0} \approx 1 + \frac{n\alpha}{2\epsilon_0}, \tag{3.81}$$

where n is the atomic density of the cloud. Since the polarizability is complex, this leads to a complex refractive index with real and imaginary parts, n_R and n_I respectively:

$$n_R = 1 - \frac{n\hbar c\Gamma}{4I_{\text{sat}}} \frac{2\Delta/\Gamma}{1 + I/I_{\text{sat}} + (2\Delta/\Gamma)^2} \tag{3.82}$$

$$n_I = \frac{n\hbar c\Gamma}{4I_{\text{sat}}} \frac{1}{1 + I/I_{\text{sat}} + (2\Delta/\Gamma)^2}. \tag{3.83}$$

A constant refractive index will modify the propagation of a plane wave as follows: $\mathbf{E} = \mathbf{E}_0 e^{i(kz-\omega t)} \rightarrow \mathbf{E}_0 e^{i(n_{\text{ref}}kz-\omega t)} = \mathbf{E}_0 e^{i(kn_R z-\omega t)} e^{-n_I kz}$. The imaginary part leads to a density-dependent exponential decay of the amplitude which is utilised in absorption imaging. For non-zero detuning, the real part of the refractive index generates a density-dependent phase shift of the incoming light. This phase shift can be used to image transparent objects by phase-contrast imaging, where the information encoded in the phase shift of the light is converted into intensity before detection. In this work, the real part of n_{ref} leads to unwanted diffraction effects when imaging dense clouds in trap. To remove this effect we can image on resonance ($\Delta = 0$), where the phase shift vanishes, however to reduce the optical density to within the dynamic range of our imaging system, we only transfer a fraction of the atoms from the $|1,1\rangle$ state to the imageable $|2,2\rangle$ state.

Absorption of photons leads to a rate of decay of intensity with propagation distance given by

$$\frac{dI}{dz} = -2n_I kI = -n\sigma I. \tag{3.84}$$

From this we extract the scattering cross-section

$$\sigma = \frac{\sigma_0}{1 + I/I_{\text{sat}} + (2\Delta/\Gamma)^2}, \tag{3.85}$$

where

$$\sigma_0 = \frac{\hbar\Gamma\omega}{2I_{\text{sat}}}. \tag{3.86}$$

The same result can be obtained by equating the rate of decay of intensity, dI/dz, to the rate of energy scattered from the cloud, $\hbar\omega R_{\rm sc} n$, and using the form of the scattering rate in (3.29). In the limit of low intensity, the effect of saturation in σ can be neglected, and equation (3.84) can be integrated to give the intensity after propagating a distance z,

$$I(x,y) = I_0(x,y) \exp\left[-\sigma \int_0^z n(x,y,z')dz'\right] \equiv I_0(x,y)e^{-D}, \tag{3.87}$$

where the optical density, D, is defined as

$$D(x,y) = \sigma \int_0^z n(x,y,z')dz' = -\ln\left(\frac{I(x,y)}{I_0(x,y)}\right). \tag{3.88}$$

Therefore by taking an image of the incident light with atoms to obtain $I(x,y)$, and an image without atoms to obtain $I_0(x,y)$, it is possible to calculate the optical density, which is proportional to the column density along the line of sight. To account for any stray light entering the camera, additional dark images are taken with no imaging light and are subtracted from the atom shadow image and the imaging beam image. The final optical density is then given by

$$D(x,y) = -\ln\left(\frac{I(x,y) - I_{\rm dark}(x,y)}{I_0(x,y) - I_{\rm dark}(x,y)}\right). \tag{3.89}$$

3.9.1 Imaging systems

Our experiment makes use of a horizontal and vertical imaging setup, both of which were designed and tested by Alexandre Dareau using the OSLO optimisation package and are detailed in his project report [74]. The horizontal direction is used to make quantitative measures of atom number and temperature, whereas the majority of the data taken on persistent currents is done using the vertical imaging system, along which vortices are visible. In both instances the imaging bias field is in the horizontal plane along the direction of the horizontal imaging. This bias field is the same used during state transfers and hence is quite large at approximately 10 G.

Horizontal imaging Our horizontal objective is based on one proposed by Wolfgang Alt [75]. The objective uses five commercially available 1" optics, the first four of which are designed such that their own respective aberrations combine to cancel one another out and the spherical aberrations introduced by the science cell wall. The fifth lens is a diffraction limited achromatic doublet used to focus the image onto the camera. This complete objective achieves a resolution of less than 2 μm and a magnification of $M_h = 2.78$. The atoms are imaged with a broad beam of σ^+ polarised light which is resonant with the $|2,2\rangle \rightarrow |3,3\rangle$ cycling transition. The steady state resonant cross-section (3.86) for σ^+ polarised light is given by [76]

$$\sigma_0^{\sigma^+} = \frac{3\lambda^2}{2\pi}. \tag{3.90}$$

Vertical imaging Our vertical objective is similar in spirit to the horizontal objective, however the additional constraint of the quadrupole coils forces the lenses to be spaced further apart. A custom meniscus is closely mounted near the science cell to maximise the numerical aperture, and the subsequent optics used are 2" in diameter to further increase light collection. This objective also achieves a resolution of less than 2 μm and a magnification of $M_v = 5.2$. Due to design constraints where the vertical direction is used for addressing the atoms with the Raman beams, the vertical imaging light is π polarised with respect to the bias field. As a result, during the imaging pulse, the atoms become distributed over a range of m_F states which makes calculation of the scattering cross-section more complicated. Calculations in [76] and [77] show that the steady state saturation intensity is given by $I_{sat} = 3.053$ mW/cm^2, giving a resonant cross-section of $\sigma_0 = 0.55\ \sigma_0^{\sigma^+}$. Typically we tend to calibrate the vertical imaging using the horizontal imaging since the transition is much simpler.

The same type of camera[1] is used for both imaging systems. This camera has a relatively modest quantum efficiency of $\sim 28\%$ and a pixel area of 6.45×6.45 μm^2. For horizontal imaging this gives an effective pixel size of 2.32×2.32 μm^2, just above the resolution limit, which is calibrated using the motion of the centre of mass of the cloud in free fall. For vertical imaging in trap this gives an effective pixel size of 1.2×1.2 μm^2, just under the resolution limit, calibrated by comparing cloud sizes in both imaging systems. We also calibrate the vertical imaging at the plane of 29 ms TOF, which is used extensively for detecting angular momentum, which gives a larger pixel size of 1.42×1.42 μm^2.

Due to the relatively low efficiency of the camera, to achieve a high signal-to-noise ratio we use quite high intensity and long imaging pulses such that each atom scatters many photons. Our imaging pulses are typically 80 μs long with an intensity $I/I_{sat} \approx 0.3$, which corresponds to scattering about 350 photons per atom. The disadvantage of this is the high intensity leads to some saturation of the imaging transition, and the scattering force during imaging can lead to a Doppler shift of resonance and an effective detuning [45].

Stern-Gerlach

To image different magnetic states we apply a Stern-Gerlach magnetic gradient during time of flight using the quadrupole coils. This exerts a state dependent force which causes the different m_F states to spatially separate as they fall. For vertical imaging we apply a gradient of 11 G/cm, which due to the bias field predominantly splits the states in the horizontal direction. The gradient is ramped off a few ms before imaging, just leaving the imaging bias field on, so as not to create a spatially varying detuning. For horizontal imaging we apply a gradient of 16 G/cm and a strong vertical field of 90

[1] PCO Pixelfly QE Double Shutter

G. This splits the states in the vertical direction, and once again the fields are ramped off a few ms before imaging.

3.9.2 Atom number calibration

As discussed in the previous section, various experimental factors will cause the true scattering cross-section to differ from σ_0, often causing an underestimate of atom number. Typical factors include imperfect polarisation, small detunings from resonance, and in our case, saturation and acceleration of the atoms during imaging. For quantitative studies of BEC this needs to rectified, and the scattering cross-section is scaled by a 'fudge-factor', $f = \sigma_0/\sigma$, to compensate for the discrepancy. The way this is done is to note that while the atom number is altered by f, the temperature, which is extracted from the width of the thermal distribution, is not. Since the BEC phase transition is a function of both temperature and atom number, the onset of condensation can be used to find the fudge factor as follows

$$fN_{\text{total}} = N_c^{\text{id}} + fN_0, \tag{3.91}$$

since for an ideal gas the thermal atom number saturates at the critical number given by (2.16)

$$N_c^{\text{id}} = 1.202 \left(\frac{k_B T}{\hbar\omega_0}\right)^3, \tag{3.92}$$

where ω_0 is the geometric mean of the trapping frequencies. The uncorrected total number, N_{total}, and condensate number, N_0, are found by fitting the absorption image, and the critical number is calculated using the fitted temperature, thus allowing us to find the fudge factor, f. As discussed in [16, 47] the effect of interactions leads to non-saturation effects which modify (3.91) and need to be considered for an accurate determination of f. For small condensates this can be suitably captured using Hartree-Fock theory which gives the total atom number as

$$N_{\text{total}} = N_0 + N_c^{\text{id}} + 1.37 N_c^{\text{id}} \frac{\mu}{k_B T}, \tag{3.93}$$

where the chemical potential, μ, is a function of the condensate number (2.44). The fudge factor is then found by solving the equations

$$fN_{\text{total}} = fN_0 + N_c^{\text{id}} + 1.37 N_c^{\text{id}} \frac{\mu}{k_B T}, \tag{3.94}$$

with the chemical potential given by

$$\mu = \frac{\hbar\omega_0}{2} \left(\frac{15 f N_0 a}{a_0}\right)^{2/5}, \tag{3.95}$$

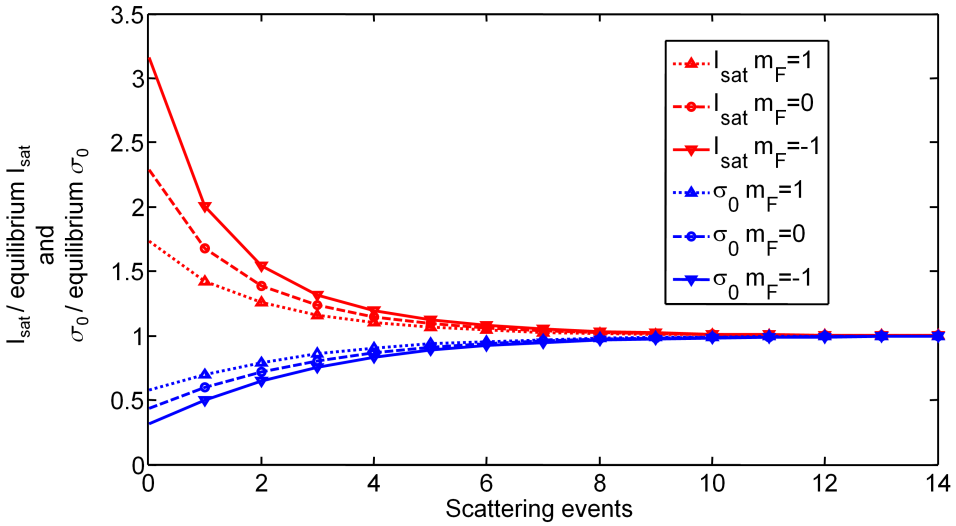

Figure 3.19: Convergence of saturation intensity and scattering cross-section with scattering events: The evolution of the saturation intensity, I_{sat} (red), and the on-resonance cross-section, σ_0 (blue), are shown as the expected populations change with absorption of σ^+ polarised imaging light and spontaneous emission. These are calculated for each of the three starting population distributions obtained by repumping $|1,1\rangle$, $|1,0\rangle$, and $|1,-1\rangle$. The vertical axis is the value of the parameters over their steady state values.

where a is the s-wave scattering length, and a_0 is the harmonic oscillator length associated with the mean trapping frequency. Higher order corrections are considered in [48] by considering modification of the critical temperature due to interactions. For our horizontal imaging system we observe a typical reduction in the cross-section by a factor of $f = 1.5 \pm 0.3$, consistent with that expected from our range of imaging parameters.

3.9.3 Imaging the $|F = 1\rangle$ state

As described in Section 3.8, our experiments on persistent currents are performed in the $F = 1$ states, whereas our imaging light is resonant for the $F = 2$ state. To image the $F = 1$ state we quickly transfer the atoms to the $F = 2$ states just before the imaging pulse. This can be done in two different ways.

1. The first is to flash a 10 μs pulse of π polarised repump light just before the imaging pulse, after releasing the atoms from the trap. This transfers the atoms into the $F' = 2$ state, and those that decay into the $F = 2$ manifold become dark to the repump light and remain there. Since each atom should end up in a dark state we are able to saturate the transition many times over and rapidly move the population into the imaging state. This method will distribute the atoms across several m_F states, however due to the significant number of scattering events during imaging, the atoms quickly reach their steady state populations and the effective cross-section is only slightly affected by the starting distribution.

To calculate this effect we use the appropriate branching ratios [78] to find the steady state populations at the end of repumping

Transition	Final populations $m_F = (-2, -1, 0, 1, 2)$
$\|1,1\rangle \rightarrow \|2,1\rangle$	$(0.01, 0.14, 0.36, 0.25, 0.23)$
$\|1,0\rangle \rightarrow \|2,0\rangle$	$(0.03, 0.42, 0.09, 0.42, 0.03)$
$\|1,-1\rangle \rightarrow \|2,-1\rangle$	$(0.23, 0.25, 0.36, 0.14, 0.01)$

From these starting populations we now simulate absorption of σ^+ polarised imaging light and spontaneous emission back to the $F = 2$ magnetic sublevels. This gives the expected population distribution as a function of scattering events, from which the saturation intensity and hence the on-resonance cross-section can be calculated. The result of this calculation is shown in figure 3.19, and shows that for all starting populations, after about 10 scattering events the population is almost entirely in the $|2,2\rangle$ state and the cross-section is equal to that found for the cycling transition (3.90). Since the imaging pulse involves about 350 scattering events, cycling the atoms into the steady state population distribution only introduces a small correction to the effective cross-section. For typical imaging parameters $I/I_{\text{sat}} = 1/3$ and a pulse time of 80 μs, the effective cross-sections are 0.995 σ_0, 0.993 σ_0, and 0.990 σ_0 for imaging the $m_F = 1, 0$, and -1 states respectively. We can therefore be confident that we image all sublevels equally and can also directly compare to the $|2,2\rangle$ state. Similar corrections are found when considering vertical imaging with π polarised imaging light.

2. The second method is to use a microwave π-pulse to flip the population from $|1, m_F\rangle \rightarrow |2, m_F + 1\rangle$. The disadvantage of this method is that it requires very stable magnetic fields, and hence cannot be used in conjunction with a Stern-Gerlach gradient used to spatially separate the magnetic states. The pulse is also only able to transfer one m_F state to an imageable state, however this can be used to our advantage to measure the spatial distribution of each m_F state *in situ*. Another advantage is that we need not transfer all the population to the imaging state, providing a simple, non-invasive way to reduce the optical density [79].

   The use of absorption imaging for quantitative analysis is typically restricted to samples with an optical density of less than 3. For optical densities above this, the image is said to be "blacked out" and the level of transmitted light is too low for reliable inference of optical densities. The cross-section can be reduced by detuning the imaging light from resonance, however this can lead to significant refraction of the imaging light beyond the aperture of the imaging system. This can affect the absolute density measurement, and importantly for *in situ* images where the density varies on small length scales, it can appear as false absorption signals in the relative density [80]. Partial transfer absorption imaging simply

involves only transferring a fraction of the atoms to the $|2,2\rangle$ imageable state. This uniformly reduces the optical density across the entire sample, bringing it within the dynamic range of our setup and providing an accurate representation of the density distribution. Since the imaging light does not affect the remaining atoms this can also be used to take several pictures of the atoms in a single sequence.

3.10 Conclusion

In conclusion we have outlined the theory and experimental stages used to produce our ^{87}Rb BEC held in an all optical dipole trap. The theory and experimental apparatus relevant to later chapters has been covered in more detail, in particular that of Rabi oscillations, optical trapping, and the creation of dressed states by atom-light coupling. The experimental protocol described in this chapter provides the starting point for all our experiments on persistent currents, which are described in the chapters to follow.

Chapter 4

Preparation and detection of persistent currents

In the previous chapter we covered our experimental sequence to create a BEC in the $|1,1\rangle$ state held in a crossed ODT (CDT). We now explain how we load this BEC into an optical ring trap to create a multiply-connected toroidal BEC, and then impart angular momentum to the BEC to create a superfluid persistent current in analogy to those created in superconducting [81–85] and superfluid liquid helium [27, 39, 86–88] experiments. Superfluid flow of a BEC in a multiply-connected ring geometry is the archetypal metastable many-body state. As discussed in Section 2.4.3, the phase of the macroscopic BEC wavefunction must wind around the ring by an integer multiple of 2π, corresponding to the charge q of a vortex trapped inside the ring. Different q states are topologically distinct and therefore transitions between them involve a macroscopic transformation of the BEC wavefunction and so are energetically unfavourable. As a result even in a stationary trap where the ground state is $q = 0$, a $q \neq 0$ persistent current can be extremely long-lived since there may be no energetically accessible decay channel. This chapter details how we prepare and detect such persistent currents, the stability and decay of which are studied in the subsequent chapters.

The outline of this chapter is as follows. Firstly we detail past ring trap experiments, describing alternate methods for their creation, previous studies on persistent currents, and applications of BECs in such geometries. The next section explains how we form our optical ring trap by intersecting a sheet beam with a tube-like Laguerre-Gauss (LG) beam. This includes the methods used to form the LG beam and how we correct for abberations in the LG beam phase profile. The next two sections describe how we then impart angular momentum to the BEC, setting up the persistent current, and how we detect the state of this persistent current following its creation. The final section illustrates the significance of the multiply-connected geometry by studying the vortex dynamics when we remove the ring trap, transforming to a simply-connected trap.

4.1 Previous ring trap experiments

Atomic BECs trapped in a ring geometry are attractive for creating stable states of non-zero circulation. As discussed in Section 2.4.3, rotation of a BEC requires a multiply-connected geometry which introduces vorticity into the system. Such vortices are fundamentally unstable and are observed to break apart and migrate towards regions of low density at the edge of the cloud [31, 32, 89], reducing the angular momentum of the system. In Section 4.5 we discuss our own observations of dynamically unstable multiply charged vortices. A ring geometry allows the study of truly stable persistent currents by pinning the vorticity to the zero density region in the centre of the ring [90, 91]. As discussed in chapter 5, the ring geometry introduces low energy states, corresponding to placing vortices inside the ring, separated by energy barriers which prevent a continuous deformation of the BEC wavefunction and loss of angular momentum. Ring shaped BECs also have several other promising applications such as interferometry, atomtronics, and fundamental studies of BECs with periodic boundary conditions.

4.1.1 Previous ring traps

Several schemes have been implemented to create multiply-connected geometries for ultracold atoms. These can be broadly divided into three types: magnetic, RF dressing, and optical. The scale of these traps are generally divided into smaller traps where the quantum coherence extends all around the ring, suitable for persistent current studies and atomtronics, and larger traps for matter-wave interferometry.

Magnetic

Various current structures have been generated for achieving large area ring waveguides based on dc magnetic fields to create ring traps suitable for interferometry [92, 93]. The disadvantage of such traps is the existence of field zeros which lead to losses by Majorana spin-flips. This can be negated by using time-averaged magnetic traps such as in [94] which reported the first BEC loaded in a circular waveguide. The disadvantage of such traps for our studies is their large scale, of the order of several mm. The low mean field of a BEC occupying such a large trap makes it unfeasible to create a continuously connected BEC, unbroken by residual azimuthal roughness.

RF dressing

Modifications to these magnetic traps have been proposed which use RF fields to dress the atoms and create time-averaged ring potentials [95, 96]. Such schemes involve using RF fields to create a dressed band with a minima isosurface at a given magnetic field value. The position of this surface can then be moved to create a time-averaged ring potential, the parameters of which can be modi-

fied by changing the RF frequency. Such traps are inherently flexible, and can produce small ring traps suitable for superflow studies. Such a trap was recently demonstrated for a BEC in [97]. The disadvantage of this solution is the trapping potential is state dependent.

Optical

Several experiments (including this one) make use of optical forces to create ring traps. The clear advantage of this is the trap is equal for different magnetic states, and the creation of small ring geometries is easily achieved. The first such traps used a repulsive blue-detuned beam aligned along the symmetry axis of a magnetic trap to create a multiply-connected geometry. This was done with both a quadrupole magnetic trap [98] and a TOP magnetic trap [99]. This setup is limited by heating and losses due to drifts in the relative alignment of the magnetic field and the plug beam.

The experiment of Ryu *et al.* [99] evolved into an all optical trap which made use of an intersecting sheet beam and tube-like Laguerre-Gauss beam [100] (see Section 4.2). This setup is very similar to ours, and both experiments [99] and [100] were also used to study persistent currents. As such, in chapter 5 we will directly compare our finding to those in [99, 100]. Other all optical ring traps have used time-averaged painted potentials [101, 102]. These experiments use a two-directional AOM to deflect a beam and trace out the trapping potential. This is done with a kHz refresh rate, allowing one to create an arbitrary time-averaged potential. Such traps show great promise for creation of dynamic atomtronic circuits.

4.1.2 Applications of ring BECs

While numerous novel proposals have been developed which make use of multiply-connected BECs [103, 104], we will limit ourselves to briefly explaining those applications which have been experimentally realised.

Persistent current studies

Persistent flow in a BEC is a striking demonstration of superfluid behaviour and facilitates studies into critical velocities and the connection between superfluidity and Bose condensation, which are still not fully understood. The only experiments to demonstrate persistent flow in a BEC are those of the NIST group [99, 100, 102], and those presented in this work [14, 15]. The NIST experiments demonstrated long-lived superflow of up to 40 s, and were able to theorise a possible decay mechanism. The results of these experiments will be contrasted with our own findings in chapter 5.

Atom interferometry

Atom interferometry is performed by coherently splitting an atom cloud into two

parts which then travel spatially different paths before recombining and interfering. If the parameter of interest acts differently on the two paths, a relative phase difference will accumulate which is read out upon interference as a population difference. Such experiments have allowed precision measurements of various quantities, including rotation [105–107], acceleration [108], magnetic gradients [109], and fundamental constants [110]. Interferometric detection of rotation makes use of the Sagnac effect which states that two interfering propagation paths enclosing an area A will experience a relative phase shift of $\Delta\phi = \frac{4\pi}{\lambda v}\mathbf{\Omega} \cdot \mathbf{A}$, where λ is the particle wavelength, which for a massive particle is the de Broglie wavelength $\lambda_{dB} = h/mv$, v is the velocity of the particle, and Ω is the rotation of the external system. As a result, the inherent sensitivity of a matter-wave gyroscope exceeds that of a photon-based system of equal area by a factor of $\frac{mc\lambda}{h} \sim 10^{10}$, where here λ is the typical photon wavelength.

Sagnac interferometry in a ring trap is attractive for several reasons: (i) for a complete loop of the trap the two paths are identical (apart from their rotation sense) and have common-mode rejection, and (ii) the area, A, can be trivially extended by allowing multiple revolutions before readout. Such a proposal is outlined in [111] for a two component BEC. This makes use of a π pulse at half the integration time termed an echo pulse, which cancels phase accumulation due to atom-atom interactions. Recently a proof of principle rotation sensor was demonstrated in [112] which uses interference of collective excitations in a toroidal-shaped BEC.

Atomtronics

Atomtronics focuses on the creation of atom analogs of electronic materials, devices, and circuits. The analogy between a strongly interacting Bose gas in a lattice potential and electrons in a solid-state crystal, has led to the proposal of P-type and N-type material analogs in ultracold systems, and from these building blocks possible diode and transistor configurations are proposed from which atom circuits could be constructed [113]. Though quite a speculative field at the present time, the first realisation of an atomtronic circuit was recently achieved in [102] with a BEC analog of a SQUID circuit. This experiment uses a toroidal BEC with a rotating weak link which is able to spin up the atoms and introduce vortices. Such an experiment is then shown to map onto a superconducting loop with a weak link in the presence of an external magnetic field.

4.2 Optical ring trap

Our ring trap is illustrated in figure 4.1. The trap is formed by the intersection of a red-detuned ($\lambda = 1070$ nm) horizontal sheet beam (Section 4.2.1) which provides vertical confinement and a red-detuned ($\lambda = 804$ nm) vertical LG beam (Section 4.2.2) to provide annular confinement. The use of a separate sheet beam was chosen to decouple

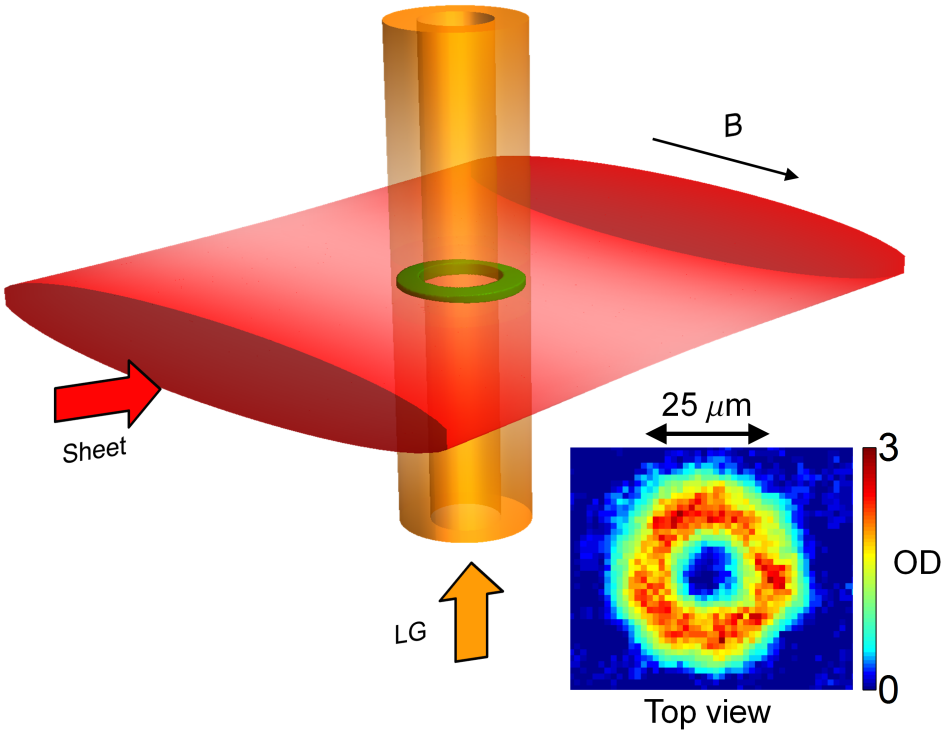

Figure 4.1: Schematic of optical ring trap: Vertical confinement is provided by an oblate sheet beam in the horizontal direction, red-detuned at $\lambda = 1070$ nm. The ring trap is formed by a tube-like Laguerre-Gauss beam in the vertical direction, red-detuned at $\lambda = 804$ nm. The trap is formed in the green region at the intersection of the two beams. Inset is a top view absorption image of a BEC loaded in the ring trap. The orientation of the uniform bias field used during state transfers is indicated by B.

vertical and horizontal confinement.

4.2.1 Sheet beam

When we evaporatively cool in the CDT we ramp the beam power down from 6.8 W to approximately 1.6 W, leaving over 5 W of $\lambda = 1070$ nm trapping light available. This power is used to produce our sheet beam, since we only load into the sheet after reducing the CDT power. The optics used to generate the sheet beam are shown in figure 4.2. The zeroth order beam from the CDT AOM is sent to a separate AOM[1], which cleans up the beam profile and provides independent control of the sheet power. A microscope slide picks off a weak reflection which is sent to a photodiode to provide a signal for a PID controller. This provides stabilisation and control of the sheet beam power as explained for our CDT in Section 3.7. A 3 : 2 telescope is inserted to provide independent control of the horizontal dimension of the sheet trap at the atoms. The beam is translated up to the atoms by a periscope and passes through a polarising beam splitter cube (PBS) which cleans up the polarisation and also aids in alignment. A free space prism pair is used to extend the beam profile in the vertical plane by a

[1]Crystal Technology 3200-115

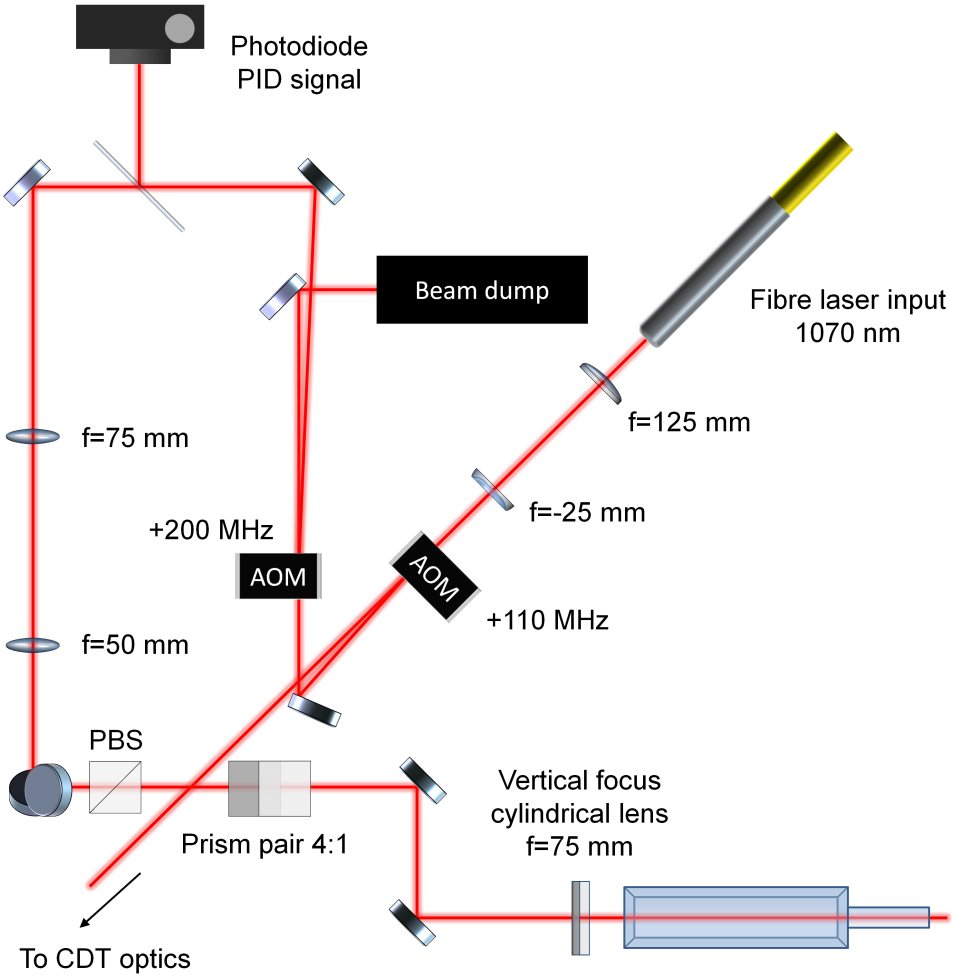

Figure 4.2: Sheet beam optics: The sheet beam uses discarded light from our CDT setup. The output of the fibre laser passes through a telescope resulting in a beam that is size-matched to the active aperture of the 110 MHz AOM. First order light is sent to the CDT optics, while zeroth order light is sent to the sheet beam optics. A 200 MHz AOM cleans up the beam profile and provides power control, with the undeflected light sent to a beam dump. A microscope slide picks off a weak monitor beam sent to a photodiode used for PID power stabilisation. A $3:2$ telescope gives added control to collimate the sheet beam at the atoms in the horizontal direction without adjusting the CDT setup. A periscope brings the light level with the atoms and then a polarising beam splitter cube (PBS) cleans up the polarisation and allows overlap of guide beams for alignment. The beam is stretched in the vertical direction by a factor $4:1$ using a free space prism pair and is then finally focused in the vertical direction only onto the atoms using a $f = 75$ mm cylindrical lens.

factor of 4, creating the profile shown in figure 4.3 (b), with a vertical waist of $w_v = 2$ mm and a horizontal waist of $w_h = 0.5$ mm. This is focused in the vertical direction only by a cylindrical lens of focal length $f = 75$ mm[1], giving an estimated vertical beam waist at the focus of $w_0 = f\lambda/(4w_v) \approx 10$ μm.

[1]Thorlabs LY1703RM-C

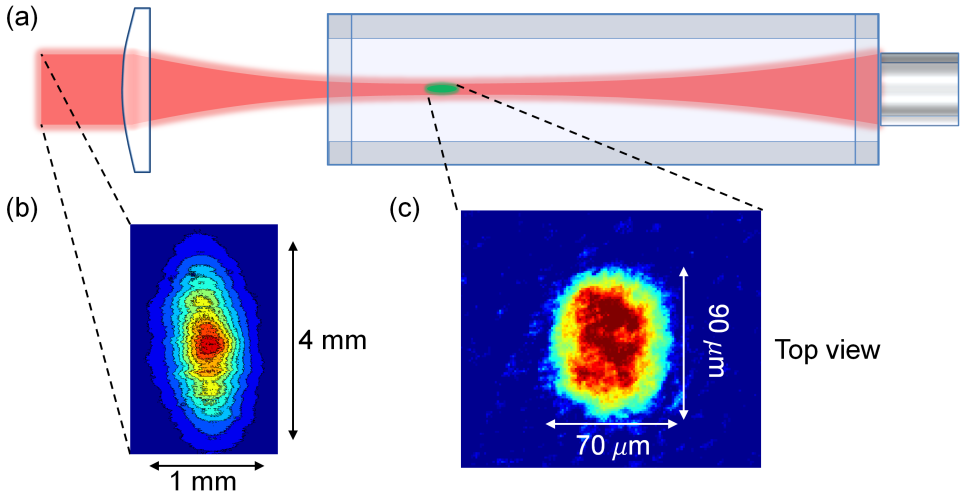

Figure 4.3: Sheet beam: (a) Side view of the cylindrical lens focusing the beam in the vertical direction only, to create a weak horizontal trap and tight vertical trap. (b) Contour plot of intensity for the input beam before the cylindrical lens. The beam is extended in the vertical direction by the prism pair to focus more tightly and strongly confine the atoms in the vertical direction. Dimensions shown are $1/e^2$ diameters. (c) Vertical absorption image of atoms loaded into the sheet beam only. The dimensions of the cloud are larger than our typical ring traps which provides an error margin should the sheet and ring drift out of alignment.

Trapping parameters

The sheet beam power used is 100 mW, corresponding to a calculated trap depth of 550 nK. This shallow trap depth ensures evaporation of any thermal atoms created during loading and a high condensate fraction, typically over 85%. For powers below 50 mW gravity dominates and the trap minimum disappears. The trapping frequencies of the sheet are measured by translation of the BEC from the trap minimum by application of a quadrupole magnetic gradient, the orientation of which is selected by application of an appropriate uniform bias field. The fields are then abruptly removed and the BEC is allowed to freely oscillate in the sheet trap. To amplify the signal we measure oscillations in the BEC position at long time-of-flight (TOF) (18 ms). The measured trapping frequencies across the sheet, along the sheet, and vertically are $\omega_x = 2\pi \times 6.3$ Hz, $\omega_y = 2\pi \times 7.1$ Hz, and $\omega_z = 2\pi \times (400 \pm 13)$ Hz respectively. Such weak in-plane trapping frequencies are important for creating a level ring trap and are also found to be beneficial for detection of angular momentum. Typically we load about 2×10^5 atoms into the sheet which, using (2.44), gives a chemical potential of $\mu \approx 460$ Hz. This gives the corresponding Thomas-Fermi radii as $R_x = 52$ μm, $R_y = 46$ μm, and $R_z = 0.8$ μm, in rough agreement with the observed density profile in figure 4.3(c).

Alignment

Due to the short Rayleigh range, $z_R = \pi w_0^2/\lambda = 0.3$ mm, alignment of the sheet beam proved very difficult. The optimal solution to finding the sheet beam was to overlap

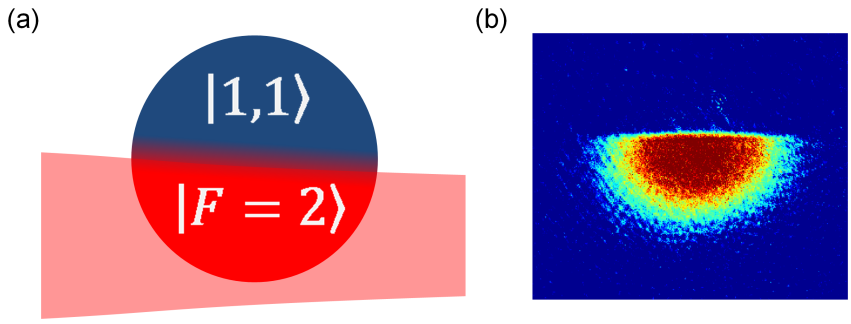

Figure 4.4: Repump sheet beam for alignment: A separate repump beam is overlapped with the sheet beam on the PBS cube before the prism pair. The repump beam produces a strong signal, pumping atoms into the imageable $F = 2$ state. (a) The repump beam is flashed on at various points during TOF. The visibility of the atoms allows us to map out the repump beam position and profile, and hence find the overlapped sheet trapping beam. (b) A horizontal absorption image of a cloud which has only partially fallen into the repump beam, hence only the bottom half is in the visible $F = 2$ state.

the beam with a repump beam on a PBS cube before the prism pair. Unlike the sheet beam, which has to be in close proximity to the atoms in trap to significantly distort their trapping potential and produce an observable signal, any $F = 1$ atoms which pass through the repump sheet will be pumped to the imageable $F = 2$ state. We therefore flash on the the repump beam during TOF, and vary TOF to determine the height of the beam. By flashing the repump on just before imaging, only a slice of the cloud is pumped to the $F = 2$ state, hence we can find the focus by minimising the thickness of this slice. Figure 4.4(a) illustrates this technique, and figure 4.4(b) is an absorption image of a cloud where only half the cloud has passed into the repump sheet. This technique was able to get the alignment close enough to observe distortion of the BEC profile due to the trapping sheet. The alignment of the sheet trap was then chosen to minimise heating upon transfer. Any tilt in both directions was removed by rotation of the cylindrical lens, and vertical walking of the beam.

A disadvantage of using an attractive sheet beam for vertical confinement is the presence of weak fringing near the focus. In our case we observe two local minima about the focus separated by ≈ 200 μm along the direction of propagation. Private correspondence with the NIST group [100] revealed that a similar problem was observed in their setup. Despite numerous attempts, the cause of the fringing could not be established and the solution was simply to load into one of the fringes. The approximate spacing of the fringes seems to be weakly dependent on the angle of incidence, hence we theorise the cause could be due to a reflection, however the fringe spacing does not fit with interference from a counter-propagating reflection, nor reflection within any optical coating. Another possible cause could be chromatic aberrations due to the broad linewidth of the fibre laser, however we would expect the spectral distribution to only have one maximum.

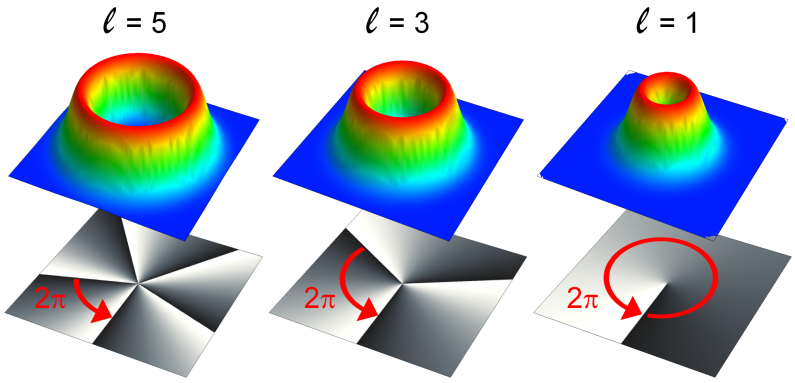

Figure 4.5: Laguerre-Gauss intensity profile and phase winding: Top figures show the intensity profile and bottom figures show the azimuthal phase winding of an LG beam for $\ell = 5, 3, 1$ from left to right. From this we observe the trend of increasing annulus radius with increasing ℓ.

4.2.2 Laguerre-Gauss beam

Our ring trap is an optical dipole trap formed by a red-detuned Laguerre-Gauss (LG) laser mode. LG modes are a complete basis set for paraxial light beams with circular symmetry about their axis of propagation. Two indices identify a given mode denoted by LG_p^ℓ, where p is the radial order which we are not concerned with and set to be 0, and ℓ is the angular order. In contrast to the planar wave fronts of the Hermite-Gaussian (HG) modes, for $\ell \neq 0$ the LG beams have an azimuthal phase term $e^{i\ell\theta}$ which results in helical wave fronts [114]. This phase winding about the beam's axis means an LG beam can be thought of as an optical vortex of topological charge ℓ.

The LG beam is integral to our experiment for two reasons: (i) an LG beam has a doughnut intensity profile [115] which creates the toroidal optical dipole trap, and (ii) the helical wave front means LG modes possess an orbital angular momentum of $\ell\hbar$ per photon [116], quite distinct from the spin angular momentum associated with the polarisation state. As discussed in Section 4.3, this is used to impart angular momentum to the ring BEC and generate a persistent current. The relation between the orbital angular momentum of an LG beam and the circular polarisation of a photon is analogous to the orbital angular momentum and spin of an electron. The orbital angular momentum is associated with the spatial mode, while spin is intrinsic to the particle.

The field amplitude of an LG laser mode is given by [115]

$$E(LG_p^\ell) \propto \exp\left[\frac{-ikr^2 z}{2(z_R^2+z^2)}\right] \exp\left[\frac{-r^2}{w^2}\right] \exp\left[-i(2p+\ell+1)\arctan\left(\frac{z}{z_R}\right)\right] \times \exp[-i\ell\phi](-1)^p \left(\frac{r\sqrt{2}}{w}\right)^\ell L_p^\ell\left(\frac{2r^2}{w^2}\right), \tag{4.1}$$

where z is the distance from the beam focus, z_R is the Rayleigh range, k is the wave number, w is the Gaussian beam waist, r is the radius, ϕ is the azimuthal angle, and

L_p^ℓ is the generalised Laguerre polynomial. From this we find the intensity profile

$$I(LG_p^\ell) = \frac{2}{\ell!}\frac{P}{\pi w^2}\left(\frac{2r^2}{w^2}\right)^\ell \left[L_p^\ell\left(\frac{2r^2}{w^2}\right)\right]^2 \exp\left[\frac{-2r^2}{w^2}\right], \tag{4.2}$$

where P is the total beam power. The intensity profile as a function of ℓ is shown in figure 4.5. This doughnut profile has clear applications in forming ring traps, as well as other features of note. The radius of the intensity minimum scales with topological charge as $R_\ell = w\sqrt{\ell/2}$, and we also observe that a true intensity zero is created within the ring due to the phase singularity. The intensity profile inside the ring scales as $r^{2\ell}$, hence a blue-detuned LG beam has applications in creating novel trapping geometries with high power laws [117–119].

In recent years LG beams have attracted much interest, and found a host of diverse applications. LG beams are used extensively in optical tweezers, which use the refraction of light about an object with higher refractive index than the surrounding liquid to optically trap and manipulate samples ranging from simple dielectric spheres to cells, chromosomes, and protein motors. LG beams offer distinct advantages in being able to trap both high and low-index particles [120], holding samples in low intensity regions where cell damage is reduced, and rotating samples due to absorption of angular momentum from the trapping LG beam [121]. LG beams were used in a recent experiment which demonstrated the possibility to use two beams of incoherent radio waves, transmitted on the same frequency but encoded in two different orbital angular momentum states, to simultaneously transmit two independent radio channels [122]. LG beams have also found numerous other applications including astronomy [123], phase contrast microscopy [124], and in secure encoding of information in orbital angular momentum states [125].

Several methods have been developed in the last two decades for the production of LG beams, or more often for the production of fields with a single dominant LG mode. While LG modes can be produced directly from a laser resonator [126], it is often simpler to obtain these modes by externally converting the HG mode output from a conventional laser. The creation of pure LG modes is possible using a cylindrical lens telescope with an input beam mode $HG_{m,n}$, aligned at 45° to the principal axis of the lens, provided either $m \neq 0$ or $n \neq 0$ [127, 128]. Approximations to LG beams can be produced using spiral phase plates [129, 130] and computer-generated holograms [131, 132]. Such devices introduce a screw-phase dislocation in the centre of a Gaussian beam, which to first order approximates the spiral wavefront of an LG beam. On propagation the phase dislocation causes destructive interference leading to the annular intensity profile and a high percentage of a given LG component, with ℓ set by the phase pitch of the spiral phase plate, or correspondingly the order of the dislocation in the hologram.

4.2.3 Spatial light modulator (SLM)

Our technique for creating LG beams uses a spatial light modulator (SLM). An SLM is a rapidly emerging tool which provides highly customisable control of light fields by locally modulating light according to a fixed spatial pixel pattern. Modulation options include amplitude only modulation used in many projectors, but to create a phase winding we require a phase modulating SLM. Simultaneous amplitude and phase modulation is available but at the cost of some coupling between the two parameters. Several SLM technologies exist, including optically-addressed SLMs and digital micromirror arrays, however the most common SLM implementations are based on liquid crystal displays (LCD), which we use here. In an LCD-based SLM the alignment of the nematic liquid crystal layer at a given pixel dictates the phase shift imparted to the light passing through that pixel. Higher phase shifts are achieved by retro-reflecting the light off a dielectric mirror positioned behind the display, to double the total phase shift. This provides a flexible way to create the phase profiles generated by spiral phase plates or holograms, without the difficulty of fabricating devices, and with greater control to achieve smoothly varying phase profiles and hence higher coupling to a single LG mode. SLMs also provide the tempting possibility to dynamically vary optical fields and create time-varying trapping potentials.

In principle, to create an LG beam we simply need to display a phase winding on the SLM where the pixel value azimuthal increases about a central point, and reflect a Gaussian beam off of it. In addition the linearity of phase imprinting can be used to add several other phase patterns on top of this and simultaneously achieve several operations:

$$e^{i\phi_{\text{winding}}} e^{i\phi_{\text{grating}}} e^{i\phi_{\text{lens}}} e^{i\phi_{\text{correction}}} = e^{i\left(\phi_{\text{winding}}+\phi_{\text{grating}}+\phi_{\text{lens}}+\phi_{\text{correction}}\right)}, \tag{4.3}$$

where our commonly used phase operations are listed below.

Operation	Phase profile
Phase winding	$\phi_{\text{winding}} = \mod(\ell\theta, 2\pi)$
Blazed grating	$\phi_{\text{grating}} = \mod(k_x x + k_y y, 2\pi)$
Lensing	$\phi_{\text{lens}} = \mod\left(-k\frac{x^2+y^2}{2f}, 2\pi\right)$
Correction	see Section 4.2.5

The phase winding ϕ_{winding} imprints the desired angular momentum onto the beam, the blazed grating ϕ_{grating} directs the beam, the lensing ϕ_{lens} controls the focus of the beam, and the correction phase pattern $\phi_{\text{correction}}$ cancels imperfections on the SLM and other parts of the optical setup. This is illustrated in figure 4.6. Since the phase shift of the SLM is in the range $\{0, 2\pi\}$, the functions are all $\mod(2\pi)$ to make use of the equivalence between 0 and 2π phase shift. We note that if the functions were all $\mod(\alpha 2\pi)$, where $\alpha < 1$, the effect would be to diffract more of the light into other orders. This means that the first diffraction order we use only contains LG modes of a

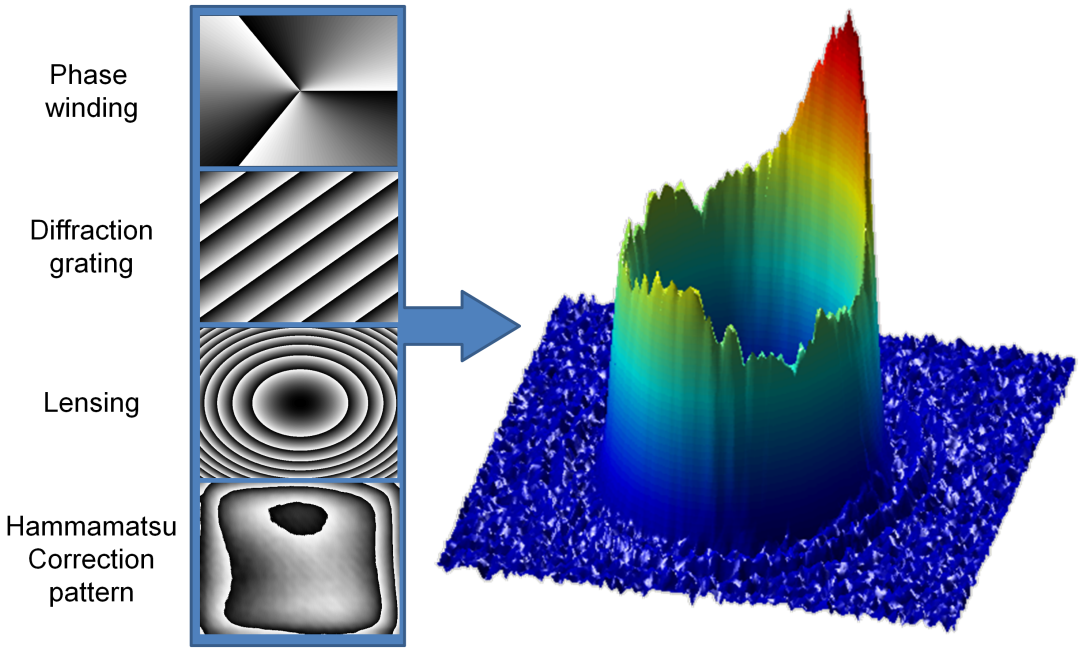

Figure 4.6: Decomposed SLM pattern and corresponding LG beam intensity profile: Left images show pixel values displayed on the SLM, where black = 0 and white = 2π. The LG beam phase winding is created by displaying an azimuthally increasing pixel value, in this case for $\ell = 3$. Additional operations are achieved by simply adding further phase profiles. A blazed diffraction grating creates a bright first order beam, spatially separated from the undiffracted light and other orders. The focus of the first order beam is adjusted by adding a lensing phase profile formed from a radially varying pixel value. Finally a correction pattern is added which compensates for abberations present in the SLM and subsequent imaging optics. In this case the provided Hammamatsu correction is used, only correcting for unwanted phase shifts on the SLM. As illustrated on the right this creates a focused LG beam in the first diffraction order, here presented for $\ell = 20$. Residual imperfections are due to the incomplete correction pattern used (see Section 4.2.5).

single ℓ value, the value of which is dictated by the periodicity of the phase winding, not the absolute phase value. Due to their design, SLMs inherently reflect a portion of the incoming light without applying any phase shift. The inclusion of a diffraction grating spatially separates the light field we want from this unmodulated light and other diffraction orders.

SLM Choice

Having decided upon a reflective, phase modulating SLM, our choice was reduced to three manufacturers: Hamamatsu, Holoeye, and Boulder Nonlinear Systems. The first criteria is efficiency, i.e. the maximum amount of light possible to diffract into a single order. This is a strong function of the back mirror, and the fill factor (the fraction of the SLM area which is usable pixels). Both Hamamatsu and Boulder provide high filling factors and high efficiency dielectric mirrors, offering efficiencies as high as 95%. Holoeye offers lower efficiency, but much higher screen resolution enabling smoother phase profiles. Although not essential to this work, the possibility to dynamically vary the

light field depends on the refresh rate of the SLM. SLMs also suffer from phase droop, where the crystal tends to relax between refreshes, creating a time varying phase profile. Both Hamamatsu and Holoeye run the SLM as a second monitor via a DVI connection and hence only refresh at 60 Hz, which is slower than the liquid crystal's free relaxation rate. In practical applications this translates to a toggle rate for dynamically changing the phase pattern of about 10 Hz. Boulder SLMs interface via PCI Express, and hence offer a refresh rate of over 6 kHz and a usable toggle rate of about 1 KHz. Boulder SLMs therefore offer a clear advantage for dynamic processes, however the PCI Express interface makes the SLM considerably more difficult to communicate with, and the response time comes at a financial cost. Experimentally, the phase droop of the Hamamatsu SLM was not observable and we could not attribute any erroneous heating to the effect. We therefore conclude that for high-efficiency, static light fields the Hamamatsu SLMs provide a good choice and use the LCOS-X10468-02 with dielectric mirror for $\lambda = 750 - 850$ nm.

The implementation of the SLM is illustrated in figure 4.7. As explained in Section 4.3, the LG beam is one beam of a two-photon Raman transition used to impart angular momentum to the atoms. Both Raman beams exit the same fibre with orthogonal polarisations and frequency shifted from one another by the relevant Zeeman energy. The horizontally polarised beam, referred to as the LG beam, is reflected off the SLM and hence picks up a phase winding and angular momentum. The vertically polarised beam, referred to as the G beam, does not, and hence the difference in angular momentum of the two beams is imparted to the atoms during the Raman transition.

Concentrating on the SLM setup for the LG beam, the beam is partially collimated out of the fibre by an achromatic doublet lens[1]. The beam is still diverging when it reaches the SLM, at which point it completely fills the SLM screen with a waist of 6 mm, before reflecting off at a shallow angle of less than 10° to the normal. Before reaching the SLM the light passes through a neutral optical density filter. Although not essential, the required power in the LG beam is several orders of magnitude less than that in the G beam, hence the filter allows the balance of power between the two Raman beams to be more comparable, and therefore small drifts in the polarisation have a smaller relative effect. The phase imprinted on the beam is shown in figure 4.6. A lensing pattern is added to the SLM which collimates the incoming beam, and a diffraction grating spatially separates the various orders. Both Raman beams are then recombined on a cube and focused onto the atoms using an aplanatic meniscus lens[2] and companion doublet[3] with a combined focal length of $f = 86$ mm.

[1] AC254-100-B-ML
[2] CVI Melles Griot 01LAM555
[3] CVI Melles Griot 01LAO555

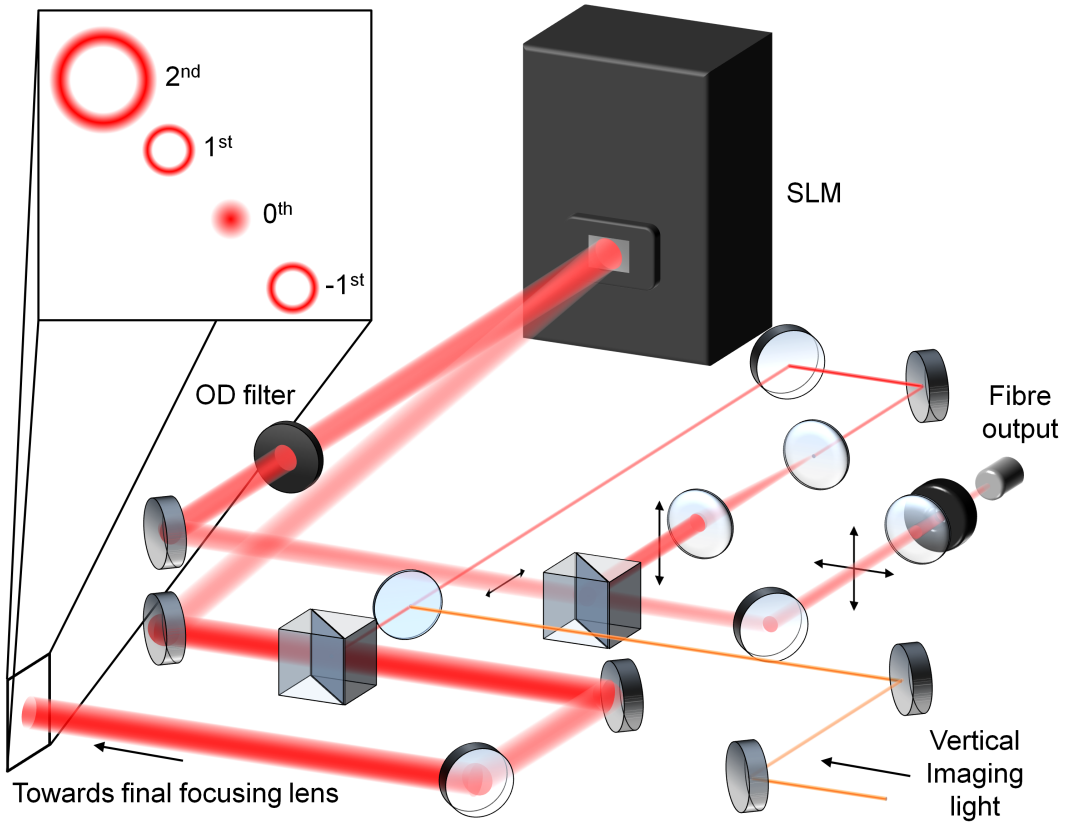

Figure 4.7: SLM optics: The two beams for the Raman transition exit the fibre with orthogonal polarisations and frequency shifted with respect to one another. The beam with vertical polarisation, referred to as the Gaussian beam, is split off a PBS cube and telescoped down so as to have a large waist at the atoms. The beam with horizontal polarisation, referred to as the LG beam, reflects off the SLM at a shallow angle, imprinting the phase displayed. Both beams are recombined on a PBS cube and sent towards the atoms. The inset plane illustrates the various orders of the LG light field before the final imaging lens. The light is focused down onto the atoms and the Gaussian beam is overlapped with the 1^{st} order LG beam.

4.2.4 Pseudo-Laguerre-Gauss beam

The SLM allows us to imprint the necessary helical wavefront onto a Gaussian beam, however this is not a true LG beam since the field intensity at the SLM does not have the characteristic annular profile. As the beam propagates, destructive interference at the phase singularity will give rise to a pseudo-LG beam with a high mode overlap with the corresponding LG^{ℓ} mode. To see this we consider the paraxial Helmholtz equation given by

$$\frac{\partial^2 f_z}{\partial x^2} + \frac{\partial^2 f_z}{\partial y^2} + 2ik\frac{\partial f_z}{\partial z} = 0, \tag{4.4}$$

where f_z is the field at position z, and $k = 2\pi/\lambda$ is the wavevector. We also define the fourier transform of the field given by

$$F_z(u,v) = \int_{-\infty}^{\infty}\int_{-\infty}^{\infty} f_z(x,y)\exp\left[-2\pi i(ux+vy)\right]dxdy. \tag{4.5}$$

From this we can easily show the effect of

1. Propagation in free space a distance z:

$$F_z(u,v) = F_0(u,v)\exp\left[-\frac{2\pi i}{k}(u^2+v^2)z\right] \tag{4.6}$$

$$f_z(x,y) = f_0(x,y) * h(x,y) \tag{4.7}$$

where

$$h(x,y) = \frac{1}{i\lambda z}\exp\left[\frac{ik}{2z}(x^2+y^2)\right]. \tag{4.8}$$

2. Action of a lens

$$f(x,y) \to f(x,y)\exp(i\phi_L(\mathbf{r})) \tag{4.9}$$

where ϕ_L is the phase shift introduced by the lens

$$\phi_L(\mathbf{r}) \approx -\frac{kr^2}{2f} \qquad \text{for} \qquad r \ll f. \tag{4.10}$$

Using these principles we numerically propagate the field at the SLM and find the field at the focus. For our experiment the distance from the SLM to the imaging lens is approximately 1 m, and we predominantly use $\ell = 3$. These calculations are shown in figure 4.8. During free propagation we observe destructive interference along the optical axis and after 1 m the field appears strongly LG-like. Significant radial ringing is observed which we can attribute to the contribution of higher p radial modes. After the imaging lens the radius of the ring intensity profile is smallest at the focus, however the central dark singularity is preserved at all positions. From these calculations we anticipate a Gaussian waist of $w \approx 5.3$ μm, and hence a ring radius for $\ell = 3$ of ≈ 6.5 μm. We find contribution from higher p modes can be significantly reduced by radially masking the SLM with a doughnut aperture, the outer radius of which is set to be the vertical height of the SLM and the inner radius is chosen to minimise ringing for a given ℓ. We implement this by simply only applying the blazed grating to an appropriately chosen doughnut area on the SLM, hence light outside this mask is not deflected towards the atoms. This increases the calculated Gaussian waist to $w \approx 9$ μm and the $\ell = 3$ radius to ≈ 11 μm. This is close to our observed radius of 12.2 μm.

The properties of such pseudo-LG beams for a fixed field at the SLM are displayed in figure 4.9. In figure 4.9 (a) we compare the intensity profile of the pseudo-LG beam with a pure LG beam of equal winding, where the waist parameter is chosen to give equal radius and the profiles are normalised. The two profiles are closely matched, with the pseudo-LG beam exhibiting small radial oscillations beyond the primary peak. The intensity profile as a function of ℓ is shown in figure 4.9 (b). Unlike for a true LG beam,

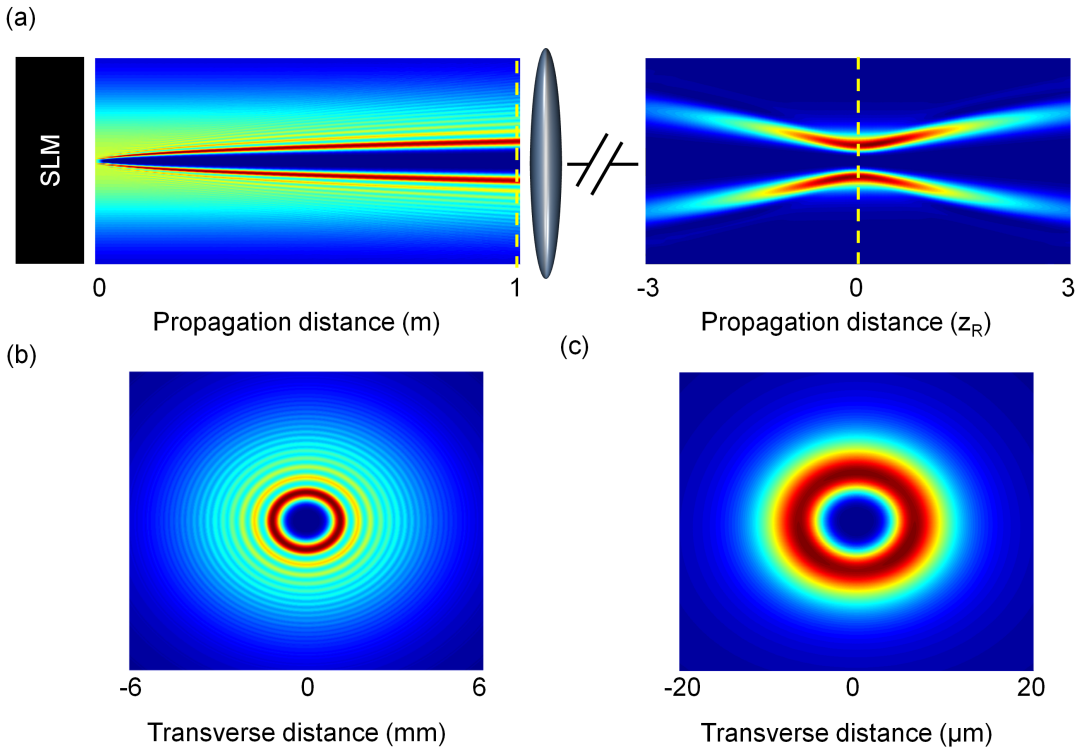

Figure 4.8: Numerical calculation of pseudo-LG beam propagation: (a) By propagating the field produced at the SLM a distance of 1 m we observe destructive interference along the optical axis and the formation of an annular intensity profile. About the focal point of the lens the radius of the annular intensity profile reduces, but the intensity zero at the centre never vanishes. (b) Intensity profile of the field at the lens after free propagation for 1 m. The profile is LG-like, but the multiple rings indicate a significant contribution of higher radial modes with $p \neq 0$. (c) Intensity profile at the focal point. The LG mode at the focus appears cleaner than that before the lens.

the ring radius scales linearly with ℓ as shown in 4.9 (c). This radius scaling is confirmed by our experimental measurements, and is observed independently in [133]. For a fixed intensity at the SLM the peak intensity at the focus scales as $\ell^{-0.8\pm0.1}$, and the radial trapping frequency scales as $\ell^{-0.45\pm0.05}$. These powers are consistent with the trapping minima being independent of ℓ if the peak intensity is held fixed.

An analytic expression for the field produced at the focus is derived in Appendix A

$$E_f(r,\theta) = E_0 i^{\ell-1}\sqrt{\pi}\frac{f^2}{z^2}\frac{w}{w_0}\frac{r}{w_0}\exp\left(-\frac{r^2}{2w_0^2}\right)\left[I_{\frac{\ell-1}{2}}\left(\frac{r^2}{2w_0^2}\right) - I_{\frac{\ell+1}{2}}\left(\frac{r^2}{2w_0^2}\right)\right] \times \exp\left[\frac{i\pi}{f\lambda}\frac{f-z}{f}r^2\right]\exp(i\ell\theta), \tag{4.11}$$

where f is the focal length of the imaging lens, z is the free propagation distance between the SLM and the lens, $I_n(z)$ is a modified Bessel function of the first kind, and $w_0 = f\lambda/\pi w$ is the diffraction limit, where w is the waist of the initial Gaussian beam. Comparison with the field for a pure LG beam in (4.1), our pseudo-LG beam displays

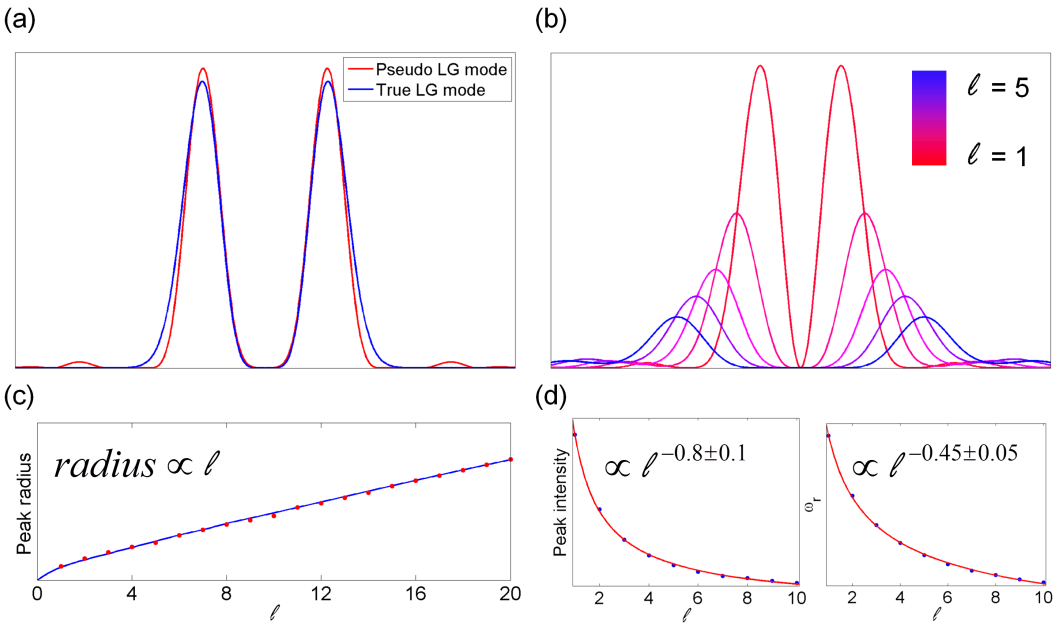

Figure 4.9: Numerical calculations of pseudo-LG beam properties produced by phase imprinting a Gaussian beam: (a) Comparison of pseudo-LG beam with true LG beam intensity (4.2). The respective waists have been chosen to give equal ring radii, and both profiles have been normalised. (b) Scaling of intensity profiles of pseudo-LG beam with ℓ. For all ℓ, the input field at the SLM is held constant, only the phase winding imprinted is changed. (c) Scaling of peak radius with ℓ for pseudo-LG beam. The red points are experimental data, and the blue line is a numerical calculation which has been scaled to lie on the data. The two show good agreement and both predict a linear relationship, in comparison to the $\sqrt{\ell}$ scaling for a true LG beam. (d) Numerical calculations of peak intensity and radial trapping frequency, ω_r, scaling with ℓ. The points are fitted to a power law function to obtain scalings of $\ell^{-0.8}$ and $\ell^{-0.45}$, for peak intensity and ω_r respectively.

the important helical wavefront, $e^{i\ell\theta}$, associated with orbital angular momentum. Taking the small argument limit of $I_n(z) \sim \frac{1}{\Gamma(n+1)}\left(\frac{z}{2}\right)^n$, retrieves the same small r limit of $E_f \propto r^\ell$.

4.2.5 Correcting for abberations

As shown in figure 4.6, the initial LG beams we generated differed from those in our calculations. We observed azimuthal variations in the intensity which had significant implications on the smoothness of our trapping potential, and hence the stability of superflow around the ring. These variations are introduced by unwanted phase aberrations present in the SLM and the optics along the LG beam path. Significant time and effort was therefore invested in minimising such variations to create the ideal trapping environment for observing persistent currents. Helpfully, due to their wide range of applications, considerable attention has already been paid to the estimation and correction of abberations in SLM-based optical systems. A phase pattern is provided with our SLM to correct for known aberrations measured at production, but further

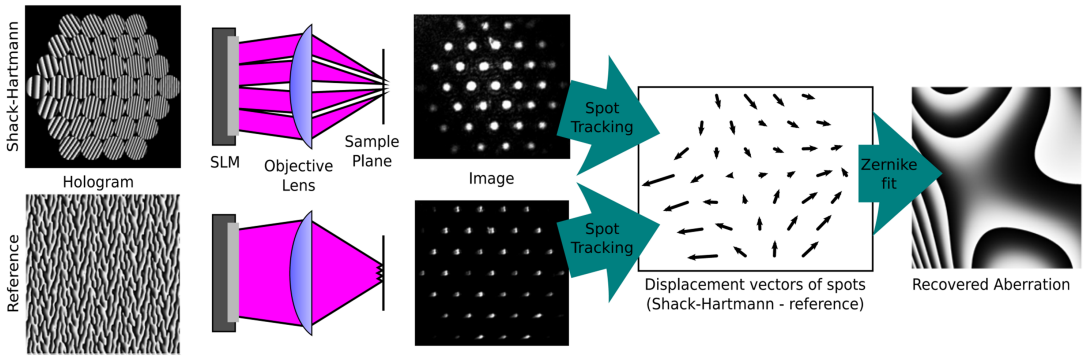

Figure 4.10: Schematic of the SLM-based Shack-Hartmann sensor (copied with permission from [134]): The Shack-Hartmann array produces a grid of spots, where aberrations affect the position of each spot. The corresponding reference array produces a grid of spots, where aberrations affect spot shape but not position. By tracking the displacement of the spot centres between the two arrays we construct a vector map which can be fit to directly recover the wavefront.

aberrations introduced by our setup needed to be minimised. Below we outline the two algorithms we implemented to detect and correct such aberrations, and our final solution based on manual correction.

Shack-Hartman algorithm

Shack-Hartmann sensors employ an array of lenslets to focus a collimated beam into an array of spots. The displacement of each spot is proportional to the tilt of the wavefront at that point, and the resultant tilt information can be integrated to recover phase information. An equivalent SLM-based Shack-Hartmann sensor is described in [134], and illustrated in figure 4.10. The Shack-Hartmann array is first displayed on the SLM, which is composed of a grid of circular apertures, each of which contains a blazed diffraction grating of different pitch, such that each aperture focuses to a different spot in the focal plane. Any aberrations present along a given spot's optical path, will displace the spot from its true position. To find these true positions the reference array is then displayed, which creates a grid of spots where each spot comes from the whole SLM. In this case aberrations will primarily affect the shape of the spots and not the geometry of the grid. By measuring the displacement of the spots between the Shack-Hartmann and the reference array, we construct a vector map of wavefront tilts which can be fitted to recover the aberration present in the optical system. We then correct for this aberration by simply displaying the negative of this phase map on the SLM, which we refer to as the correction pattern.

The vector map of spot displacements are fitted to a linear combination of Zernike polynomials, listed in table 4.1. Firstly this ensures a smoothly varying correction pattern, and secondly it also ensures the correction pattern cannot include phase singularities. This is significant as it guarantees the correction pattern cannot change the

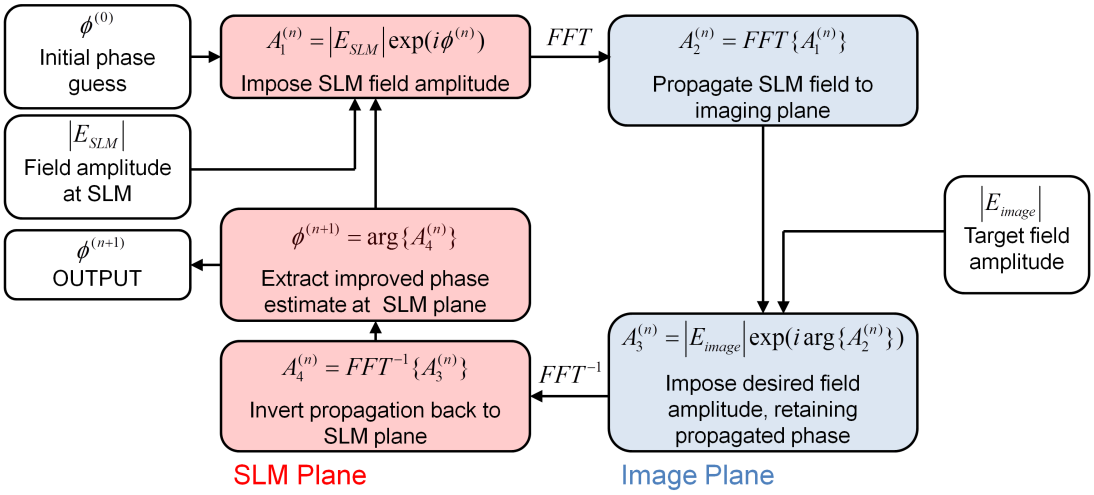

Figure 4.11: Diagram of Gerchberg-Saxton algorithm for finding phase errors: The initial conditions consist of the modulus of the field amplitude at the SLM plane $|E_{\mathrm{SLM}}|$, which in this case is a Gaussian, and an initial phase guess ϕ_0, which in this case is an $\ell = 1$ phase winding. The field A_1 is propagated to the imaging plane by a fast Fourier transform (FFT) creating the field A_2. The amplitude of the field is replaced by the modulus of the target intensity $|E_{\mathrm{image}}|$, in this case an image of the uncorrected LG beam, to create the field A_3. This field is inverse propagated back to the SLM plane to create the field A_4, the phase of which is our improved estimate of the phase required to create the target image. This process is iterated until convergence.

winding number of the SLM and hence the topological charge of the LG beam produced. The Shack-Hartmann algorithm provides a robust way to cancel aberrations and significantly improved the quality of our LG beams. For bench-top tests, the algorithm allowed us to obtain highly circular LG beams with a peak-to-peak variation in azimuthal intensity of approximately 30%.

Unfortunately this algorithm has a major drawback for cold-atom experiments where the focal plane of interest is always within a vacuum system and hence inaccessible. To observe the relevant spot arrays at the focal plane of the atoms we had to use our vertical imaging systems, hence the algorithm cannot distinguish between aberrations introduced before the focal plane, and those inherent in the imaging system. To efficiently track spot displacements it is advantageous to have a large grid of many spots filling up as much of the field of view as possible, but as we discovered our vertical imaging system introduces significant distortion when imaging off the optical axis. This resulted in the algorithm introducing a lot of lensing aberration at the focal plane of the atoms to compensate for the distortion of the imaging system, and hence the algorithm could not be implemented in our system.

Gerchberg-Saxton algorithm

The Gerchberg-Saxton (GS) algorithm is a phase retrieval technique designed to deal with the problem of finding the phase $\phi_{\mathrm{SLM}}(x, y)$ of a light field by just knowing the

modulus $|E_{\text{image}}(k_x, k_y)|$ of its Fourier transform, and the modulus of the light field $|E_{\text{SLM}}(x, y)|$:

$$|E_{\text{image}}(k_x, k_y)| \exp[i\phi_{\text{image}}(k_x, k_y)] = FFT\{|E_{\text{SLM}}(x, y)| \exp[i\phi_{\text{SLM}}(x, y)]\} \quad (4.12)$$

In the paraxial approximation the light field at the imaging plane of a lens and the light field at the SLM plane are related by a scaled Fourier transform. From this, one can see the general problem of finding the SLM phase to apply to a known field modulus in order to achieve a desired field modulus at the imaging plane, is a member of the class of problems described by (4.12). As such, the GS algorithm (and extensions thereof) has been implemented by several groups to calculate SLM patterns required to create complex light fields and trapping potentials [118, 135, 136]. We note that incomplete knowledge about the phase at the imaging plane means there may exist many phase functions with amplitudes close to $|E_{\text{image}}(k_x, k_y)|$ which define local minima that may prevent us from finding the global minimum. GS is a computationally efficient optimisation method for finding phases $\phi_{\text{SLM}}(x, y)$ which minimise the difference between $|E_{\text{image}}(k_x, k_y)|$ and $|FFT\{|E_{\text{SLM}}(x, y)| \exp[i\phi_{\text{SLM}}(x, y)]\}|$.

The basic GS algorithm is sketched in figure 4.11. One provides the field modulus at the SLM, $|E_{\text{SLM}}(x, y)|$, the target field modulus at the imaging plane, $|E_{\text{image}}(x, y)|$, and an initial phase guess at the SLM plane, $\phi^{(0)}$. The initial field (A_1) is propagated to the image plane by a fast Fourier transform (FFT) and the modulus of this field is replaced by the target field modulus, $|E_{\text{image}}(x, y)|$. This field (A_3) is back propagated to the SLM plane by an inverse FFT and the modulus of this field is replaced by the known SLM field modulus, $|E_{\text{SLM}}(x, y)|$. This process is iteratively repeated until convergence and the algorithm provides a best estimate of the phase to display on the SLM which most closely solves (4.12).

This algorithm places no restrictions on the phase of the image field, which helps by providing additional freedom to achieve the target modulus. However for the case of our LG beam the phase at the image plane is vitally important as we need to preserve the phase winding associated with the orbital angular momentum of the beam. As detailed in [137] one can still use the GS algorithm to detect and correct for aberrations by using an image of an uncorrected LG beam as the target amplitude and the phase winding $\phi^{(0)} = \ell\theta$ as the initial phase guess. The GS algorithm will then converge on the phase profile $\phi_{\text{SLM}} = \ell\theta + \phi_{\text{aberration}}$, providing the correction pattern $\phi_{\text{correction}} = \ell\theta - \phi_{\text{SLM}}$.

Due to the phase freedom inherent in the GS algorithm, convergence to this particular solution is strongly dependent on the amount of aberration present in the system. Uncorrected LG beams which differ too greatly from a perfect LG beam will converge to phase solutions differing from the addition of a phase winding and smooth, singularity-free aberrations, and cannot be corrected using this method. Experimental implementation of this method also suffers from several other pitfalls, namely accurate knowledge of the input field modulus, $|E_{\text{SLM}}(x, y)|$, and precise centring and scaling of

the target image to match the propagated SLM field intensity. These uncertainties can lead to unnecessary lensing and phase singularities near the centre of the correction pattern. Though difficult to implement, we were able to achieve peak-to-peak variations in azimuthal intensity of approximately 50%, and could use this method in the actual system.

Manual correction

The two algorithms described above were instrumental steps along the way to achieving smooth LG beams, but in the end we utilise neither. Our final correction procedure is based on observations made during our attempts to implement these algorithms. As shown in table 4.1, we can identify the addition of a given Zernike mode with a characteristic distortion of the LG beam (column 4), and correspondingly in the atom density (column 5). We can therefore approximately identify from the LG beam shape and intensity profile which of the low order Zernike polynomials is present in the aberrations and compensate by subtracting them from the correction pattern. The general procedure is as follows

1. Careful alignment of the SLM optics is essential for getting sufficiently close to implement any correction procedure. All optics should be kept clean and any transmissive optics should be positioned as close to normal to the beam as possible. The quality of the initial beam on the SLM is very significant and any fringing, or diffraction rings due to the fibre output package should be minimised.

2. Apply the desired phase winding, diffraction grating, and lensing to the SLM (The correction is not universal and will not work for different windings or substantially different gratings and lensings.) Also ensure the supplied Hamamatsu correction pattern is added which corrects for most of the aberrations.

3. By looking at an image of the light on the camera one can remove nearly all of the $Z(2,-2)$ and $Z(2,2)$ Zernike modes by walking the beam in the horizontal and vertical direction. The target should be to produce an LG beam as close to circular as possible.

4. Addition and subtraction of the eight Zernike modes listed in table 4.1 can be done in real time by looking at the camera image and trying to produce as smooth an LG beam as possible. Using this technique we can achieve azimuthal peak-to-peak variations in the intensity of $\lesssim 10\%$. Use of higher order Zernike modes is not necessary and identifying their presence is beyond our imaging resolution and not feasible to do by eye.

5. Aberrations present in our imaging system mean the true ring intensity profile differs slightly from that imaged on the camera. Therefore, as we are concerned

Zernike mode	Function	Phase profile	Effect on LG beam (theory)	Observed effect on atoms
$Z(2,-2)$	$\frac{r^2}{\sqrt{6}}\sin(2\theta)$	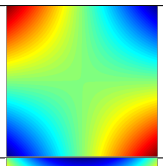	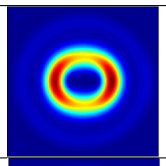	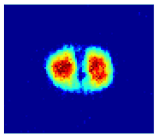
$Z(2,2)$	$\frac{r^2}{\sqrt{6}}\cos(2\theta)$	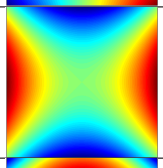	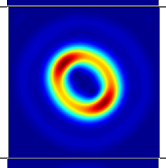	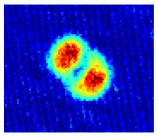
$Z(3,-1)$	$\frac{3r^3-2r}{\sqrt{8}}\sin(\theta)$	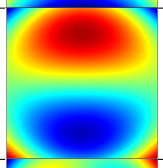	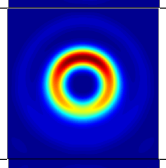	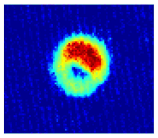
$Z(3,1)$	$\frac{3r^3-2r}{\sqrt{8}}\cos(\theta)$	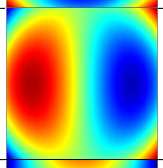	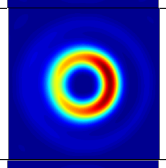	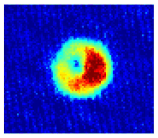
$Z(3,-3)$	$\frac{r^3}{\sqrt{8}}\sin(3\theta)$	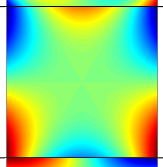	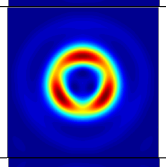	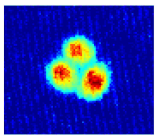
$Z(3,3)$	$\frac{r^3}{\sqrt{8}}\cos(3\theta)$	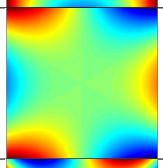	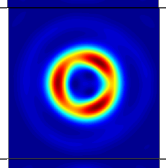	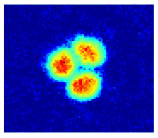
$Z(4,-4)$	$\frac{r^4}{\sqrt{10}}\sin(4\theta)$	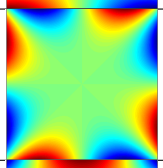	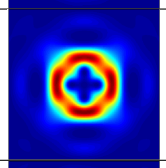	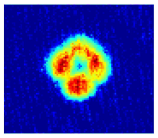
$Z(4,4)$	$\frac{r^4}{\sqrt{10}}\cos(4\theta)$	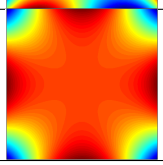	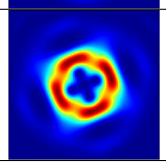	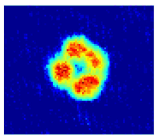

Table 4.1: Table of Zernike polynomials: The first three columns list the Zernike polynomials which we use to correct for aberrations, including the functional form and phase profile. The fourth column is a numerical calculation to illustrate how addition of the corresponding Zernike polynomial to the SLM phase modifies the LG intensity profile at the focus. The fifth column is an absorption image of atoms loaded into the corresponding LG beam. This distinctive mapping between atomic density profile and Zernike polynomial allows us to manually subtract excess Zernike orders, and hence cancel aberrations and achieve a smooth density profile.

with optimising the true trapping potential, we now modify our correction pattern further by identifying Zernike modes present in the actual atom density, as shown in column 5 of table 4.1. This stage is the slowest as correction cannot be done in

real time as a new BEC must be loaded into the ring trap and destructively imaged *in situ* to measure the effect of modifying the correction pattern. Typically within 20 iterations we estimate azimuthal peak-to-peak variations in LG intensity are reduced to $< 10\%$. Due to diffraction effects discussed in Section 3.9.3, to obtain a true measure of the density profile it's important to image on resonance, and hence we use partial transfer absorption imaging to reduce the optical density [79].

While laborious, this manual correction procedure is necessary for producing smooth ring traps needed for sustaining superflow with very low atom density or in deep ring traps using a high intensity LG beam.

4.2.6 Loading procedure

The normal criteria for loading a trap are maximising atom number transfer and minimising heating. When loading our atoms from the CDT to our ring trap, these criteria are satisfied for a range of loading procedures, however we must consider a third, stricter criterion. Due to the multiply-connected geometry of the ring trap, any oscillations induced during transfer which would normally dissipate and contribute to heating, can now lead to unwanted, long-lived superflow. Our initial loading procedure was done over 2 seconds, as no visible gains were observed for longer loading times. When we then impart angular momentum, $\hbar\ell$, to the atoms by a two-photon Raman transition (see Section 4.3) we observe a scatter of angular momentum states with a mean magnitude of $\hbar(\ell + 1)$. To prove this scatter was induced at loading we reverse the frequencies of the Raman beams, hence reversing the ordering of absorption and stimulated emission, and thereby imparting angular momentum $-\hbar\ell$ to the atoms. The observed angular momentum states retain the same scatter but the mean magnitude is reduced to $\hbar(\ell - 1)$. Hence we conclude the loading procedure quasi-randomly stirs the condensate with an average angular momentum $+\hbar$. We therefore increased the loading time to 6 seconds as shown in figure 4.14 and no longer observed any mechanical stirring on loading.

Unfortunately we observe a slow drift in the position of our LG beam when the experiment is running. Typically the experiment needs to run for over an hour (approximately 40 cycles) before the LG beam stabilises, by which point the beam has moved approximately 30 μm at the atoms from its original starting position. The magnitude of this motion is sufficiently large so as to misalign the LG beam with respect to the sheet potential and create a pooling of atoms to one side of the ring trap. The origin of this drift could not be discovered, so instead the system is allowed to "warm-up" for a couple of hours before overlapping the ring and sheet potentials, by which point the residual drift is much smaller and slower.

4.3 Imparting angular momentum

Traditionally, orbital angular momentum has been transferred to BECs by some form of mechanical stirring such as by a laser beam or an optical lattice. Such methods have proven successful for many studies, including the creation of large vortex lattices [31, 32], critical velocity studies [138–140], and the observation of vortex dynamics and nucleation [141]. In general however, mechanical methods impart an unknown amount of orbital angular momentum to the system and cannot be used to deterministically prepare states of a given circulation. Recently an exception to this was achieved in [102], where a well defined and deterministic ladder of circulation states was observed as the rotation frequency of a rotating weak link was increased.

Another class of methods exist which involve imprinting a well defined phase winding onto the BEC wavefunction to deterministically prepare a state of known circulation. The first generation of a vortex in a BEC employed such phase engineering by using a rapidly rotating Gaussian laser beam to couple the external motion to internal Rabi oscillations, allowing creation of a state with exactly one unit of circulation [30]. Doubly quantised vortices have also been topologically imprinted in condensates by inversion of the axial bias field in a Ioffe-Pritchard magnetic trap [89, 142]. As the bias field is inverted, the atomic spins adiabatically follow the field direction, remaining in the same state with respect to the local magnetic field, but transitioning to a different magnetic state with respect to the fixed lab frame. The nature of the field rotation varies azimuthally and hence a topological phase factor is imprinted on the atoms which can be interpreted as a manifestation of Berry's phase [143]. This technique has also been used to generate novel spin structures such as coreless vortices [144] and Skyrmion states [145].

As discussed previously, LG beams carry well defined quanta of orbital angular momentum along their direction of propagation, associated with their azimuthal phase winding. As a result, several experiments have made use of this feature by coherently transferring atoms with such a beam, and thereby imparting this angular momentum to the atoms, or equivalently, imprinting the phase winding onto the condensate. To coherently transfer the atoms to a stable state, these experiments use two-photon transfers, which avoid population of the short-lived excited state and return the BEC to the stable ground state, as explained in Section 3.2.3. The total angular momentum transferred in such a transition is then the difference between the two beams, which for the Gaussian (G) plus LG beam configuration is simply $\ell\hbar$ per atom, where ℓ is the angular mode of the LG beam. For efficient transfer and to prevent multi-photon processes, the initial and final state have to be energetically separated from one another. The energy associated with rotation is typical of the order of a few Hz and is therefore insufficient to prevent additional coupling of the final state.

The first experimental observations of such transfers are reported in [99, 146]. These

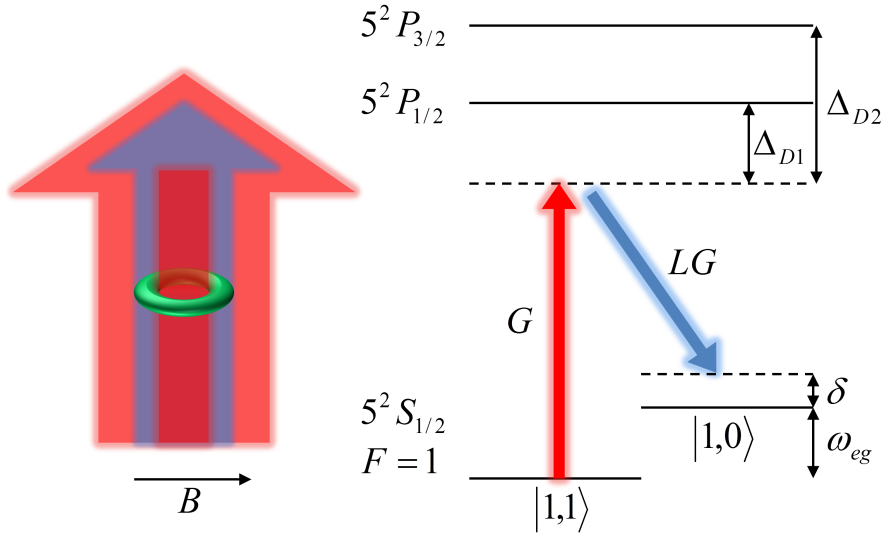

Figure 4.12: Scheme for two-photon Raman transfer using G plus LG beams: The two Raman beams are composed of our trapping LG beam which forms the ring trap, and a second, broad Gaussian beam, co-propagating in the vertical direction. The basis of states we transfer between are the $m_F = 1$ and $m_F = 0$ magnetic states of the $F = 1$ hyperfine level which are energetically separated by $\omega_{eg} \approx 7$ MHz in an external bias field of ≈ 10 G orientated in the plane of the sheet trapping beam. The frequency difference between the G and LG beam is equal to the Zeeman splitting, ω_{eg}, plus the two-photon detuning, δ. The Raman beams are both far red detuned of the $D1$ and $D2$ transitions by an amount Δ_{D1} and Δ_{D2} respectively to prevent population of the upper state. With respect to the field the G beam is π polarised and the LG beam is equal parts σ^+ and σ^- polarised.

experiments were similar to Bragg diffraction, in that the initial and final states are different momentum states of the same atomic state differing by $2\hbar k$, coupled by a counter-propagating Gaussian and LG_0^1 beam. Atoms which undergo the transfer absorb a photon from one beam and stimulatedly emit a photon into the second beam acquiring both linear momentum of $2\hbar k$, and orbital angular momentum of $\hbar$. The recoil energy associated with this linear momentum, $E_r = 4(\hbar k)^2/2m$, is sufficiently large to energetically separate the initial and final states, however the linear momentum kick causes oscillations of the final state within the trap. This problem is circumvented in [99] by initially Bragg scattering the atoms into the $2\hbar k$ state, and then after half a trap oscillation period, the LG plus G transfer removes this linear momentum and imparts orbital angular momentum.

For studying the decay of persistent currents it's imperative that we prepare the same circulation state every time. Therefore we employ the phase-engineering approach described above, utilising the phase profile of an LG beam. Our method involves Raman coupling two different magnetic sublevels of the $|5^2S_{1/2}, F = 1\rangle$ hyperfine state, $|F = 1, m_F = 1\rangle$ and $|F = 1, m_F = 0\rangle$, using co-propagating LG and G beams, as illustrated in figure 4.12. This method is similar to that used in [100] and [147]. Unlike [100], we use our LG trapping beam as one of our Raman beams, automatically ensur-

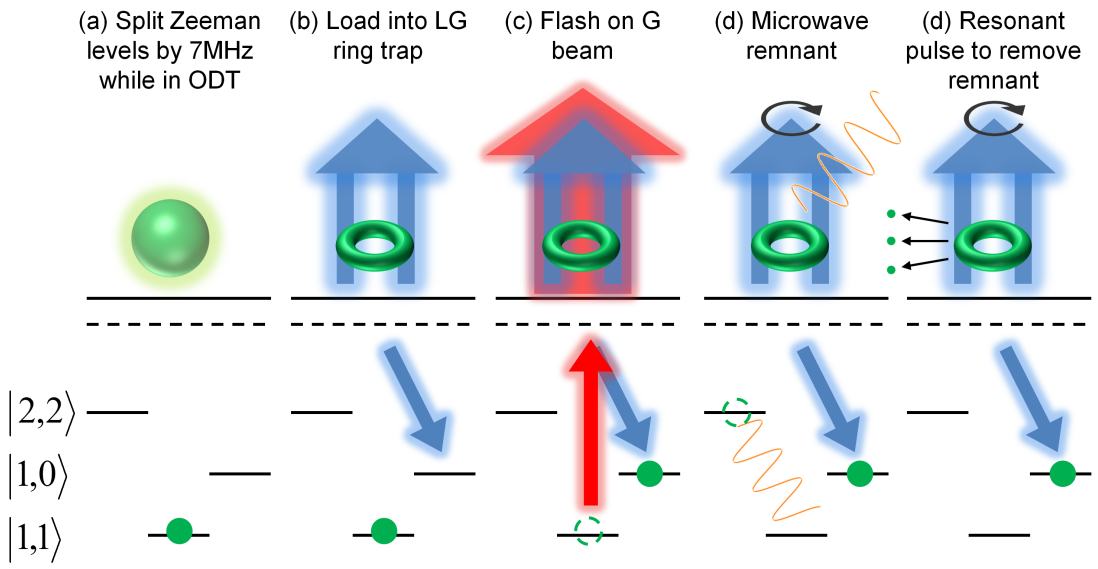

Figure 4.13: Protocol for imparting rotation to ring shaped BEC: (a) While still in the CDT the bias field of 10 G is applied to give time for the field to stabilise (step 3 in figure 4.14). (b) As described in Section 4.2.6 the BEC is loaded into the ring trap, where the LG beam acts as both trapping beam and one of the Raman beams (steps 4-6 in figure 4.14). (c) The second Gaussian Raman beam is flashed on for ~ 200 μs. The atoms undergo a two-photon π pulse to the $|1,0\rangle$ state, acquiring $\ell\hbar$ units of orbital angular momentum. (d) The small, non-rotating remnant ($\approx 5\%$) left in the $|1,1\rangle$ state is immediately microwave π pulsed to the $|2,2\rangle$ state in ≈ 40 μs. (e) A short imaging pulse (≈ 10 μs) scatters the $|2,2\rangle$ atoms out of the trap leaving only $|1,0\rangle$ atoms rotating in the ring trap. Steps (c)-(e) are all performed sequentially in step 7 in figure 4.14.

ing maximal spatial overlap between the BEC and the Raman beams. A second broad Gaussian beam couples the two m_F states, with both beams far red-detuned from both the $D1$ and $D2$ transitions to minimise spontaneous emission and heating. The $m_F = 1$ and $m_F = 0$ states are energetically split by $\omega_{eg} \approx 7$ MHz by the application of a uniform bias field of about 10 G. The frequency difference between the Raman beams is therefore equal to ω_{eg} plus the two-photon detuning, δ, which we aim to equal zero. As discussed in Section 3.5, at this field the Zeeman splitting $E(|1,0\rangle \rightarrow |1,1\rangle)$ differs from $E(|1,-1\rangle \rightarrow |1,0\rangle)$ by 14.4 kHz, hence provided the two-photon Rabi frequency is significantly smaller than this energy difference, the $m_F = -1$ state can be considered far detuned and the $F = 1$ manifold reduces to a two state, or spin-1/2 system. The polarisation of the Gaussian beam with respect to the field direction is π, and the LG is equal amounts of σ^+ and σ^- polarisation. Due to the energy difference of the beams only the σ^+ polarised light contributes to the Raman transition and hence the two-photon Rabi frequency, however both polarisations contribute to the dipole potential and inelastic scattering.

4.3.1 Rotation procedure

The rotation protocol used in Chapters 5 and 6 is outlined in figure 4.13.

(a) While still in the CDT the states $|1,1\rangle$ and $|1,0\rangle$ are Zeeman split using the antibias[1] field to apply a uniform field of 10 G. Early application gives time for the field to stabilise and eddy currents to dissipate during loading of the ring trap.

(b) The BEC is then loaded into the ring trap, where the trapping LG beam also acts as one of the two Raman beams.

(c) The second Raman beam, a broad co-propagating Gaussian beam, is flashed on two-photon resonance ($\delta = 0$) for a time $t_\pi = \pi/\Omega_R \approx 200$ μs, performing a π pulse and flipping the state vector from pure $|1,1\rangle$ to pure $|1,0\rangle$. The atoms absorb a photon from the Gaussian beam and stimulatedly emit one into the LG beam, acquiring orbital angular momentum $-\ell\hbar$, but no linear momentum. The short pulse time and broad Gaussian minimise any oscillations induced by the sudden change in the dipole potential.

(d) Uncertainties in the Raman beam power and field detuning mean a small fraction ($\approx 5-10\%$) of the atoms remain in the $|1,1\rangle$ state. This small component is found to fundamentally reduce the stability of persistent currents and has to be removed. This is done by first transfering this remnant to the $|2,2\rangle$ state using a microwave π pulse of $t_\pi \approx 40$ μs. The high Rabi frequency of the microwave coupling dominates any fluctuations in detuning and ensures perfect transfer.

(e) We then apply a short resonant imaging pulse of ≈ 10 μs which scatters the $|2,2\rangle$ atoms out of the trap without affecting the rotating $|1,0\rangle$ state.

Following this rotation protocol the LG beam intensity is then typically ramped to its final value over 3 seconds. The complete sequence diagram is shown in figure 4.14. We note that cleaning up the non-rotating remnant is of vital importance to the stability of the resultant superflow. This is in contrast to the results of Chapter 6 where we study the stability of co-rotating mixtures and find all mixtures are stable for a few seconds. Here we find that due to the relative rotation of the remnant in $|1,1\rangle$ and the bulk in $|1,0\rangle$ any instability manifests itself within about 100 ms, and so we must remove the remnant immediately following the Raman transfer.

A limitation of this setup is that the transfer procedure prepares a BEC with circulation equal to ℓ, the winding of the LG beam. To change the prepared circulation of the BEC we change the azimuthal mode of the LG beam, and hence change the trapping potential. Direct comparison of BECs with different initial phase winding in the same trapping potential is therefore not possible.

[1]Power supply: Delta Elektronika SM 18-50

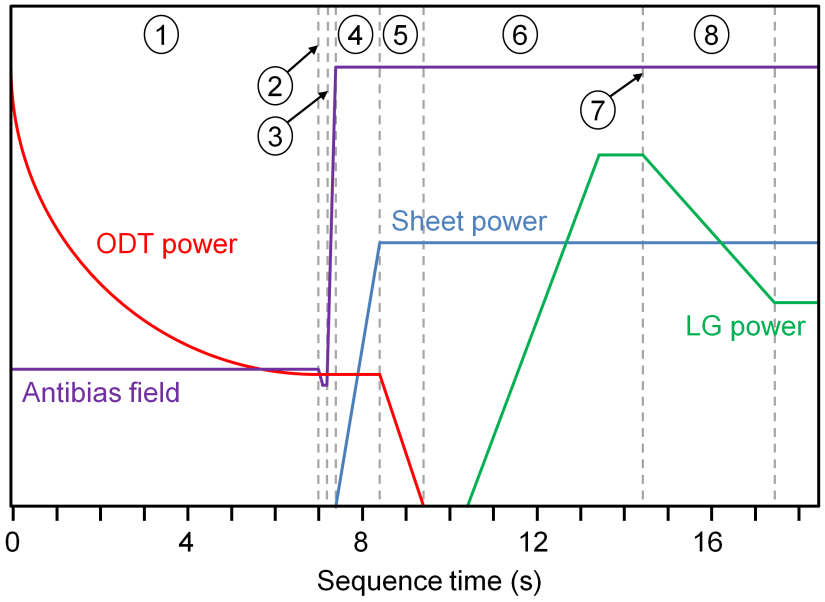

Figure 4.14: Experimental protocol for preparing a persistent current: Red lines show the ODT power, purple lines show the antibias field, blue lines show the sheet beam power, and green lines show the LG beam power. The stages of the protocol are as follows: (1) 7 s: evaporative cooling in CDT by ramping power down to 2.5 W (Section 3.7). (2) 200 ms: adiabatic state transfer $|2,2\rangle \rightarrow |1,1\rangle$ (Section 3.8) and clean up remnant $|2,2\rangle$ atoms. (3) 200 ms: ramp antibias field to final value of 10 G for state transfers. (4) 1 s: ramp up sheet power to 100 mW. (5) 1 s: ramp down CDT. (6) 5 s: hold in sheet only for 1 s, then ramp up LG beam over 3 s and hold for 1 s. (7) ≈ 200 μs: two-photon raman transfer $|1,1\rangle \rightarrow |1,0\rangle$ to rotating state. (8) 3 s: ramp LG power to final hold value.

4.3.2 Raman wavelength

The absolute wavelength of the Raman beams is important for determining not only the Rabi frequency, but also the dipole potential, U_{dip}, and the inelastic scattering rate, R_{sc}. This is especially important in Chapter 7 where we consider continuous application of the Raman coupling. Using the far detuned limit for the dipole potential and scattering rate derived in (3.42) and (3.43) respectively, and the form of the two-photon Rabi frequency, Ω_R, given in (3.30), the relevant parameters of interest are

$$U_{\text{dip}} = \sum_{D1} \frac{\hbar(\Omega_{LG,D1}^2 + \Omega_{G,D1}^2)}{4\Delta_{D1}} + \sum_{D2} \frac{\hbar(\Omega_{LG,D2}^2 + \Omega_{G,D2}^2)}{4\Delta_{D2}}, \tag{4.13}$$

$$R_{\text{sc}} = \Gamma \left(\sum_{D1} \frac{(\Omega_{LG,D1}^2 + \Omega_{G,D1}^2)}{4\Delta_{D1}^2} + \sum_{D2} \frac{(\Omega_{LG,D2}^2 + \Omega_{G,D2}^2)}{4\Delta_{D2}^2} \right), \tag{4.14}$$

$$\Omega_R = \sum_{D1} \frac{\Omega_{LG,D1}\Omega_{G,D1}}{2\Delta_{D1}} + \sum_{D2} \frac{\hbar\Omega_{LG,D2}\Omega_{G,D2}}{2\Delta_{D2}}, \tag{4.15}$$

where $\Omega_{i,j}$ is the Rabi frequency for the single beam $i = \{G, LG\}$ for the transition $j = \{D1, D2\}$, and $\sum_{D1}$ and $\sum_{D2}$ are sums over the excited states of the $D1$ and $D2$ transitions respectively. Here we have explicitly considered the $D1$ and $D2$ lines

separately as we will use a single-photon detuning comparable to the energy difference between the two transitions.

To calculate the Rabi frequency we sum over all allowed upper states in the two-photon $|1,1\rangle \rightarrow |1,0\rangle$ transfer, including both $D1$ and $D2$ transitions. The appropriate dipole matrix elements are found in [76] and lead to the expression

$$\Omega_R = \sqrt{\frac{I_{LG}I_G}{2}}\frac{2}{\hbar^2\epsilon_0 c}\left[\frac{|\langle J=1/2|\, e\mathbf{r}\,|J'=1/2\rangle|^2}{2\Delta_{D1}}\left(-\sqrt{\frac{1}{4}}\sqrt{\frac{1}{4}}+\sqrt{\frac{1}{12}}\sqrt{\frac{1}{12}}\right)\right.$$
$$\left.+\frac{|\langle J=1/2|\, e\mathbf{r}\,|J'=3/2\rangle|^2}{2\Delta_{D2}}\left(\sqrt{\frac{5}{24}}\sqrt{\frac{5}{24}}-\sqrt{\frac{1}{8}}\sqrt{\frac{1}{8}}\right)\right]. \quad (4.16)$$

Here we have included a factor of $\sqrt{1/2}$ as only half the LG polarisation is of the correct handedness, and we assume we are sufficiently detuned that we can neglect energy splittings within the hyperfine levels. We can simplify the expressions for the scattering rate and dipole potential by using the relation [76]

$$\langle J|\, e\mathbf{r}\,\big|J'\big\rangle \equiv \langle LSJ|\, e\mathbf{r}\,\big|L'S'J'\big\rangle$$
$$= \langle L|\, e\mathbf{r}\,\big|L'\big\rangle\,(-1)^{J'+L+1+S}\sqrt{(2'+1)(2L+1)}\begin{Bmatrix} L & L' & 1 \\ J' & J & S\end{Bmatrix}, \quad (4.17)$$

where the final term is a Wigner $6-j$ symbol. Using this we relate the two dipole matrix elements

$$\langle J=1/2|\, e\mathbf{r}\,\big|J'=1/2\big\rangle = \langle L=0|\, e\mathbf{r}\,|L=1\rangle \quad (4.18)$$
$$\langle J=1/2|\, e\mathbf{r}\,\big|J'=3/2\big\rangle = \sqrt{2}\,\langle L=0|\, e\mathbf{r}\,|L=1\rangle\,. \quad (4.19)$$

Making use of the relationship between linewidth and dipole matrix element

$$\Gamma = \frac{\omega_{D1}^3}{3\pi\epsilon_0\hbar c^3}|\mathbf{d}|^2, \quad (4.20)$$

where $\mathbf{d} = \langle L=0|\, e\mathbf{r}\,|L'=1\rangle$ is the matrix dipole element and ω_{D1} is the $D1$ transition frequency, we obtain the general expressions for the dipole potential and inelastic scattering rate [58]

$$U_{\rm dip}(\mathbf{r}) = \frac{\pi c^2\Gamma}{2\omega_{D1}^3}\left(\frac{2+Pg_Fm_F}{\Delta_{D2}}+\frac{1-Pg_Fm_F}{\Delta_{D1}}\right)I(\mathbf{r}) \quad (4.21)$$
$$R_{\rm sc}(\mathbf{r}) = \frac{\pi c^2\Gamma^2}{2\hbar\omega_{D1}^3}\left(\frac{2+Pg_Fm_F}{\Delta_{D2}^2}+\frac{1-Pg_Fm_F}{\Delta_{D1}^2}\right)I(\mathbf{r}), \quad (4.22)$$

where P characterise the laser polarisation ($P=0,\pm1$ for linearly and circularly $\sigma^\pm$ polarised light respectively). Our Gaussian light is π polarised ($P=0$) and the LG light is equal σ^+ and σ^- polarised, hence the dipole potential (4.13), scattering rate

(4.14), and Rabi frequency (4.15) for the Raman setup simplify to

$$U_{\rm dip}(\mathbf{r}) = \frac{\pi c^2 \Gamma}{2\omega_{D1}^3}\left(\frac{2}{\Delta_{D2}} + \frac{1}{\Delta_{D1}}\right)\left(I_{LG}(\mathbf{r}) + I_G(\mathbf{r})\right) \tag{4.23}$$

$$R_{\rm sc}(\mathbf{r}) = \frac{\pi c^2 \Gamma^2}{2\hbar\omega_{D1}^3}\left(\frac{2}{\Delta_{D2}^2} + \frac{1}{\Delta_{D1}^2}\right)\left(I_{LG}(\mathbf{r}) + I_G(\mathbf{r})\right) \tag{4.24}$$

$$\Omega_R(\mathbf{r}) = \frac{\pi c^2 \Gamma}{2\pi\hbar\omega_{D1}^3}\left(\frac{1}{\Delta_{D2}} - \frac{1}{\Delta_{D1}}\right)\sqrt{\frac{I_{LG}(\mathbf{r})I_G(\mathbf{r})}{2}}. \tag{4.25}$$

The Rabi frequency, dipole potential, and scattering rate are plotted in figure 4.15 as a function of Raman beam wavelength. Both the scattering rate and Rabi frequency scale as $1/\Delta^2$, hence to minimise heating and decoherence effects, we wish to detune far from single-photon resonance, so long as the laser power is still sufficient to drive the transition. The lower threshold for the Rabi frequency is limited by the field stability. As shown in (3.11), the BEC undergoes Rabi oscillations at an effective frequency which is dependent on the on-resonance Rabi frequency, Ω_R, and the detuning from resonance, δ. Therefore to accurately perform a π pulse, Ω_R must dominate fluctuations in the detuning. We empirically estimate our field fluctuations to be ≈ 300 Hz, and hence aim for a Rabi frequency of about 3-4 kHz.

The optimal configuration to maximise the Rabi frequency is to have equal intensities in the LG and Gaussian beams, however residual roughness in the LG beam profile demands that to maximise superflow stability we must use the minimum LG power required to create a multiply-connected geometry. This will also minimise the heating rate while the superflow persists in the ring trap, and hence maximise the BEC lifetime. The LG power required to produce a ring trap is only on the order of tens of μW, hence to achieve high Rabi frequencies we need the majority of the power in the Gaussian beam. To minimise the dipole effect produced during the π pulse when the Gaussian beam is flashed on, a large Gaussian beam waist of ≈ 100 μm is used to minimise the force from gradients in the dipole potential. Based on these criteria we chose a Raman wavelength of $\lambda = 804$ nm which produces a low scattering rate. The power in the LG beam is limited to tens of μW by the requirement of a smooth ring potential, and hence to compensate for the low Rabi frequency at this wavelength we use several hundred mW of power in the Gaussian beam.

We also note that due to interactions with both $D1$ and $D2$ lines, a special point exists at $\lambda = 790$ nm where the dipole potential vanishes, but the Rabi frequency remains large. This has potential applications for achieving strong Rabi coupling without modifying the trapping potential of the atoms.

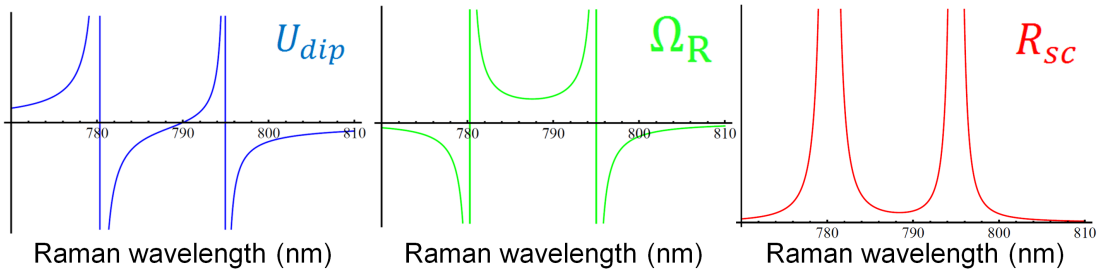

Figure 4.15: Effect of Raman beam wavelength on dipole potential, two-photon Rabi frequency, and inelastic scatting rate: The left plot illustrates the effect of Raman wavelength on dipole potential, which scales as $1/\Delta$ for large detuning. The middle plot shows the two-photon Rabi frequency and the right plot shows the inelastic scattering rate, both of which scale as $1/\Delta^2$ far from resonance.

4.3.3 Raman beam setup

We generate the two Raman laser beams using the setup illustrated in figure 4.16. The laser light is produced using a Ti:Sapphire laser[1] pumped with an 18 W green laser[2]. The Ti:Sapphire is a CW laser with tunable wavelength over the range 700 to 1030 nm, providing complete freedom in the wavelength of our Raman beams. Importantly the rms linewidth of the laser is < 75 kHz, equivalent to a coherence length of over 4 km. This ensures coherence between the two Raman beams regardless of their relative path difference. The large output power of the Ti:Sapphire of up to 4 W permits us to achieve high Rabi frequencies and compensates for significant losses within the dual-pass AOMs and fibre coupling.

We create our two Raman beams of orthogonal polarisation and relative frequency difference ω_{eg}, by passing the light through an 80 MHz AOM[3] and splitting it off a PBS cube into two beams of orthogonal polarisation with relative power controlled by a half-waveplate. We then shift the frequency of each of these beams using a dual-pass AOM[4] setup, with the Gaussian beam frequency shifted by 2×80 MHz and the LG beam frequency shifted by $2 \times (80\text{ MHz} - \omega_{eg}/2)$, thus matching the two-photon resonance condition. Using two dual-pass AOM setups allows us to vary the frequency of the Raman beams without altering the alignment into the fibre. To ensure phase coherence between the two beams we drive the two AOMs by function generators[5] connected in a phase-lock-loop configuration, where one acts as the master oscillator for the other. To provide precise control of the AOM switching times needed for π pulses, we use an RF switch[6] to control the signal to each AOM.

Power stabilisation of the two Raman beams is achieved by picking off weak reflec-

[1] Coherent Ti:Sapphire MBR-110
[2] Coherent Verdi V18
[3] Crystal Technology Inc. 3080-125
[4] Crystal Technology Inc. 3080-125
[5] Agilent 33250A
[6] Mini-Circuits ZYSWA-2-50-DR

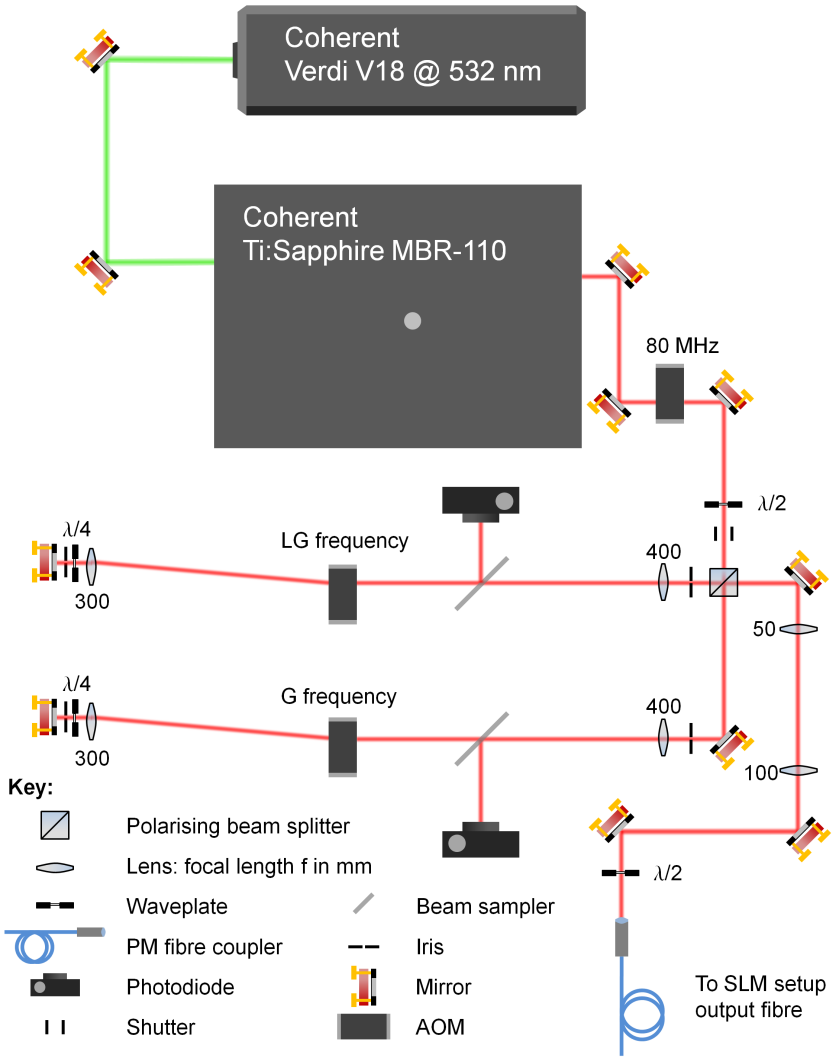

Figure 4.16: Overview of Raman laser system: The Raman laser light is generated by an optically pumped tuneable wavelength Ti:Sapphire laser capable of outputting up to 4 W of laser light. An AOM provides switching for both Raman beams and power stabilisation for the Gaussian beam. The relative power distribution between the LG and Gaussian arms is controlled by a half-waveplate before the first PBS cube. Both LG and Gaussian light then go through a dual-pass AOM, shifting the frequency of the Gaussian light by 2×80 MHz and that of the LG light by $2 \times (80\text{ MHz} - \omega_{eg}/2)$ to match the energy difference between the $|1,1\rangle$ and $|1,0\rangle$ states. Both arms include microscope slides which pick off weak reflections towards photodiodes used for PID-based power stabilisation. The frequency shifted Raman beams are then recombined on the PBS cube and are coupled into a polarisation-maintaining fibre. The output of this fibre is that shown in figure 4.7.

tions towards monitor photodiodes using microscope slides inserted in each beam path. The photodiodes provides a signal for a PID which alters the AOM efficiency to match the monitor signal to a reference signal provided by the control software. The same setup is used to stabilise the CDT (Section 3.7) and sheet beam (Section 4.2.1) powers. The LG beam power is stabilised by changing the LG frequency AOM efficiency while monitoring the light level after the dual-pass AOM. This cannot be done for the

Gaussian arm, as the G frequency AOM is only flashed on for a few 100 μs during the Raman π pulse which is too fast for the PID to respond to. We therefore only stabilise the power incoming to the Gaussian dual-pass AOM by altering the efficiency of the first AOM which is common to both Raman beams.

After passage through the dual-pass AOMs the two polarisations are then recombined on the PBS cube and coupled into a single-mode polarisation maintaining fibre[1]. To ensure the polarisations of the different frequency components remain orthogonal the input polarisation is aligned with the axis of the fibre using a half-waveplate. While we do observe some contamination of the polarisation for each frequency at the fibre exit, this is on the order of a couple percent and has no discernible effect on the Raman transfer.

The two Raman beams exit the fibre shown in figure 4.7. As described in Section 4.2.3 the LG beam with horizontal polarisation and frequency shifted $-\omega_{eg}$ with respect to the Gaussian beam is sent towards the SLM. The Gaussian beam with vertical polarisation and frequency shifted $+\omega_{eg}$ with respect to the LG beam is telescoped down $\approx 10:1$. This produces a small beam which focuses to a large beam at the atoms. This minimises the optical force exerted during the π pulse and helps ensure the Rabi frequency is equal at all points around the ring. The vertical imaging light is overlapped with the Gaussian beam on a $90:10$ glass sampler inserted in the Gaussian path, thus discarding 10% of the Gaussian light and 90% of the vertical imaging light.

4.3.4 Coherent Raman Rabi oscillations

To test the suitability of our Raman beams for performing coherent Rabi oscillations we first used two Gaussian beams in a modest field of 1.67 G, corresponding to a Zeeman splitting of 1.17 MHz. At this field the splitting between the $|1,1\rangle$, $|1,0\rangle$, and $|1,-1\rangle$ states are essentially equal and the Raman beams couple all three states. Our initial attempts at Rabi oscillations are illustrated by the plot in figure 4.17 (a), where we observed clear decoherence and the system quickly tended towards equal populations in all three states. The phase coherence between the Raman beams was checked by interfering the two Raman beams and observing phase stability well below 1 Hz.

The cause of the decoherence was indicated by the absorption image in figure 4.17 (b), which is an 18 ms TOF image of the Raman-coupled BEC without a Stern-Gerlach field applied. We observe two satellite lobes above and below the BEC, the position of which is not due to any magnetic gradient acting on different magnetic sublevels. The position of these lobes is consistent with atoms receiving a momentum impulse of $\pm 2\hbar k$ during the Raman coupling, hence the co-propagating Raman beams were able to Bragg scatter some fraction of the BEC. This is consistent with the Raman beams interacting with a weak counter-propagating reflection, enabling coupling to different momentum states. In addition we observed significant heating and atom loss when applying Raman

[1] Thorlabs P3-630PM-FC-10

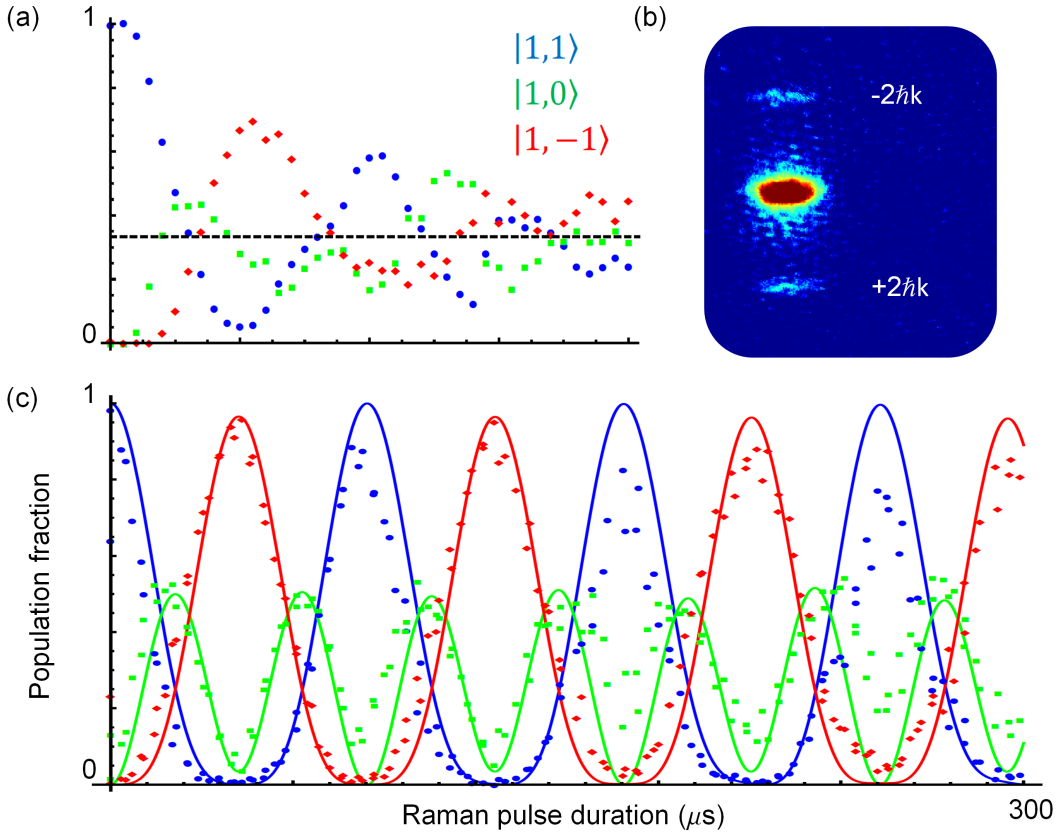

Figure 4.17: Plots of both incoherent and coherent Raman Rabi oscillations: (a) Strongly damped, incoherent, Raman Rabi oscillations are observed due to weak counter-propagating reflections coupling different momentum states. (b) 18 ms TOF horizontal absorption image of the BEC following Raman coupling. The position of the small clouds above and below the BEC are consistent with the momentum states $\pm 2\hbar k$. Such momentum states are due to Raman coupling from the Raman beams and weak counter-propagating reflections from the vertical imaging camera, and are absent if the camera path is blocked. (c) Coherent Raman Rabi oscillations with the vertical camera reflection blocked. The data is fitted to a three-state solution of the rate equations, from which we extract the two-photon Rabi frequency, $\Omega = 20$ kHz, and the two-photon detuning, $\delta = 1.8$ kHz.

coupling near resonance. The problem was solved by placing a shutter in front of the vertical imaging camera which was the main source of the reflection. A short-pass filter ($\lambda < 790$) nm was also placed in front of the camera to transmit imaging light but block Raman light which would otherwise saturate the camera.

The resultant Raman Rabi oscillations are shown in figure 4.17 (c). Without coupling to different momentum states we now observe coherent population transfer over multiple cycles. Fitting this data with the appropriate three state model, we find a Rabi frequency of ≈ 20 kHz and a two-photon detuning of ≈ 1.8 kHz. Similar coherent transfer is observed for our Gaussian and LG setup with lower Rabi frequency, permitting use of a coherent π pulse to impart angular momentum to the BEC.

4.4 Detecting angular momentum

Following our rotation procedure we transfer over 90% of the atoms to the $|1,0\rangle$ state, which flows around the ring trap with orbital angular momentum $\ell\hbar$ per atom. Fundamentally though, the atomic density observed is identical to the stationary case, and therefore measuring the angular momentum present can be challenging. This is especially true when considering the energy associated with the rotation is $E_r = (\ell\hbar)^2/(2mR^2)$, where m is the atomic mass, and R is the radius of the ring. For our typical trap parameters ($R = 12$ μm) this only corresponds to $E_r/h \approx 0.4\ell^2$ Hz.

Circulation in a BEC is usually detected by a kinematic method, where an absorption image is taken at long TOF and density dips are observed associated with vortices. The characteristic size of a vortex in trap is equal to the healing length, $\xi = \sqrt{1/8\pi na}$ as derived in (2.64), which is typically less than a μm, and hence cannot usually be resolved by an *in situ* image. By allowing the condensate to freely expand before imaging, the velocity associated with the azimuthal flow around a vortex core causes the hole to expand to a size above imaging resolution. The presence of a vortex in a condensate has also been detected by measuring the resultant precession in the axes of the quadrupole mode in the direction of the circulating vortex flow. The circulating velocity breaks time-reversal symmetry and splits the two otherwise degenerate modes which contribute to quadrupole oscillations. The magnitude of the splitting is dependent on the angular momentum present in the system and can be directly inferred from the rate of precession of the mode [38]. The phase winding present in a rotating condensate has also been directly observed using matter-wave interference [30, 33].

Here we detect the circulation present in our ring BEC by both a matter-wave interference method, and by observing the formation of density dips at long TOF. Due to the necessity of a non-rotating, reference state for the interferometric method, the quantitative studies on persistent currents presented in Chapters 5 and 6 exclusively use the kinematic detection method.

4.4.1 Matter-wave interference

The procedure for converting the phase winding to a density modulation by matter-wave interference is shown in figure 4.18 (a). The initially stationary ring BEC in the $|1,1\rangle$ state is coherently transferred to an equal superposition of the rotating $|1,0\rangle$ and stationary $|1,1\rangle$ states by a Raman $\pi/2$ pulse. A subsequent RF $\pi/2$ pulse mixes the two states, creating an equal superposition of stationary and rotating atoms in each spin state. The resultant interference creates a density modulation, with the number of interference peaks equal to ℓ. Imaging just one of the spin states using a microwave transfer to the $F = 2$ state, we obtain the absorption images shown in figure 4.18 (b), confirming the phase imprinted by the LG plus G Raman transfer. The density modulations of the two spin states are π out of phase, hence imaging the total density

of both states by repumping to the $F = 2$ state, we only observe the initial smooth density profile.

We can quantitatively explain this procedure by describing the BEC in a coherent superposition of internal states 1 and 2, labeled by the two-component vector

$$\bar{\Psi}(\theta) = \begin{pmatrix} \Psi_1(\theta) \\ \Psi_2(\theta) \end{pmatrix}, \tag{4.26}$$

which for our initial state is

$$\bar{\Psi}_0(\theta) = \frac{1}{\sqrt{2\pi}} \begin{pmatrix} 1 \\ 0 \end{pmatrix}. \tag{4.27}$$

We can then define the Raman $\pi/2$ and RF $\pi/2$ operations by the matrix operators

$$U_{(\mathrm{Raman}),\pi/2} = \frac{1}{\sqrt{2}} \begin{pmatrix} 1 & e^{-\ell\theta} \\ e^{-i\ell\theta} & -1 \end{pmatrix}, \quad \text{and} \quad U_{(\mathrm{RF}),\pi/2} = \frac{1}{\sqrt{2}} \begin{pmatrix} 1 & 1 \\ 1 & -1 \end{pmatrix} \tag{4.28}$$

respectively. With this notation the final state of our interference protocol is

$$\bar{\Psi}(\theta) = U_{(\mathrm{RF}),\pi/2} U_{(\mathrm{Raman}),\pi/2} \bar{\Psi}_0(\theta) \tag{4.29}$$

$$= \frac{1}{2\sqrt{2\pi}} \begin{pmatrix} 1 + e^{-i\ell\theta} \\ 1 - e^{-i\ell\theta} \end{pmatrix}. \tag{4.30}$$

The final density distributions of the two spin states are then given by

$$n_1(\theta) = |\Psi_1(\theta)|^2 = \frac{1}{2\pi} \sin^2(\ell\theta/2) \tag{4.31}$$

$$n_2(\theta) = |\Psi_2(\theta)|^2 = \frac{1}{2\pi} \cos^2(\ell\theta/2), \tag{4.32}$$

in agreement with our experimental findings. In principle one can include a delay between the Raman and RF pulses. The number of density fringes is then a measure of the circulation which persists beyond the delay time, and the observed precession of the fringes is sensitive to rotation of the frame of reference, acting as a Sagnac interferometer. In reality we observe a rapid degradation of the interference pattern for delays longer than 50 ms due to the presence of two effectively counter-rotating spin states. This is true even with the inclusion of an "echo" RF π pulse at half the delay time, which swaps the spin states and should negate the accumulated relative phase between the two states[1]. This is in contrast to the calculations of [111] where the fringe pattern is predicted to be stable due to the relatively close inter and intra-state scattering lengths. The effect of having two spin states in the ring is discussed further in Chapters 6 and 7.

[1]Exact cancelation of the accumulated phase is only expected in the single mode approximation where only the zero energy mode contributes [148]

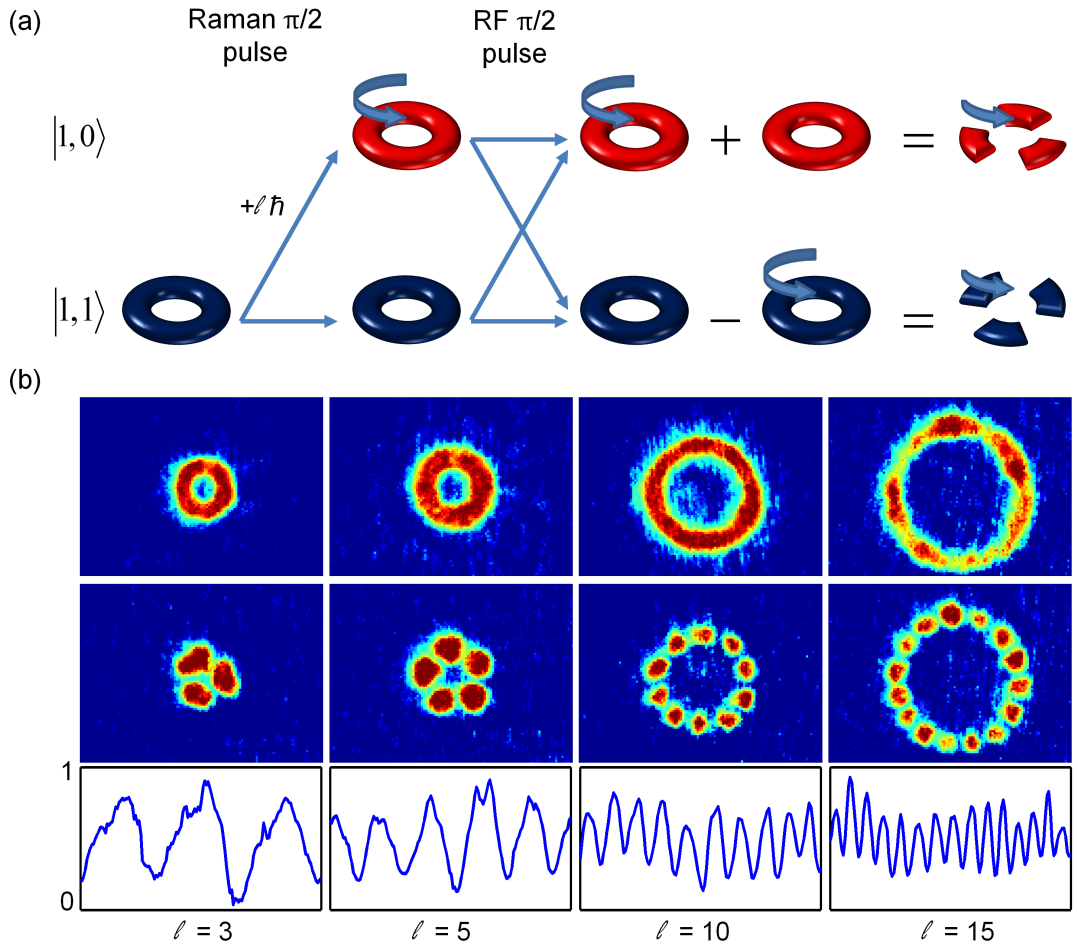

Figure 4.18: Interferometric detection of the imprinted phase winding: (a) Interference protocol for interfering a rotating BEC with a stationary BEC. A Raman $\pi/2$ pulse coherently transfers only half the population into the rotating $|1,0\rangle$ state. A subsequent $\pi/2$ RF pulse, which carries no angular momentum, mixes the states so that in each spin state we get an interference of rotating and non-rotating atoms. This matter-wave interference converts the phase winding into a density modulation in each spin state, with the number of density peaks equal to ℓ. (b) Absorption images of the original ring density profile and the resultant pattern in the $|1,1\rangle$ state following the interference protocol for $\ell = 3, 5, 10$, and 15. Bottom plots show the atom density of the interference fringes as a function of the azimuthal coordinate, normalised to the original atom density.

4.4.2 Kinematic detection in time-of-flight

As discussed in Section 2.4.3, the flow velocity about a vortex scales as $1/r$ and hence is associated with an angular momentum barrier, $\hbar^2\ell^2/2mr^2$, leading to a density singularity along the vortex core. Due to the mean-field energy of the cloud in trap, the atoms can climb this $1/r^2$ potential and acquire kinetic energy as tangential flow velocity. When the BEC is released in TOF the mean-field energy is given up to ballistic expansion, however the angular momentum barrier due to circulation persists and causes the density dip due to the vortex core to expand and become resolvable. Numerical simulations of such expansion from a rotating annular BEC are done in [149],

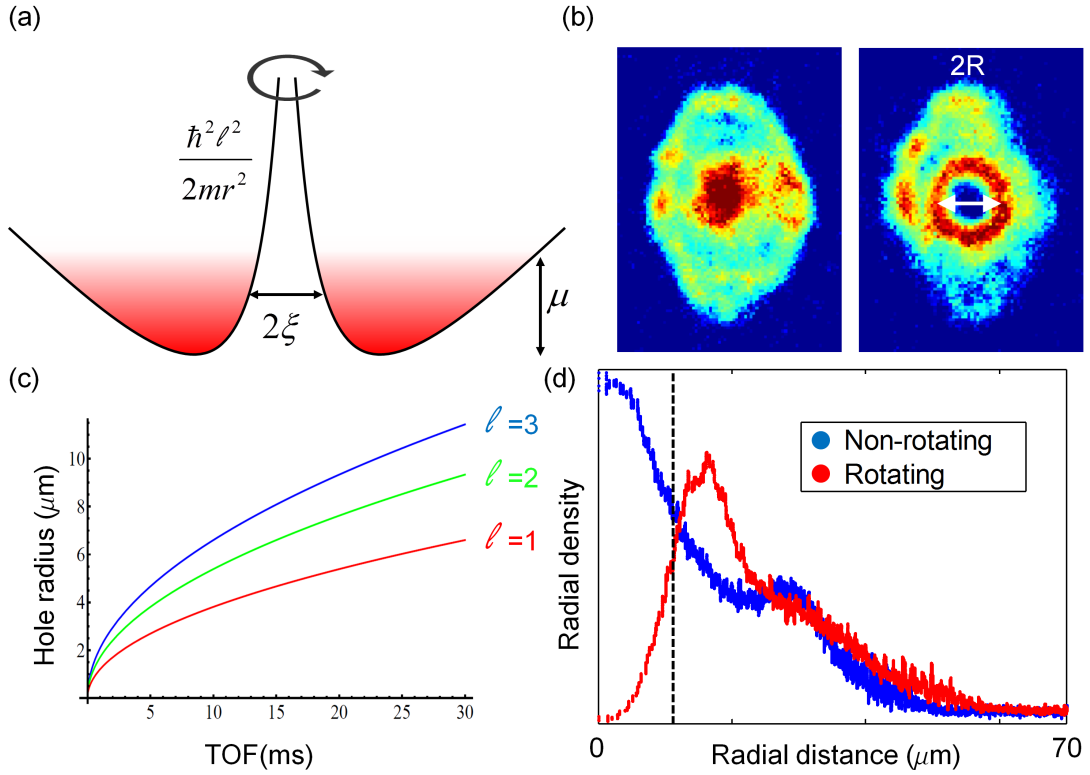

Figure 4.19: Kinematic detection of circulation in TOF expansion: (a) By ramping down the LG beam and transforming to the simply connected sheet trap, the BEC pushes up against the angular momentum barrier. The size of the vortex hole, ξ, is set by equating the interaction energy, given by μ, and the kinetic energy associated with rotation, given by $\hbar^2\ell^2/2mr^2$. Removing the trapping potential causes atoms to move away from the angular momentum barrier and a central hole to form in TOF, the size of which depends on ℓ. (b) Top view absorption images of non-rotating (left) and $\ell = 3$ rotating (right) BECs after 29 ms TOF expansion from the reconnected trap in (a). We use the fitted radius, R, to quantify the rotation of the cloud. (c) Calculation of central density hole radius versus TOF for the circulation states $\ell = 3$ (blue), $\ell = 2$ (green), and $\ell = 1$ (red). This calculation assumes ballistic expansion of the cloud and calculates the minimal radius at which the density is non-zero. (d) Azimuthally averaged radial density profiles of the images in (b) for both the rotating (red) and non-rotating (blue) clouds. This illustrates the sharp density cutoff due to rotation, which is in reasonable agreement with the cutoff predicted by our simple calculation, $R_{\ell=3}$, indicated by the dashed black line.

where the size of the hole formed in TOF is shown to be dependent on ℓ, and hence can be used to detect the rotational state of the condensate in the trap.

In our ring trap the atoms are held far from the axis of rotation by the ring trapping potential and hence have a low azimuthal flow velocity. For our typical parameters of ring radius $r_M = 12$ μm, and circulation $\ell = 3$, the flow velocity is $v_s = \ell\hbar/mr_M \approx 0.18$ mm/s. When the atoms are released from the ring trap, the interaction energy is converted to kinetic energy and the atoms expand in all directions, including inwards towards the axis of rotation. The initial radial velocity dominates over the initial tangential velocity associated with any rotation present, allowing atoms to approach very close to the vortex core. While the density singularity at the centre never vanishes, this

method requires very long TOF before the density dip due to rotation is observable.

In order to resolve the density hole from rotation we find it necessary to first gradually remove the LG beam and transform the trap into a simply-connected geometry formed by the sheet trap alone. This has the advantage of bringing atoms close to the axis of rotation and increasing the azimuthal flow velocity. It also reduces the mean field energy, reducing the expansion velocity upon release, and since the vertical confinement now dominates over the horizontal confinement, the mean field energy is predominantly released in the vertical direction. The LG beam is ramped off slowly over about 100 ms, before the sheet beam is turned off a few ms later. As discussed in Section 4.5, once the ring trap is removed the rotating state is no longer protected and eventually decays. To gain an accurate measure of the angular momentum, the BEC is only briefly held in this reconnected trap before the vortices have a chance to break apart to lower-angular momentum states. The BEC is then imaged at 29 ms TOF along the axis of rotation. Figure 4.19 (b) shows a typical absorption image of a non-rotating BEC, and a BEC transferred to the rotating state using $\ell = 3$. The non-rotating BEC has a density maximum at the centre as expected, whereas the rotating BEC exhibits a central density hole. We fit the high density ring surrounding this hole to an ellipse, and quantify the rotation of the cloud by the geometric mean of the major and minor axes, R. The circular symmetry of the density ring in TOF is found to be strongly dependent on the alignment of the ring trap with the sheet trap. We therefore align the LG beam with the sheet trap minimum looking at the density ring in TOF, with the aim of having circularly symmetric density.

Figure 4.19 (a) illustrates a BEC held in the reconnected sheet trap with a centrifugal barrier at the origin due to rotation with ℓ units of circulation. We can obtain a reasonable estimate of the radius of the density hole due to rotation at long TOF by considering the expansion as ballistic, and neglecting the effect of interactions during TOF. To first order this is correct since the vertical trapping frequency in the sheet dominates over that in the plane, and therefore nearly all the mean field energy quickly goes into the vertical expansion of the cloud. Equating the force due to the potential gradient and the radial acceleration, we obtain the equation of motion for atoms at position r

$$\frac{d^2r(t)}{dt^2} = \frac{\hbar^2\ell^2}{m^2r^3(t)}. \tag{4.33}$$

Solving this for the initial conditions, $r(t = 0) = r_0$ and $dr(t)/dt = 0$ gives

$$r^2(t) = r_0^2 + \frac{\hbar^2\ell^2}{m^2r_0^2}t^2. \tag{4.34}$$

To illustrate the density profile we might expect to evolve during TOF we consider the trajectory of the point in the trap, r^*, which travels the shortest distance from the axis

of rotation during time-of-flight, t. This if found by solving $dr(t)/dr_0 = 0$:

$$r^* = \left(\frac{\hbar^2 \ell^2 t^2}{m^2}\right)^{1/4}. \tag{4.35}$$

In our simple picture, atoms located at r^* in the trap end up closest to the axis of rotation in TOF, with all other positions in-trap travelling further from the origin. Using our expression for r^* as the starting point r_0 in equation (4.34), we obtain the radius, $R_\ell(t) = \sqrt{2}r^*$, of the density hole in TOF within which the density is zero due to rotation. We therefore find that the area of the hole formed in TOF is proportional to the angular momentum state of the atoms, $R(\ell)^2 \propto \ell$. The radius $R(\ell)$ is plotted as a function of t for the circulation states $\ell = 3, 2$ and 1 in figure 4.19 (c). From this we anticipate that at 29 ms TOF the zero-density hole will have a radius 6.5 μm, 9.2 μm, and 11.2 μm for the circulation states $\ell = 1, 2$, and 3 respectively. Calculating the ballistic expansion of the initial Thomas-Fermi density for a BEC in the sheet plus centrifugal barrier potential shown in figure 4.19 (a), we find that the density in TOF monotonically increases with decreasing radius, until reaching the cutoff value $R_\ell(t)$.

In figure 4.19 (d) the azimuthally averaged radial density profiles of the rotating and non-rotating clouds at 29 ms TOF are shown. The black dashed line indicates our calculated density cutoff, $R_{\ell=3} = 11.2$ μm, which is in surprisingly close agreement with the inflection point of the profile. Due to the effect of interactions during TOF which we neglected, this cutoff is rounded off and the peak density is actually shifted to a slightly larger radius than R_ℓ. The size of this discrepancy is empirically found to be a function of atom number, with the value of the peak radius for a given circulation state decreasing with atom loss, and tending towards values in agreement with R_ℓ.

4.5 Vortex dynamics in a connected geometry

In the next chapter we unequivocally show that superflow in a ring shaped BEC is fundamentally stable and protected from decay due to the trapping geometry. We first conclude this chapter with a brief discussion of vortex dynamics and decay in a simply-connected BEC. Vortices are excited states of motion and therefore energetically unstable towards relaxation to the ground state where the condensate is at rest. However, as discussed in Section 2.4.3, quantisation of circulation constrains the decay, and a vortex in a BEC cannot simply fade away by continuously dissipating its energy. As calculated in equation (2.97) the energy of a multiply charged vortex scales as the square of the circulation, and therefore it is energetically preferable for a vortex of charge q to break up into q singly charged vortices. It has been shown both numerically [150] and experimentally [89] that multiply charged vortices in a harmonic potential are not energetically stable. Multiply quantised vortices are found to decay into singly quantised vortices and transfer their kinetic energy to excitation modes. Such insta-

bility is referred to as dynamic instability and is driven by atomic interactions even at zero temperature, and is different from dissipation due to interactions with the thermal component [151]. The timescales of such dynamic instabilities is fairly short, quickly establishing the large vortex lattices observed in [31, 32].

Such multiply charged vortices can become stable under sufficient rotation of the system [152] or by the presence of localised pinning potentials [90]. For pinning locations of sufficient size, the energy reduction of localising several vortices at the density dip and creating a 'giant' vortex state can outweigh the cost of having multiple circulation. Such multiply quantised vortices have been observed at pinning sites in superconducting systems [153] and BECs [91]. Equivalently, the large density hole we measure in TOF in figure 4.19 (b) is essentially a multiply quantised vortex which forms due to the pinning potential of our ring trap, where the vortices are pinned inside the ring trap where the density vanishes. In [154], giant vortex states are prepared by applying a blue-detuned laser to a vortex aggregate of many singly charged vortices which pins many vortices creating a giant vortex core of up to 60 phase singularities. Other proposals for the formation of stable multiply charged vortices involve rapid rotation of a BEC in a high power-law trap [150, 152].

A singly charged vortex is dynamically stable and therefore the vortex state can only decay by annihilation with another vortex of opposite circulation or in the presence of dissipative processes. At finite temperatures the vortex scatters from thermal excitations, transferring energy from the vortex to the thermal cloud causing the vortex to spiral outwards towards the border of the condensate where it then decays to elementary excitations [155]. There have been several experimental studies on vortex dynamics, including single vortices [156], small clusters of co-rotating vortices [89, 157, 158], and vortex dipoles [141] which are of particular interest for understanding the Berezinskii-Kosterlitz-Thouless (BKT) transition [159].

In figure 4.20 we present our observations of the decay of a multiply charged vortex held in a reconnected trap with initial charge $q = 5$ and $q = 3$ for (a) and (b) respectively. We first prepare superflow in the ring trap using the rotation procedure explained in Section 4.3.1, using LG beams of different azimuthal modes $\ell = 5$ and $\ell = 3$ for the two sequences. The LG beam is then ramped down over 3 seconds and the BEC is held in the simply connected sheet trap only. In the ring trap, motion of vortices through the BEC has an associated energy cost, hence the circulating state is metastable and does not decay. Once the ring trap is removed this protection is also removed and the lowest energy configuration is for the vortices to redistribute themselves within the BEC. For both sequences the initial multiply quantised vortex of charge $q = \ell$ takes about 5 seconds to break up into ℓ singly charged vortices, after which these vortices move to the BEC edge and decay over the following 10 seconds or so. The dynamics timescale for vortices to break apart and the dissipative timescale we observe for vortices to decay are both quite long compared to those reported in

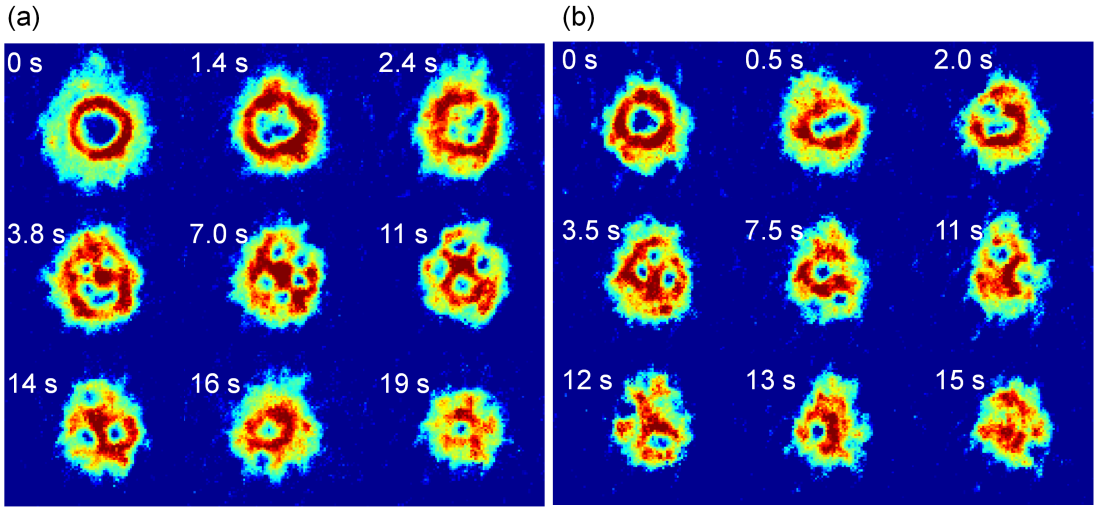

Figure 4.20: Vortex dynamics in reconnected sheet trap: For both sequences we prepare superflow in the ring trap with ℓ units of circulation, where $\ell = 5$ and $\ell = 3$ for (a) and (b) respectively. The LG beam power is then immediately ramped down over 3 seconds and the rotating BEC is held in just the sheet trap for a variable time before we absorption image at 29 ms TOF. (a) The giant vortex with charge $q = 5$ persists for a couple seconds but quickly distorts in shape. Within 7 seconds the giant vortex has completely broken up into 5 singly charged vortices. Over the next 10 seconds the vortices gradually migrate to the cloud edge and dissipate due to interactions with the residual thermal atoms. The final single vortex is found to typically persist for over 20 seconds. (b) The same sequence is repeatedly for a giant vortex with initial charge $q = 3$. The dynamics and decay in this case occur in a similar fashion and timescale to that observed for the $q = 5$ vortex.

[89, 158]. Several of the images exhibit pleasing symmetry which we could interpret as the formation of stable vortex structures as reported elsewhere [157, 158], however this would require further statistics or real-time imaging as done in [156] to confirm.

For both cases we observe images where the giant vortex has broken up into singly charged vortices, the number of which equals the initial circulation of the BEC, ℓ. Apart from being a quasi-random process, this is not a true measure of the angular momentum state, L, of the BEC like the kinematic detection method in Section 4.4.2. As explained in equation (2.96), L for a cylindrically symmetric BEC containing a vortex is only equal to $\hbar$ per atom if the vortex is on the axis of symmetry. If the vortex moves towards the BEC edge, although the circulation is still quantised, L decreases and is dependent on the vortex position. Both the number of vortices and their position are dependent on L, so simply counting phase singularities in TOF cannot unambiguously tell us the angular momentum state of the BEC in the ring.

4.6 Conclusion

This chapter has outlined the experimental implementation of our ring trap, and the procedure we use for both preparing and detecting angular momentum states. Particular care has been taken to explain the aspects of the experiment we found integral to

preparing a state of well defined and known circulation. This forms the backbone for our studies on persistent currents, in which we always infer any decay events by assuming the initial state of the BEC. We have provided a brief overview of ring traps and their uses in ultracold gases, and have illustrated their significance to the preservation of persistent currents by observing vortex dynamics and decay in a simply connected trap. In the following chapters the ring trap is kept on and the methodology explained above is used to prepare persistent currents and study their stability.

Chapter 5

Quantised decay of persistent currents

Having discussed how we prepare a persistent current of well defined initial angular momentum in Chapter 4, in this chapter we study the stability and decay of such superflow. To clarify our discussion we introduce the parameter q, where the phase of the BEC wave function, $\Phi(\mathbf{r})$, winds around the ring an integer multiple, q, times 2π:

$$\Phi(r, \theta, z) = \Phi(r, z)e^{iq\theta}, \tag{5.1}$$

where we assume azimuthal symmetry of the condensate density. This is to distinguish q from ℓ, the phase winding of the LG beam which forms our ring trap, and which is initially imprinted on the condensate wavefunction. Hence at $t = 0$ the phase winding of the condensate and LG beam are equivalent, $q = \ell$, but as the superflow decays q will decrease, and it is this evolution which we study.

The physical origin of supercurrent metastability is qualitatively illustrated in figure 5.1 (a). For N atoms held in a ring trap, the angular momentum for any atom is quantised, however the average angular momentum per particle in general need not be. For a superfluid gas, the presence of the condensate means that such quantisation is energetically preferred, and hence we can map the rotational state of a ring shaped superfluid onto the parabolic washboard landscape in figure 5.1 (a) which depicts the energy E of the superfluid system for different fixed values of the total angular momentum L[1]. The local minima of E correspond to topologically distinct metastable states with $L/N = q\hbar$. A direct $\Delta q = 1$ transition between two such minima involves a discontinuous 2π phase slip in the condensate wave function, occurring when a singly charged vortex crosses the annulus. The energy barrier between two adjacent minima corresponds to the barrier felt from a vortex core when trying to move toward a region of higher density, arising from the nonlinearity of the GPE.

The origin of such metastable energy minima at integer q can be demonstrated using a simple toy model presented in [13]. Here we consider a weakly interacting Bose gas at $T = 0$ trapped in a narrow annulus with thickness much smaller than its radius R. If we only considers occupation of the non-rotating state $|0\rangle$, and the state with angular momentum $\hbar$ per particle, $|1\rangle$, the energy of this system has the familiar Noziéres

[1] At nonzero temperature the same picture holds but with E replaced by the free energy.

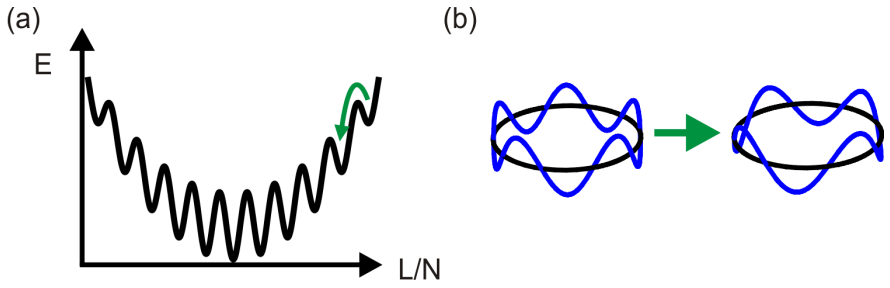

Figure 5.1: Origin of metastability and decay of supercurrents: (a) Energy landscape of a ring-shaped superfluid. Local minima correspond to metastable states with quantised angular momentum per particle, $L/N = q\hbar$. Energy barriers correspond to placement of a vortex within the superfluid, reducing the total angular momentum and modifying the condensate wavefunction. (b) Decay between the discrete q states involves a vortex-mediated phase slip, illustrated here for $q = 5 \to 4$.

form [12]

$$E = \frac{\hbar^2 N_1}{2mR^2} + \frac{g}{2V}(N_0^2 + N_1^2 + 4N_0N_1), \tag{5.2}$$

where V is the system volume, R is the radius of the ring trap, g is the strength of contact interactions (2.32), and N_0 and N_1 are the number of particles in the $|0\rangle$ and $|1\rangle$ states respectively. Hence in general, fragmentation of the condensate is energetically inhibited due to interactions, leading to energy minima at quantised angular momenta for $N_1 = N$ and $N_0 = N$, similar to that shown in figure 5.1 (a). For suitably weak interactions the energy minimum at $N = N_1$ disappears and the system cannot support persistent currents, as was shown in [160, 161]. The criteria for stability of $q = 1$ supercurrents is then simply given by

$$\left.\frac{\partial E}{\partial N_1}\right|_{N_1=N} < 0 \tag{5.3}$$

$$\frac{\hbar^2}{2mR^2} < \frac{gN}{V} \tag{5.4}$$

$$v_s < \sqrt{\frac{2gN}{mV}}, \tag{5.5}$$

where we have used the form of the superflow velocity $v_s = \hbar/mR$. From the expression for the sound speed in a uniform system (2.62) $c = \sqrt{gN/mV}$, we see, apart from a factor of $\sqrt{2}$, this takes the familiar form of the Landau criterion with a critical velocity set by the speed of sound, $v_s < c$. Such a simple calculation captures the behaviour of our system surprisingly well, but we note that even at zero temperature, due to interactions one should really consider the population of many higher angular momentum rotation states.

More generally, a superfluid can, in principle, also shed angular momentum in ways that break the L/N quantisation. Such a proposed decay mechanism is the formation of grey solitons which allow a continuous change in angular momentum [162]. Another

way is condensate fragmentation, where the BEC splits into two or more condensates with differing angular momenta per particle, however such a mechanism is expected to be suppressed due to the factor of 2 in the interaction energy arising for distinguishable particles. The dominant superflow decay mechanism depends on the system's geometry, temperature, and the strength of interactions. Associated with this decay mechanism is a critical velocity, v_c, where for flow speeds $v_s > v_c$, the superflow is unstable in the thermodynamic sense and decay occurs inevitably and on the millisecond scale. In contrast for $v_s \ll v_c$ the decay is strongly suppressed and the metastable superflow can be almost perfectly stable, as for example observed in bulk superconductors. In between these two extremes, metastable superflow should persist for much longer than the characteristic microscopic time scale of the physical system, but rare stochastic decay events can still occur through quantum or thermal fluctuations [82–84].

In this chapter we study the supercurrent decay of condensates initially prepared in the $q = \ell = 3$ state. We observe $q = 3$ superflow persisting for up to a minute in a multiply-connected trap (Section 5.3) and explicitly show that the supercurrent is indeed quantised (Section 5.2). The persistent current therefore decays in a cascade of quantised decay steps which unambiguously confirms that 2π phase slips are the supercurrent decay mechanism. We find that the critical velocities for different q states quantitatively agree with numerical simulations (Section 5.5). Our ability to resolve quantised rotational states opens the possibility to study the dynamics of phase slips, allowing us to observe both rapid $q \to q - 1$ decay events for $v_s(q) \geq v_c(q)$, and stochastic phase slips for $v_s < v_c$ (Section 5.6).

5.1 Previous studies on supercurrents

The persistent current in our condensate is analogous to electrical current flowing without resistance in superconductors, and dissipationless flow of superfluid ^{4}He in a toroidal container. The stability and decay of supercurrents have long been studied in ^{4}He superfluids and thin-wire superconductors, and as yet are still not fully understood. Much of the difficulty stems from the existence of several breakdown mechanisms, the relative importance of which depends strongly on the system parameters. In superfluid helium experiments in a toroidal geometry, the critical velocities observed in practise were often significantly less than the Landau value [163]. It is suspected however, that in most cases this was due to the presence of a tangle of vortices which formed during the quench through the BEC transition. For superfluid ^{4}He flow through small orifices, Anderson predicted that dissipation can occur when a quantised vortex passes across the orifice [26]. If the vortex crosses all the flow lines passing through the orifice, the quantum phase difference across the hole changes by 2π. Such phase slips have since been observed in several experiments [27, 88, 164]. One therefore anticipates the onset of such phase slips is given by the Feynman critical velocity, v_c^F, (2.103) derived in Sec-

tion 2.4.3, which gives the velocity above which vortex rings can enter the flow channel. However, v_c^F neglects the nucleation mechanism and subsequent trajectory of such vortex rings and cannot give quantitative agreement with experimental observations [27]. In addition, experimental studies of critical velocities for phase slips in narrow channels for high flow velocity [27, 88, 164] also show a temperature dependence which cannot be explained by the Feynman criteria. In this regime the normal component is negligible, and therefore it is proposed that the dependence arises due to the energy barrier for nucleating vortices. Hence as the temperature decreases the effective critical velocity at which decay occurs is observed to increase as the rate at which vortices are thermally nucleated decreases. Below about 200mK the observed critical velocity becomes almost temperature independent, and quantum tunneling dominates the phase-slip nucleation process [88]. The fundamental theoretical challenge is then understanding the nucleation process, and as yet no theory connects all these observations [165–167].

Phase slips in the superconducting order-parameter have been shown to cause residual electrical resistance in superconducting nanowires [84, 85]. In analogy to superfluid ^{4}He, at higher temperatures phase slips between current-carrying states occur though the process of thermal barrier-crossing by the order-parameter field [81], whereas at low temperatures quantum phase slips occur by topological quantum fluctuations of the superconducting order-parameter field [84]. Such superconducting nanowires have important applications for realising qubits [168], and the use of coherent quantum phase slips to build a current standard has been proposed in [169].

Persistent currents in annular BECs clearly offer a complementary route to further understanding these experiments on superfluid ^{4}He and superconducting nanowires. In contrast to liquid helium, since BECs are dilute and relatively weakly interacting, they are often described very well by the mean-field GPE which provides a reliable theoretical model for studying the instability mechanisms and dynamics. Prior to this work, the only realisation of supercurrents in a BEC was achieved in [99, 100], where $q = 1$ superflow persisting for up to 40 s was observed, and studies of flow through a weak link created by a potential barrier revealed a well defined superflow critical velocity v_c. The observed v_c was found to be consistent with the Feynamn estimate v_c^F, from which it was suggested that the dominant supercurrent decay mechanism was a vortex-induced phase slip, analogous to decay in superconducting and liquid ^{4}He experiments.

Our work extends these studies to multiply charged superflow ($q > 1$). This allows us to prove supercurrent quantisation, and from this, we unambiguously confirm phase slips as the decay mechanism, independent of any calculations. We calculate the flow velocity at decay and show it to be consistent with the order of magnitude Feynman estimate. Further to this, by explicit calculation of the excitation spectrum of the ring BEC we find quantitative agreement with a different critical velocity, which more accurately predicts the decay in our system. These calculations suggest decay by formation of vortex-antivortex pairs due to phonon-like excitations. Our use of $q > 1$ superflow

also opens the possibility to study dynamics and correlations between phase slip events.

5.2 Supercurrent quantization

To demonstrate the quantised nature of the supercurrent decay we initially prepare the system in the $q = 3$ rotational state using the protocol explained in Chapter 4. Following the transfer of orbital angular momentum to the BEC, we then increase the power of the LG beam by a factor of 2.4 over 3 seconds to ≈ 200 μW. From this point we then hold for various times and then release the cloud and absorption-image it after 29 ms of TOF. We detect the angular momentum state of the condensate by fitting the radius of the density ring, R, due to rotation, as explained in Section 4.4.2. The purpose of increasing the ring power is to increase the significance of the residual azimuthal roughness due to imperfections in the profile of our LG beam. The potential barriers due to roughness will scale linearly with LG intensity, I_{LG}, whereas the chemical potential, μ, only scales as ${I_{LG}}^{1/4}$ through the radial trapping frequency, hence the superflow stability decreases with increasing LG power. This has the advantage of significantly reducing the supercurrent lifetime to below the atom number decay time. As discussed in Section 4.4.2, the fitted hole radius in TOF, R, has a weak dependence on atom number, N, so increasing the ring power minimises this effect, providing us with the cleanest signal in which to observe the quantised nature of the supercurrent.

In figure 5.2 (b) we plot the evolution of the radius R with time after the superfluid was set into rotation. The quantisation of R, and therefore of the angular momentum of the condensate, is strikingly obvious, and we can assign a q state to each individual image with high fidelity. To further illustrate the quantised nature of the superflow, in figure 5.2 (c) we plot a histogram of R values, from which we clearly identify three separate peaks corresponding to the three states of $q = 3$, $q = 2$, and $q = 1$. The shaded colour backgrounds indicate our q-value assignments, matching the data-point colours in the scatter plot. Sample absorption images of the four allowed rotation states are shown in figure 5.2 (a), illustrating that the quantisation of supercurrent states is sufficiently evident as to allow the q states of individual images to be called by eye. We also mention that we find such quantisation in several thousand other images taken under different experimental conditions.

We consider the quantisation of the supercurrent decay the primary experimental evidence for vortex-induced phase slips as the decay mechanism. Condensate fragmentation or collective excitations such as solitons would break the quantisation of R [162], while individual particles which break away from the superflow would gradually fill up the hole in the centre of the expanding cloud; we see no clear evidence of this occurring. Observation of quantised decay events is also used as experimental proof of phase slips in liquid helium experiments [27, 88, 164], and benefits from not relying on any critical velocity calculations.

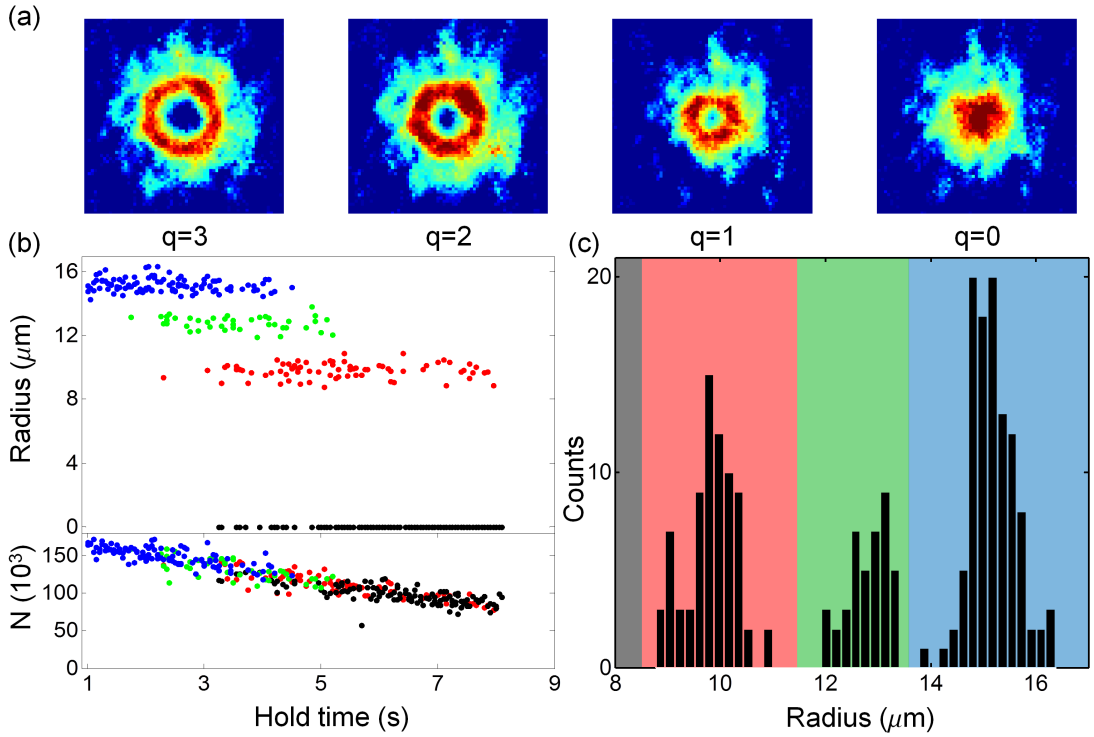

Figure 5.2: Quantised superflow decay: A superfluid prepared in the $q = 3$ state is held in a ring trap of depth $V_r \approx 4\mu$. (a) TOF absorption images of the respective $q = 3, 2, 1,$ and 0 states. (b) Top panel: radius R as a function of hold time t. The R values fall into 4 distinct bands corresponding to (top to bottom) $q = 3$ (blue), 2 (green), 1 (red), and 0 (black). Bottom panel: atom number, N versus t for the same data set. (c) High-contrast histogram of the measured R values confirms that we can assign a q value to each individual image with near-unity fidelity. The shaded backgrounds indicate our q-value assignments.

The initial $q = 3$ state is observed to be fundamentally stable for approximately 2 seconds, corresponding to ≈ 5 complete revolutions of the condensate. In Section 5.3, by using a low power LG beam, we show that this metastable state can be extended to over a minute. We therefore conclude that the decay of the supercurrent is brought about by the gradual decay of N plotted in the bottom panel of figure 5.2 (b). This is discussed further in Section 5.5 as the gradual loss of atoms bringing about the condition $v_s > v_c$. The broad $q = 2$ and $q = 1$ plateaus in figure 5.2 (b) show that the intermediate $0 < q < \ell$ states are metastable even after the supercurrent decay is initiated by the first phase slip. In the analogy with a particle moving in a washboard potential as in figure 5.1 (a), this corresponds to a strongly damped motion: when the system escapes from a local energy minimum, it gets trapped in a new local minimum rather than rapidly decaying to the $q = 0$ ground state.

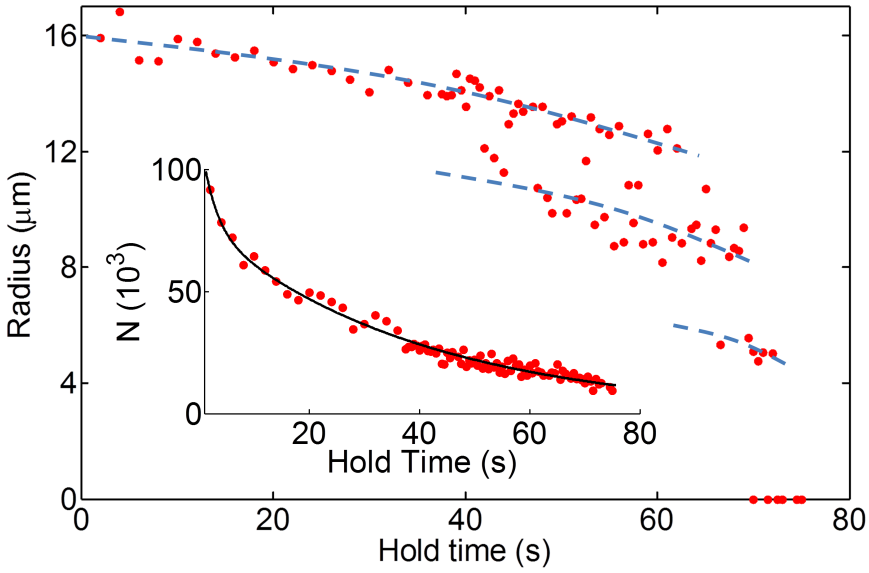

Figure 5.3: Long-lived $q = 3$ superflow: R is plotted as a function of hold time in a shallow ring trap, showing persistent current for longer than a minute. The blue dashed lines are guides to the eye, indicating the bands of R values corresponding to different q states. The inset shows the decaying BEC atom number, N, for the same data set: the solid line is a double-exponential fit to the data with characteristic decay times of 2.5 s and 40 s corresponding to the rate of three-body decay and background losses respectively.

5.3 Long-lived superflow

Having demonstrated the quantised nature of supercurrents, we now test the limits of supercurrent metastability in our setup by performing the same experiment in a very shallow ring trap. Following the Raman transfer we now reduce the power of the LG beam by a factor of 2.47 over 3 seconds to $\approx 30\ \mu$W, such that the depth of the ring trap, V_r, is approximately equal to the chemical potential, μ. This ensures the trap is still multiply-connected, protecting the system from vortex dynamics. Since the roughness of the trapping potential scales with V_r, reducing the ring depth to $\approx \mu$ results in the smoothest trap we can achieve. This makes the condensate density almost perfectly uniform around the ring and minimises the probability of weak links where the local μ diminishes and phase slips are more likely.

In figure 5.3 we show the evolution of R for a superfluid prepared in the $q = 3$ state and rotating in a shallow ring trap. The non-zero superflow ($R > 0$) now persists for more than a minute and decays only once the condensate number itself has decayed to about 30% of its starting value. As discussed in Section 4.4.2, the radius R shows a weak dependence on the atom number, N, making the supercurrent quantisation less striking than in figure 5.2, where the fractional variation of N over the relevant time scale is smaller. However, we can still see that the R values fall into distinguishable bands corresponding to the $q = 3, 2$, and 1 states. This allows us to conclude that the $q = 3$ state is perfectly stable for ~ 40 seconds and can persist for up to a minute. We

confirm that the slow bending of the q bands with time is just a consequence of the weak dependence of R on the decaying N (for fixed q) by preparing the initial $q = 3$ state with deliberately reduced initial atom number.

It's worth mentioning at this point that in subsequent experiments carried out with greater care and understanding, the $q = 3$ state could be made perfectly stable for up to a minute with no observable decay. As moreover will be discussed in Chapter 6, by using an RF π pulse to flip the BEC back to the $|1, 1\rangle$ state following the Raman transfer, we observe the $q = 3$ state to be perfectly stable for up to 90 seconds, equivalent to over 200 revolutions of the condensate. By this point the condensate number decays to approximately 12% of its initial starting value. These results demonstrate the extreme metastability of such states, persisting far longer than any relevant timescale of the system, and limited only by the decaying atom number. In similar experiments in higher ℓ traps, the larger trap volume due to the larger ring radius reduces the local condensate density, and hence reduces the stability of superflow. Nevertheless, even for $\ell = 10$ we can still observe superflow persisting for up to 20 seconds before any decay events occur.

5.4 Superflow velocity

Having identified the decay mechanism as vortex-induced phase-slips, we now turn to a quantitative study of the dynamics of the supercurrent decay for different superflow speeds. Generally as the number of atoms in a rotating BEC decays with time, superfluidity becomes less robust. In the spirit of the Landau criterion, we identify this with the flow velocity approaching the critical velocity, $v_s \to v_c$. Once v_s equals the critical velocity for a given decay mechanism, the energy barrier to create such an excitation in the moving frame of the condensate vanishes, accompanied with the onset of viscosity. In our setup, the relevant decay mechanism has been shown to be a phase slip which reduces the angular momentum of the condensate by $N\hbar$, reducing the flow velocity v_s back below v_c. As a result we anticipate a staircase of q values, where atom loss brings about the condition $v_s(q) > v_c$, where $v_s(q)$ is the flow velocity of a given q state. This causes a $\Delta q = -1$ phase slip, reducing the flow velocity to below the critical velocity for further phase slips, $v_s(q-1) < v_c$, and hence the $q-1$ state persists until further atom loss brings about the condition $v_s(q-1) > v_c$, and the next phase slip...

To confirm such a picture we need to calculate the flow velocity of the BEC in a given q state for our ring trap. In an ideal case of a perfectly smooth ring trap with cylindrical symmetry the flow velocity is azimuthally uniform around the ring, and given by the condition for quantised circulation,

$$\mathbf{v}_s(r) = \frac{\hbar q}{mr}\hat{\theta}. \tag{5.6}$$

In our real trap, variations in the local density result in changes in the flow velocity. While the condition for quantised circulation must always hold, the circulation is achieved by a spatially varying velocity. In general, calculating the dynamics of a superfluid is a difficult problem. This difficulty stems from the fact that the fluid is composed of two components with a total momentum density given by

$$\mathbf{j} = \rho_s \mathbf{v}_s + \rho_n \mathbf{v}_n. \tag{5.7}$$

As was shown in Section 2.4.2, the density of the two components depends on the temperature, excitation spectrum, and relative velocity of the two components, $\mathbf{v}_s - \mathbf{v}_n$. A complete discussion of how to go about solving such a problem is given in [170]. Here we make the simplifying assumption that the normal component can be ignored, and hence any particle flux is due to the motion of the superfluid only. This assumption is based on the fact that our condensate fraction is typically over 85%, and secondly, we are only interested in the long-time steady state of the system at which point the normal component can be considered at rest. Using these assumptions we obtain the zero temperature hydrodynamic equations [170]

$$\frac{\partial n}{\partial t} + \nabla \cdot (n\mathbf{v}_s) = 0 \tag{5.8}$$

$$m\frac{\partial \mathbf{v}_s}{\partial t} + \nabla\left(\mu + V_{\text{ext}} + \frac{1}{2}mv_s^2\right) = 0. \tag{5.9}$$

The first of these equations is simply the conservation of particle flux, where here we consider $n = n_s$. The decay events we are interested in occur several seconds after the initial transfer of angular momentum to the system, hence it's sufficient to only find the steady state solutions. This assumes that the gradual atom loss is sufficiently slow that we may consider the properties of the system to be given by those of the equilibrium state. We also make the simplifying assumption that the energy associated with the flow velocity in (5.9), is negligible compared to the mean field energy. From this we obtain the two relations

$$\mathbf{v}_s(\mathbf{r}) \propto \frac{1}{n(\mathbf{r})} \tag{5.10}$$

$$\mu_{\text{local}}(\mathbf{r}) = \mu_0 - V_{\text{ext}}(\mathbf{r}), \tag{5.11}$$

where μ_0 is the global chemical potential for the system. The first of these relations simply states that to conserve particle flux, the flow velocity in regions of lower density must be higher than that in regions of higher density. The second relation is equivalent to the local density approximation, relating the local chemical potential and hence density, to the external trapping potential and the global chemical potential, set by the total particle number. In steady state one can define a flow path, $\mathbf{l}(\mathbf{r})$, forming a closed loop around the ring, where $\mathbf{r}$ defines the position along the flow path. To constrain

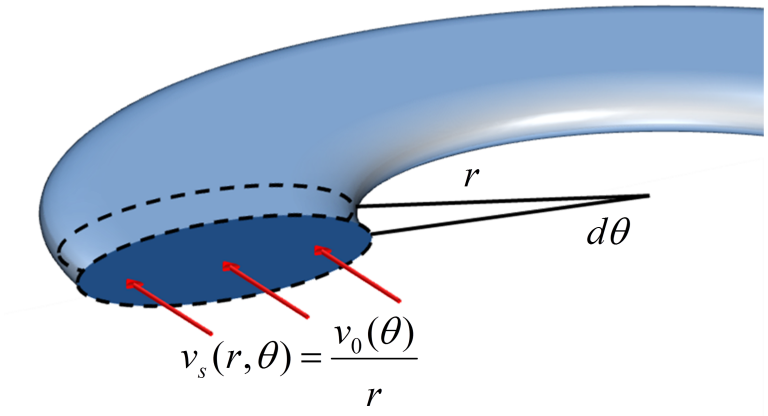

Figure 5.4: Particle flux in an angular segment: We consider an angular segment, $d\theta$, within which we can define a chemical potential, $\mu(\theta)$. Within this segment we consider the flow velocity to be parallel to the boundaries, varying as $1/r$ across the radial extent of the segment.

the constant of proportionality in (5.10), we use the condition for quantised circulation along such a path,

$$\oint \mathbf{v}_s.d\mathbf{l} = 2\pi q\frac{\hbar}{m}. \tag{5.12}$$

To simplify the problem further we consider an angular segment of the ring, $d\theta$, illustrated in figure 5.4. This allows us to define a chemical potential $\mu(\theta)$ for that given segment, which can be found from the local density (5.21). For a sufficiently slowly varying trapping potential we can consider the flow velocity in such a segment to be purely in the angular direction. The local velocity in such a segment has no z dependence, but due to the velocity profile about a vortex line, varies as $1/r$ across the width of the annulus,

$$v_s(r,\theta) = \frac{v_0(\theta)}{r}. \tag{5.13}$$

The requirement of particle flux conservation now requires the flux through any segment, $d\theta$, to be equal, and hence equation (5.10) takes the form

$$\int\int n(r,\theta,z)v_s(r,\theta)rdrdz = \text{constant}, \tag{5.14}$$

where the velocity is given by (5.13). To make further progress we need to consider the density profile within an annular trap.

5.4.1 BEC density in a ring trap

The density profile of a condensate in an annular trap is covered extensively in the thesis [171] relating to [100]. We model the ring trapping potential as a harmonic

oscillator about the trap minimum in both the radial and vertical directions,

$$V_{\text{ext}}(r,\theta,z) = \frac{1}{2}m\omega_z^2 z^2 + \frac{1}{2}m\omega_r^2(r-r_M)^2, \tag{5.15}$$

where r_M is the radius of the ring potential. As discussed in Section 4.2.1, we measure the vertical trapping frequency from the sheet potential as $\omega_z = 2\pi \times 400$ Hz. The radial trapping frequency due to the ring potential, ω_r, is measured by applying a weak attractive potential at the centre of the ring trap using the CDT, pulling the atoms towards the inner radius. Quickly turning off this potential, the atoms oscillate freely in the radial direction of the ring trap and we extract the trapping frequency by observing oscillations in the radius of the density distribution at short TOF. From this we find $\omega_r = 2\pi \times 180$ Hz for the ring trap used to obtain the data in Section 5.2, and presented in figure 5.2. The radius of the ring trap is equal to $r_M = 12.3$ μm.

The condensate wavefunction is found by solving the GP equation (2.40) with external trapping potential given by (5.15),

$$\left(-\frac{\hbar^2\nabla^2}{2m} + V_{\text{ext}}(\mathbf{r}) + g|\Phi(\mathbf{r})|^2\right)\Phi(\mathbf{r}) = \mu\Phi(\mathbf{r}). \tag{5.16}$$

To simplify this problem one typically makes the Thomas-Fermi (TF) assumption (Section 2.2.3) where, for large atom number, the kinetic energy is assumed to be negligible compared to the interaction energy. In this regime the condensate wavefunction takes the form of the inverted trapping potential. This assumption is valid provided the extent of the condensate is much larger than the healing length [172]. For an annular trap this corresponds to the condition $\mu \gg \hbar\omega_i$, for the condensate to be in the TF regime along the i^{th} direction. In the opposite regime where the kinetic energy dominates over the interaction energy the many particle ground state is identical to the single particle ground state, which for a harmonic trap is a Gaussian wavefunction.

For our experiment we find that at the initial atom number, $N = 180,000$, for all points in the ring $\mu(\theta) > \hbar\omega_z > \hbar\omega_r$, and hence the system is fully in the TF regime. As the number decays the chemical potential decreases at all points in the ring, and we find that for the relevant parameters over which phase slips occur, the density at certain points in the ring is sufficiently low that $\hbar\omega_z > \mu(\theta) > \hbar\omega_r$, and the dynamics in the z direction are frozen out and locally the BEC is two dimensional. The condensate therefore has a TF profile in the radial direction, but a Gaussian profile in the vertical direction. To fully solve the flow velocity profile at all points in the ring, we therefore need to relate the density and chemical potential for both of these regimes:

Fully TF regime

In the fully Thomas-Fermi regime the particle density is given by

$$n_{TF}(r,\theta,z) = \frac{\mu(\theta)}{g}\left(1 - \frac{z^2}{R_z^2} - \frac{(r-r_M)^2}{R_r^2}\right) \quad \text{for} \quad V_{\text{ext}}(r,\theta,z) < \mu(\theta) \tag{5.17}$$

$$= 0 \quad \text{otherwise,} \tag{5.18}$$

where $R_z = \sqrt{2\mu(\theta)/m\omega_z^2}$ is the vertical Thomas-Fermi radius, $R_r = \sqrt{2\mu(\theta)/m\omega_r^2}$ is the radial Thomas-Fermi radius, and $\mu(\theta)$ is the local chemical potential defined as $\mu(\theta) = \mu_0 - V_{\text{ext}}(r = r_M, \theta, z = 0)$. The relevant quantities are the 2D column density integrated along z, and the 1D angular density integrated along both z and r:

$$\begin{aligned} n_{2D}(r,\theta) &= \int n_{TF}(r,\theta,z)dz \\ &= \frac{4\mu(\theta)}{3g}R_z\left(1 - \frac{(r-r_M)^2}{R_r^2}\right)^{3/2} \end{aligned} \tag{5.19}$$

$$\begin{aligned} n_{1D}(\theta) &= \int n_{2D}(r,\theta)rdr = \frac{dN}{d\theta} \\ &= \frac{\mu(\theta)R_z R_r r_M \pi}{2g} \end{aligned} \tag{5.20}$$

Noting that R_z and R_r also depend on the local chemical potential,

$$n_{1D}(\theta) = \frac{\mu^2(\theta)\pi r_M}{mg\omega_r\omega_z}. \tag{5.21}$$

These expressions allow us to relate an observed local density to a local chemical potential which we will use to calculate how the flow velocity evolves as the atom number decays. The equation for 1D flux conservation in (5.14) can now be calculated for the TF regime density profile

$$\int\int n_{TF}(r,\theta,z)\frac{v_0(\theta)}{r}rdrdz = \text{constant} = C, \tag{5.22}$$

where we label the constant as C, and have made use of the $1/r$ form of the flow velocity (5.13). Using the result of (5.19) we find

$$C = \frac{n_{1D}(\theta)v_0(\theta)}{r_M}, \tag{5.23}$$

and hence the local velocity constant, $v_0(\theta)$ is simply inversely proportional to the local 1D density, $n_{1D}(\theta)$. We now use the condition for quantised circulation along a

connected path, $\mathbf{l}(\mathbf{r})$, to determine the constant C,

$$\oint \mathbf{v}_s \cdot d\mathbf{l} = 2\pi q \frac{\hbar}{m} \tag{5.24}$$

$$\oint \frac{v_0(\theta)}{r} r d\theta = C \oint \frac{r_M}{n_{1D}(\theta)} d\theta, \tag{5.25}$$

therefore

$$C = \frac{2\pi q\hbar}{r_M m} \Big/ \oint \frac{1}{n_{1D}(\theta)} d\theta, \tag{5.26}$$

$$v_s(\theta) = \frac{v_0}{r} = \frac{2\pi q\hbar}{mr} \frac{1}{n_{1D}(\theta)} \Big/ \oint \frac{1}{n_{1D}(\theta)} d\theta. \tag{5.27}$$

This equation shows us that due to the geometry of the system, the flow velocity at a given point depends on the global density profile of the entire trap and not just the local density at that point.

Radially TF regime

In the radially Thomas-Fermi regime, anticipated when atom loss reduces the local chemical potential to below the vertical trapping frequency, the particle density is given by

$$n_{RTF}(r,\theta,z) = e^{-z^2/a_z^2} \frac{\mu(\theta)}{g} \left(1 - \frac{(r-r_M)^2}{R_r^2}\right) \quad \text{for} \quad |r - r_M| < R_r \tag{5.28}$$

$$= 0 \quad \text{otherwise}, \tag{5.29}$$

where $a_z = \sqrt{\hbar/m\omega_z}$ is the vertical harmonic oscillator length. Once again we calculate the 2D and 1D densities in the same manner

$$n_{2D}(r,\theta) = \frac{\mu(\theta)\sqrt{\pi}a_z}{g} \left(1 - \frac{(r-r_M)^2}{R_r^2}\right) \tag{5.30}$$

$$n_{1D}(\theta) = \frac{4\mu(\theta)\sqrt{\pi}a_z r_M R_r}{3g} \tag{5.31}$$

$$= \frac{4}{3g}\sqrt{\frac{2\pi}{m}} \frac{\mu^{3/2}(\theta)}{\omega_r} r_M a_z. \tag{5.32}$$

We therefore see that the local 1D density has a different power law dependence on the local chemical potential than in the full TF regime. The relation between the flow velocity and 1D density is the same as in the fully TF regime derived in (5.27).

5.4.2 Effect of azimuthal roughness

With the relations above we can now deduce the flow velocity by simply measuring the azimuthal profile of the 1D density. The procedure for this is outlined in figure 5.5. As shown in figure 5.5 (a), taking an absorption image of the condensate in the ring trap,

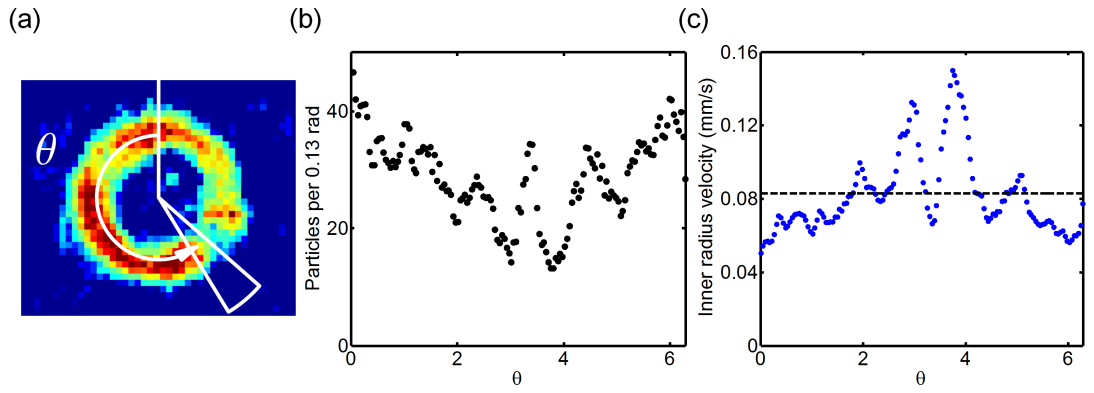

Figure 5.5: Calculation of azimuthal variation in flow velocity: (a) In trap absorption image of the condensate density. The one dimensional density is obtained by summing pixels within an angular segment, centred at the angle θ. (b) Extracted one dimensional particle density versus angle around the ring trap. (c) Using (5.27) one can relate the 1D density profile to a flow velocity profile, here plotted for the inner radius of the trap, $r = r_M - R_r$, where the velocity is highest. The correlation between regions of low density and regions of faster flow is clear. The black dashed line is the inner radius velocity for a perfectly smooth ring trap with the same μ_0.

we obtain the 1D density by summing pixels within an angular segment, $d\theta$, centred at angle θ. The angular width of this segment is $2\pi/48$, chosen to span approximately the imaging resolution at the atoms, however the final result is the same for smaller segments. To smooth the density profile obtained we use 144 segments which each have 2/3 overlap with the adjacent segment. The extracted profile of $n_{1D}(\theta)$ is shown in figure 5.5 (b). Using this and equation (5.27), we can immediately calculate the velocity $v_s(r, \theta)$ at any point in the ring. We plot the velocity on the inner edge of the ring for $r = r_M - R_r(\theta)$ as a function of θ in figure 5.5 (b), accounting for the variation in the radial TF radius, R_r, due to changes in the local chemical potential. In our discussions we always consider the flow velocity on the inner surface since this is where the condensate flows fastest, and hence will reach critical velocity first. From this we can see that to conserve particle flux, regions of low density have the highest flow velocity, and hence the superflow will destabilise here first.

In our experiment, for the initial atom number, we find the superflow is stable and no phase slips occur, corresponding to $v_s < v_c$. To understand how atom loss destabilises the flow, we need to calculate the time evolution of the flow velocity profile plotted in figure 5.5 (c). Using the local density approximation (5.11), we relate the local chemical potential to a global one by

$$\mu(\theta) = \mu_0 - V_{\text{ext}}(r = r_M, \theta, z = 0) \tag{5.33}$$

In figure 5.6 (a) we plot $\mu(\theta)$, calculated from $n_{1D}(\theta)$, using the relations (5.21) and (5.32). We define the global chemical potential as the average of $\mu(\theta)$, shown by the dashed black line, and therefore the difference gives us the local trap roughness, $V_{\text{ext}}(r =$

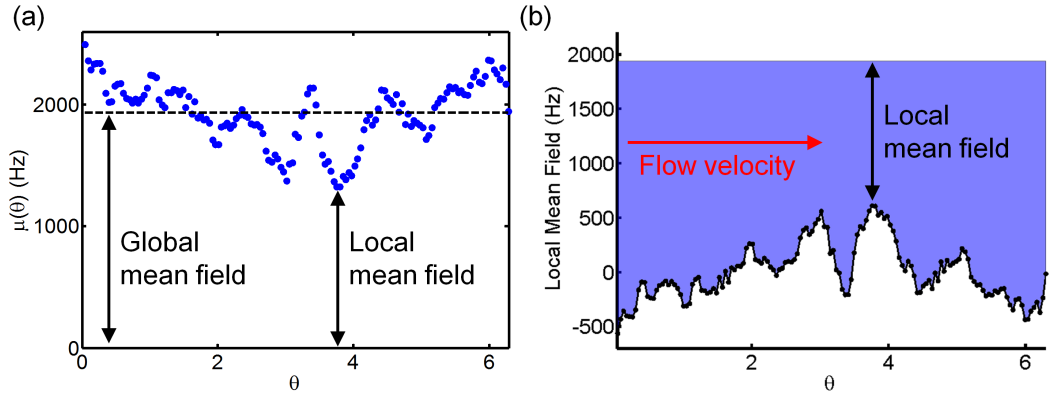

Figure 5.6: Local chemical potential in a rough trap: (a) To calculate the flow velocity at all points in the ring as a function of total atom number we extract the local chemical potential, $\mu(\theta)$, plotted as a function of the angle θ around the ring. (b) River analogy of figure (a). We now consider the local mean field as the difference between a global chemical potential, μ_0, (the water level), and a spatially varying trap roughness (the river bed). As the atom number decays the value of μ_0 decreases (water level falls), but the trap roughness (river bed) stays constant.

$r_M, \theta, z = 0) = \mu_0 - \mu(\theta)$.

To illustrate this further, in figure 5.6 (b) we plot μ_0 and $V_{\text{ext}}(r = r_M, \theta, z = 0)$ as a function of θ. In analogy to fluid flow in a river, μ_0 defines the global fluid level, and $V_{\text{ext}}(r = r_M, \theta, z = 0)$ defines the roughness of the river bed. The local chemical potential gives us the depth of the fluid at a given point. As the atom number falls the global fluid level falls, but the channel roughness remains the same, fixed by imperfections in the light which forms our trapping potential. This allows us to calculate how $\mu(\theta)$ (the depth of the fluid) evolves with changing atom number, and from this we recalculate the 1D density profile, $n_{1D}(\theta)$, and the velocity profile, $v_s(r, \theta)$[1].

Before applying this calculation to find the flow velocity evolution during decay, we must first consider the effect of imaging resolution on the calculation. This was found to have a significant effect on our results, and must be considered to bring the data close to our models of the critical velocity [173].

5.4.3 Imaging resolution

The in-trap absorption images from which we have estimated the condensate density profile are inherently blurred from the true density profile due to the effects of finite imaging resolution and pixelation of the image. The true columnar density profile is related to the imaged columnar density profile by convolution with a 2D point spread

[1]Due to the non-trivial relationship between total atom number and μ_0, this calculation is actually done in reverse. Changing μ_0 slightly, we then find $\mu(\theta)$ using equation (5.33) and the fixed trap roughness. From this we can find the 1D density, and hence the total atom number which corresponds to the revised μ_0.

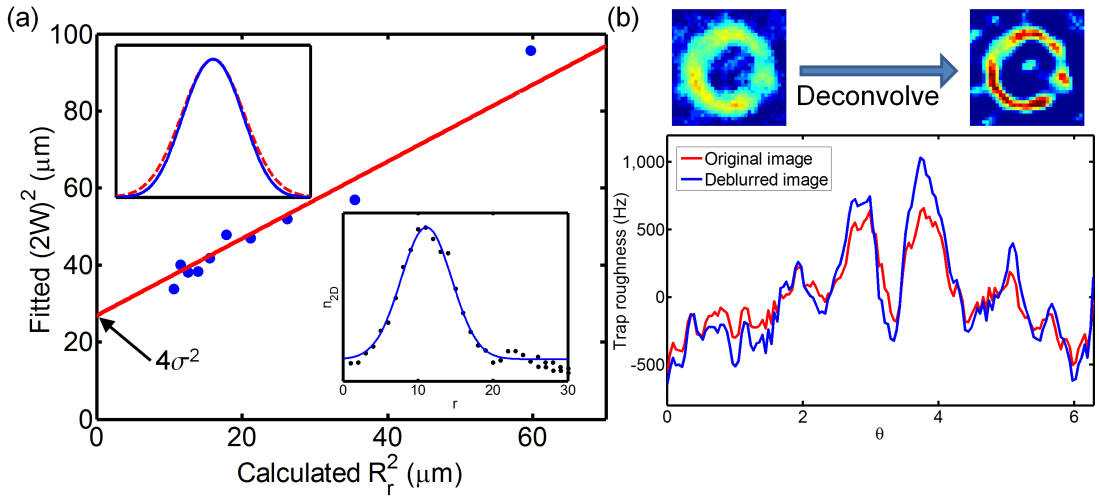

Figure 5.7: Effect of imaging resolution on flow velocity: (a) To experimentally determine the width of the point spread function (PSF) due to our imaging resolution and pixelation, we fit the radial profile of the ring to n_{2D} at various powers of the LG beam and extract a fitted width, W. Plotting the square of $2W$ against the square of the calculated value of R_r, we can extract the width of the PSF from the intercept with the axis. Top-left inset: Comparison of Gaussian profile with waist given by equation (5.36) (dashed red) versus blurred image produced by convolution with PSF (solid blue). Bottom-right inset: Example radial fit, from which W is extracted. (b) The original image is 'deblurred' using the measured width of the PSF to obtain an estimate of the true density profile. The validity of this step is confirmed by convolving the deblurred image with the PSF and restoring the original image. Plotted is the azimuthal variation in the trap roughness for both the original and deblurred image.

function (PSF) which we assume to be Gaussian,

$$n_{2D}^{(\text{image})}(r,\theta) = [n_{2D} * PSF](r,\theta), \tag{5.34}$$

$$PSF(r,\theta) = \frac{1}{2\pi\sigma^2}\exp\left(-\frac{r^2}{2\sigma^2}\right), \tag{5.35}$$

where sigma defines the waist of the point spread function. The true columnar density in trap has a TF profile, given by n_{2D} in equation (5.19). The radial profile of the imaged columnar density, found by convolving n_{2D} with the PSF, is well approximated by a Gaussian profile with a waist given by

$$W = \sqrt{\left(\frac{R_r^2}{2}\right)^2 + \sigma^2}. \tag{5.36}$$

This is illustrated in the top-left inset of figure 5.7 (a). The Gaussian profile with a waist given by W is indicated by the dashed red line. The radial profile formed by convolution of the original TF profile of radius R_r with the PSF is shown in blue. The good agreement between the two suggests we can find the σ of our imaging system by fitting the radial profiles of images to extract W, and calculating R_r from the measured atom number and trapping frequencies of our system.

This is done by measuring the fitted Gaussian width, W, for 10 different values of the true Thomas-Fermi radius, R_r. We vary R_r by changing the intensity of the LG trapping beam to alter the radial trapping frequency, ω_r. For each value of ω_r we fit the radial density profiles at 8 different angles θ, and define the average Gaussian width W, as the root mean square of the fitted widths. This value is compared against the average of the true Thomas Fermi radius R_r, which we calculate from our total atom number and measured trapping frequency. In figure 5.7 (a) is plotted $(2W)^2$ versus the square of R_r, fitted to a straight line with a fixed gradient of 1. Each data point is an average of two images. The close agreement between the data and the fixed linear fit is confirmation of equation (5.36). The intercept at the y axis gives the width of the PSF as $\sigma = 2.6 \pm 0.3$ μm. This result is reasonable when compared to our estimated imaging resolution of 2 μm and pixel size of 1.2 μm.

To find the true columnar density profile we now need to deconvolve the image with a PSF of width σ. This is clearly a non-trivial problem, since many density profiles can be convolved with the same PSF to obtain profiles close to our imaged density. This step is carried out using in-built tools in Matlab designed for such a problem. To prevent the procedure from introducing small features into the deconvolved image which cannot be inferred from the original image, we provide the function with a measure of the signal-to-noise ratio in the image, calculated from the ratio of the variance at the atoms compared to that in an empty control shot. An example of this deconvolving process is shown in figure 5.7 (b). By repeated calculations of trap roughness from successive images, we estimate our uncertainty in the calculated trap profile at $\approx 5\%$, due to atom number and trap fluctuations, and variations in our methodology.

Importantly, this uncertainty does not account for systematic errors. The deconvolution process we have used here simply provides us with an estimate of the atom density which is consistent with our observations. To confirm this estimate, we check that reconvolving with the measured PSF produces a density profile in good agreement with our images. In addition, we also adjust the parameters of the deconvolution step such that the Thomas Fermi radius of the deconvolved image is consistent with our calculated value. Nevertheless, this stage in our calculations introduces a large source of systematic uncertainty. Unfortunately, accounting for finite imaging resolution proves to be an important step in accurately calculating the flow velocity and critical velocity, but one must keep in mind the inherent uncertainties that such a process involves.

The trap roughness calculated from the deconvolved image is anticipated to be closer to the true trap roughness, and can clearly be seen to be a more sharply peaked version of the profile extracted from the original image. The larger range of this trap roughness leads to faster maximal flow at the weakest parts of the ring, and slower flow at the deepest parts of the ring. The complete protocol for extracting the flow velocity as a function of N is then given as

1. Deblur image by deconvolving with PSF of $\sigma = 2.6$ μm

2. Extract $n_{1D}(\theta)$ by summing pixels in angular segments such that $\int n_{1D}(\theta)d\theta = N$
3. Extract $\mu(\theta)$ from $n_{1D}(\theta)$ using equations (5.21) and (5.32)
4. Extract global mean field, μ_0, from the average of $\mu(\theta)$
5. Extract trap roughness, $V_{\text{ext}}(r = r_M, \theta, z = 0) = \mu_0 - \mu(\theta)$
   (a) Recalculate $\mu(\theta) = \mu_0 - V_{\text{ext}}(r = r_M, \theta, z = 0)$
   (b) Recalculate $n_{1D}(\theta)$ from $\mu(\theta)$ using equations (5.21) and (5.32)
   (c) Recalculate $v_s(r, \theta)$ from $n_{1D}(\theta)$ using equation (5.27)
   (d) Recalculate atom number, $N = \int n_{1D}(\theta)d\theta$
   (e) Reduce μ_0 slightly and repeat steps 5a→5e

The results of this calculation are shown in figure 5.8 (a), where we plot the maximal flow velocity versus atom number, N, for the narrowest point in the ring, where the local density and $\mu(\theta)$ are lowest. We plot this for the $q = 3, 2$, and 1 states, indicated by the solid blue, green, and red lines respectively. As expected, the loss of atom number further constricts the flow at the narrowest parts causing the velocity to increase. For N approaching $50,000$, the flow velocity diverges, corresponding to the condensate density fragmenting due to the global chemical potential, μ_0, falling below the trapping potential at the roughest part of the trap.

For comparison with our data on phase slips presented in figure 5.2, we eliminate the time variable and plot the observed R (and equivalently q) values versus N (figure 5.8 (b)). As in figure 5.2, the same colour code is used to indicate different q states. We find each rotational state is observed up to a critical atom number $N_c(q)$, beyond which decay to a lower angular momentum state is inevitable. We thus empirically associate this critical atom number with the condition $v_s(q) = v_c$. Using figure 5.8 (a), we relate this critical atom number to a maximal flow velocity for each q state, $v_{\max}(q)$. From the data in figure 5.8 we find $v_{\max}(3) = 1.29$ mm/s, $v_{\max}(2) = 0.96$ mm/s, and $v_{\max}(1) = 0.78$ mm/s. The changing maximal flow velocity for the three q states is therefore due to the critical velocity decreasing with decaying atom number. In figure 5.8 (b) we also observe phase slips for $v_s < v_c$. This is discussed further in Section 5.6, where we attribute this to rare stochastic decay events, most likely due to thermal activation over the energy barrier to decay which is still present for $v_s < v_c$.

To see whether we can understand these results further, we now consider what mechanism defines the critical velocity in our ring BEC.

5.5 Critical velocity

Having calculated the evolution of the superfluid velocity over which we observe phase slips, we are now in a position to contrast our data to a possible model of the critical

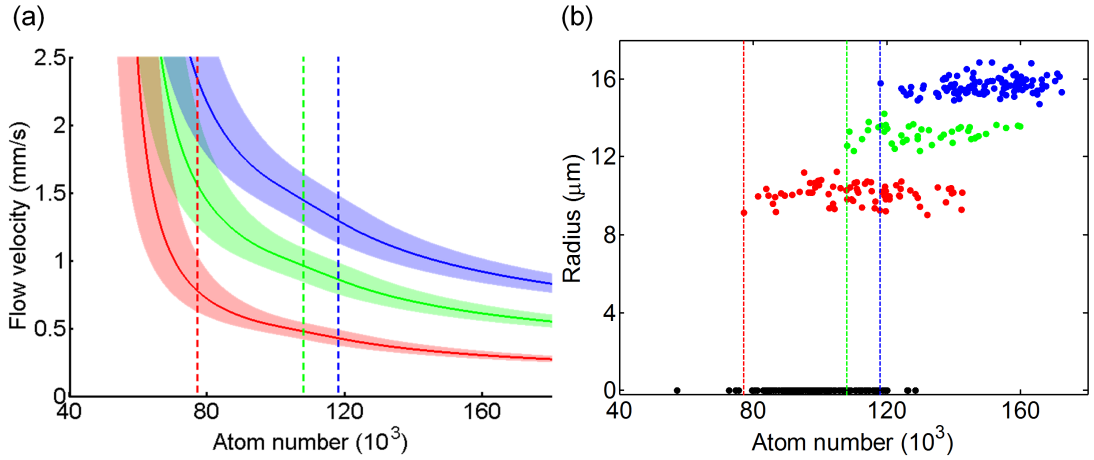

Figure 5.8: Evolution of peak flow velocity for decaying atom number: (a) Peak flow velocities for the $q = 3$, $q = 2$, and $q = 1$ states are illustrated by the solid blue, green, and red lines respectively. The shaded regions about each line, illustrate the variation introduced by the estimated 5% fluctuations in the trap roughness and atom number. The vertical dashed lines indicate the lowest N at which we observe each q state, with the same colour coding applied. (b) We plot the same data as in figure 5.2, now plotted against atom number. We see that each q plateau extends up to a minimum N, which using figure (a) we can now relate to a maximum flow velocity $v_s(q)$.

velocity. To do this we first consider three different analytic calculations of v_c: the Feynman velocity, v_c^F, the speed of sound, c, and the surface critical velocity, v_c^s. Of these three we find our data agrees closest with a critical velocity given by the speed of sound, a result predicted in several numerical studies solving the GPE for an annular BEC with a repulsive barrier potential [40, 173–175]. The propagation speed of surface modes localised at the edge of the cloud, v_c^s, also gives reasonable agreement with our data, since over the parameter space considered, v_c^s and c are very similar. In Section 5.5.4 we numerically calculate the excitation spectrum of an annular BEC and show the relevant excitation which sets v_c switches from surface modes to phonons below a certain local chemical potential. We therefore conclude that the phase slips we observe in figure 5.8 (b) are indeed nucleated by phonon modes, and hence the relevant critical velocity is given by c. Finally, we note that the Feynman critical velocity, v_c^F, only provides an order of magnitude estimate and does not provide quantitative agreement with our measured critical velocity, nor predict the reduction in $v_{\max}(q)$ with decreasing N, which we observe.

5.5.1 Feynman velocity

In Section 2.4.3 we derived the Feynman critical velocity by considering the minimum energy cost of inserting a vortex ring into a flow channel of radius R:

$$v_c^F = \frac{\hbar}{mR} \ln \frac{R}{\xi}, \tag{5.37}$$

where ξ is the vortex core size, given by the healing length. In a toroidal flow such a vortex ring will form at the walls of the channel before shrinking in on itself and annihilating, completing a full single phase slip [40]. The geometry of this excitation is three dimensional and applies to cylindrical flow channels. Our annular BEC is asymmetric, with a vertical trapping frequency over twice the radial. For the densities over which we observe phase slips, the condensate at the weakest part of the ring where the decay events occur is quasi 2D, with $\mu(\theta) < \hbar\omega_z$. Indeed for the very lowest densities at which we observe $q = 1 \rightarrow q = 0$ phase slips, the condensate is approaching 1D at the weakest point. The relevant excitation to then consider in a two dimensional geometry is not vortex rings, but straight vortex lines of vortex-antivortex pairs aligned along the vertical direction, which either cross the annulus and annihilate one another in the bulk, or nucleate in the bulk and move apart towards the edge of the condensate, decaying to elementary excitations at the surface. While a single vortex line can also cause a 2π phase slip, the energy associated with a vortex-antivortex phase slip is lower. For a vortex-antivortex pair separated by a distance D in a background flow of velocity v_s, the energy in the frame moving with the flow is given by

$$E' = 2\pi\frac{\hbar^2 n_{2D}}{m}\ln\frac{D}{\xi} - 2\pi\hbar n_{2D} D v_s, \tag{5.38}$$

and hence the critical velocity is given by

$$v_c^F = \frac{\hbar}{mD}\ln\frac{D}{\xi}. \tag{5.39}$$

For our annular flow, $D = 2R_r$, and the healing length ξ, is an effective healing length, ξ_{1D}, integrated over the vertical and radial dimensions to account for the varying density across the annulus.

Using the expression for the healing length in a uniform condensate in (2.64), and the expression for the sound speed in a uniform condensate in (2.62), we can show that the two quantities are related by

$$\xi = \frac{\hbar}{\sqrt{2}mc}. \tag{5.40}$$

Using this we can rewrite the Feynman velocity (5.39) in the form

$$\frac{v_c^F}{c_{1D}} = \sqrt{2}\frac{\xi_{1D}}{D}\ln\frac{D}{\xi_{1D}}, \tag{5.41}$$

where c_{1D} is similarly an effective sound speed averaged over the cross section of the annulus. Since the expression for the Feynman velocity is only valid for the condition $D \gg \xi_{1D}$, where the channel width is much larger than the vortex core size, we have the condition that the Feynman velocity is always much lower than the sound velocity. The maximal value of the Feynman velocity is therefore found to be $v_c^F = 0.52 c_{1D}$, occurring for a channel width $D = 2.7\xi$.

5.5.2 Speed of sound

The speed of sound is defined as the flow velocity above which it is energetically beneficial to excite phonon modes in the condensate. In Section 2.3.1 we considered perturbations in the wavefunction of a uniform condensate to derive the sound velocity as

$$c = \sqrt{ng/m}, \tag{5.42}$$

where n is the particle density, and g is the interaction parameter given in (2.32). In real experiments with inhomogeneous density, the sound velocity is maximal at the trap centre and falls to zero at the surface. To compare this criteria to our system we therefore need to define an effective sound velocity c_{1D}, which integrates over the varying density in the z and r direction [176]. Such an effective sound velocity is given by [149]

$$c_{1D} = \sqrt{\frac{n_{1D}}{m}\frac{\partial\mu}{\partial n_{1D}}}, \tag{5.43}$$

where n_{1D} is the 1D density defined in (5.21) and (5.32). Since our phase slip events occur where the condensate is in the radial TF regime, using equation (5.32), we find an expression for the local effective sound velocity as

$$c_{1D}(\theta) = \sqrt{\frac{2\mu(\theta)}{3m}}. \tag{5.44}$$

We therefore anticipate a local Landau criterion, where for $\max(v_s(r,\theta)) > c_{1D}$, phonon modes will be excited and the supercurrent will decay. The precise mechanism by which such phonon modes then go on to nucleate vortices and cause a phase slip is still not fully understood [173].

5.5.3 Surface modes velocity

In experiments on simply-connected rotating atomic gases [31, 32, 177, 178] it was often found that the critical velocity for a vortex entering the condensate was higher than that predicted purely by global energetic arguments [179]. This higher v_c is associated with dynamic instabilities of surface excitations, which provide the necessary microscopic route for vortex nucleation. The surface mode model aims to find the local critical velocity over the TF surface above which such unstable surface excitations form. This model produces a general theory based on the idea that the TF surface of a large condensate enters a bulk regime in which the physics of vortex formation is local. In general, an energetically unstable surface mode must first appear for vortices to enter the cloud, therefore the Landau criterion is universal to vortex formation. For large enough condensates where the surface length scale is much smaller than their overall extent, the local Landau critical velocity may be determined by solving one universal equation.

For a large enough condensate one can neglect the curvature of the TF surface and approximate the trapping potential to a linear ramp, $V = Fr$, where F is the potential gradient at the TF surface given by

$$F = \left.\frac{dV}{dr}\right|_{r=R_r} = \sqrt{2\mu m\omega_r^2}, \tag{5.45}$$

for a harmonic trap. One then considers the instability to form in a surface boundary of depth

$$\delta = \left(\frac{\hbar^2}{2mF}\right)^{1/3}. \tag{5.46}$$

The surface mode model is then valid in the regime where $R_r \gg \delta$, which simplifies to

$$\frac{R_r}{\delta} = 2\left(\frac{\mu}{\hbar\omega_r}\right)^{2/3} \gg 1. \tag{5.47}$$

The relevant GPE equation then reads

$$i\hbar\frac{\partial\Phi}{\partial t} = \left(-\frac{\hbar^2\nabla^2}{2m} + Fr + g|\Phi|^2\right)\Phi, \tag{5.48}$$

where the origin of r is at the TF surface. The excitation spectrum of such a system was solved numerically in [180], where it was found that the critical velocity is given exactly by

$$v_c^s = \left(\frac{2\hbar F}{m^2}\right)^{1/3} = \sqrt{\frac{2\hbar\omega_r}{m}}\left(\frac{\mu}{\hbar\omega_r}\right)^{1/6}. \tag{5.49}$$

The arguments of the surface model are local and hence the theory should be equally applicable to rotating annular condensates as long as both the width of the annulus and its inner radius are much large than the surface depth δ. Indeed the surface mode theory was extended to a 2D ring geometry by Dubessy *et al.* [181]. By explicit calculation of the excitation spectrum of an annular condensate, the calculated value of the critical velocity was shown to be equal to v_c^s. In Section 5.5.4 we repeat this calculation, arriving at the same conclusion for sufficiently large condensates. Here however, we show that for low densities the nature of the excitation changes. Below a certain chemical potential the radial extent of the annulus becomes comparable to δ and the instability changes from a surface mode with $v_c = v_c^s$, to a phonon mode located in the condensate bulk with $v_c = c_{1D}$.

5.5.4 Excitation spectrum of a ring BEC

We now calculate the excitation spectrum of a two dimensional Bose gas trapped in a smooth ring potential, as was done in [181]. From this we find the critical angular velocity above which the system must be rotated before vortices are excited. By varying the total atom number in the trap we calculate the value of this critical velocity as a function of the chemical potential (here $\mu(\theta) \equiv \mu_0$, since we consider a cylindrically

symmetric trap). In this case of a rotating trap and a stationary condensate, the critical velocity is first exceeded at the outer radius of the condensate. In our experiment of a rotating superfluid and a stationary trap, the same critical velocity applies, but now the fluid velocity is largest on the inner radius.

We consider the GPE at zero temperature for a 2D ring. This most closely matches our geometry of interest, where we find phase slips occur in the quasi-2D regime. As before, the trapping annular potential is written as a harmonic potential of frequency ω_r centred at radius r_M. We use the associated scales for energy ($\hbar\omega_r$), time (ω_r^{-1}), and length $a_r = \sqrt{\hbar/(m\omega_r)}$. The dimensionless 2D GPE then reads

$$i\partial_t\Phi = \left(-\frac{\Delta}{2} + \frac{1}{2}(r - r_0)^2 + g|\Phi|^2\right)\Phi, \tag{5.50}$$

where the condensate wavefunction, $\Phi = \Phi(r, \theta, t)$, is normalised to unity, $\Delta = \partial_r^2 + \partial_r/r + \partial_\theta^2/r^2$ is the Laplacian in polar coordinates, $r_0 = r_M/a_r$ is the dimensionless ring radius, and $g = N\sqrt{8\pi}\frac{a}{a_z}$ is the dimensionless 2D interaction constant, where N is the atom number, a is the s-wave scattering length, and a_z is the harmonic oscillator length in the z direction [182].

From the rotational invariance of (5.50), we consider solutions of the form

$$\Phi(r, \theta, t) = e^{-i\mu t}[\Phi(r) + \delta\Phi_m(r, \theta, t)], \tag{5.51}$$

where

$$\delta\Phi_m(r, \theta, t) = u_m(r)e^{-i(\omega t - m\theta)} + v_m(r)^* e^{i(\omega^* t - m\theta)}. \tag{5.52}$$

Φ denotes the stationary ground state of the system, μ is the global chemical potential, and $\delta\Phi$ is a small perturbation parameterised by the angular wavenumber m. A detailed explanation of how this problem is solved is given in Appendix B. We first calculate the ground state for a given N by imaginary time propagation of a test TF profile, stopped when the relative variation in μ falls below 10^{-12}. The Bogoliubov-de Gennes equations for $u_m(r)$ and $v_m(r)$ are then solved by diagonalisation. We obtain real frequencies with a dispersion relation $\omega = \omega(m)$, the lowest branch of which allows us to compute the critical angular velocity $\Omega_c = \min(\omega(m)/m)$. The density profile of the excitation is found by $\delta n_m(r) = 2\mathrm{Re}[\Phi(r)^*(u_m(r) + v_m(r)^*)]$.

The results of this calculation are shown in figure 5.9. Here we plot the lowest branch of the dispersion relation for three different values of the total particle number, N. The critical angular velocity is indicated by the dashed grey line, $\omega = m\Omega_c$. At small m values the lowest branch is linear, and can be associated with rotating soundlike waves. For larger atom numbers, at higher m values, this branch exhibits a small negative curvature that makes the critical angular velocity smaller than the angular speed of sound. The radial density profile of the excitation, shown in the inset, is

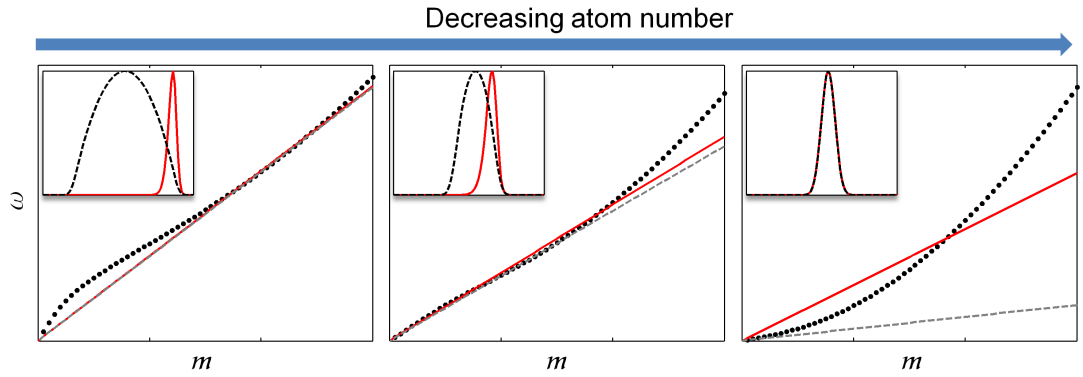

Figure 5.9: Numerical calculation of 2D annular BEC excitation spectrum: The three plots are the eigenfrequencies, ω, and the angular wavenumber, m, for the lowest branch of the dispersion relation, plotted for three different values of the total particle number. The black data points are the results of our numerical calculation, obtained by diagonalisation of the Bogoliubov-de Gennes equations. The grey dashed line is the critical angular velocity, $\Omega_c = \min(\omega(m)/m)$. The solid red line is the critical angular velocity, as predicted by the surface model. The inset of each plot shows the radial density profile of the condensate (black dashed line) and the density profile of the excitation (red line), normalised to have the same peak value.

strongly localised on the outer radius and we thus expect that the mode corresponding to the critical angular velocity will be correctly described by the surface mode model in Section 5.5.3. The critical angular velocity within the surface mode model is simply given by

$$\Omega_c^s = \frac{v_c^s}{r_e}, \tag{5.53}$$

where r_e is the radius of the excitation. For this case of a rotating trap and stationary BEC, the critical velocity is first reached on the outer surface, and hence $r_e = r_M + R_r$. This critical angular velocity is indicated by the red line in figure 5.9. We therefore see that for the largest atom number, where the assumptions of the surface model are most valid, Ω_c and Ω_c^s are in excellent agreement as was concluded in [181].

As illustrated in figure 5.9, as the particle number decreases the negative curvature at large m values disappears. Eventually at low numbers the critical velocity is equal to the speed of sound, set by the linear part of the spectrum near $m = 0$. The excitations are then phonons and are no longer localised at the surface but distributed over the entire condensate profile. This is associated with a failure of the surface model, with the value of Ω_c significantly less than Ω_c^s. This disagreement with the surface model at low N is intuitive, since at low densities the extent of the condensate becomes comparable to the surface depth.

The critical velocity as determined by the numerically calculated excitation spectrum is simply found from the critical angular velocity as

$$v_c^e = \Omega_c(r_M + R_r), \tag{5.54}$$

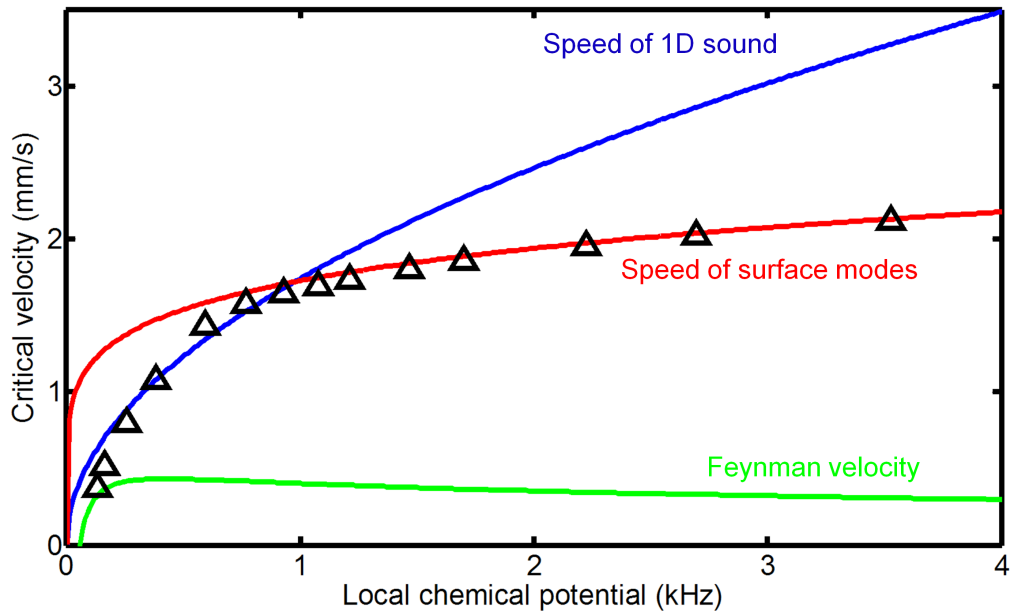

Figure 5.10: Comparison of critical velocity models: Plotted is the critical velocity versus local chemical potential for all models considered: Feynman velocity, v_c^F (green), effective sound speed, c_{1D} (blue), surface modes velocity, v_c^s (red), and the critical velocity extracted from numerical calculations of the excitation spectrum of an annular BEC, v_c^e (black triangles). We observe a transition at $\approx 1kHz$, above which the critical velocity is determined by surface mode instabilities, and below which it is set by excitation of phonon modes. We note that our data on phase slips is in the regime where the critical velocity is sound like.

since the maximum velocity at a given rotation Ω is at the outer radius. In figure 5.10, the value of v_c^e is plotted as a function of chemical potential, as indicated by the black triangles. To compare this result with our analytic models, the Feynman velocity, v_c^F, the effective sound velocity, c_{1D}, and the surface mode velocity, v_c^s, are also plotted on the same axes. For large μ, the critical velocity agrees with v_c^s, in agreement with the results of [181]. For values of μ below around 1kHz, the sound velocity falls below the surface mode velocity, and the relevant excitation becomes phonon like and is no longer localised at the surface. This deviation from the surface model occurs when the ratio of the condensate extent to the surface depth falls below $R_r/\delta \lesssim 6.3$. The value of v_c^e then closely follows the effective sound velocity, c_{1D}, with the small discrepancy possibly due to the continuous change in dimensionality, and hence averaging of c. This agreement between the speed of sound and v_c^e found by solving the GPE is in agreement with the results of [40, 173–175]. We also observe that the Feynman critical velocity, v_c^F, is considerably lower than the others and only gives reasonable agreement with the numerical result at very low chemical potentials.

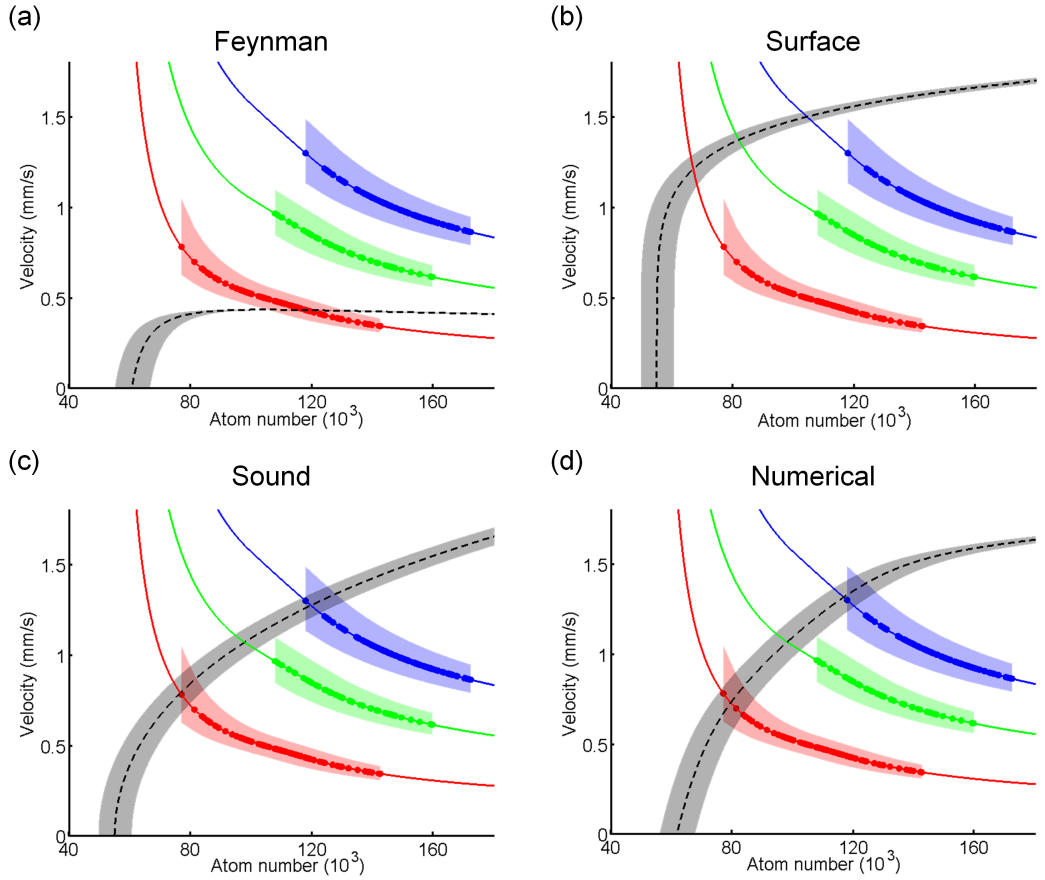

Figure 5.11: Comparison of critical velocity models with flow velocities calculated from data for different q states: The data points are the calculated flow velocities versus atom number for the data points in figure 5.8, where the blue, green and red points indicate the $q = 3, 2$, and 1 states respectively. The solid lines in blue, green, and red plot the functions $v_s(q)$ versus N for the $q = 3, 2$ and 1 states respectively. The shaded areas around each q data set illustrate the uncertainty in flow velocity due to 5% fluctuations as in figure 5.8 (a). The dashed black line is the critical velocity versus N for the model considered. The shaded area around this line again illustrates the error introduced by the fluctuations. The models used are the Feynman critical velocity, v_c^F, in (a), the surface mode critical velocity, v_c^s, in (b), the averaged speed of sound, c_{1D}, in (c), and the numerically calculated critical velocity, v_c^e, in (d).

5.5.5 Critical velocity discussion

To test our calculations of v_c we now need to compare them to our data in figure 5.8, where we have the distribution of q states with atom number N, and our calculations of how to convert a given N and q to a peak flow velocity $v_s(q, N)$. The results of this comparison are plotted in figure 5.11 for all four critical velocities: Feynman, v_c^F, surface mode, v_c^s, averaged sound, c_{1D}, and the numerical result, v_c^e, in figures $(a) \rightarrow (d)$ respectively. The data points are our measured $v_s(q, N)$ values versus N, where the blue, green, and red points indicate the $q = 3, 2$, and 1 rotations states, originally assigned in figure 5.2 using the quantisation of R. The shaded area around each q data set illustrates our uncertainty in calculating $v_s(q, N)$ due to fluctuations, as in figure

5.8(a). The right edge of this area therefore indicates the highest N/lowest $v_s(q)$ at which we observed each q state and the left edge indicates the lowest N/highest $v_s(q)$ at which we observe each q state. We therefore identify the left edge with the condition $v_s(q) = v_c$. The respective critical velocity is also plotted as the dashed black line, and the black shaded area similarly represents the effect of fluctuations in calculating v_c. Good agreement between our data and a given v_c model would then be indicated by the maximum $v_s(q)$ for each q state (left edge of the coloured shaded areas) lying close to the critical velocity (black shaded area).

The Feynman critical velocity (5.39), plotted in figure 5.11 (a), is clearly too low and predicts immediate decay of all $q > 1$ states and decay of the $q = 1$ state at $N \approx 120 \times 10^3$. We also note that the form of the Feynman velocity has a very weak dependence on N and therefore cannot explain the decrease in $v_{\max}(q)$ with decaying N which we observe.

The critical velocity of the surface model (5.49), plotted in figure 5.11 (b), shows better agreement with the data, though predicts a larger v_c than we observe. For our data, the ratio of the condensate extent to surface depth R_r/δ is in the range $2 - 4$, and therefore the criteria for applying the surface model is marginal. In our original discussion of these results in [14], the deconvolution method adopted was slightly different and we allowed the width of the PSF to vary to best match our data, finding good agreement between the data and the surface model for $\sigma \simeq 2.9$ μm, in reasonable agreement with our measured σ. With the additional insight from the numerical calculations in Section 5.5.4, we now see that in the regime of our results, the condition for the surface model to hold is not strictly met, and we anticipate the critical velocity to be in better agreement with the local sound velocity. In this discussion, we therefore fixed σ at its measured value to directly compare our data to both models. This original agreement with the surface model does however highlight the systematic uncertainty introduced by the deconvolution step in our calculation.

The averaged speed of sound (5.44), plotted in figure 5.11 (c), shows excellent agreement with our data, closely predicting the minimum N, and therefore maximum $v_s(q)$, for all three q states. The critical velocity extracted from our numerical calculations (5.54) is plotted in figure 5.11 (d), and as expected is very close to the result for the 1D sound velocity. From this we conclude that our data is in agreement with the critical velocity predicted by the GPE, which for our regime is very closely related to the local 1D sound speed.

To further confirm our results we perform another experiment in which we exploit the fact that the roughness of our ring potential grows with V_r. We calculate how much further we would need to increase the trap roughness, by increasing the intensity of the LG beam, before the $q = 3$ and $q = 1$ state were inherently unstable and decayed immediately at the starting atom number. Our calculations predict that the an increase of LG intensity by $30 \pm 10\%$ would cause immediate decay of

the $q = 3$ state ($v_s(q = 3, N = 180 \times 10^3) > c_{1D}(N = 180 \times 10^3)$), and an increase of LG intensity by $70 \pm 10\%$ would cause immediate decay of the $q = 1$ state ($v_s(q = 1, N = 180 \times 10^3) > c_{1D}(N = 180 \times 10^3)$). Experimentally we find agreement with the values in the upper end of this range, typically needing to increase the LG intensity by 40% to deterministically kill $q = 3$ flow, and by 80% to deterministically kill all superflow. This suggests that the true value of our superflow velocity lies towards the lower end of our error region, and the critical velocity lies towards the upper end of the error region. Since the two quantities have negative correlation, this would be consistent with a small systematic underestimate in determining atom number, or overestimate in determining trap roughness.

While our results do show excellent agreement with a critical velocity given by $v_c = c_{1D}$, it's important to note that our calculations of the flow velocity and critical velocity are built upon several steps, each of which introduces uncertainties. While we have tried to account for errors in our analysis arising from fluctuations in atom number and trapping potential, possible systematic effects such as atom number calibration, trapping frequency measurements, and accounting for our finite imaging resolution, can also effect our results. In our original analysis for example, by considering a slightly larger PSF we found reasonable agreement between our data and the surface model calculation of the critical velocity. It is therefore important to keep in mind that the deconvolution step which accounts for our finite imaging resolution, only provides an estimate of the true density profile. Such systematic uncertainties make it difficult to reliably distinguish between v_s and c_{1D} which, over the range where we observe phase slips, offer similar predictions of the critical velocity. Nevertheless, the fact that our data is in such close agreement with $v_c = c_{1D}$ for a range of atom numbers and flow velocities, is strongly suggestive that the critical velocity in our system is set by the local effective sound velocity.

Comparison to previous measurements

We now compare our findings to those in [100], which provides the only other experimental measure of the critical velocity in an annular condensate. In this experiment, $q = 1$ superflow was prepared using phase imprinting and a repulsive potential barrier was raised, reducing the density at a point in the ring. For $q = 1$ superflow, the detection was binary, and hence they plotted the survival probability of circulation versus barrier height. For a barrier height above a certain value they observed a dramatic reduction in survival probability, associated with flow above the critical velocity in the barrier region. Using similar methods to estimate the superflow velocity at the barrier, they find their measured v_c to be consistent with the Feynman velocity v_c^F, and from this infer the decay mechanism to be phase slips. In contrast, for our experiment we found the Feynman velocity did not provide an accurate prediction of the critical velocity we observed, and more importantly could not explain the variation in critical

velocity we observed with changing atom number. At first glance then these two results seem incompatible, however closer inspection actually reveals agreement between the two measurements, and only a difference in interpretation.

Importantly for the experiment in [100], the local chemical potential in the barrier region is only on the order 100-200 Hz, and hence is bordering the quasi-1D regime. For such a low chemical potential, the small radial extent of the annulus means the ratio of the Feynman critical velocity to the effective sound velocity is close to its maximal value (5.41). While their measured critical velocity is found to agree with v_c^F, in their case this actually corresponds to $v_c \approx 60\% c_{1D}$, and therefore the discrepancy is not as large as first seemed. The remaining difference in critical velocity between their experiment and ours can be explained by the differing definitions of the critical velocity which were used.

In our experiment we define the critical velocity as the flow velocity above which decay is ultimately inevitable and occurs on the millisecond scale. Therefore we assign the condition $v_s(q) = v_c$ to the largest flow velocity we observe for a given q state. For $v_s < v_c$ we still observe phase slips, however we interpret these as rare stochastic decay events which can occur through thermal or quantum fluctuations, as observed in liquid helium and superconducting nanowire systems. In contrast, the condition for reaching the critical velocity in [100] is defined as the velocity at which $\langle q \rangle = 1/2$. While they do observe some width to this transition, they attribute this to technical fluctuations rather than any stochastic nature of the decay events. To distinguish this definition from our own, we label such a velocity as an effective critical velocity $\bar{v_c}$. This effective critical velocity does not therefore define the maximal allowed flow velocity without decay, but instead defines the velocity above which supercurrent decay becomes likely. Looking at our data in figure 5.11, we observe that such a definition decreases the critical flow velocity we consider by around 20%, and increases the sound velocity we consider by around 25%. Therefore we find our data is also consistent with $\bar{v_c}/c_{1D} \approx 0.6 - 0.8$. This suggests that the two data sets are not necessarily inconsistent, simply that the interpretations of flow reaching the critical velocity are different. Importantly however, since our experiment uses data from several q states with decay at higher values of the chemical potential, we are able to conclusively discount the Feynman criteria as an accurate quantitative measure of the critical velocity. This enables us to interpret our data as stochastic phase slips as $v_s \to v_c$, and a hard cutoff for superflow above the local sound velocity, c_{1D}, where decay is inevitable.

5.6 Statistics of stochastic phase slips

In our discussion of the critical velocity, we defined the critical velocity as the minimum superflow velocity of the system above which the superflow would decay both rapidly

and inevitably. This is consistent with numerical solutions of the GPE which find that for flow above the critical velocity, phase slip events occurring via vortex-antivortex annihilation take place within about 0.5 ms [173]. At absolute zero temperature in the absence quantum tunneling of the order parameter, one would then expect a given q state to remain perfectly stable until gradual atom loss brought about the condition $v_s(q) = v_c$, at which point a phase slip would occur to the $q-1$ state. Returning to the particle in a washboard analogy in figure 5.1, the condition $v_s = v_c$ then corresponds to the energy barrier disappearing, and the local energy minima at $L/N = q\hbar$ vanishing, causing decay to the next local energy minima.

Looking at our data in figure 5.11 (d), we clearly observe a less deterministic process. We observe stochastic phase slips occurring for $v_s < v_c$, corresponding to particles escaping their local energy minima before the energy barrier reaches zero. Purely experimentally, this is directly observed in the horizontal overlaps of the different q plateaus as a function of N in figure 5.8 (b). Similar overlaps are seen in the time domain in figure 5.2 (b), showing that the observed q is not a deterministic function of either t or N. From figure 5.11 (d), we see that only a small fraction of this overlap can be attributed to technical fluctuations in our experiment. Factoring in the atom number and trap fluctuations indicated by the shaded areas in figure 5.11 together with shot-to-shot variations in atom number detection of $\sim 6\%$, such technical fluctuations can only account for $\approx 25\%$ of the observed overlap in q-state plateaus.

We therefore conclude that there exists a significant parameter space where the superfluid flow is subcritical but stochastic phase slips still occur on a time scale of seconds. We can then consider the supercurrent state, q, for $v_s(q) < v_c$, as in an energy minimum where there still exists an energy barrier preventing decay to the $q-1$ state. As $v_s \to v_c$, the size of this barrier tends towards zero, and hence the probability of crossing the barrier and causing a phase slip increases exponentially. As was observed in helium and superconducting nanowire experiments, the nature of this barrier crossing could be due to either thermal or quantum fluctuations.

The possibility of thermal activation of phase slips for $v_s < v_c$ was considered in [175], where a numerical implementation of the truncated Wigner approximation was used to simulate the experiment of Ramanathan *et al.* in [100] at finite temperature. These calculations found the observed reduction in the effective critical velocity $\bar{v_c} = 0.6c_{1D}$ from the zero temperature GPE value of $\bar{v_c} = v_c = c_{1D}$ was consistent with a temperature of ≈ 35 nK. For our experiment we find an effective critical velocity for the $q = 3 \to 2$ transition[1] of $\bar{v_c} = 0.73c_{1D}$, and we independently measure our temperature by fitting the thermal component in TOF as $T = 29 \pm 3$ nK. Such a result is certainly of a similar order to that of the calculation and, provisionally at least, suggests the stochastic decay events we observe may be explained by thermal activation of the

[1] We cannot easily define similar critical velocities for subsequent phase slips since the initial population in these q states depends on decay from higher q states.

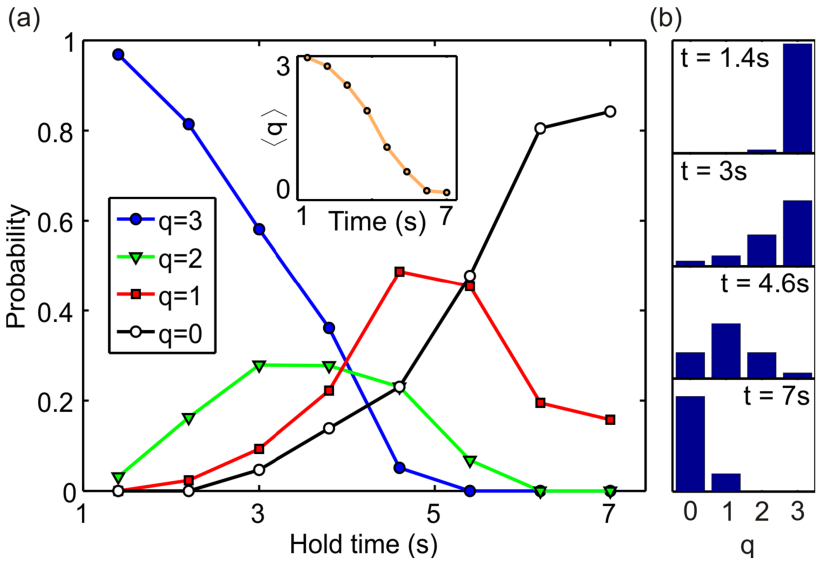

Figure 5.12: Counting statistics of phase slips: (a) For the data shown in figure 5.2 we plot the distribution of the observed q values as a function of rotation time t. Each data point is an average over a 0.8 second time bin. The inset shows the smooth evolution of $\langle q \rangle$ with t. (b) Histogram of q values for four representative rotation times.

system over an energy barrier. Such a hypothesis could then by tested by repeating this experiment as a function of temperature. With increasing temperature the system could be excited over a larger energy barrier at smaller values of v_s/v_c, and hence one would expect to observe phase slips at larger values of N.

Our ability to resolve q states allows us to study the evolution of the q distribution in time. This in essence provides full time-resolved counting statistics of phase slips, and should provide excellent input for further theoretical modeling and understanding of our observed stochastic decay dynamics. In figure 5.12 we present such an evolution in time for the same data set as in figure 5.2, which forms the basis of our critical velocity analysis. We note that this accelerating decay process is not Markovian since the phase slip probability grows as v_s/v_c increases through the gradual decay of N. For larger data sets this opens the possibility to fit this to solutions of the rate equation, and thereby extract how the phase-slip probability evolves with time. Such results could provide insights into the form of the energy barrier, and therefore shed light on the decay process and the role of thermal and quantum fluctuations. We also note that the mean rotational state, $\langle q \rangle$, decays smoothly with time (inset of figure 5.12), so our ability to experimentally resolve different q states with high fidelity will be essential to further understanding phase slip dynamics.

5.7 Conclusion

In conclusion, we have demonstrated and studied long-lived multiply charged superflow in an annular atomic BEC. We resolve with high fidelity quantised steps in the decay

of the supercurrent, which corresponds to vortex-induced 2π phase slips. This result allows us to unambiguously identify the decay mechanism as phase slips, independent of any calculations. The supercurrent decays rapidly if the flow velocity approaches a critical velocity that is in agreement with our numerical calculations of the excitation spectrum. Our numerical calculations identify a transition from a large condensate regime where the relevant excitations are surface instabilities and $v_c = v_c^s$, to a small condensate regime where the relevant excitations are phonons localised in the condensate bulk and $v_c = c_{1D}$. For our data on phase slips we are in the small condensate regime, and hence observe a critical velocity in agreement with the averaged speed of sound, as predicted by numerical solutions of the GPE.

While our calculated v_c is in good agreement with the maximal flow velocity we observe, we also find stochastic phase slips occur at a much lower rate, for lower flow speeds. An important question for future work is whether these rare phase slip events occur via quantum or thermal fluctuations. This obviously points towards further experiments studying the dynamics of phase slips as a function of temperature. Such an experiment would be analogous to those performed in liquid helium [88] and superconducting nanowire [84] systems, which have been able to identify two distinct regimes dominated by either thermal or quantum fluctuations. It should also be possible to reach the regime of one dimensional superflow, where it's possible the supercurrent decay could be fundamentally different.

Another important direction for future study would be to measure the critical velocity for higher charge superflow. One of the main sources of uncertainty in both our experiment and that in [100], is that for modest q values the flow velocity only approached the critical velocity for low values of the local chemical potential. In particular for our experiment, the deconvolution step introduces a systematic uncertainty which is quite small as a fraction of the trap roughness. However, when compared to the local chemical potential at which we observe decay, this uncertainty becomes significant. In contrast, high charged superflow would decay at larger values of the local chemical potential where uncertainties in calculating the flow velocity and critical velocity would be lessened. For now however, we decided to explore a different direction by studying the role of the spinor degree of freedom on supercurrent stability, the results of which are presented in the following chapter.

Chapter 6

Persistent currents in spinor condensates

In the previous chapter we studied the stability and decay of persistent currents in single-component condensates. We showed that decay occurred through stochastic, vortex-induced phase slips, the probability of which increased as the flow velocity approached the critical velocity. In this chapter we extend our studies to multi-component systems, in particular those involving two spin states. Such an extension is essential for the further understanding of superfluids with a vectorial order parameter, such as those in d-wave and p-wave superconductors, and certain phases of superfluid ^{3}He. These experiments are also pertinent to the application of ultracold atom systems, with persistent currents in multi-component systems a necessary aspect of many atom interferometers. Persistent currents in two-component Bose gases have been studied theoretically [183–187] but many issues remain open. Even the central question of whether, and under what conditions, this system supports persistent currents has not been settled.

In this chapter we study the stability of supercurrents in a toroidal two-component gas consisting of ^{87}Rb atoms in two different spin states. For a large spin-population imbalance we recover the long-lived metastable behaviour of the single component case in Chapter 5, with superflow persisting for over two minutes and limited only by the atom-number decay. However at a small population imbalance the onset of supercurrent decay occurs within a few seconds. We demonstrate the existence of a well-defined critical spin polarisation separating the stable and unstable current regimes. We also study the connection between spin coherence and superflow stability, and show that in our system only the modulus of the spin-polarisation vector is relevant for the stability of the supercurrent.

6.1 Multi-component condensates

Multi-component condensates are defined as systems where two or more internal quantum states are macroscopically populated. Such systems then possess internal degrees of freedom relating to the relative population and phase of each component, in addition to the usual external degrees of freedom of a single-component condensate. The

interplay between these external and internal degrees of freedom in multi-component systems can then lead to a range of phenomena not present in scalar condensates. In this section we aim to introduce some of the theory of multicomponent systems. We emphasise that a complete theoretical understanding of our observations regarding the stability and decay of a two-component superflow is still lacking. The topics covered here are therefore not intended to offer an explanation of the measurements which follow, but simply touch on some of the theory which we feel may be relevant.

The requirements for studying multi-component condensates are two fold. First the possibility of studying multi-component condensates is dependent on the collision properties of the given mixture. Many configurations suffer from the presence of scattering resonances and scattering channels with negative s-wave scattering length, leading to heating and condensate collapse respectively. Second, one requires a trapping potential capable of confining both states with non-trivial overlap. For magnetic traps this equates to studying states which posses equal magnetic moments. In a conventional magnetic trap, the spins of the atoms are frozen, constrained to follow the field direction. As a result, even though the atoms carry spin, they behave like scalar particles. Possible multi-component condensates in magnetic traps are then restricted to different hyperfine states of the same isotope, and mixtures of two different species of bosons. Conversely, in an optical trap the spins of the atoms are essentially free, providing us with an additional non-trivial degree of freedom. Possible multi-component condensates in optical traps then also include different magnetic states of a single hyperfine level. This leads to the natural distinction of multi-component condensates into two categories: mixtures and spinors.

6.1.1 Spinor condensates

A spinor is defined as a multi-component condensate containing all magnetic sublevels of a manifold of states with a single value of the hyperfine spin F. For the $F = 1$ state which we consider here, this corresponds to a condensate in the three hyperfine spin states $m_F = 1, 0$, and -1. The internal states of a spinor condensate are then related by rotational symmetry in spin space. Experimentally, long-lived spinor gases have been realised in three spin manifolds: the $F = 1$ hyperfine manifold of both ^{23}Na [188] and ^{87}Rb [189], and also the upper $F = 2$ manifold of ^{87}Rb [190]. The significance of such a system is that while the total particle number is conserved, due to the possibility of spin-exchange collisions the particle number for any one m_F state is not. For example, an atom in the $m_F = 1$ state may inelastically scatter with another in the $m_F = -1$ state to give two atoms in the $m_F = 0$ state, or vice versa.

The general formalism of the low energy Hamiltonian for a spinor condensate is given in [191, 192]. Collisions in the system are described by a pairwise interaction that is rotationally invariant in the hyperfine spin space and preserves the hyperfine spin of the individual atoms. Two identical bosons with $F = 1$ in an s-state of their

relative motion can couple to make states with total angular momentum, $\mathcal{F} = 0$ or 2, since the requirement that the wave function is symmetric under particle exchange rules out collisions with $\mathcal{F} = 1$. The general form of the interaction is then given by

$$V(\mathbf{r}_1 - \mathbf{r}_2) = \delta(\mathbf{r}_1 - \mathbf{r}_2)(g_0\mathcal{P}_0 + g_2\mathcal{P}_2), \tag{6.1}$$

where $g_\mathcal{F} = 4\pi\hbar^2 a_\mathcal{F}/m$, the operators $\mathcal{P}_\mathcal{F}$ project the wave function of a pair of atoms onto a state of total angular momentum $\mathcal{F}$, and a_0 and a_2 are the corresponding scattering lengths for the singlet and triplet channels respectively. This is usually expressed in terms of the operators for the angular momentum of the two atoms, denoted by $\mathbf{F}_1$ and $\mathbf{F}_2$. The contact interaction may then be expressed as

$$g_0\mathcal{P}_0 + g_2\mathcal{P}_2 = c_0 + c_2\mathbf{F}_1 \cdot \mathbf{F}_2, \tag{6.2}$$

where

$$c_0 = \frac{4\pi\hbar^2}{m}\frac{2a_2 + a_0}{3}, \qquad c_2 = \frac{4\pi\hbar^2}{m}\frac{a_2 - a_0}{3}. \tag{6.3}$$

The Hamiltonian in second quantised form is then

$$\begin{aligned}\hat{H} = \int d\mathbf{r} \Bigg(&\frac{\hbar^2}{2m}\nabla\hat{\Psi}_a^\dagger \cdot \nabla\hat{\Psi}_a + V_{\text{ext}}\hat{\Psi}_a^\dagger\hat{\Psi}_a \\ &+\frac{c_0}{2}\hat{\Psi}_a^\dagger\hat{\Psi}_{a'}^\dagger\hat{\Psi}_{a'}\hat{\Psi}_a + \frac{c_2}{2}\hat{\Psi}_a^\dagger\hat{\Psi}_{a'}^\dagger\mathbf{F}_{ab}\cdot\mathbf{F}_{a'b'}\hat{\Psi}_{b'}\hat{\Psi}_b\Bigg),\end{aligned} \tag{6.4}$$

where $\hat{\Psi}_a$ is the field annihilation operator for an atom in the hyperfine state $m_F = a$ ($a = 1, 0, -1$) at point $\mathbf{r}$, and the angular momentum matrices are written as

$$F_x = \frac{1}{\sqrt{2}}\begin{pmatrix}0 & 1 & 0\\ 1 & 0 & 1\\ 0 & 1 & 0\end{pmatrix}, \qquad F_y = \frac{i}{\sqrt{2}}\begin{pmatrix}0 & -1 & 0\\ 1 & 0 & -1\\ 0 & 1 & 0\end{pmatrix}, \qquad F_z = \begin{pmatrix}1 & 0 & 0\\ 0 & 0 & 0\\ 0 & 0 & -1\end{pmatrix}. \tag{6.5}$$

We note that in the absence of an external magnetic field to break the symmetry, the Hamiltonian is rotationally symmetric in spin space.

The time evolution of the field operator can be found by using the Heisenberg

equation with the Hamiltonian (6.4):

$$i\hbar\frac{\partial\hat{\Psi}_1}{\partial t} = -\frac{\hbar^2}{2m}\nabla^2\hat{\Psi}_1 + [V_{\text{ext}} - \mu_1]\hat{\Psi}_1 + (c_0 + c_2)\left[\sum_i \hat{\Psi}_i^\dagger\hat{\Psi}_i\right]\hat{\Psi}_1 + c_2\left(\hat{\Psi}_{-1}^\dagger\hat{\Psi}_0\hat{\Psi}_0 - 2\hat{\Psi}_{-1}^\dagger\hat{\Psi}_{-1}\hat{\Psi}_1\right), \tag{6.6}$$

$$i\hbar\frac{\partial\hat{\Psi}_0}{\partial t} = -\frac{\hbar^2}{2m}\nabla^2\hat{\Psi}_0 + [V_{\text{ext}} - \mu_0]\hat{\Psi}_0 + (c_0 + c_2)\left[\sum_i \hat{\Psi}_i^\dagger\hat{\Psi}_i\right]\hat{\Psi}_0 + c_2\left(2\hat{\Psi}_0^\dagger\hat{\Psi}_1\hat{\Psi}_{-1} - \hat{\Psi}_0^\dagger\hat{\Psi}_0\hat{\Psi}_0\right), \tag{6.7}$$

$$i\hbar\frac{\partial\hat{\Psi}_{-1}}{\partial t} = -\frac{\hbar^2}{2m}\nabla^2\hat{\Psi}_{-1} + [V_{\text{ext}} - \mu_{-1}]\hat{\Psi}_{-1} + (c_0 + c_2)\left[\sum_i \hat{\Psi}_i^\dagger\hat{\Psi}_i\right]\hat{\Psi}_{-1} + c_2\left(\hat{\Psi}_1^\dagger\hat{\Psi}_0\hat{\Psi}_0 - 2\hat{\Psi}_1^\dagger\hat{\Psi}_1\hat{\Psi}_{-1}\right), \tag{6.8}$$

where the three chemical potentials μ_i, are defined such that the total particle number and magnetisation are conserved. In this formalism one can explicitly identify the spin mixing terms. Importantly, such spin exchanging collisions coherently transfer populations between different spin states, with coherent oscillations observed in m_F populations due to such collisions [193, 194]. Coherent spin dynamics preserve the coherence between the different internal state components of a spinor BEC, and many of the characteristic phenomena of spinors, such as spontaneous magnetisation and symmetry breaking, are physical consequences of this coherence. In a mixture where such spin-exchange terms are absent, while there can still be coherence between the internal state populations, such coherence does not affect how the physical system evolves. Therefore, while a mixture can be considered to evolve as an incoherent overlap of individual condensates, such a picture is not valid for spinor gases.

The significance of spin dependent interactions is determined by the value of c_2, which is generally much smaller in magnitude than c_0. Nevertheless, the sign and magnitude of c_2 is found to have significant implications on the properties of a spinor gas, including its ground state structure, spin wave modes, and possible topological spin structures such as coreless vortex states. So far we have neglected any possible effect due to long-range magnetic dipole-dipole interactions (MDDI). For most ultracold atom experiments the MDDI is negligible in comparison to the spin-independent contact interaction[1]. For spinor gases however, since the MDDI is both spin-dependent and long-ranged, it is expected to play a significant role in determining the low field ground state [197], and the long range formation of spin structures [198]. Experimental evidence for the role of MDDI in spinor condensates has even been observed in [199], where the spontaneous dissolution of long-wavelength spin textures in a ^{87}Rb $F = 1$ spinor BEC was attributed to long-range magnetic dipole interactions. As we have alluded to,

[1]This is not the case for condensates of ^{52}Cr [195] and ^{164}Dy [196], which have exceptionally large magnetic dipole moments, where the energy associated with long-range dipole interactions can become comparable to that of the mean-field interaction energy.

spinor condensates exhibit a dizzying array of static and dynamic properties. Reviews of some of the pertinent experiments and directions of research in this expansive field are available in [200] and [201]. We now consider the often simpler case of a condensate mixture, where spin exchange collisions are forbidden.

6.1.2 Mixtures

A mixture is defined as a multi-component condensate where the particle number for each species is strictly conserved. If we consider a mixture of two-components labeled 1 and 2 with equal mass, which experience the same trapping potential, the GP energy functional is given by [19]

$$E = \int d\mathbf{r} \left(\frac{\hbar^2}{2m}|\nabla\Psi_1|^2 + V_{\text{ext}}(\mathbf{r})|\Psi_1|^2 + \frac{\hbar^2}{2m}|\nabla\Psi_2|^2 + V_{\text{ext}}(\mathbf{r})|\Psi_1|^2 + \frac{g_{11}}{2}|\Psi_1|^4 + \frac{g_{22}}{2}|\Psi_2|^4 + g_{12}|\Psi_1|^2|\Psi_2|^2 \right). \tag{6.9}$$

The interaction parameters g_{11}, g_{22}, and $g_{12} = g_{21}$ are related to the respective scattering lengths a_{11}, a_{22}, and a_{12} by $g_{ij} = 4\pi\hbar^2 a_{ij}/m$. Minimising this energy for fixed particle number one obtains the time-independent coupled GP equations

$$-\frac{\hbar^2}{2m}\nabla^2\Psi_1 + V_{\text{ext}}(\mathbf{r})\Psi_1 + g_{11}|\Psi_1|^2\Psi_1 + g_{12}|\Psi_2|^2\Psi_1 = \mu_1\Psi_1 \tag{6.10}$$

$$-\frac{\hbar^2}{2m}\nabla^2\Psi_2 + V_{\text{ext}}(\mathbf{r})\Psi_2 + g_{22}|\Psi_2|^2\Psi_2 + g_{12}|\Psi_1|^2\Psi_2 = \mu_2\Psi_2. \tag{6.11}$$

We therefore see that for a mixture, each component simply experiences the mean field potential arising from both populations. The coupling between the two components through the intercomponent mean field as determined by the value of g_{12}, yields structures and dynamics which are not present in a single-component BEC.

The two-component persistent current we study is a mixture of atoms in the $|F = 1, m_F = 1\rangle$ and $|F = 1, m_F = 0\rangle$ magnetic states, and therefore is a spinor gas. We note however that our system is in an external magnetic field of 10 G, and therefore due to the quadratic Zeeman shift, the energy gap between the $m_F = -1$ and $m_F = 0$ states is 14.4 kHz larger than the energy gap between the populated $m_F = 1$ and $m_F = 0$ states. Spin exchange collisions to the $m_F = -1$ are therefore energetically prohibited, and for an initial state where the $m_F = -1$ state is not populated, the populations of the $m_F = 1$ and $m_F = 0$ states are conserved. Taking the time dependent GPE equations for a spinor in (6.6) and (6.7) and removing spin-exchange terms, one retrieves the equations of motion for a mixture with inter and intra-species scattering lengths given by

$$a_{11} = a_2, \qquad a_{00} = \frac{2a_2 + a_0}{3}, \qquad a_{10} = a_2. \tag{6.12}$$

We therefore anticipate our spinor condensate to be described by a mixture with the appropriate scattering lengths given above in terms of the singlet and triplet scattering lengths. Such a view is confirmed experimentally by the fact that we observe no population of the $m_F = -1$ state due to coherent scattering from the $m_F = 0$ state.

Calculation of the scattering lengths in terms of singlet and triplet scattering lengths can also be done by decomposing the states of total angular momentum $|\mathcal{F}, m_\mathcal{F}\rangle$ using the appropriate Clebsch-Gordan coefficients

$$|\mathcal{F}, m_\mathcal{F}\rangle = \sum_{m_1=-F_1}^{m_1=F_1} \sum_{m_2=-F_2}^{m_2=F_2} |F_1, m_{F1}, F_2, m_{F2}\rangle \langle F_1, F_2; m_{F1}, m_{F2}| \, |\mathcal{F}, m_\mathcal{F}\rangle \,, \tag{6.13}$$

where $F_1 = 1$ and $F_2 = 1$. One can then express the state of the two incident particles $|F, m_{F1}, F, m_{F2}\rangle$ in terms of states of their combined total angular momentum $\mathcal{F}$:

$$|m_{F1} = 1, m_{F2} = 1\rangle = |\mathcal{F} = 2, m_\mathcal{F} = 2\rangle \tag{6.14}$$

$$|m_{F1} = 0, m_{F2} = 0\rangle = \sqrt{\frac{2}{3}} \, |\mathcal{F} = 2, m_\mathcal{F} = 0\rangle - \sqrt{\frac{1}{3}} \, |\mathcal{F} = 0, m_\mathcal{F} = 0\rangle \tag{6.15}$$

$$\frac{1}{\sqrt{2}} \left(|m_{F1} = 0, m_{F2} = 1\rangle + |m_{F1} = 1, m_{F2} = 0\rangle\right) = |\mathcal{F} = 2, m_\mathcal{F} = 1\rangle \,. \tag{6.16}$$

from which one confirms the results of (6.12). The values of a_0 and a_2 for the $F = 1$ state of ^{87}Rb are given as [68, 202] $a_0 = (101.78 \pm 0.2)a_B$ and $a_2 = (100.4 \pm 0.1)a_B$, where a_B is the Bohr radius. From this one calculates the relevant inter and intra-species scattering lengths for our system as

$$a_{11} = (100.4 \pm 0.1)a_B, \quad a_{00} = (100.86 \pm 0.13)a_B, \quad a_{10} = (100.4 \pm 0.1)a_B. \tag{6.17}$$

As we discuss in Section 6.1.4, the fact that these values are so close has important consequences for the ground state and dynamics of our system. Strictly speaking, one may only decompose the scattering lengths in terms of singlet and triplet channels at low magnetic fields where F is a good quantum number [191]. We assume this decomposition is valid in our experiment since the associated Zeeman energies are much smaller than the hyperfine splitting.

In this chapter we use the pseudo-spin representation, where our two-component mixture is represented by a spin-1/2 BEC [203]. Introducing the normalised spinor $\chi(\mathbf{r}) = [\chi_1, \chi_2]^T = [|\chi_1|e^{i\theta_1}, |\chi_2|e^{i\theta_2}]^T$, we can decompose the wave function of each component as $\Psi_i = \sqrt{n(\mathbf{r})}\chi_i(\mathbf{r})$, where $n(\mathbf{r})$ is the total density of both components. Defining the spin density as $\mathbf{S} = \chi(\mathbf{r})^\dagger \sigma \chi(\mathbf{r})$, where σ is the Pauli spin matrix, the unit spin vector is then defined as

$$\begin{pmatrix} S_x \\ S_y \\ S_z \end{pmatrix} = \begin{pmatrix} 2\mathrm{Re}(\chi_1\chi_2^*) \\ 2\mathrm{Im}(\chi_1\chi_2^*) \\ |\chi_1|^2 - |\chi_2|^2 \end{pmatrix}. \tag{6.18}$$

We therefore represent our two-component spinor BEC as a unit vector on the Bloch sphere, where $m_F = 1$ and $m_F = 0$ are the up and down components of the spin 1/2 spinor respectively. This formalism implies a relative phase coherence between the up and down states. Decoherence then corresponds to a shortening of the state vector from $|\mathbf{S}| = 1$. The energy functional (6.9) can then be written in the form

$$E = \int d\mathbf{r} \left(\frac{\hbar^2}{2m}(\nabla\sqrt{n})^2 + \frac{\hbar^2 n}{8m}(\nabla\mathbf{S})^2 + \frac{mn}{2}\mathbf{v}_{\text{eff}}^2 + V_{\text{ext}} + \frac{n^2}{2}(\gamma_0 + \gamma_1 S_z + \gamma_2 S_z^2) \right), \tag{6.19}$$

where we define the coupling constants

$$\begin{aligned} \gamma_0 &= \frac{g_{11} + g_{22} + 2g_{12}}{4}, \\ \gamma_1 &= \frac{g_{11} - g_{22}}{2}, \\ \gamma_2 &= \frac{g_{11} + g_{22} - 2g_{12}}{4}, \end{aligned} \tag{6.20}$$

the spin stiffness

$$(\nabla\mathbf{S})^2 = (\nabla S_x)^2 + (\nabla S_y)^2 + (\nabla S_z)^2, \tag{6.21}$$

and the effective velocity

$$\mathbf{v}_{\text{eff}} = \frac{\hbar}{2im}(\chi_1^*\nabla\chi_1 - \chi_1\nabla\chi_1^* + \chi_2^*\nabla\chi_2 - \chi_2\nabla\chi_2^*) \tag{6.22}$$

$$= \frac{\hbar}{2m}\left[\nabla(\theta_1 + \theta_2) + \frac{S_z(S_y\nabla S_x - S_x\nabla S_y)}{S_x^2 + S_y^2}\right], \tag{6.23}$$

which depends both on the gradient of the total phase and that of the pseudo-spin. This form illustrates that for a general mixture where $g_{11} \neq g_{22} \neq g_{12}$, the system experiences a fictitious interaction-induced linear and quadratic Zeeman shift which breaks the rotational symmetry in our pseudo-spin space. The form of the effective velocity also has important connotations for the stability of persistent currents in a Bose mixture. In general we note that there is now an interplay between mass currents, associated with the gradient of the phase, and spatial variations in the spin vector. Formation of spin textures is energetically costly due to the presence of the $(\nabla\mathbf{S})^2$ term, which introduces a spin stiffness to the system. This equation is analogous to the classical nonlinear sigma model which describes Heisenberg ferromagnets.

6.1.3 Dynamic stability

In Chapter 5 we found that the onset for superflow decay by phase slips could be understood by considering the excitation spectrum of the system. In that same spirit we now consider the excitation spectrum for a two-component mixture described by equations (6.10) and (6.11). For a uniform system the time-dependent GPE takes the

form

$$i\hbar\frac{\partial\Psi_1}{\partial t} = \left[-\frac{\hbar^2}{2m}\nabla^2 + g_{11}|\Psi_1|^2 + g_{12}|\Psi_2|^2\right]\Psi_1 \tag{6.24}$$

$$i\hbar\frac{\partial\Psi_2}{\partial t} = \left[-\frac{\hbar^2}{2m}\nabla^2 + g_{22}|\Psi_2|^2 + g_{12}|\Psi_1|^2\right]\Psi_2, \tag{6.25}$$

where the wavefunctions are normalised as $|\Psi_i|^2 = n_i$, where $n_i = N_i/V$ is the particle density for component i. As before, when we calculated the excitations of a single species uniform condensate in Section 2.3.1, we consider plane wave perturbations to the ground state of the form

$$\Psi_i(t) = e^{-i\mu_i t/\hbar}(\Psi_i^{(0)} + \delta\Psi_i(t)), \tag{6.26}$$

where

$$\delta\Psi_i(t) = u_i e^{-i(\omega t - \mathbf{q}\cdot\mathbf{r})} + v_i^* e^{i(\omega t - \mathbf{q}\cdot\mathbf{r})} \tag{6.27}$$

$$\mu_i = g_{ii}n_i + g_{ij}n_j, \tag{6.28}$$

for the two components $\{i, j\} = \{1, 2\}$. Inserting this into the coupled, time-dependent GP equations we obtain the matrix equation

$$\hbar\omega\begin{pmatrix} u_1 \\ v_1 \\ u_2 \\ v_2 \end{pmatrix} = \begin{pmatrix} \epsilon_q + g_{11}n_1 & g_{11}n_1 & g_{12}\sqrt{n_1n_2} & g_{12}\sqrt{n_1n_2} \\ -g_{11}n_1 & -\epsilon_q - g_{11}n_1 & -g_{12}\sqrt{n_1n_2} & -g_{12}\sqrt{n_1n_2} \\ g_{12}\sqrt{n_1n_2} & g_{12}\sqrt{n_1n_2} & \epsilon_q + g_{22}n_2 & g_{22}n_2 \\ -g_{12}\sqrt{n_1n_2} & -g_{12}\sqrt{n_1n_2} & -g_{22}n_2 & -\epsilon_q - g_{22}n_2 \end{pmatrix}, \tag{6.29}$$

where $\epsilon_q = \hbar^2q^2/2m$ is the free particle energy. The energies of the excitations are then given by the determinant of this matrix as

$$(\hbar\omega)^2 = \frac{1}{2}(\epsilon_1^2 + \epsilon_2^2) \pm \frac{1}{2}\sqrt{(\epsilon_1^2 - \epsilon_2^2)^2 + 16\epsilon_q^2 n_1 n_2 g_{12}^2}, \tag{6.30}$$

where

$$\epsilon_1^2 = 2g_{11}n_1\epsilon_q + \epsilon_q^2 \tag{6.31}$$

$$\epsilon_2^2 = 2g_{22}n_2\epsilon_q + \epsilon_q^2. \tag{6.32}$$

In the limit that we remove the inter-species coupling ($g_{12} = 0$), or the density of one of the components goes to zero, we retrieve the excitation spectrum for a uniform single species condensate which we derived in Section 2.3.1. The condition for dynamic stability is that all the eigenfrequencies are real. From (6.30) this correspond to the condition

$$g_{11}g_{22} > {g_{12}}^2. \tag{6.33}$$

This is often expressed as the criterion for the two components to be miscible. If this condition is not met, the mean field energy each component experiences from the other species is greater than that which it experiences from itself, and hence the lowest energy configuration is for the two-components to separate spatially. If this is the case, the time scale of this phase separation is given by the value of the largest imaginary eigenvalue, and the length scale of the spin textures which form is given by the wavenumber q associated with this eigenfrequency. The dynamics of such phase separation have been observed experimentally in [204–206].

For our two components, $m_F = 1$ and $m_F = 0$, the scattering lengths (6.17) are such that we anticipate our system to be dynamically stable and therefore miscible. As the scattering lengths are so close however, the maximum energy barrier towards phase separation, occurring for equal populations in each component, is only 3 Hz per particle. We therefore find that our two-component system is extremely sensitive to external factors such as magnetic field gradients and the polarisation of our optical trap, which can differentiate between the two states and overcome this small energy barrier towards phase separation. The cancelation of such effects is discussed in Section 6.1.4. Due to fluctuations of both the experiment, and inherent thermal and quantum fluctuations of the system [148], over very long times we find the system is unstable towards the formation of spin textures. Our measurements of this effect are presented in Section 6.1.5.

Our calculations of the excitation spectrum for a two-component condensate in a ring are shown in figure 6.1. This calculation was done by extending our numerical calculation for the 2D single species BEC in a ring (explained in Appendix B) to the two-component case. A similar result is obtained by mapping the excitation spectrum calculated for a uniform two-component condensate in (6.30), to that of a one dimensional system on a ring. This amounts to simply replacing the interaction parameters, g_{ij}, with effective 1D parameters averaged over the radial and vertical directions. Due to the very small spin dependent energy, we find that the dispersion relation is very close to quadratic. The energy barrier to formation of long-wavelength excitations is therefore very small, however the restriction that the wavefunction is single valued leads to quantised values of the angular wavenumber m, which increases this somewhat. The form of the excitation spectrum is very similar for all ratios of the two populations. The inset, which shows the spectrum at small values of m for three different ratios of the two populations, actually shows that the case of equal populations in each component is the most stable. As the population imbalance becomes larger the system becomes less stable.

Unlike the single species case, inferring the stability of persistent currents from calculations of dynamic stability is clearly not correct for the two-component case. All this calculation tells us is that if one adds a small admixture of a second component to the system, the energy barrier to creating spin textures is very small. As the ad-

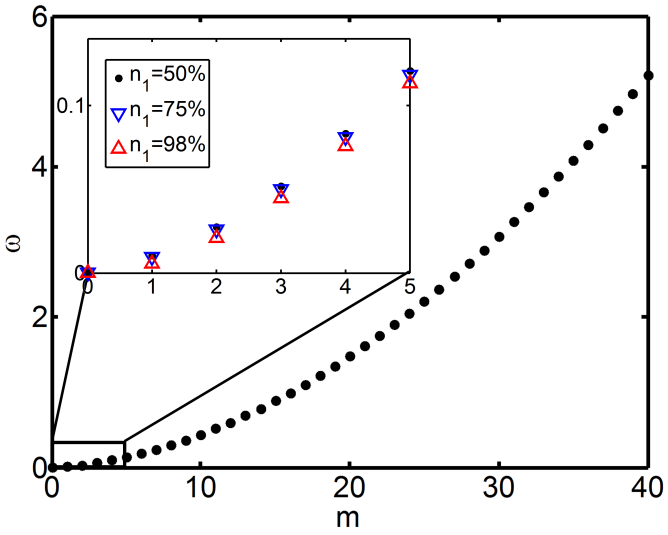

Figure 6.1: Excitation spectrum for an annular two-component BEC: Plotted is the excitation energy (in units of $\hbar\omega_r$) versus angular wavenumber for numerical solutions of the 2D GPE for a two-component mixture in a ring with equal populations in the $m_F = 1$ and $m_F = 0$ states. This calculation predicts an excitation energy close to quadratic in m, and therefore a small energy barrier to the formation of long-wavelength excitations. Inset is the initial part of the slope for the three different mixture populations $N(m_F = 1) : N(m_F = 0) = 0.5 : 0.5, 0.75 : 0.25$, and $0.98 : 0.02$, as indicated by the black dots, blue triangles, and red triangles respectively. The spectrum is close to identical under exchange of the relative populations of the two components, $N(m_F = 1)$ and $N(m_F = 0)$.

mixture becomes larger, the energy cost of creating such spin textures increases in a trivial manner. The stability of the system against forming such excitations does not directly tell us about the stability of the system against dissipating angular momentum. Indeed such a calculation shows us that if we take the single species system, which we have shown to possess a large critical velocity, and add a vanishing small admixture of the second component, this critical velocity all but vanishes. Such a discontinuity in behaviour is unphysical, and clearly indicates that the excitations we are considering in the two-component case are distinct from those in the single-component case, and do not relate directly to the decay of supercurrents.

The primary tool by which we were able to understand the onset of superfluid instability in the single species case does not then seem to apply to the two-component case. As we will show, while we have been able to accurately measure the conditions under which a two-component persistent current becomes unstable, as yet we do not fully understand this condition. This problem is therefore perfectly poised for further theoretical work to both explain our findings, and point the way to future experiments.

6.1.4 Phase separation

To observe long-lived persistent currents in a two-component condensate, it was first important to remove environmental factors which would differentiate between the two

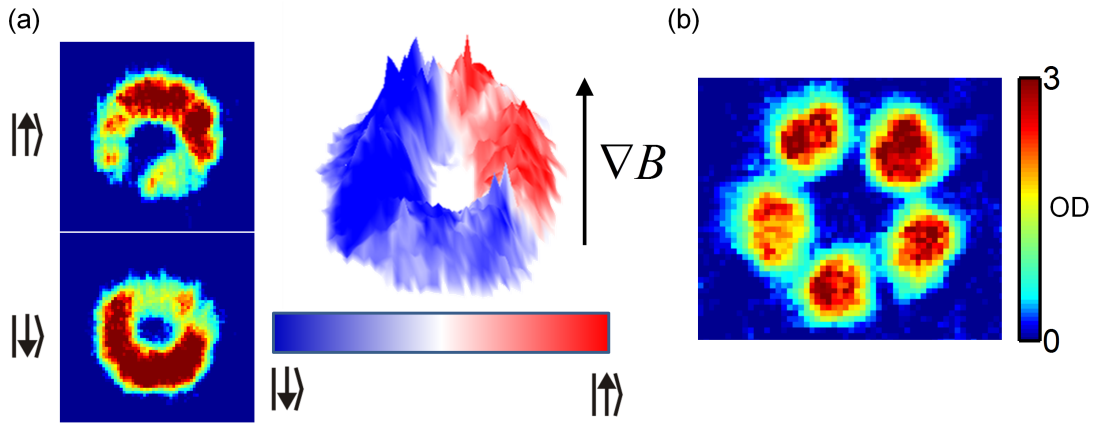

Figure 6.2: Phase separation: (a) Absorption images of the $m_F = 1$ ($|\uparrow\rangle$) and $m_F = 0$ ($|\downarrow\rangle$) states phase separating in the presence of a weak magnetic field gradient. The surface plot shows the total density, which is observed to remain constant during the phase separation. The colour of the surface indicates the relative population of the two components. (b) Absorption image of the $m_F = 1$ state only, in an $\ell = 5$ LG beam ring trap in the presence of a small amount of leakage Gaussian light. The density of the $m_F = 0$ state is the inverse of this, such that the total density is uniform around the ring.

states. For the $m_F = 1$ and $m_F = 0$ states which have different magnetic moments, the primary concern is magnetic field gradients. In the presence of in-plane gradients the two-component gas is extremely susceptible to phase separation. In figure 6.2 (a) we show in-trap absorption images of the $m_F = 1$ ($|\uparrow\rangle$) and $m_F = 0$ ($|\downarrow\rangle$) states phase separating due to a small field gradient. The total density is uniform around the ring, and only by simultaneously trapping two components can one detect the presence of the magnetic gradient. The orientation of the phase separation is repeatable, and therefore we were able to cancel this gradient by the use of two orthogonal compensation coils positioned close to the atoms. The sensitivity of the two-component gas is remarkable, and by ensuring the two states showed perfect and repeatable spatial overlap even after 10 seconds hold time, we minimised in-plane magnetic gradients to $< 5 \times 10^{-5}$ G/cm, roughly equivalent to an energy difference across the ring of 1 Hz per particle.

A second, less obvious, cause of phase separation turned out to be the imperfect polarisation of our ring trap light. As derived in Section 4.3.2, the dipole potential for a multilevel system depends on the product of the polarisation of the trapping light and m_F state of the atom. Our LG trapping beam has equal components of σ^+ and σ^- polarised light, and hence should trap all m_F states equally. In reality, slight misalignment with respect to the field direction or polarisation dependent reflections will cause a marginal imbalance in the polarisations, and hence one m_F state will see a deeper trap than the other. For most situations this simply manifests as a small global shift in the potential and has no effect on the experiment. Due to our Raman setup (figure 4.7), a small amount of LG light propagates along the Gaussian path and does not pick up a $2\pi\ell$ phase winding. Interference of these two beams at the atoms creates a

small azimuthal corrugation in the LG intensity, which for a single species condensate is undetectable. If we trap two species however, the combination of this interference and the imperfect polarisation, cause a phase separation of the like shown in figure 6.2 (b). The state which experiences the slightly deeper potential moves into the minima of the corrugation, and the other spin state fills the gaps to preserve the total density. This effect appears identical to the matter-wave interference of Section 4.4.1, but is simply due to the trapping potential. To remove this effect we place a shutter in the path of the Gaussian light, which is only briefly opened during the Raman transfer.

Having canceled these two effects, we observe the two states remain mixed after 10 seconds hold time. As shown in the next Section, at even longer times we find the system is unstable towards forming variations in the densities of the two individual components. Neither the direction nor degree of such spin textures is repeatable however, and therefore we cannot identify the source of these dynamics as being either technical, or as inherent fluctuations present in the two-component condensate.

6.1.5 Spin domain formation

There have been many studies on spin mixing dynamics in degenerate spinor Bose gases [200]. Such dynamics are associated with the redistribution of atomic populations among spin states and the formation of spin domains and spin textures. Of those experiments, [206] and [207] also studied two-component $F = 1$ spinor gases in the presence of large quadratic Zeeman shifts, where spin-exchange scattering to the third m_F state was energetically eliminated. Both of these studies used immiscible mixtures, where the gas was dynamically unstable to phase separation. Due to the small spin dependent energies, such systems take several seconds to reach equilibrium, and exhibit interesting features such as the growth and coarsening of large scale spin domains which are nucleated by initial fluctuations.

In our case of $m_F = 1$ and $m_F = 0$, the two states are miscible. To characterise our two-component state we define the longitudinal spin polarisation

$$P_z = \frac{N_\uparrow - N_\downarrow}{N_\uparrow + N_\downarrow}, \tag{6.34}$$

where $N_\uparrow(N_\downarrow)$ is the number of atoms in the $m_F = 1(m_F = 0)$ state. Using an RF $\pi/2$ pulse we prepare an initial superposition state, $|\Psi\rangle = (|\uparrow\rangle + |\downarrow\rangle)/\sqrt{2}$ with equal magnetic state populations ($P_z = 0$), and then hold for various times. We then measure the local variation of P_z by imaging only the $m_F = 1$ state using a microwave π pulse to transfer the population to the imageable $|2, 2\rangle$ state. In our system, for the starting atom number, the width of the annulus ($R_r \approx 6$ μm) is comparable to the spin healing length ($\xi_s = 1/\sqrt{8\pi n \frac{a_0 - a_2}{3}} \approx 4$ μm)[1] [199]. As the atom number decays during

[1]The spin healing length is similarly determined as the length below which the kinetic energy of spins wins over the spin-dependent interaction energy.

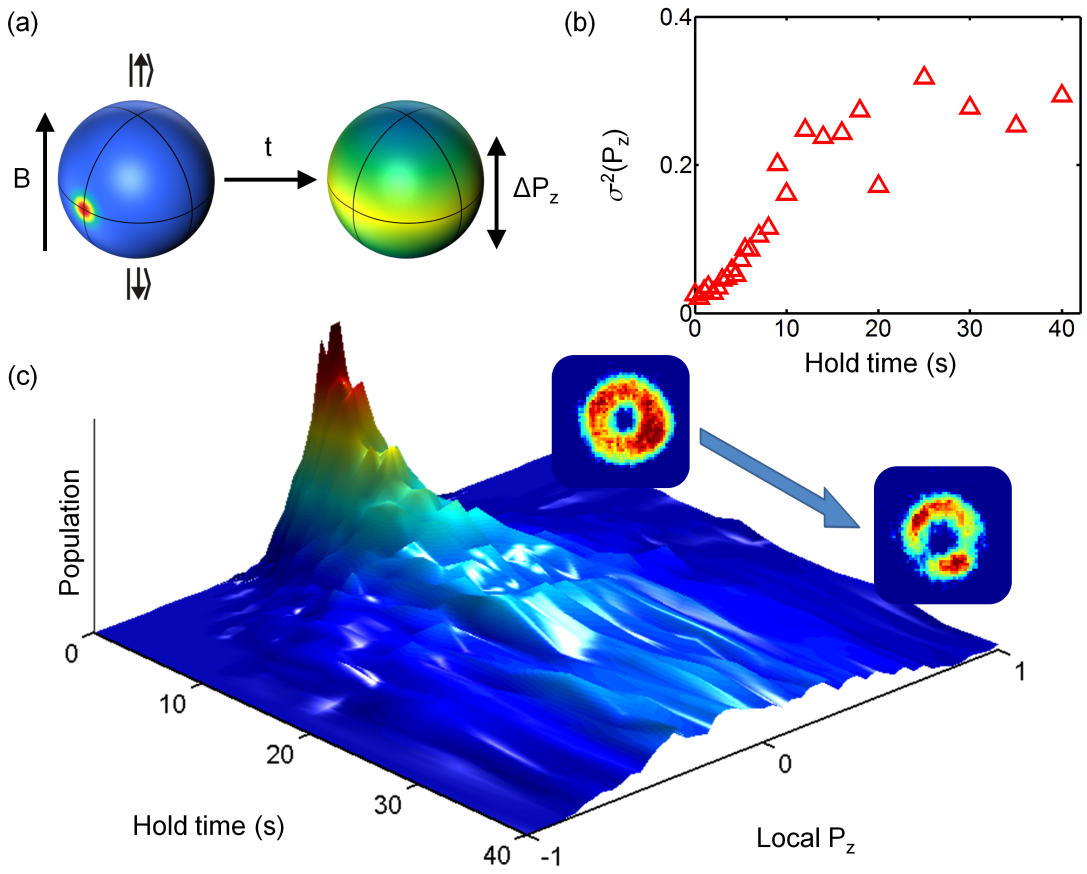

Figure 6.3: Spin domain formation: (a) Using an RF $\pi/2$ pulse at $t = 0$ we prepare a spin-superposition state with equal populations in each magnetic state ($P_z = 0$). Allowing the state to evolve in time, the superposition decoheres and the transverse spin polarisation decays (Section 6.3). We also observe a spreading in P_z values about the mean which we detect by imaging only the $|\uparrow\rangle$ state using a microwave transfer. (b) Evolution of the variance of P_z with hold time. Each data point is an average of 8 images, and normalised to control shots which account for variations in the total density due to the imperfect trapping potential. (c) The distribution of measured local P_z as a function of hold time. Insets show typical absorption images of the $|\uparrow\rangle$ state only, at short and long hold times. At all times the total density is uniform.

evolution, the width of the annulus decreases while ξ_s increases, and hence the spin degree of freedom becomes increasingly one-dimensional. We therefore approximate that the spin structure only varies significantly azimuthally around the ring and not across the width of the annulus. Hence we integrate the density over the radial direction when measuring P_z.

The results of this measurement are shown in figure 6.3. While the total P_z is conserved, we observe the formation of local spin domains of high and low P_z, the variance of which is plotted against hold time in figure 6.3 (b). We find the fluctuations in P_z grow over the first 20 seconds and then saturate. The saturation value is close to the value of 1/3, which one would obtain if the distribution of P_z values was uniform

between -1 and 1. In figure 6.3 (c) we plot the evolution of the P_z distribution with time. At short times the P_z values are tightly distributed about the initial $P_z = 0$ value, corresponding to all state vectors lying on the equator of the Bloch sphere. With increasing hold time an increasing range of P_z values is observed, corresponding to atoms moving off the equator of the Bloch sphere. At very long times the distribution is close to uniform for all P_z values, corresponding to a uniform distribution of state vectors over the Bloch sphere. This particular data is taken for an initial superposition state which is rotating with $q = 3$ at $t = 0$. The same evolution of P_z values is observed for the non-rotating case. The fact that the distribution of P_z values shows no angular dependence around the ring suggests this is not a technical artifact resulting from remnant magnetic gradients.

If one only considers the s-wave contact interaction, then our spinor BEC should be dynamically stable and the observed formation of spin textures at long hold times is difficult to explain. The fact that the energy barrier to phase separation is so small though, means additional mechanisms which one usually neglects may have a significant effect. In the experiment of Vengalatorre *et al.* [199] for example, it was found for a ^{87}Rb $F = 1$ spinor condensate that the role of magnetic dipole-dipole interactions could have a significant effect on the stability of spin structures. The influence of dipolar interactions on the spinor gas was evidenced by the spontaneous dissolution of deliberately imposed long-wavelength spin structures, in favour of a finely modulated pattern of spin domains. This effect was ascribed to the magnetic dipole energy which disfavours the homogenously magnetised state. One could therefore hypothesise that the spin dynamics we observe may similarly be driven by magnetic dipole interactions.

6.2 Two-component supercurrent

To prepare our two-component supercurrent we first prepare a single-component persistent current using the same method explained in Chapter 4. As before, we load our condensate into the ring trap created by intersecting the sheet laser beam with an LG^{ℓ} beam of $\ell = 3$. Due to changes in the sheet beam optics, the vertical trapping frequency is reduced to $\omega_z = 2\pi \times 340$ Hz. Initially we load about $N \approx 150 \times 10^3$ atoms into the ring trap, which we then hold for 6 seconds to reduce the starting atom number for our measurements to $N \approx 100 \times 10^3$. This reduction in atom number has no discernible effect on the supercurrent stability, but is found to make the angular momentum state of the two-component supercurrent easier to measure. Due to spin dynamics, the presence of both spin states leads to azimuthal density variations in the density holes which we observe at long TOF. These density variations can make the radius of the hole, and hence the angular momentum of the state, harder to accurately quantify. Empirically we find a reduced atom number improves our fitting procedure and enhances the signal of quantisation.

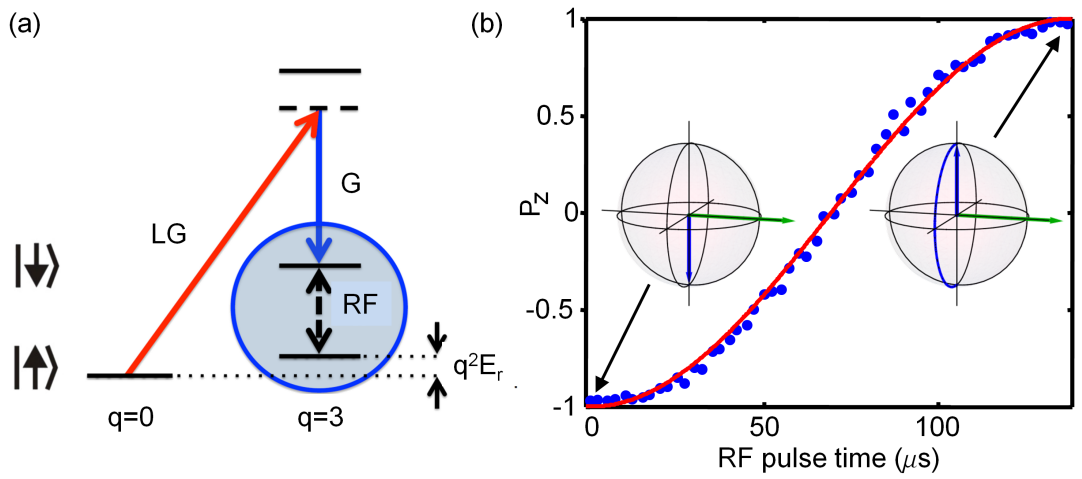

Figure 6.4: Preparation of a two-component supercurrent: (a) Supercurrent is induced in a single component condensate by a Raman transfer of atoms between the two spin states $|\uparrow\rangle$ and $|\downarrow\rangle$, using the LG beam and an auxiliary Gaussian (G) beam. A two-component gas is then created by coupling the same $|\uparrow\rangle$ and $|\downarrow\rangle$ states with an RF field which imparts no angular momentum to the system. Here we denote the energy difference between the stationary and rotating $|\uparrow\rangle$ state of q^2E_r, with $E_r/h \approx 0.4$ Hz. (b) Plot of measured spin polarisation, P_z, versus RF pulse time. By varying the time of the RF pulse between $t_{RF} = 0$ and $t_{RF} = t_\pi = 140$ μs we can prepare a state of any given P_z. Also shown is the Bloch sphere representation of the rotation of the initial state vector of our spin 1/2 system with RF pulse time. The blue arrow denotes our two-component state vector, while the green arrow denotes the effective magnetic field created by the RF coupling, which the state vector then precesses about.

To set the gas into rotation the auxiliary Gaussian beam is flashed on briefly, transferring the atoms via a two-photon Raman transfer between the initial $|F = 1, m_F = 1\rangle$ state and the final $|F = 1, m_F = 0\rangle$ state with angular momentum $3\hbar$ per atom. Any atoms which are not transferred are removed from the trap by a microwave transfer and resonant imaging pulse, as described in Section 4.3.1, creating a pure single-component persistent current. To amplify any difference between the single and two-component supercurrent, we maximise the single-component superflow lifetime by reducing the intensity of the LG trapping light to create the smoothest trap possible. Our final ring trap has radius 12 μm, radial trapping frequency $\omega_r = 2\pi \times (53 \pm 5)$ Hz, and the trap depth is about twice the BEC chemical potential, $\mu_0/h \approx 750$ Hz. At this point the azimuthal variations in the local chemical potential are less than 10% and the single component superflow persists for up to two minutes, limited only by the eventual atom loss.

The $|F = 1, m_F = 1\rangle$ and $|F = 1, m_F = 0\rangle$ states also define the $|\uparrow\rangle$ and $|\downarrow\rangle$ states, respectively, of the spin space for our two-component supercurrents. Since the $m_F = 1$ and 0 states are split in an external field of 10 G, the $m_F = -1$ state is detuned from Raman and RF resonances by 14.4 kHz. We therefore observe negligible population of the $m_F = -1$ state during state transfers, and population of the $m_F = -1$ state by spin exchange collisions is prohibited by energy conservation. To first order, the large

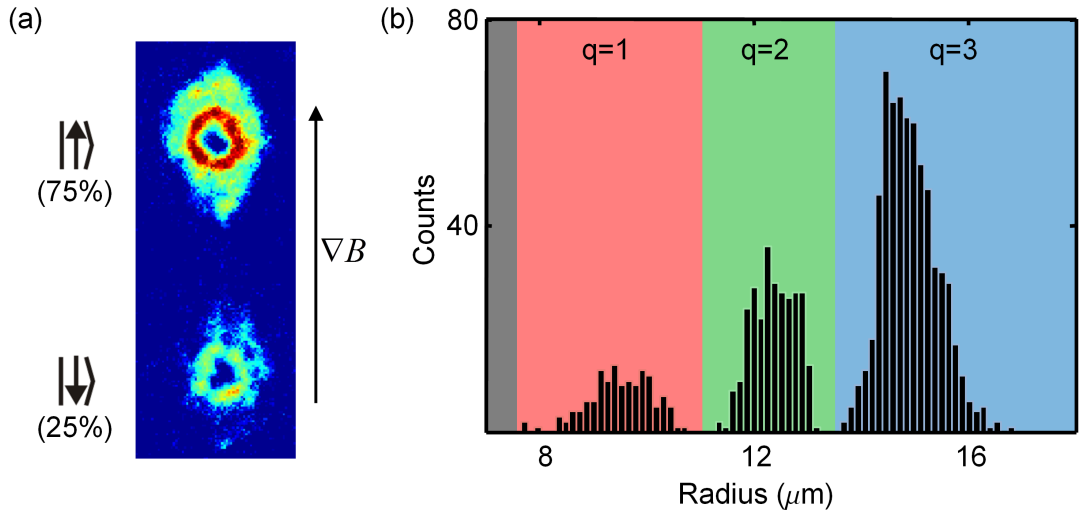

Figure 6.5: Detection of two-component supercurrent: (a) Time-of-flight absorption image of the atoms, with spin states separated using a Stern-Gerlach gradient. The rotational state q is deduced from the radius R characterising the central hole in the density distribution. The longitudinal polarisation P_z is measured directly from the image using the relative populations of the two spin states. The image shown was taken after $t = 4$ s of rotation; $P_z = 0.44$ and $q = 3$ for both spin states. (b) Histogram of ≈ 900 measurements of R at various P_z and t. Once again the background colours indicate the corresponding q state for a given R, with $q = 3$, 2, 1, and 0 indicated by the blue, green, red, and black regions respectively.

bias field has eliminated the presence of the $m_F = -1$ state, reducing the parameter space of our system of our $F = 1$ spinor to a two-component mixture.

The protocol for preparing a two-component supercurrent is illustrated in figure 6.4 (a). After preparing a pure $|q = 3, \downarrow\rangle$ rotating state, we couple $|\uparrow\rangle$ and $|\downarrow\rangle$ by an RF field which carries no orbital angular momentum and does not affect the motional state of the atoms. As shown in figure 6.4 (b), by varying the length of the RF pulse t_{RF} in the range $0 \leq t_{RF} \leq t_\pi$, one can prepare a state of arbitrary longitudinal spin polarisation, P_z. The prepared state is then in a superposition of the $m_F = 1$ and $m_F = 0$ state, both rotating in the same direction with angular momentum $3\hbar$ per atom:

$$|\Psi(\phi)\rangle = (\sin(\phi/2)\,|\uparrow\rangle + \cos(\phi/2)\,|\downarrow\rangle)e^{-iq\theta}. \tag{6.35}$$

Here $\phi = \Omega_{RF} t_{RF}$, where Ω_{RF} is the RF Rabi frequency. In this state $P_z = \cos(\phi)$ and the gas is still fully spin polarised with polarisation vector $\vec{P} = [\sin(\phi), 0, -\cos(\phi)]$ and $|\vec{P}| \equiv P = 1$.

After preparing a co-rotating ($q = 3$) two-component supercurrent in a specific spin state, we let it evolve in the ring trap for a time t and then probe it by absorption imaging after 29 ms time-of-flight expansion as explained in Section 4.4.2. We separate the two spin components with a Stern-Gerlach gradient and directly detect the longitudinal spin polarisation, P_z, by measuring the populations of the two spin states. As before, the rotational state, $0 \leq q \leq 3$, is seen in the size R of the central density hole

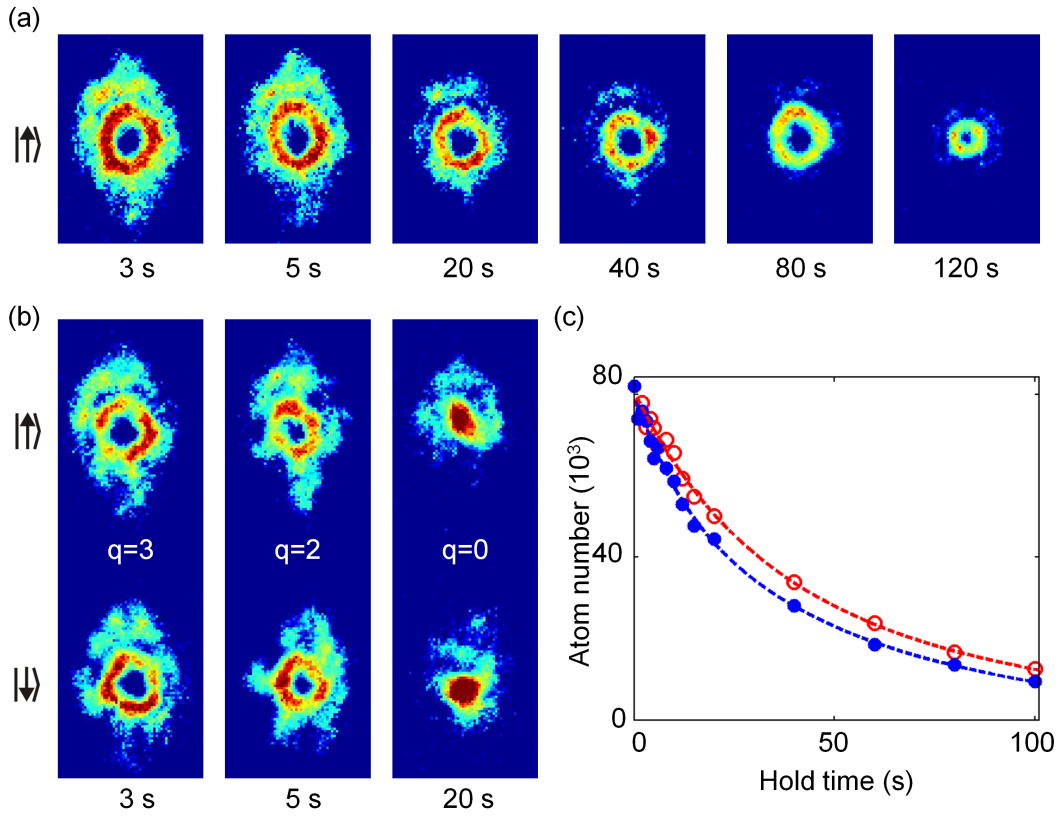

Figure 6.6: Single versus two-component supercurrent stability: (a) In a pure $|\uparrow\rangle$ state with $P_z = 1$ supercurrent is observed to persist for over 2 minutes, with no phase slips occurring for ≈ 90 s. (b) At $P_z = 0$ the first phase slip occurs within 5 seconds and we observe no rotation beyond 20 seconds. (c) Total atom number decay for $P_z = 1$ in open red symbols, and $P_z = 0$ in solid blue symbols. Dashed lines are double-exponential fits.

in the atomic distribution, arising due to the centrifugal barrier. An example image is shown in figure 6.5 (a). A histogram of fitted R values for the full range of P_z values and hold times in the range $0 \leq t \leq 20$ s[1] is shown in figure 6.5 (b). The R values are clearly quantised for all P_z, allowing us to determine q with near perfect fidelity. For spin polarisations sufficiently close to zero, where we are able to assign a q state to both spin states, we always observe the two components to be in the same q state. This explicitly identifies that the superflow decay mechanism is once again a 2π phase slip which affects both spin states simultaneously. Our observation do not however preclude the possibility that the supercurrent may first only decay in one of the spin components, after which the relative flow velocity between the two states causes a rapid secondary phase slip in the faster component.

6.2.1 Single versus two-component supercurrrent

In figure 6.6 we illustrate the dramatic difference between superflow stability in a $P_z = 1$ single-component gas and a $P_z = 0$ two-component system with equal populations in each spin state. The two different P_z states are created respectively, by a (140 μs) π and (70 μs) $\pi/2$ RF pulse at $t = 0$. In the pure $|\uparrow\rangle$ state (figure 6.6 (a)) the current persists for over two minutes, with the BEC always remaining in the $q = 3$ state for ≈ 90 s. In contrast at $P_z = 0$ (figure 6.6 (b)) the first phase slip occurs within 5 seconds and the current completely decays within 20 seconds.

As we demonstrated in Chapter 5, supercurrent stability generally depends on the number of condensed atoms and at $P_z = 0$ the atom number per spin state is halved. However, from the N decay curved in figure 6.6 (c) we see that this alone cannot explain the difference in superflow stability. At $P_z = 1$ rotation still persists for $N \approx 10^4$ while at $P_z = 0$ it stops already at $N > 4 \times 10^4$. Moreover, if we apply a $\pi/2$ pulse at $t = 0$ but then immediately remove all the $|\uparrow\rangle$ atoms from the trap using a combination of microwave π pulse and resonant light pulse, we observe the pure $|\downarrow\rangle$ state with half the initial atom number is once again stable, with supercurrent again persisting for over a minute. This unambiguously confirms that in figure 6.6 (b) the superflow is inhibited by the presence of *both* spin components. We therefore conclude that the two-component superflow decay mechanism is facilitated by the internal degrees of freedom introduced by the pseudo-spin, and is different from the single-component mechanism.

6.2.2 Stability phase diagram

We now turn to a quantitative study of the supercurrent stability as a function of the spin-population imbalance (see figure 6.7). We tune P_z by varying the length t_{RF} of the RF pulse applied at $t = 0$, and measure the q state of the majority spin component, $|\uparrow\rangle$, as a function of t. Whenever the radius R is fittable for the minority component we get the same q state for both spin components in $> 99\%$ of cases. However, for $N_\downarrow < 10^4$ we cannot determine q for the minority component.

Based on over 1600 measurements of $q(P_z, t)$, in figure 6.7 we reconstruct the complete current stability phase diagram for $0 \leq P_z \leq 1$. The contour plot of $\langle q(P_z, t)\rangle$ is obtained by spline interpolation through a 3D mesh of data points with integer q values. The blue-shaded region corresponds to rotation times for which no phase slips occur, whereas the black-shaded region corresponds to times at which all rotation has decayed. We clearly distinguish two qualitatively different regimes. For large P_z the superflow is fundamentally stable and limited only by the atom number decay. In this regime the additional internal degree of freedom is insufficient to facilitate decay beyond that present in the scalar BEC case. For low P_z the current starts to decay within

[1] Over this time the decay in particle number is sufficiently small that the weak dependence of R on N can be neglected. To account for this effect at longer hold times we establish quantisation independently for a given t before assigning q states.

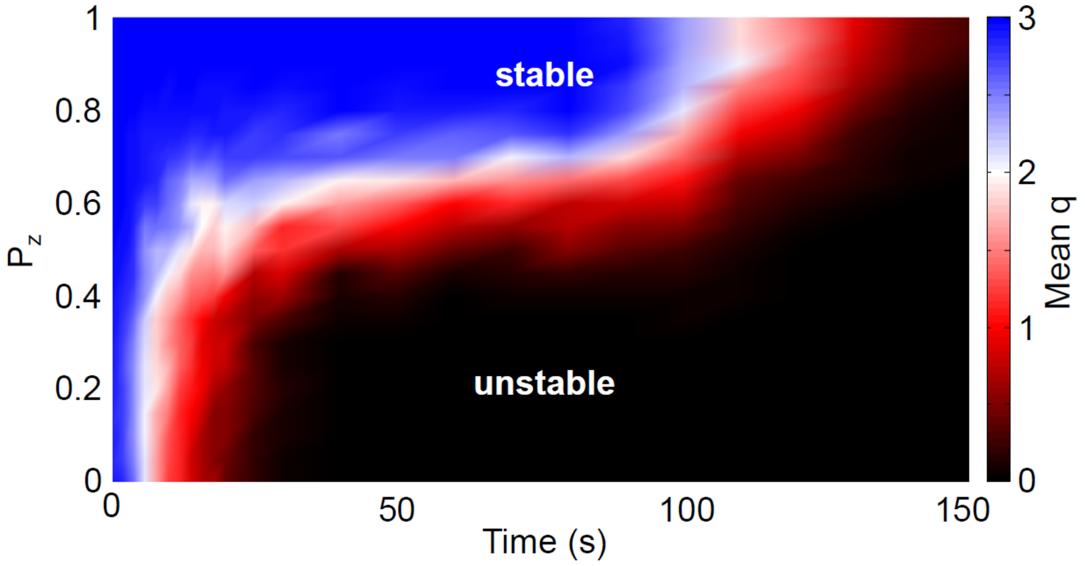

Figure 6.7: Supercurrent stability in a partially spin-polarised gas: The statistically averaged supercurrent state, $\langle q \rangle$, of the majority spin component is shown as a function of P_z and the evolution time t. The contour plot is based on over 1600 measurements of $q(P_z, t)$. The transition between stable and unstable current regimes occurs at $0.6 < P_z < 0.7$. In the stable regime the current eventually decays due to the atom number decay, equivalent to the eventual decay of the scalar-condensate superflow studied in Chapter 5.

a few seconds. A sharp transition between the two regimes occurs at $0.6 < P_z < 0.7$. Based on an additional ≈ 500 measurements we find close to symmetric behaviour for the $P_z < 0$ portion of the diagram. One small difference is that no phase slips occur for about 70 seconds for $P_z \to -1$, as apposed to 90 seconds for $P_z \to 1$. The transition between the two stability regimes is observed to occur at approximately the same value of $|P_z|$. This slight asymmetry between the two spin states might be attributed to the existence of the $m_F = -1$ state, or the presence of small terms in (6.19) which depend explicitly on S_z, breaking the symmetry between the $m_F = 1$ and $m_F = 0$ states.

6.3 Spin dephasing

To fully understand these observations, we need to distinguish a coherent superposition of $|\uparrow\rangle$ and $|\downarrow\rangle$ states from an incoherent mixture. The RF pulse at $t = 0$ corresponds to rotation around the y axis on the Bloch sphere and puts the BEC into a superposition state, $|\Psi(\phi)\rangle$, with a well defined phase relation between the two components. Importantly, this new state is still a pure BEC corresponding to the macroscopic occupation of a single state. Due to the near perfect spin-symmetry of our two state basis arising from the almost equal inter and intra-state scattering lengths, this rotated state should have almost identical properties to the original state. The significant difference however, is that the superposition state is no longer an eigenstate of the system. We therefore find that while the longitudinal polarisation of the state P_z is a conserved

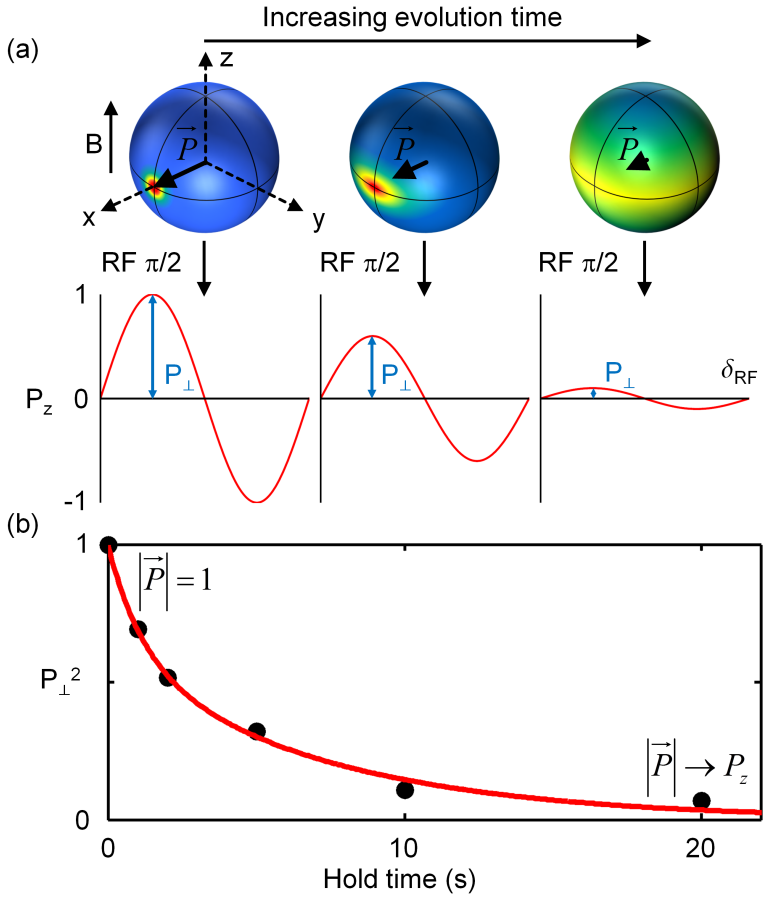

Figure 6.8: Phase diffusion: (a) Ramsey-style experiment to study the decay of transverse spin polarisation with time. Starting in the pure rotating ($q = 3$) $|\downarrow\rangle$ state, we apply an RF $\pi/2$ pulse to rotate the state vector onto the purely transverse spin state, $\vec{P} = (1, 0, 0)$. Allowing this state to evolve for a variable hold time, we then apply a second RF $\pi/2$ pulse which maps the decaying $|\vec{P}|$ into P_z. The P_z signal which we observe varies sinusoidally with the relative RF phase δ_{RF}, and with an amplitude equal to the length of the global state vector, $|\vec{P}|$. (b) By measuring the variance of the P_z values observed, we obtain a direct measure of the transverse polarisation decay. The solid red line is a double-exponential fit which gives the decay function $f(t)$.

quantity, the relative phase between the two components undergoes a complicated evolution causing the transverse polarisation to decay. This decohered state can now no longer be considered a single pure BEC, but corresponds to a mixture of two macroscopically occupied $|\uparrow\rangle$ and $|\downarrow\rangle$ states.

To study this decay of transverse polarisation, we perform a Ramsey-type experiment, illustrated in figure 6.8 (a). Starting in the pure $|\downarrow\rangle$ state we apply two $\pi/2$ RF pulses separated by time t and then measure P_z. The first pulse rotates the state vector on the Bloch sphere about the y axis, creating a purely transverse spin state $\vec{P} = (1, 0, 0)$ with a well-defined relative phase between the two components. The relative phase between the the two states evolves at a rate proportional to the local difference in chemical potentials between the two states ω_{21}, which in general is a func-

tion of both time and space. During the evolution time, couplings to the environment, quantum fluctuations [148], and finite temperature effects [208] can induce additional diffusive precession of the relative phase, leading to an uncertainty in its value. We illustrate this uncertainty in the relative phase as a probability distribution function of the state vector on the Bloch sphere which spreads with time and acts to shorten the global state vector for the whole system. During the same time, the RF coupling drive accumulates a phase $\omega_{RF}t$. The second RF $\pi/2$ pulse with phase δ_{RF} relative to the first pulse then maps the transverse polarisation onto longitudinal polarisation P_z, which we measure by separating the two states in TOF with a Stern-Gerlach field.

$$\delta_{RF}(t) = \int_0^t \omega_{21} dt - \omega_{RF} t. \tag{6.36}$$

P_z then varies sinusoidally as a function of δ_{RF}

$$P_z(t) = \mathcal{V}(t)\cos(\delta_{RF}(t)), \tag{6.37}$$

where the coherence between the two state is quantified by the visibility of the Ramsey fringes, $\mathcal{V}(t) = P_\perp$, where $P_\perp = \sqrt{P^2 - P_z^2}$ is the transverse polarisation.

Due to the very long spin-coherence time we observe, shot-to-shot variations in the relative phase δ_{RF} prevent us from measuring $\mathcal{V}$ directly by observing Ramsey fringes. Instead we take 40 shots at a given hold time t and infer $\mathcal{V}(t)$ from the standard deviation of the P_z values we observe. Assuming sufficient fluctuations that we sample δ_{RF} uniformly in the range 0 to 2π, the probability distribution of P_z values is given by

$$\mathcal{P}(P_z \to P_z + dP_z) = \frac{dP_z}{\pi\mathcal{V}\sqrt{1-(P_z/\mathcal{V})^2}}. \tag{6.38}$$

The variance in P_z is then directly related to the Ramsey visibility, and hence transverse polarisation, by

$$\sigma^2(P_z) = \frac{P_\perp^2}{2}. \tag{6.39}$$

Using this method, we measure the decay of $P_\perp$ as a function of hold time, as shown in figure 6.8 (b). We see the phase coherence decays very slowly with a characteristic spin-coherence time $t_{\text{coh}} \sim 10$ s. This means that in the unstable regime in figure 6.7 phase slips occur already at $t \lesssim t_{\text{coh}}$, when we cannot equate P and P_z. By fitting a double exponential to $P_\perp^2(t)$ we obtain a decay function $f(t)$ which allows us to calculate the total spin polarisation as a function of time

$$P(t) = \sqrt{P_z^2 + (1 - P_z^2) f(t)}. \tag{6.40}$$

Here we have assumed to first order that we can neglect the dependence of $f(t)$ on the value of P_z, simply using the characteristic decay function we measure at $P_z = 0$ to infer the decay of transverse polarisation at all P_z.

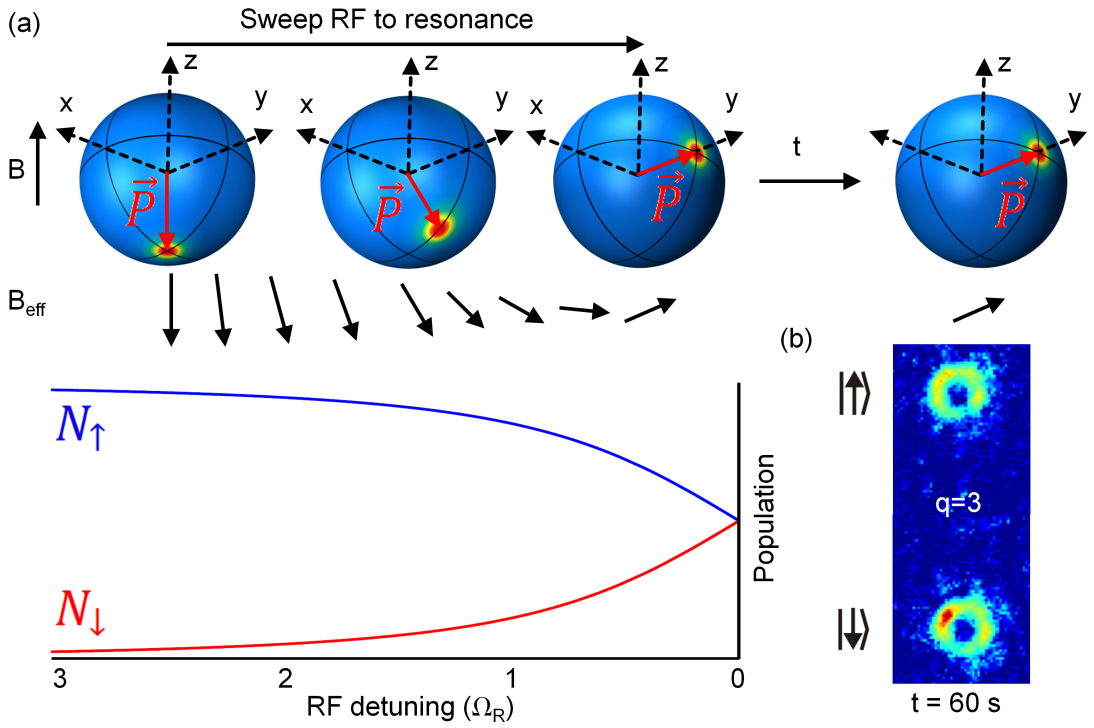

Figure 6.9: Adiabatic dressing of the spin state: (a) By sweeping the RF frequency from far above resonance to zero detuning, the effective magnetic field rotates from the $-z$ direction to the y direction. Adiabatic following transforms the initial $|\downarrow\rangle$ with $P_z = -1$ to the dressed $P_z = 0$ state $|y\rangle$, which is now an eigenstate of the effective Hamiltonian. Retaining the RF coupling during the evolution time, the dressed state does not undergo phase diffusion and remains a pure single component state. (b) This dressed state now exhibits long-lived persistent currents, even though $P_z = 0$. This confirms that the relevant quantity is the absolute spin polarisation P, and not P_z.

6.4 Coherently coupled two-component supercurrent

To further understand the role of transverse coherence in preserving supercurrent stability we also perform a complimentary experiment in which we adiabatically dress the rotating BEC with the RF field. In the presence of the RF field of frequency ω_{RF}, the effective magnetic field is $\vec{B}_{\text{eff}} = (2\hbar/\mu_B)(0, \Omega_R, -\delta)$, where μ_B is the Bohr magneton and $\delta = \omega_{RF} - \mu_B B/(2\hbar)$ is the detuning from resonance (derived in Section 3.2.2). For large detuning, $\vec{B}_{\text{eff}} \propto -\vec{z}$, and on resonance $\vec{B}_{\text{eff}} \propto \vec{y}$. Starting in the initial rotating $|\downarrow\rangle$ state, we apply an RF field far detuned (100 kHz) above resonance with a Rabi frequency $\Omega_R \approx 25$ kHz. At such a large detuning the RF dressed state is effectively equivalent to the $|\downarrow\rangle$ state, hence we have loaded into the lowest band of the dressed state. At $t = 0$ we adiabatically sweep δ to zero over 200 ms, rotating the direction of the effective magnetic field from $-\vec{z}$ to $\vec{y}$. The system remains in the lowest dressed state, adiabatically following the effective field, thus preparing a $P_z = 0$ superposition state $|y\rangle = (|\uparrow\rangle + i\,|\downarrow\rangle)/\sqrt{2}$ (figure 6.9 (a)). At this point, $|y\rangle$ is equivalent to the $|\Psi(\pi/2)\rangle$ state prepare by an RF pulse, which does not show long-term current

stability, decaying form the $q = 3$ state within a few seconds. However, if we leave the RF field on during the in-trap evolution, $|y\rangle$ is an eigenstate of the Hamiltonian and the coherence between $|\uparrow\rangle$ and $|\downarrow\rangle$ does not decay[1]. In this case $P_z = 0$ supercurrent is stable and persists for more than a minute, as shown in figure 6.9 (b).

These experiments clearly show that for analysing current stability in a partially polarised gas we must distinguish P_z and $|\vec{P}|$. The long phase decoherence times we measure suggest that the non-zero lifetime of supercurrents we observe at all P_z arises due to the non-zero time taken by the system to evolve from an initially pure single-component BEC with $|\vec{P}| = 1$, to an incoherent mixture with $|\vec{P}| < 1$. Secondly, the long lived supercurrrents observed in the $P_z = 0$ RF-dressed state confirms that, due to the spin-symmetry of our system, the value of P_z alone has no bearing on the decay of superflow. Instead, the supercurrent stability can be attributed to the RF coupling modifying the Hamiltonian such that the $P_z = 0$ state is now an eigenstate of the system, and therefore in the absence of phase decoherence $|\vec{P}|$ remains equal to unity.

6.5 Spin symmetric phase diagram

With this understanding, we now quantitatively characterise the onset of the supercurrent decay in figure 6.7 by the time τ at which the probability that the first phase slip ($q = 3 \to 2$) has occurred is 50%; this closely corresponds to the border between the blue and white-shaded regions. This is done by binning the data in P_z and plotting the occurrence of $q = 3$ states as a function of evolution time. To quantify the transition between times when $q = 3$ superflow is likely, to later times when $q = 3$ superflow has decayed, we fit this data to a sigmoid function

$$\mathcal{P}(q = 3) = \frac{1}{1 + e^{\frac{t-\tau}{\sigma}}}, \tag{6.41}$$

where τ characterises the typical decay time, and σ the width of the transition in time. The resultant τ are plotted as a function of P_z in figure 6.10 (a). The horizontal errors are given by the standard deviation of P_z for a given bin, and the vertical errors are given by the fitted uncertainty in τ. We see that τ rapidly increases for $P_z \gtrsim 0.64$, saturating at 100 seconds due to N decay. However, our observations of phase diffusion and long-lived RF-dressed supercurrent suggested that the absolute spin polarisation is the significant quantity, and not P_z. We therefore now combine our measurements of τ, defining the characteristic onset of decay, with the transverse polarisation decay function $f(t)$ (figure 6.8 (b)), to calculate the characteristic total spin polarisation at the onset of supercurrent decay:

$$P(\tau) = \sqrt{P_z^2 + (1 - P_z^2) f(\tau)}. \tag{6.42}$$

[1] We checked for t up to 100 seconds that we can always convert $|y\rangle$ into pure $|\downarrow\rangle$ by sweeping δ far from resonance.

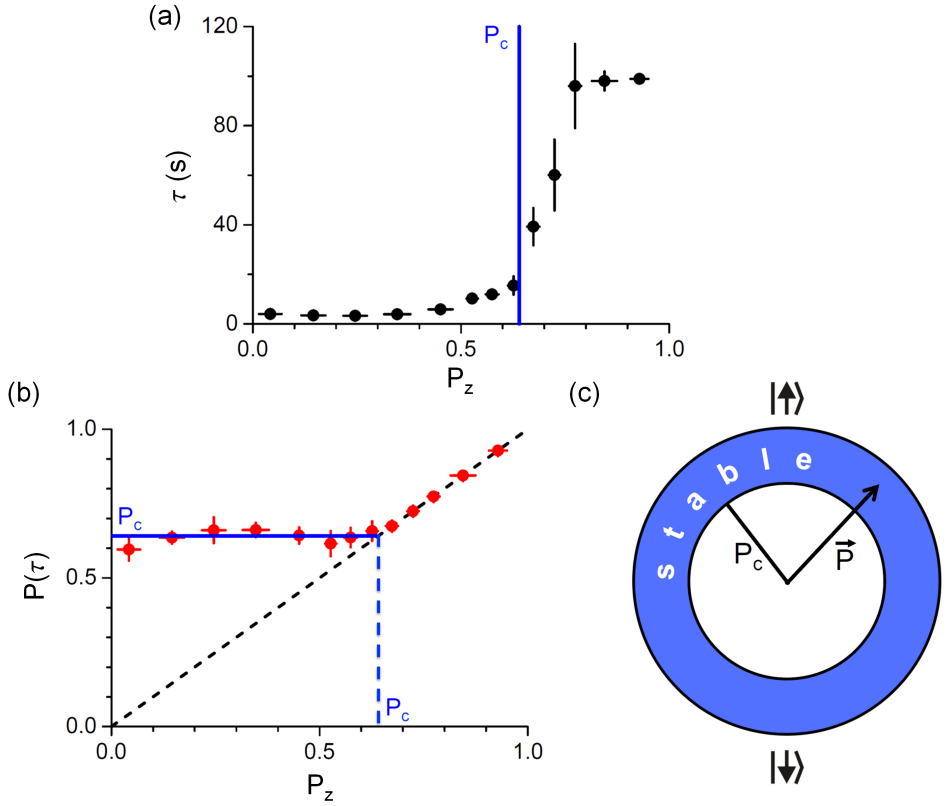

Figure 6.10: Critical spin polarisation P_c: (a) Characteristic time of the first phase slip, τ, versus P_z. Vertical blue line marks P_c, accurately determined in (b). (b) Modulus of the spin-polarisation vector at the onset of the supercurrent decay, $P(\tau)$, versus P_z. Fit to the points with $P(\tau) > P_z$ (horizontal solid blue line) gives $P_c = 0.64(1)$. (c) Stability diagram on the Bloch sphere. The blue-shaded region in figure 6.7 maps into the outer shell $|\vec{P}| > P_c = 0.64$. (A cut through the sphere is drawn for clarity.)

$P(\tau)$ is plotted as a function of P_z in figure 6.10 (b). We can now clearly distinguish two distinct regimes: one where $P(\tau)$ is constant within errors and one where $P(\tau) = P_z$. We thus complete our physical picture and accurately determine the critical spin polarisation P_c. The two regimes thus correspond to:

1. If $P_z > P_c$, then $|\vec{P}|$ can never drop below P_c. The supercurrent is fundamentally stable and long-lived, $\tau \gg t_{\text{coh}}$ and therefore $P(\tau) = P_z$.

2. If $P_z < P_c$, supercurrent decay starts at $\tau \lesssim t_{\text{coh}}$, when the decaying P becomes equal to P_c.

From all the data in the second regime we obtain $P_c = 0.64(1)$. For $0 \leq P_z \leq P_c$ the value of τ varies from 4 to 15 seconds and the orientation of $\vec{P}(\tau) = (\sqrt{P_c^2 - P_z^2}, 0, P_z)$ in spin space varies from purely transverse to purely longitudinal, but the onset of the supercurrent decay always occurs at the same $|\vec{P}|$. We thus conclude that the region of supercurrent stability is in fact the outer shell of the Bloch sphere where $|\vec{P}| > P_c$, as shown in figure 6.10 (c).

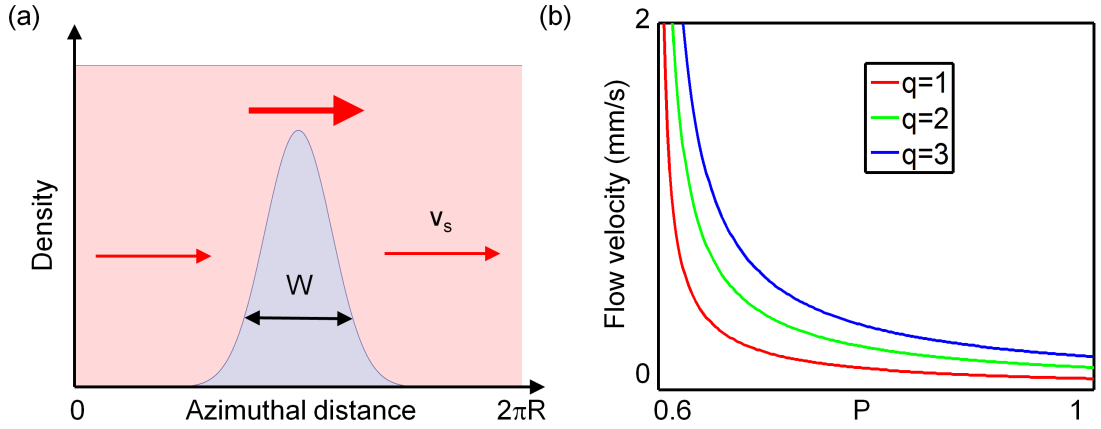

Figure 6.11: Two component barrier model: (a) Schematic of one component creating a density barrier which constricts the flow of the second component. The total density at all points around the ring is constant, however the density of the majority component (indicated in red) and that of the minority component (indicated in blue) can vary azimuthally. Here we consider the worst-case scenario where one component forms a density peak of minimum width $W(\xi_s)$. (b) Calculated flow velocity of the majority component as a function of P for the $q = 3, 2$, and 1 states at the peak density of the minority component for $W = 6.5$ μm.

The spin-rotational symmetry of our stability criteria arises intuitively from the near equivalence of the inter and intra-component scattering lengths. As we saw in equation (6.19), the small difference leads to symmetry breaking terms dependant on the value of S_z, however these terms are $\approx 0.2\%$ of the spin-independent term. We do observe a very slight asymmetry between the stability of $P_z > 0$ and $P_z < 0$ supercurrents, however we cannot reliably attribute this difference to the small spin-dependence of the system. We also note from our data the existence of critical polarisations for the $q = 2$ and $q = 1$ states at $P_c(q = 2) \approx 0.60$ and $P_c(q = 1) \approx 0.55$. Due to the fact that we focused most of our data on studying the $q = 3 \rightarrow 2$ transition, the errors on these values are much larger. We also note once again that these states are themselves formed from decay of the initial $q = 3$ state, and therefore are constrained to posses lower values of P_c.

6.6 Two-state barrier model

We now present a simple model which provides a possible explanation for the critical spin polarisation which we observe. Starting from a stable single-component superflow, we consider the addition of a minority component. If the density of this minority component is uniform around the ring, this has no effect on the flow velocity of either component. Here we consider the worst-case scenario, where the density of the minority component is strongly localised at one point in the ring, effectively acting as a barrier to the flow of the majority component. The minimum width of the the minority component

density profile, $W(\xi_s)$, is dependent on the spin healing length, ξ_s. Since ξ_s gives the length scale over which the value of the spin changes between its extremal values, one would expect the minimum minority component width to be in the range $\xi_s < W(\xi_s) < 2\xi_s$. For our system and starting atom number the spin healing length is $\xi_s \approx 4$ μm, and then increases as the atom number decays. With the constraint that the total density is uniform around the ring, the presence of the minority component creates a local reduction in the majority component density, and by the requirement of particle flux conservation, this leads to an increased flow velocity of the majority component, as shown in figure 6.11 (a). Our simple model is then to fix the width of the minority component density bump at $W(\xi_s)$, and calculate how the majority flow velocity increases as we reduce the population imbalance.

For the purposes of providing a qualitative explanation, we assume a Gaussian density distribution of the minority component of the form

$$n_1 = \frac{N_1}{\sqrt{2\pi W^2}} \exp\left(\frac{-x^2}{2W^2}\right), \tag{6.43}$$

where N_1 is the atom number in component 1, x is the azimuthal direction, and we have integrated out the vertical and radial directions, only considering variations in spin polarisation in the azimuthal direction. By restraining the total density to be uniform, the majority component density is simply given by

$$n_2 = n_{\text{tot}} - n_1. \tag{6.44}$$

We now apply the same criteria to calculate the flow velocity as we did in Section 5.4, namely conservation of particle flux

$$n_2 v_2 = \text{constant} = C, \tag{6.45}$$

and quantised circulation

$$\oint \mathbf{v_2}.d\mathbf{l} = 2\pi q \frac{\hbar}{m}. \tag{6.46}$$

The flow velocity is then given by

$$v_2(x) = \frac{L}{N} \frac{C}{1 - \frac{N_1}{N}\frac{L}{W}\frac{1}{\sqrt{2\pi}} \exp\left(\frac{-x^2}{2W^2}\right)}, \tag{6.47}$$

where the constant is given by

$$C = 2\pi q \frac{\hbar}{m}\frac{N}{L} \Bigg/ \int_{-L/2}^{L/2} dx \left[1 - \frac{N_1}{N}\frac{L}{W}\frac{1}{\sqrt{2\pi}} \exp\left(\frac{-x^2}{2W^2}\right)\right]^{-1} \tag{6.48}$$

We therefore see that the flow velocity is independent of the total atom number N, and only depends on the ratio N_1/N and W/L. In figure 6.11 (b), we plot the calculated flow velocity of the majority component for $W = 6.5$ μm, for the rotation states $q = 3, 2$,

and 1. This value of W is chosen to best match the critical spin polarisation which we observe, and is consistent with our anticipated range of allowed W values. We see that as the spin polarisation decreases from 1, the size of the barrier we can form with the minority component increases, and hence the peak flow velocity increases. At around $P = 0.6$, the density in the minority component is sufficient to fragment the majority component and all flow stops. Comparing this to typical values of the local sound velocity $c \approx 1$mm/s, we see that such a healing length gives the correct value of $P_c(q = 3)$, and predicts the relatively close values of P_c for the $q = 2$ and $q = 1$ states.

Although quite a crude calculation, it does illustrate that the formation of out of phase density fluctuations can lead to a non-trivial critical spin polarisation. The fundamental questions left by this model are two fold. Firstly, we ask what drives the formation of such spin structures? In spite of our two components being miscible and eliminating any systematic differences in the potentials of the two-states, as shown in Section 6.1.5, we do still observe the formation of spin structures. Modeling such spin diffusion could also explain whether both components always decay together, or whether above a certain population imbalance the minority component fragments and stops rotating, while the majority persists. The second question is then what sets the critical velocity? While one would assume the local sound velocity sets an upper bound on v_c, it may be possible that the coexistence of two components also facilitates a different, lower critical velocity. This may be especially true since the local flow velocity increase experienced by one component will correspond to a local flow velocity decrease in the other component, and hence a large relative velocity between the two components. As shown in [209–211], sufficiently high counterflow velocity between two components can lead to excitations with imaginary frequencies and the onset of dynamic instability.

6.7 Conclusion

In summary, we have observed persistent currents in multiply connected spinor condensates, demonstrated the existence of a critical spin polarisation for stable superflow, and elucidated the role of spin coherence in supercurrent stability. Empirically we have shown that the supercurrents in both spin states are constrained to decay quasi-simultaneously, and by establishing two-component superflow quantisation, we confirm the decay mechanism is still 2π phase slips, as observed in the single condensate case. By studying the stability of supercurrents as a function of the total spin polarisation P, we have identified and accurately measured the transition between two distinct regimes with different decay mechanisms. For $P > P_c$ the superflow is fundamentally stable and decays in a manner identical to that of a pure single-component supercurrent. For $P < P_c$ the internal spin degree of freedom facilitates an additional decay mechanism which causes the supercurrent to be fundamentally unstable.

The existence of a critical population imbalance for superflow stability was predicted in [185–187], assuming equal intra and inter-component interactions and no inter-component coherence. The supercurrent instability was associated with out-of-phase density fluctuations in the two components. However, an agreement on the value of P_c has not been reached. In references [185, 186] it was predicted that any $q > 1$ flow is unstable for essentially any $P < 1$, but according to [187] such current was found to be stable above some nontrivial interaction-dependent P_c. The latter conclusion qualitatively agrees with our observations, however none of the existing theories is quantitatively applicable to our experiments, since they are limited to the simplified cases of reduced dimensionality and very weak interactions.

The simple two-state barrier model we have presented provides at least a qualitative description of how a non-trivial critical spin polarisation of the form observed can arise. This model also highlights the need for further theoretical work to understand the dynamics of phase decoherence and spin fluctuations in our system. In general however, we cannot yet establish how the spin degree of freedom and the supercurrent decay mechanism are microscopically related. In one picture the spin degrees of freedom evolve independent of the rotation, and once sufficient spin fluctuations have formed the supercurrent decays in a manner similar to that explained by the two-state barrier model. A second, more exciting, alternative exists, where the supercurrent decay mechanism intrinsically uses the additional spin degree of freedom to unwind the scalar phase associated with superflow. Such decay mechanisms could relate to dark-bright solitons or magnons on a 1D Heisenberg chain. For these mechanisms, the global value of the spin polarisation could permit sufficient freedom in the local spin vector for accumulation of a Berry phase resulting in a phase slip.

Much of the interesting behaviour of our system then seems to arise from the near equality of the scattering lengths involved. Within the single-mode-approximation, the phase decoherence of a two-component system results from a spread in the distribution of populations in the initial state which are converted into phase fluctuations by the nonlinear interactions during the evolution. Therefore the rate of decoherence should be proportional to the difference in scattering lengths $a_s = (a_{11} + a_{00} - 2a_{10})/\sqrt{2}$ [212]. Similarly the spin healing length also depends on the difference in scattering lengths, and as a result our mixture exhibits long coherence times and large scale spin structures. These two features respectively explain the lifetime of persistent currents of several seconds for all values of P_z, and also, at least in the two-state barrier model, the significant deviation of P_c from 1. An important next step would then be to study supercurrents in a two-species system with significantly different intra and inter-component interactions to confirm these conclusions.

Chapter 7

Towards an azimuthal gauge potential

Ultracold atoms offer an appealing system for the study of many-body correlated states relevant to condensed matter physics. One of the primary challenges however, is to engineer a Hamiltonian for which neutral atoms behave as charged particles in a strong magnetic field. Such a technique is required to realise exotic topological phases, such as the fractional quantum hall effect (FQHE) in two-dimensional systems, which only exists at high magnetic fields where the ratio of flux quanta to particles is of order unity. The standard way to produce an artificial magnetic field is to rotate an atomic cloud which produces a non-trivial vector potential in the rotating frame of reference [29]. Such an approach however is limited to only modest fields, and as a result there have been a wealth of proposals to create effective magnetic fields without rotation. These can broadly be divided into two categories: asymmetric tunneling in optical lattices [213–215], and geometric gauge potentials. We will be focusing on the second approach, whereby atoms with two or more ground states are optically dressed, and the position dependence of the dressed internal states leads to geometric vector and scalar potentials [216].

The field of geometric gauge potentials has been driven forward primarily by the experiments of Spielman *et al* [66, 217–220]. By dressing the $F = 1$ magnetic sublevels of a BEC with two counterpropagating Raman laser beams they were able to couple the internal spin states with linear momentum differing by twice the photon momentum. This gives rise to a spatial gradient of the phase difference between spin components of the dressed state, achieving the first light-induced vector gauge potential [66]. By subsequently varying this gauge potential both spatially, and temporally, they were able to synthesise both artificial magnetic [218] and electric [219] fields respectively. By engineering a dressed band with two minima, they have also managed to realise an ultracold atom analogue of spin-orbit coupling [220].

In this chapter we discuss our progress in realising an azimuthal gauge potential, where the internal spin components of the dressed state are coupled to the angular momentum. We start by reviewing the theory behind linear gauge potentials, and then show how our setup is a simple mapping from linear to azimuthal motion. Our azimuthal gauge setup exhibits additional exciting possibilities which arise due to the

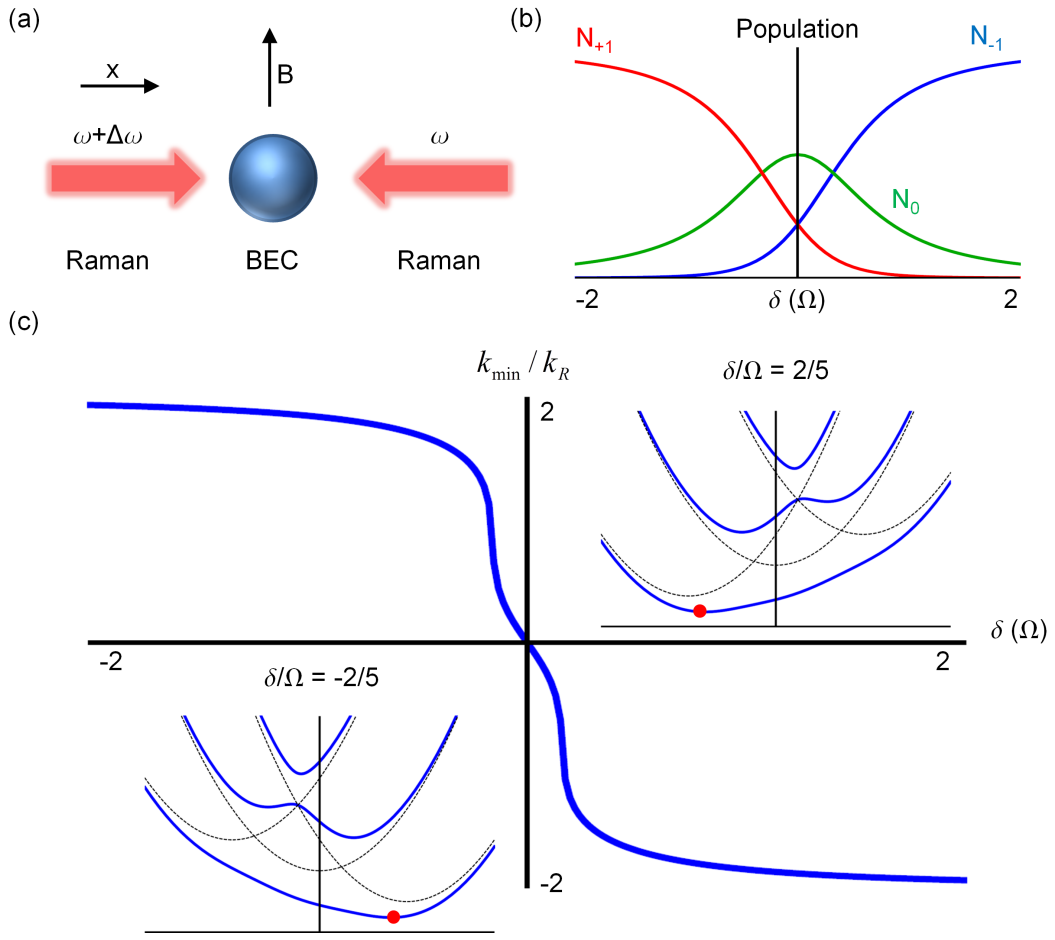

Figure 7.1: Linear gauge potential: (a) The BEC is dressed by two counterpropagating Raman beams with frequencies ω and $\omega + \Delta\omega$, linearly polarised along orthogonal axes. The Raman beams couple the m_F magnetic sublevels of the $F = 1$ manifold, which is split in an external magnetic field B. (b) Population of the three m_F spin states in the lowest dressed band as a function of Raman detuning, δ, for $\hbar\Omega = 5E_r$ and k_x=k_{min}. (c) Position of the band minimum k_{min} in momentum space as a function of Raman detuning for $\hbar\Omega = 5E_r$. The insets show the energy of the dressed bands (blue) as a function of k_x for the cases of positive and negative detuning. The dashed black lines indicate the original bare states. The red dot indicates the minimum of the lowest dressed state, which due to the confining potential, the BEC will adiabatically follow.

translational symmetry afforded to us by our ring geometry. To illustrate this, we then describe a proposed superfluid fraction measurement, where the spin-orbit coupling allows us to relate the rotational state of the system to the spin populations. The final section presents the experimental progress made so far, as well as the technical challenges which remain.

7.1 Linear gauge potentials

In this section we briefly explain the linear gauge setup realised by Spielman *et al.* and detailed in [66, 217]. We start by dressing a BEC in the $F = 1$ ground state with two

Raman beams of frequency difference $\Delta\omega$, counterpropagating along $\hat{x}$, as shown in figure 7.1 (a). These beams couple states $|m_F, k_x\rangle$ differing in their internal state by $\Delta m_F = \pm 1$ and differing in linear momentum $\hbar k_x$ by $2\hbar k_r$, where $\hbar k_r = h/\lambda$ is the single-photon recoil momentum. We also define $E_r = \hbar^2 k_r^2/2m$ as the associated recoil energy. The spin and momentum states $|m_F, k_x\rangle$ coupled by the Raman beams are grouped into families of states labeled by the momentum $\hbar k_x$:

$$\Psi(k_x) = \{|-1, k_x + 2k_r\rangle, |0, k_x\rangle, |+1, k_x - 2k_r\rangle\}. \tag{7.1}$$

In the rotating wave approximation for the frame rotating at $\Delta\omega$, the Hamiltonian expressed in the state basis of the family $\Psi(k_x)$ is given by

$$H = \hbar \begin{pmatrix} \frac{\hbar}{2m}(k_x + 2k_r)^2 - \delta & \Omega/2 & 0 \\ \Omega/2 & \frac{\hbar}{2m}(k_x)^2 - \epsilon & \Omega/2 \\ 0 & \Omega/2 & \frac{\hbar}{2m}(k_x - 2k_r)^2 + \delta \end{pmatrix}. \tag{7.2}$$

Here $\delta = g_F \mu_B B\hbar$ is the detuning from Raman resonance, Ω is the resonant Raman Rabi frequency, and ϵ accounts for the quadratic Zeeman shift. For each k_x, diagonalising H gives three eigenvalues $E_j(k_x)(j = 1, 2, 3)$. For dressed atoms in state j, this eigenenergy as a function of k_x is the effective dispersion relation, and depends on the experimental parameters, δ, Ω, and ϵ, as shown in the insets of figure 7.1 (c). Concentrating on the lowest energy dressed band, the number of energy minima and their positions $k_{\min}$ are thus experimentally tuneable. Around the band minimum $k_{\min}$, the dispersion relation can be expanded as

$$E(k_x) \approx \frac{\hbar^2}{2m^*}(k_x - k_{\min})^2, \tag{7.3}$$

where m^* is the effective mass. Considering the Hamiltonian for a particle of charge q in a magnetic vector potential $\mathbf{A}$

$$H = \frac{(\mathbf{p} - q\mathbf{A})^2}{2m}, \tag{7.4}$$

we can then identify $k_{\min}$ with the light-induced vector gauge potential

$$q\mathbf{A} = \hbar k_{\min} \hat{x}. \tag{7.5}$$

In figure 7.1 (c) we calculate the value of $k_{\min}$, and therefore the effective magnetic vector potential $q\mathbf{A}/\hbar$, for the lowest dressed band as a function of the Raman detuning δ.

The mechanical momentum is defined as

$$p_{\text{mech}} = m\dot{x} = m\frac{\partial H}{\partial p_{\text{can}}} \tag{7.6}$$

$$= \frac{m}{\hbar}\frac{\partial H}{\partial k_x}, \tag{7.7}$$

where p_{can} is the canonical momentum. We therefore identify the mechanical motion of the dressed state as the gradient of the energy band with respect to k_x. In [66] the condensate was adiabatically loaded into the minimum of the lowest dressed band for zero Raman detuning, $\delta = 0$, corresponding to the band minimum at $k_{\text{min}} = 0$. From the populations of the m_F states plotted in figure 7.1 (b) as a function of δ, we see this dressed state corresponds to a superposition of all three m_F states. From equation (7.7), for such a state at the band minimum, the mechanical momentum is zero and the dressed atoms are stationary in the lab frame. The momenta of the individual spin components however are nonzero. To see this, one can project the dressed state onto its original spin and momentum components (shown by the dashed black lines in figure 7.1 (c)) by abruptly removing the Raman coupling. One then decomposes the dressed state into the $m_F = 1$, $m_F = 0$, and $m_F = -1$ states with mechanical momenta $-2\hbar k_r$, 0, and $2\hbar k_r$ respectively.

If one first adiabatically sweeps the Raman detuning to $\hbar\delta = -2E_r$ (Inset of figure 7.1 (c)), the minimum of the energy band is shifted to a non-zero k_{min}, corresponding to application of a vector gauge potential in the $\hat{x}$ direction. Due to the trapping potential the dressed state of the atoms are confined to follow the minimum of the band, and hence the mechanical momentum of the dresses state is restricted to be zero in the lab frame. From figure 7.1 (b), we see that the spin composition of the dressed state has changed to predominantly the $m_F = 1$ state. The presence of a non-zero k_{min} is then confirmed by projecting into the bare states, where one then observes the appropriate decomposition of the $m_F = 1$, $m_F = 0$, and $m_F = -1$ states, but now with respective mechanical momenta $-2\hbar k_r + \hbar k_{\text{min}}$, $0 + \hbar k_{\text{min}}$, and $2\hbar k_r + \hbar k_{\text{min}}$.

These experiments showed that one can utilise light fields to create vector gauge potentials for neutral atoms, which can be easily manipulated by varying the detuning of the Raman coupling. This basic setup was then extended by the addition of a magnetic field gradient to create a spatially varying $\mathbf{A}(\mathbf{r})$, and therefore an effective magnetic field $\mathbf{B} = \nabla \times \mathbf{A}(\mathbf{r})$ [218]. Varying the value of the detuning and therefore $\mathbf{A}(t)$ in time they also created an ultracold atom analogue of an electric field $\mathbf{E} = -\partial\mathbf{A}(t)/\partial t$ [219].

7.2 Azimuthal gauge potential

In this section we detail our experimental setup, which though similar in spirit, instead couples the internal spin state to angular, rather than linear, momentum. We start by considering a BEC held in a ring trap formed by a red-detuned LG beam, which

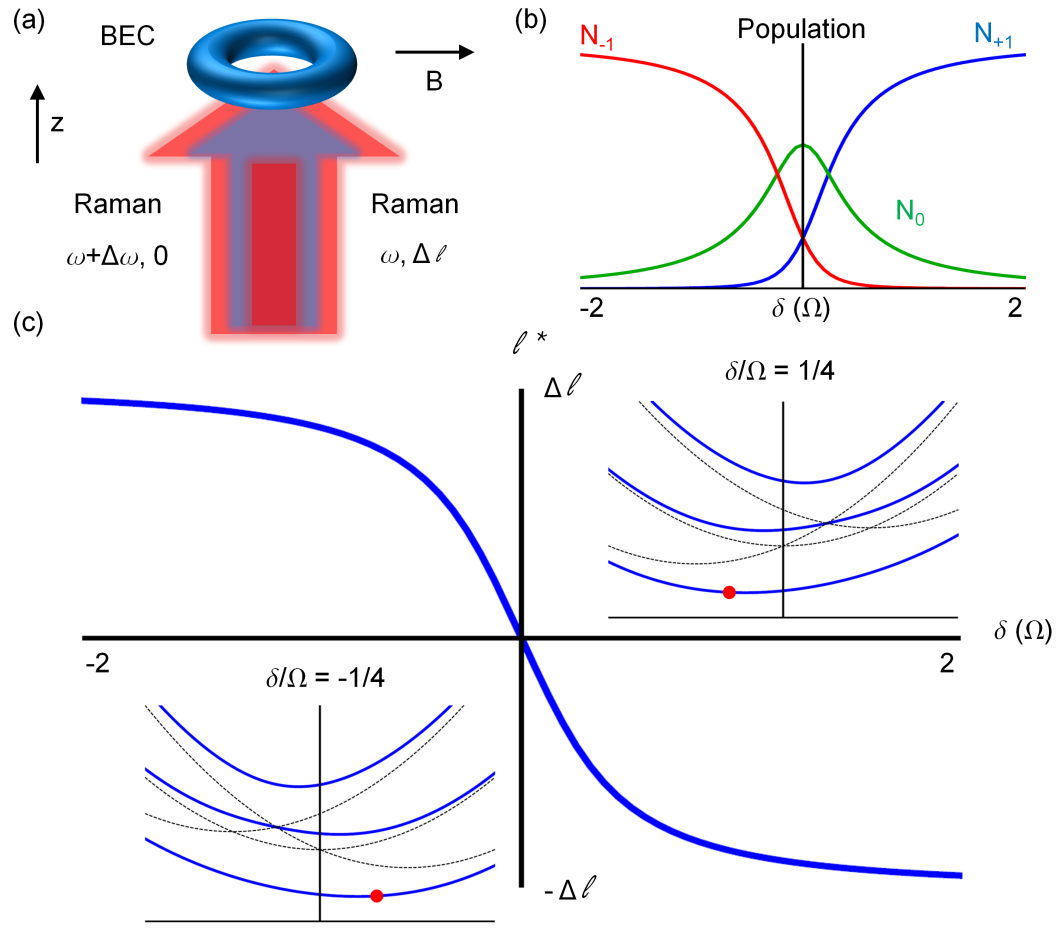

Figure 7.2: Azimuthal gauge potential: (a) The ring BEC is dressed by two copropagating Raman beams with frequencies ω and $\omega + \Delta\omega$, linearly polarised along orthogonal axes. The Raman beams couple the m_F magnetic sublevels of the $F = 1$ manifold, which is split in an external magnetic field B. One of the Raman beams is a broad Gaussian beam, while the second is an LG beam of phase winding $\Delta\ell$. (b) Population of the three m_F spin states in the lowest dressed band as a function of Raman detuning, δ, for $\hbar\Omega = 5E_{\rm rot}$ and $\ell{=}\ell^*$. (c) Position of the band minimum ℓ^* in angular momentum space as a function of Raman detuning for $\hbar\Omega = 5E_{\rm rot}$. The insets show the energy of the dressed bands (blue) as a function of ℓ for the cases of positive and negative detuning. The dashed black lines indicate the original bare states. The red dot indicates the minimum of the lowest dressed state.

also acts as one of the Raman beams. To generate an azimuthal vector potential, we Raman-couple the m_F magnetic states of the $F = 1$ ground state using the LG beam and secondary Gaussian beam, co-propagating in the vertical direction $\hat{z}$, perpendicular to the toroidal trap. In this sense, our setup is identical to the one we introduced in Chapter 4 to create persistent currents. The only distinction is that now rather than using the Raman transition to Rabi flop to a state with different angular momentum, we will continuously couple the magnetic states to create new dressed states. Our experimental setup is illustrated in figure 7.2 (a).

Our Raman transition couples states $|m_F, \ell\rangle$ differing in their internal state by $\Delta m_F = \pm 1$ and differing in angular momentum $\hbar\ell$ by $\hbar\Delta\ell$, where $\hbar\Delta\ell$ is the angular

momentum carried by the LG beam. The relevant energy is now the rotational energy $E_{\text{rot}} = \hbar^2(\Delta\ell)^2/2mR^2$, where R is the radius of the ring trap. The family of coupled states is now given by:

$$\Psi(\ell) = \{|-1, \ell + \Delta\ell\rangle, |0, \ell\rangle, |+1, \ell - \Delta\ell\rangle\}. \tag{7.8}$$

In the rotating wave approximation for the frame rotating at $\Delta\omega$, the Hamiltonian expressed in the state basis of the family $\Psi(\ell)$ is given by

$$H = \hbar \begin{pmatrix} \frac{\hbar}{2mR^2}(\ell + \Delta\ell)^2 - \delta & \Omega/2 & 0 \\ \Omega/2 & \frac{\hbar}{2mR^2}(\ell)^2 - \epsilon & \Omega/2 \\ 0 & \Omega/2 & \frac{\hbar}{2mR^2}(\ell - \Delta\ell)^2 + \delta \end{pmatrix}. \tag{7.9}$$

This Hamiltonian is identical to that for the linear momentum case in (7.2) with the following mapping

$$\frac{\hbar^2}{2m} \to \frac{\hbar^2}{2mR^2}; \qquad k_x \to \ell; \qquad 2k_r \to \Delta\ell. \tag{7.10}$$

Once again we diagonalise H to obtain the dressed state energy bands, which we expand about the minimum as

$$E(\ell) \approx \frac{\hbar^2}{2m^*R^2}(\ell - \ell^*)^2. \tag{7.11}$$

This is equivalent to the Hamiltonian

$$H = \frac{(\mathbf{p}_\theta - q\mathbf{A}_\theta)^2}{2m}, \tag{7.12}$$

where we have identified the azimuthal momentum and azimuthal vector potential as

$$\mathbf{p}_\theta = \frac{\hbar\ell}{R}\hat{\theta}; \qquad q\mathbf{A}_\theta = \frac{\hbar\ell^*}{R}\hat{\theta}. \tag{7.13}$$

As shown in figure 7.2 (c), the position of the band minimum can be varied in the range $-\Delta\ell \to \Delta\ell$ by changing the Raman detuning δ, which also changes the spin composition of the dressed state as shown in figure 7.2 (b).

We note that unlike for the linear gauge case, the fact that our vector potential is in the azimuthal direction means it automatically corresponds to a non-zero magnetic flux threading the ring. If we shift the band minimum to $\ell^* \neq 0$, we create an azimuthal vector potential, equal in magnitude at all points on the ring. Using Stoke's theorem we see this corresponds to a flux, Φ, threading the ring

$$\Phi = \int\int \mathbf{B} \cdot d\mathbf{S} = \oint \mathbf{A} \cdot d\mathbf{l} = \frac{2\pi\hbar\ell^*}{q}. \tag{7.14}$$

The form of the effective magnetic field is then given by

$$\mathbf{B} = \nabla \times \mathbf{A} = \frac{1}{R}\frac{\partial R A_\theta}{\partial R}\hat{z} \tag{7.15}$$

$$= \frac{1}{R}\frac{\partial}{\partial R}\left(\frac{\hbar \ell^*}{q}\right)\hat{z}. \tag{7.16}$$

This is in general a nontrivial function, since ℓ^* depends on Ω which varies with the intensity of the Raman beams. To first order though $\partial \ell^*/\partial R = 0$ at the atoms since the maximum Ω also defines the trap minimum, and hence the magnetic field can be considered zero at the atoms. The angular momentum acquired by the dressed state, $\hbar \ell^*$, can therefore be viewed as an Aharanov-Bohm type effect. Alternately one can also explain it as a cold atom analogue of Faraday induction, where the angular momentum acquired as we vary the effective magnetic field is equivalent to generating an electrical current in a coil as the magnetic flux enclosed is varied in time. We now further explain the properties of this system by describing a proposed experiment to measure the superfluid fraction of an atomic gas which makes explicit use of the azimuthal nature of our created vector gauge potential.

7.2.1 Superfluid fraction measurement

As discussed in Section 2.4.2, while the concepts of superfluidity and BEC are intrinsically linked, the superfluid fraction and condensed fraction of a gas or fluid in general take very different values. While the condensed fraction can be measured by mapping the momentum distribution to real space in time-of-flight expansion, a quantitative measure of the superfluid fraction is harder to achieve. Such a measurement however is important for investigating the properties of interacting Bose gases. Specific cases of interest include strong interactions which can lead to condensate depletion without loss of superfluid fraction, and the Kosterlitz-Thouless phase transition in a quasi-2D geometry which manifests itself in a universal jump in the superfluid density [221, 222]. Recently the first measure of superfluid fraction in a quantum gas was realised in a degenerate Fermi system by measuring the speed of second sound [223]. Here we present an alternate approach using our azimuthal gauge potential, which was first proposed in [104].

The basic principle of the experiment is shown in figure 7.3. Starting for example in the pure $m_F = -1$ state, one can load into the lowest dressed band by adiabatically turning on the second Gaussian Raman beam with the detuning $\delta \ll 0$. As shown in the left panel of figure 7.3 (a), this loads both normal and superfluid components into the band minimum at $\ell^* = 0$. Since the gradient of the dispersion relation is zero at the minimum, $p_{\text{mech}} = 0$, both components are at rest in the lab frame. By then sweeping the Raman detuning towards zero, we shift the band minimum and impose our azimuthal vector potential (right panel figure 7.3 (a)). Due to interactions with the trapping potential, the normal component is constrained to follow the band minimum

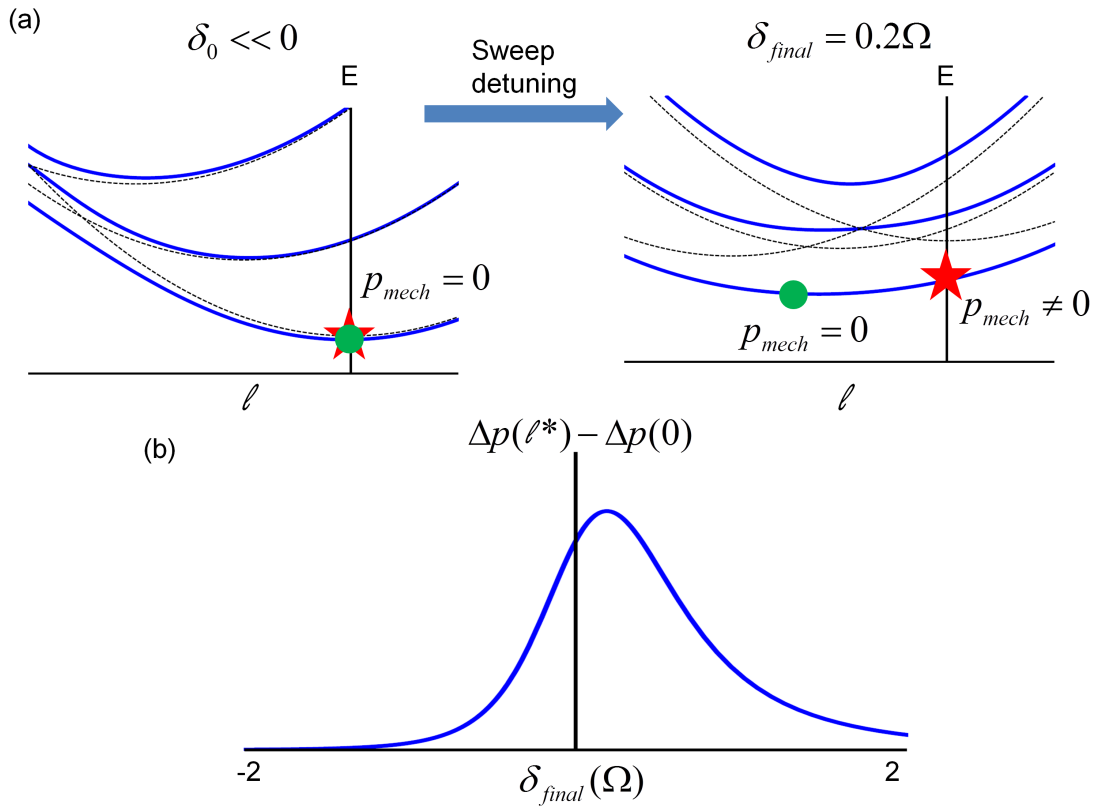

Figure 7.3: Superfluid fraction measurement: (a) Starting with the Raman coupling far detuned, $|\delta| \gg \Omega$, we adiabatically load the pure $m_F = -1$ state into the minimum of the lowest dressed band by ramping on the Gaussian beam. Both normal component (green circle) and superfluid component (red star) are then at the band minimum $\ell = \ell^* = 0$. By sweeping the detuning towards resonance, the band minimum shifts and the spin composition changes. The normal component interacts with the walls of the trap and relaxes, following the band minimum such that $p_{\rm mech} = 0$ and $\ell = \ell^*$. The superfluid component cannot relax and remains at the original $\ell = 0$, and therefore starts to rotate in the lab frame. (b) As well as a difference in mechanical momentum between the two components, the spin composition of the dressed state at $\ell = \ell^*$ differs slightly from that at $\ell = 0$, which allows one to perform a spectroscopic superfluid fraction measurement. Plotted is this difference as a function of the final detuning.

where it is stationary with respect to the lab frame. In contrast the superfluid component is unable to relax and follow the band minimum, remaining at the original angular momentum $\ell = 0$. The gradient of the dispersion relation at this point increases as the detuning is changed, causing the superfluid component to rotate in the lab frame with $p_{\rm mech} \neq 0$. This distinction provides the definition of the superfluid fraction [13]. This behaviour in a toroidal trap with an azimuthal vector potential is in marked contrast to the case of a linear vector potential, where, due to the lack of translational invariance along the direction of the vector potential, both components must relax and follow the band minimum.

A key element of this proposal is that one can measure this distinction between normal and superfluid behaviour using spectroscopic methods. The wavefunction of the lowest band is a linear superposition of the three magnetic levels, with amplitudes

which vary with ℓ. For a given detuning, the spin composition of a normal state at the band minimum $\ell = \ell^*$, differs slightly from the spin composition of a superfluid state which remains at $\ell = 0$. One can quantify this by the difference in the number of particles in the $m_F = \pm 1$ states

$$\Delta p(\ell) = \frac{N_{-1} - N_1}{N}. \tag{7.17}$$

In figure 7.3 (b) we plot the difference in Δp between the normal component ($\ell = \ell^*$) and the superfluid component ($\ell = 0$). Initially the population imbalance is identical for both the purely normal and purely superfluid states, however for final detunings close to zero, the distinction between Δp peaks at a few percent, before tending towards zero again at $\delta_{\text{final}} \gg 0$. This difference in population imbalances forms the basis of the proposed measurement. Sweeping the detuning to $\delta_{\text{final}} = 0.2\Omega$ where the signal peaks, if our gas was purely normal we would measure a population imbalance $\Delta p(\ell^*)$. Alternately if our gas was purely superfluid we would measure a different population imbalance $\Delta p(0)$, differing from $\Delta p(\ell^*)$ by a few percent. If our gas had both components, one could therefore calculation the superfluid fraction as

$$\frac{\rho_s}{\rho} = \frac{\Delta p(\ell^*) - \Delta p}{\Delta p(\ell^*) - \Delta p(0)}, \tag{7.18}$$

where Δp is the measured imbalance, while $\Delta p(0)$ and $\Delta p(\ell^*)$ are calculated using the known values of Ω, δ_{final}, and ϵ.

This proposed experiment illustrates how one can make use of an azimuthal vector potential to directly link superfluid motion and spin composition. While in principle we have the experimental setup required to perform this experiment, a key step is to prove that the Raman coupling is coherent and that the atoms remain in the lowest dressed state only. Incoherent processes can lead to population of higher bands which will alter the measured spin composition, destroying the few percent signal we need to observe. In the next section we detail the progress we have made so far in implementing such an azimuthal vector potential, and also some of the technical issues which remain.

7.3 Experimental progress

The current status of our experimental progress is illustrated by figure 7.4. By coupling the $F = 1$ manifold with our $\ell = 3$ LG and Gaussian Raman setup, we have managed to engineer the azimuthal vector potential proposed above. Through varying the detuning of the Raman coupling we can demonstrate the changing mechanical rotation and spin composition of the superfluid state as the band minimum is shifted. We can also force the superfluid state to relax to the band minimum by ramping up a repulsive green laser beam overlapped with the toroidal trap to create a barrier to the superflow. Using these tools we now demonstrate six distinct dressed states. The appropriate band

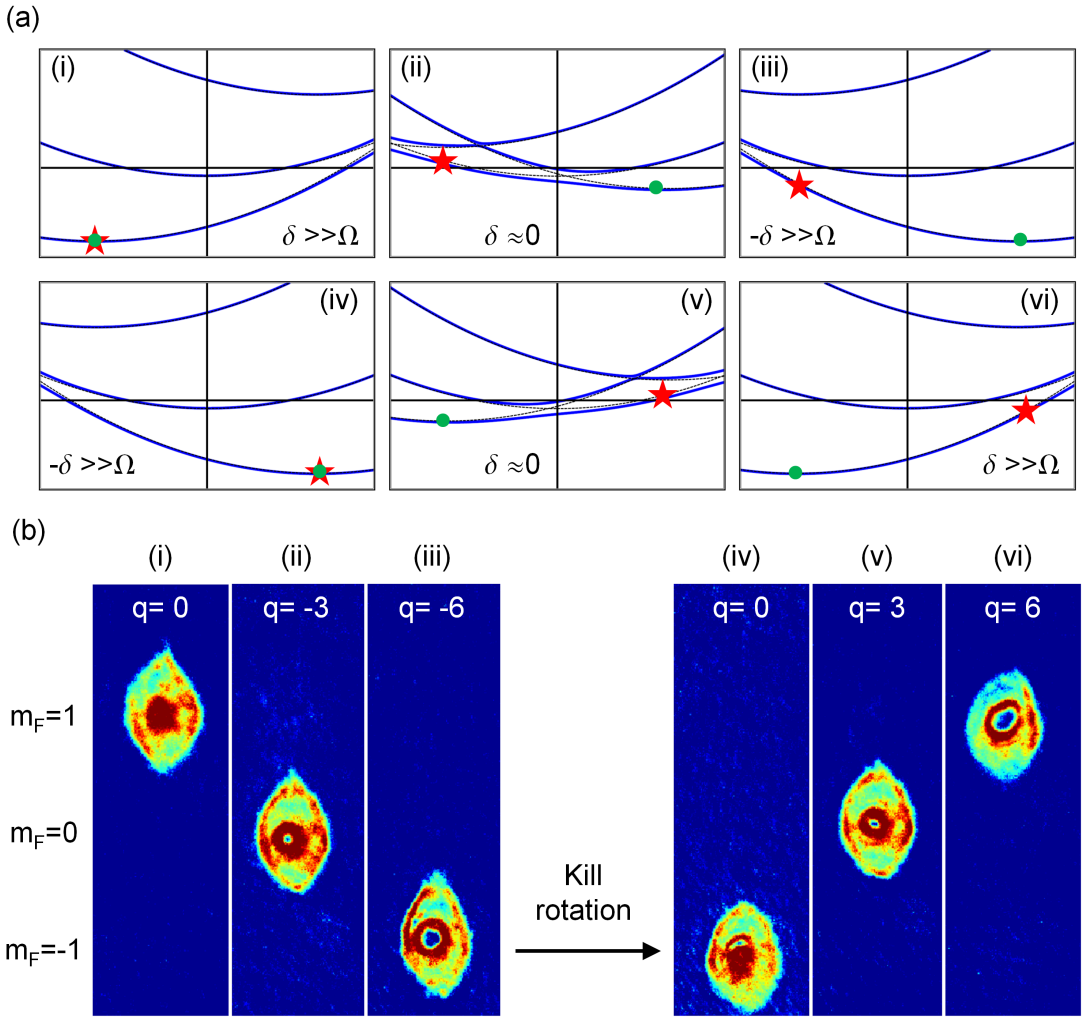

Figure 7.4: Far-detuned azimuthal vector potential: (a) Relevant dressed state dispersion relations $E(\ell)$. The angular momentum ℓ is indicated for the superfluid component by the red star, and for the normal component by the green circle. As we work with a pure condensate we only ever observe behaviour consistent with a pure superfluid. (b) Absorption images of the dressed state projected onto the original basis states at 29 ms TOF in the presence of a Stern-Gerlach field which splits the different m_F states along the vertical direction. The q state of each image is measured kinematically by fitting the size of the central density hole formed in TOF. The protocol to prepare each measurement (i)→(vi) is explained in the text.

structure for these states is shown in figure 7.4 (a), and the projection of the dressed state onto the original basis $|m_F, \ell\rangle$ is shown in figure 7.4 (b).

In this experiment we prepare the dressed state in an external field of 10 G, where the second order Zeeman shift $\epsilon \approx 7$ kHz, and use a modest Rabi frequency of only $\Omega \approx 500$ Hz. As a result our Raman beams do not simultaneously couple all three m_F states, and therefore for a window of detuning near zero, the spin composition of the dressed state is purely $m_F = 0$. The reasoning behind limiting ourselves to this simplified case will be explained in the following section.

We now describe the six experimental sequences, relating to the appropriately labeled band diagrams and absorption images in figure 7.4. In all cases the dressed state

is projected into the $|m_F, \ell\rangle$ basis just before TOF by abruptly jumping the Raman detuning far from resonance. The spin composition of the dressed state is measured by separating the m_F states during TOF by application of a Stern-Gerlach gradient. The angular momentum ℓ of the dressed state is measured by fitting the size of the density hole formed in TOF, as explained in Section 4.4.2.

(i) Starting in the pure $m_F = 1$ state, the Raman coupling is ramped up with δ far above resonance: This loads the condensate into the lowest dressed band with spin composition $\Psi(\ell = -3) = \{|m_F = 1, \ell + 3\rangle, |m_F = 0, \ell\rangle, |m_F = -1, \ell - 3\rangle\} = \{1, 0, 0\}$ and band minimum $\ell^* = -3$. This is confirmed by observing only the non-rotating $|m_F = 1, \ell = 0\rangle$ state in TOF.

(ii) Sweeping the detuning to below the $m_F = 1 \to m_F = 0$ resonance: This shifts the band minimum to $\ell^* \to 3$, however our superfluid remains at $\ell = -3$ and therefore we prepare the dressed state with spin composition $\Psi(\ell = -3) = \{0, 1, 0\}$. This is confirmed by observing only the $|m_F = 0, \ell = -3\rangle$ state in TOF.

(iii) Sweeping the detuning far below both the $m_F = 1 \to m_F = 0$ and $m_F = 0 \to m_F = -1$ resonances: Our superfluid remains at $\ell = -3$ and we prepare the dressed state with spin composition $\Psi(\ell = -3) = \{0, 0, 1\}$. This is confirmed by observing only the $|m_F = -1, \ell = -6\rangle$ state in TOF.

(iv) Preparing state (iii), we then kill rotation by ramping up and down the repulsive barrier beam over 500 ms: The superfluid velocity exceeds critical velocity at the barrier and relaxes to the band minimum at $\ell^* = 3$. The relaxed dressed state then has spin composition $\Psi(\ell = 3) = \{0, 0, 1\}$. This is confirmed by observing only the non-rotating $|m_F = -1, \ell = 0\rangle$ state in TOF.

(v) Preparing state (iv), we then then sweep the detuning above the $m_F = 0 \to m_F = -1$ resonance: This shifts the band minimum back to $\ell^* \to -3$, but our superfluid which has relaxed to $\ell = 3$ by application of the barrier, does not follow. We therefore prepare the dressed state with spin composition $\Psi(\ell = 3) = \{0, 1, 0\}$. This is confirmed by observing only the $|m_F = 0, \ell = 3\rangle$ state in TOF.

(vi) Preparing state (iv), we then sweep the detuning far above both the $m_F = 0 \to m_F = -1$ and $m_F = 1 \to m_F = 0$ resonances: Our superfluid remains at $\ell = 3$ and we prepare the dressed state with spin composition $\Psi(\ell = 3) = \{1, 0, 0\}$. This is confirmed by observing only the $|m_F = 1, \ell = 6\rangle$ state in TOF.

In principle then, we have demonstrated a tuneable light-induced azimuthal vector potential. The next important step would then be to prepare a dressed state with non-trivial occupation of more than one m_F state. Unfortunately our research so far has highlighted several technical difficulties which prevent us from further manipulating and quantifying dressed states composed of multiple spin states.

7.3.1 Technical challenges

In the hope of guiding future work on this project, we now outline some of the technical problems observed in our setup which remain unsolved:

1. Dressed states prepared near resonance, which therefore are composed of more than one spin state, are observed to decohere on timescales of ≈100 ms. This is confirmed by preparing and holding such a state, and then sweeping the Raman detuning far below resonance. We observe occupation of more than one m_F state, corresponding to population of higher dressed states. The rotational state of the $m_F = -1$ component is also found to decrease the longer we hold near resonance.

2. To detect the rotational state we need to accurately measure the size of the density hole formed in TOF due to the presence of a centrifugal barrier. This technique requires us to first ramp down the ring trap over ≈ 100 ms before release, for the hole to expand sufficiently over the 29 ms TOF (See Section 4.4.2). We find that for spin mixtures prepared by projecting the Raman dressed state, complex dynamics occur over this timescale which prevent us from measuring the rotational state of each spin component upon projection. The reason why this is in such stark contrast to the mixtures prepared by RF coupling in Chapter 6 is not clear.

3. To deterministically kill rotation and force the dressed state to relax, the repulsive potential barrier must be raised and lowered very slowly so as not to induce an unknown quantity of circulation through mechanical stirring. While we have been able to readily achieve this in the limit of large detuning, due to the decohering processes we find near resonance, the time to do so is not available for dressed states with non-trivial spin composition.

4. Finally, we also note that our Raman beams exert a significant dipole potential on the atoms, and therefore the high intensities required to generate large Rabi frequencies will alter the ring potential. Due to the requirement that our ring potential remains sufficiently smooth, circularly symmetric, and multiply-connected for superflow to persist, the maximum Rabi frequency we can achieve is limited. This problem can be solved by changing the Raman wavelength to nearer 790 nm where the dipole potential is smaller, but at the cost of increased light scattering.

7.4 Conclusion

In conclusion, by Raman coupling different m_F states with different angular momenta, we have managed to generate an azimuthal vector potential. Through varying the detuning of the Raman beams we have demonstrated control of this vector potential, and therefore the magnetic flux which threads the ring. Due to the toroidal geometry

of our system, we have shown that in contrast to the case of a linear vector potential, we can prepare both dressed states which conserve angular momentum by rotating in the lab frame, and those which relax to the minimum of the dispersion relation and are stationary. Technical challenges still need to be addressed however, including maintaining coherence near resonance, deterministically forcing the dressed state to relax, and measuring the rotation of multi-component states.

Chapter 8

Summary and outlook

It is my hope that the work in this thesis has both demonstrated, and in some part furthered our understanding of, the intricate physics at play in persistent currents. In many regards the study of metastable superfluid flows and their decay feels quite traditional, building on a century of experimental and theoretical research. As we discovered while researching the mechanisms at play in our toroidal condensate superfluid, many of the questions which we have tried to address in this work have been posed decades before in the context of either superfluid helium or superconducting nanowire experiments. The hope then is that while the physics may be universal and long-standing, the realisation of persistent currents in dilute atomic condensates, presented both in this work and that of NIST, will offer a unique alternate route to further probe these phenomena.

The key achievements of our work can be summarised as follows:

- We have created a long-lived multiply-charged persistent current in a toroidal-shaped BEC. By using an SLM to generate our LG beam, we are able to imprint a well-defined and variable phase winding onto the condensate wavefunction, preparing a state of known angular momentum. The SLM also allows us to correct for abberations in our system, enabling us to achieve a ring trap with azimuthal variations of less than 10%. With this setup we have demonstrated supercurrents persisting for two minutes, limited only by the gradual decay of atom number.

- For the first time we have demonstrated that the angular momentum state of the persistent current decays in a quantised fashion, corresponding to collective jumps of the atoms between metastable minima. This unambiguously confirms the decay mechanism as vortex-induced 2π phase slips.

- Our ability to resolve individual phase slips also opens the possibility to study the dynamics of phase slips. We find that the supercurrent decays rapidly if the superflow speed exceeds a critical velocity in good agreement with numerical simulations, and we also observe rare stochastic phase slips for superflow speeds

below the critical velocity. From this, we attribute the onset of decay to the excitation of phonon modes when the superflow velocity exceeds the local sound velocity, in agreement with numerical solutions of the GPE.

- We study persistent currents in a toroidal two-component Bose gas for the first time. In contrast to many theoretical predictions, we find that the supercurrent is stable for spin polarisations above a well defined, and non-trivial, critical value. Below this value we find the supercurrent is unstable, and decays due to the presence of the second component. We also investigate the role of phase coherence between the two spin states and show that only the magnitude of the spin-polarisation vector, rather than its orientation in spin space, is relevant for supercurrent stability.

8.1 Outlook

The outlook for future work on this system falls into two categories. The first of these are experiments which further the understanding of our observations so far. One of the main question posed by our observations of stochastic phase slips is the role of temperature in the stability of persistent currents. By studying supercurrent decay as a function of temperature it might be possible to understand how the energy barrier to decay changes as a function of atom number. One could also extrapolate the data down to $T = 0$, possibly allowing further confirmation of the zero temperature GPE result, or perhaps one might find evidence of quantum tunneling, as was observed in superfluid helium and superconducting nanowire systems. Studying how the critical velocity changes, if at all, as the dimensionality of the system changes, could also offer further insight into the connection between superfluidity and BEC.

Persistent currents in multi-component condensates offer a wealth of complex physics, and here the challenge is more in trying to restrict oneself to a limited subset of the possible mechanisms at play. Even in the absence of superflow, the evolution of a two-component condensate with periodic boundary conditions is an interesting and challenging problem. One of the main conclusions of our studies was the significance of the inter and intra-species scattering lengths. For the two components we used, the fact that they were almost equal, lead to a spin-symmetric stability criteria and long timescale decoherence and spin dynamics. Clearly it would be beneficial to put our results in context, by studying either a two-component condensate with significantly different scattering lengths, or even a dynamically unstable mixture. This could perhaps also further our understanding of the mechanisms which give rise to spin structures, and whether these out of phase density fluctuations do indeed play a significant role in disrupting the supercurrent stability, as predicted by our simple two-state barrier model.

The second category of future experiments are those which use our setup to branch

out into new areas of physics. As we discussed in Chapter 7, one of the most exciting possibilities is the opportunity to generate an azimuthal vector potential, not least as a means of measuring the superfluid fraction. While we have been able to demonstrate some preliminary results, the truly interesting physics comes about once the dressed state has a non-trivial spin composition. In such a situation one can demonstrate the coupling between spin-composition and angular momentum, and even counter-intuitively induce rotation in one spin-state by forcing the atoms to relax in the dressed band. Several mappings have been proposed for the response of this system, including interpretations as Faraday induction, an Aharanov-Bohm type effect, and the Einstein-de Haas effect. While several technical challenges currently bar our progress, this system is certainly interesting enough to merit further persistence.

An alternate direction we have considered, is to use our ring trap to study the Kibble-Zurek mechanism [103]. The principle of this measurement is that in a second-order phase transition, the relaxation time of the system diverges near the critical point, and hence every such transition traversed at a finite rate is a non-equilibrium process. If one considers Bose-Einstein condensation in a ring trap, then the phase of the macroscopic wavefunction is first established locally, with a domain size dependent on the rate at which one quenches through the transition. As the condensate then comes into equilibrium, these regions merge and can potentially create topological defects forming quantised vortices. Such a mechanism has been observed in [224]. If one performs this quench in a ring trap, it is possible to test the predicted scaling laws of the Kibble-Zurek mechanism, by measuring the distribution of supercurrent states formed as a function of quench rate.

Finally, we also note that our ring trap also forms an ideal system for fundamental studies in a periodic potential. One such study, which would also further illuminate our results on multi-component persistent currents, would be to study spin diffusion on a 1D periodic lattice. By reducing the radial extent of our trap to below the spin healing length, we can effectively create a 1D chain of spin domains. Such a system would then be analogous to a Heisenberg spin chain, allowing us to study the system's response to both rotations of the global spin, and the propagation of local spin defects. Such a setup could then also be used to study both single and two-component solitons in a periodic potential. Many of these proposed experiments can also be done with ^{39}K, where the additional freedom to precisely tune the scattering length over a wide range opens up a wealth of further possibilities.

Appendix A

Analytic form of pseudo-LG beam

To compare our pseudo-LG beam to the true LG field we now derive an analytic expression for the field at the focus. As illustrated in figure A.1, we define the field at the SLM as $f_0(x_0, y_0)$, the field directly before the lens as $f_z(x_1, y_1)$ after propagating a distance z, and the field at the focus as $g_f(x_2, y_2)$. Using the rules defined in Section 4.2.4, we identify these fields as

$$f_0(x_0, y_0) = E_0 \exp\left(-\frac{r_0^2}{w^2}\right) \exp\left(-\ell\theta_0\right) \tag{A.1}$$

$$f_z(x_1, y_1) = \frac{1}{i\lambda z} \int\int f_0(x_0, y_0) \exp\left[\frac{ik}{2z}((x_1 - x_0)^2 + (y_1 - y_0)^2)\right] dx_0 dy_0 \tag{A.2}$$

$$\begin{aligned} g_f(x_2, y_2) &= \frac{1}{i\lambda f} \int\int f_z(x_1, y_1) \exp\left[-\frac{ik}{2f}(x_1^2 + y_1^2)\right] \\ &\quad \times \exp\left[\frac{ik}{2f}((x_2 - x_1)^2 + (y_2 - y_1)^2)\right] dx_1 dy_1 \\ &= \frac{1}{i\lambda f} \exp\left[\frac{ik}{2f}(x_2^2 + y_2^2)\right] F_z\left(\frac{x_2}{f\lambda}, \frac{y_2}{f\lambda}\right) \\ &= \frac{1}{i\lambda f} \exp\left[\frac{ik}{2f}(x_2^2 + y_2^2)\right] F_0\left(\frac{x_2}{f\lambda}, \frac{y_2}{f\lambda}\right) \exp\left[-\frac{2\pi i}{k}\frac{(x_2^2 + y_2^2)z}{f^2\lambda^2}\right] \\ &= \frac{1}{i\lambda}\frac{f}{z^2} \exp\left[\frac{i\pi}{f\lambda}\frac{f - z}{f}(x_2^2 + y_2^2)\right] F_0\left(\frac{x_2}{f\lambda}, \frac{y_2}{f\lambda}\right), \end{aligned} \tag{A.3}$$

where

$$\begin{aligned} F_0\left(\frac{x_2}{f\lambda}, \frac{y_2}{f\lambda}\right) &= \int\int f_0(x_0, y_0) \exp\left(\frac{2\pi i}{f\lambda}(x_0 x_2 + y_0 y_2)\right) dx_0 dy_0 \\ &= E_0 \int\int \exp\left(-\frac{r_0^2}{w^2}\right) \exp(i\ell\theta_0) \\ &\quad \times \exp\left(\frac{2i\pi r_0 r_2}{f\lambda}\cos(\theta_0 - \theta_2)\right) r_0 dr_0 d\theta_0 \end{aligned}$$

Using the identity

$$J_n(z) = \frac{1}{2\pi i^n} \int_0^{2\pi} \exp(iz\cos\theta) \exp(in\theta) d\theta, \tag{A.4}$$

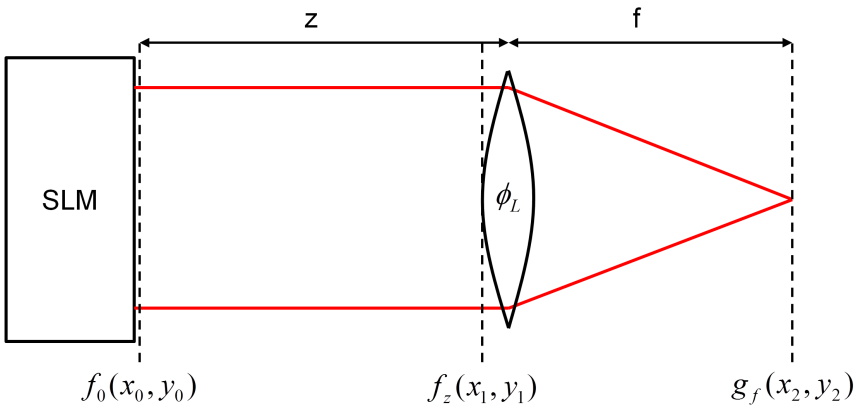

Figure A.1: Schematic of field propagation within LG setup: The field at the SLM, $f_0(x_0, y_0)$, is composed of the incoming Gaussian intensity profile with the phase of the SLM imprinted. For this calculation we only consider the effect of the azimuthal phase winding. The field after freely propagating a distance z is defined as $f_z(x_1, y_1)$. The action of the lens is to impart a spatially varying phase delay, ϕ_L, defined in (4.10). The field of interest is that at the focal point, $g_f(x_2, y_2)$.

where $J_n(z)$ is the Bessel function of the first kind. One then finds

$$g_f(x_2, y_2) = E_0 \frac{2\pi i^{\ell-1}}{\lambda} \frac{f}{z^2} \exp\left[\frac{i\pi}{f\lambda}\frac{f-z}{f} r_2^2\right] \exp(i\ell\theta_2) \times \int r_0 \exp\left(-\frac{r_0^2}{w^2}\right) J_\ell\left(\frac{2\pi r_0 r_2}{f\lambda}\right) dr_0. \tag{A.5}$$

We have now extracted the azimuthal phase winding, showing that the field at the focus carries angular momentum. The radial function can be slightly simplified using the identities [225]

$$\int_0^\infty J_n(bz) \exp(-p^2 z^2) dz = \frac{\sqrt{\pi}}{2p} \exp\left(\frac{b^2}{8p^2}\right) I_{n/2}\left(\frac{b^2}{8p^2}\right), \tag{A.6}$$

where $I_n(z)$ is a modified Bessel function of the first kind, and

$$\frac{dJ_n(z)}{dz} = \frac{J_{n-1}(z) - J_{n+1}(z)}{2}. \tag{A.7}$$

Integrating the radial function by parts we obtain the final expression

$$g_f(x_2, y_2) = E_0 i^{\ell-1} \sqrt{\pi} \frac{f^2}{z^2} \frac{w}{w_0} \frac{r_2}{w_0} \exp\left(-\frac{r_2^2}{2w_0^2}\right) \left[I_{\frac{\ell-1}{2}}\left(\frac{r_2^2}{2w_0^2}\right) - I_{\frac{\ell+1}{2}}\left(\frac{r_2^2}{2w_0^2}\right)\right] \times \exp\left[\frac{i\pi}{f\lambda}\frac{f-z}{f} r_2^2\right] \exp(i\ell\theta_2), \tag{A.8}$$

where we define the diffraction limit $w_0 = f\lambda/\pi w$. We note that unlike the numerical calculations presented in Section 4.2.4, this result does not account for the finite apertures of the SLM and the imaging lens which are found to reduce radial oscillations.

Appendix B

Numerical calculation of ring BEC excitation spectrum

To consider the relevance of the various analytic models of critical velocity considered in Section 5.5, we independently calculate the Bogoliubov excitation spectrum for a nonrotating, two dimensional Bose gas confined in a ring potential. This calculation is presented in [181], but here we present further details of our implementation. Repeating this calculation was necessary to extend the results down to low atom numbers, relevant to our experimental conditions where we observe phase slips. In doing so, we find the conclusion of [181], that the spectrum is well approximated by the surface mode model of [180], is only valid above a critical chemical potential, μ_c. Below μ_c we find that the critical velocity for sound excitations becomes the lowest, and hence relevant, critical velocity. This is accompanied by a change in the nature of the excitations from surface instabilities, to phonon modes.

The condensate is described by the 2D GPE

$$i\partial_t\Phi = \left(-\frac{\Delta}{2} + \frac{1}{2}(r-r_0)^2 + g|\Phi|^2\right)\Phi, \tag{B.1}$$

where we use the associated scale for energy ($\hbar\omega_r$), time (ω_r^{-1}), and length $a_r = \sqrt{\hbar/(m\omega_r)}$. The condensate wavefunction, $\Phi = \Phi(r,\theta,t)$, is normalised to unity, $\Delta = \partial_r^2 + \partial_r/r + \partial_\theta^2/r^2$ is the Laplacian in polar coordinates, $r_0 = r_M/a_r$ is the dimensionless ring radius, and $g = N\sqrt{8\pi}\frac{a}{a_z}$ is the dimensionless 2D interaction constant, where N is the atom number, a is the s-wave scattering length, and a_z is the harmonic oscillator length in the z direction [182].

The initial ground state of the system is found by propagation in imaginary time. If we consider the wavefunction as a superposition of eigenstates $\phi_m(\mathbf{r})$ with time-dependent amplitudes $a_m(t)$ and eigenenergies $E_m(t)$, by making the substitution $\Delta t \to -i\Delta t$, the time evolution operator leads to an exponential decay of the wavefunction, and a corresponding decay of the eignestates via

$$\Phi(\mathbf{r}, t+\Delta t) = \sum_m a_m(t)\phi_m(\mathbf{r})\exp(-E_m\Delta t). \tag{B.2}$$

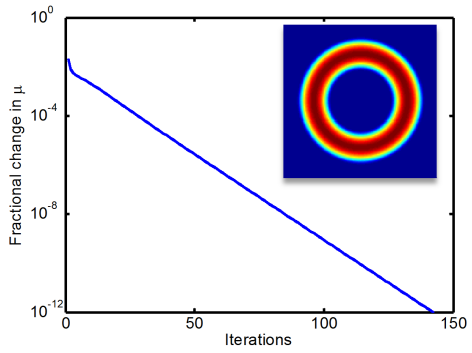

Figure B.1: Convergence of ground state calculation: Plotted is the fractional change in the calculated chemical potential and a function of iteration number. The relative change in μ exponentially decays with iteration number, and the calculation stops when the desired accuracy of 10^{-12} is obtained. Inset is an example plot of the calculated ground state density.

Crucially, the eigenenergy governs the decay rate, and so the eigenstate with the lowest energy decays slowest. From some trial wavefunction and by renormalisation of the wavefunction during the imaginary time propagation, the wavefunction will tend towards the ground state of the system.

We perform this calculation on a mesh grid in both real space and Fourier space. We split the evolution into two steps, the first acts on the real space wavefunction with the real space energy terms associated with the external trapping potential and mean field interactions. The second step Fourier transforms the wavefunction to the momentum space and acts upon it with the momentum term. Fourier transforming back to real space and renormalising, we obtain the wavefunction propagated in imaginary time. For sufficiently small time steps the wavefunction will then converge to the ground state. The corresponding MATLAB code for this calculation is presented in CalculateGroundState.m. An example of the obtained convergence to the ground state is presented in figure B.1.

To find the excitation spectrum we use the rotational invariance of B.1, and consider perturbations of the form

$$\Phi(r,\theta,t) = e^{-i\mu t}[\Phi(r) + \delta\Phi_m(r,\theta,t)], \tag{B.3}$$

where

$$\delta\Phi_m(r,\theta,t) = u_m(r)e^{-i(\omega t - m\theta)} + v_m(r)^* e^{i(\omega^* t - m\theta)}. \tag{B.4}$$

Φ denotes the stationary ground state of the system, μ is the global chemical potential, and $\delta\Phi$ is a small perturbation parameterised by the angular wavenumber m. Insertion of this trial solution into the GPE we obtain the Bogoliubov-de Gennes equations to first order in $\delta\Phi$:

$$\omega u(r) = \left(-\partial_r^2 - \frac{1}{r}\partial_r + \frac{m^2}{r^2} + \frac{1}{2}(r-r_0)^2 + 2g|\Phi|^2 - \mu\right)u(r) + g\Phi^2 v(r), \tag{B.5}$$

$$\omega v(r) = \left(\partial_r^2 + \frac{1}{r}\partial_r - \frac{m^2}{r^2} - \frac{1}{2}(r-r_0)^2 - 2g|\Phi|^2 + \mu\right)u(r) - g\Phi^{*2}u(r). \tag{B.6}$$

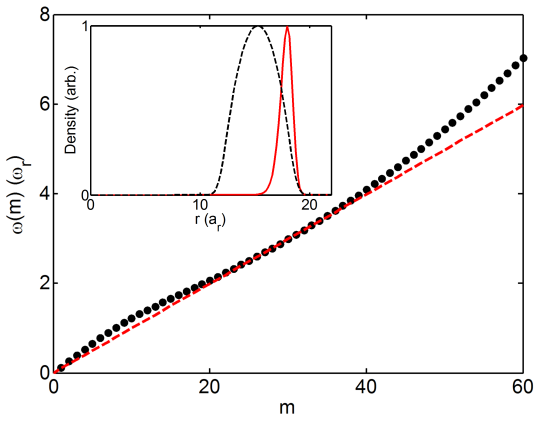

Figure B.2: Typical calculation of 2D annular BEC excitation spectrum: Plotted is the eigenfrequency, ω, versus the angular wavenumber, m, for the lowest branch of the dispersion relation. The black data points are the results of our numerical calculation, obtained by diagonalisation of the Bogoliubov-de Gennes equations. The red dashed line is the critical angular velocity, $\Omega_c = \min(\omega(m)/m)$. The inset shows the radial density profile of the condensate (black dashed line) and the density profile of the excitation (red line), normalised to have the same peak value.

To solve this problem we make use of the cylindrical symmetry of the problem and reduce it to a one dimensional problem in the positive radial direction. For our mesh of points in the radial direction $r_1 ... r_i ... r_N$, we define the vector of length $2N$, $X_i = [u(r_1), ...u(r_i), ...u(r_N), v(r_1), ...v(r_i)..., v(r_N)]$. The Bogoliubov-de Gennes equations can then be expressed as the matrix problem

$$M_{i,j} X_i = \omega X_j, \tag{B.7}$$

where M_{ij} is a two dimensional matrix obtained from equations (B.5) and (B.6). To discretise the gradient operators we use the standard form

$$\partial_r u(r_i) \approx \frac{u(r_{i+1}) - u(r_i)}{\Delta r} \tag{B.8}$$

and

$$\partial_r^2 u(r_i) \approx \frac{u(r_{i+1}) - 2u(r_i) + u(r_{i-1})}{\Delta r^2} \tag{B.9}$$

Calculating the eigenenergies of the excitations, ω, then amounts to finding the eigenvalues of a $2N \times 2N$ matrix, the lowest branch of which gives the critical angular velocity, $\Omega_c = \min(\omega(m)/m)$. One can also obtain further insight from the density distribution of the excitation, given by $\delta n_m(r) = 2\mathrm{Re}[\Phi(r)^*(u_m(r) + v_m(r)^*)]$.

An example excitation spectrum is shown in figure B.2, along with the density profile of the excitation in the inset. We note that to extend our calculations to very low atom numbers, large mesh sizes are required to minimise the introduction of errors as the width of the annulus becomes comparable to the grid spacing. A more efficient formalism could make use of variable mesh spacing, implementing a coarse mesh in the empty regions of the problem, and a finer mesh at the atoms.

MATLAB code for calculating the ground state:

```
1 function Phi = CalculateGroundState()
```

```
2
3       %Set up mesh grid for calculation
4       %Size of grid in radial oscillator lengths
5       L = 50;
6       %Number of points per dimension in grid
7       Ngrid = 512;
8       %Iteration step size in imaginary time
9       tau = 0.04;
10      %Distance between points in grid
11      Δx = L/Ngrid;
12      %Real space grid
13      [x,y] = meshgrid(-L/2:Δx:L/2);
14      %Momentum space grid
15      [px,py] = meshgrid(-pi*Ngrid/L:2*pi/L:pi*Ngrid/L);
16      %Real space grid in cylindrical polar coordinates
17      [theta, r] = cart2pol(x,y);
18      %Convergence required for ground state calculation
19      lim = 10^-12;
20
21      %=================Find the Ground State================%
22      %Guess initial trial wavefunction based on 2D TF profile
23      Phi0 = real(sqrt(real((1-((r-r0)/RTF).^2).^(3/2))));
24
25      Phi0 = Normalise(Phi0);
26      Phi = Phi0;
27      Δu = 1;
28
29      %Iterate to find ground state
30      while (abs(Δu)>lim)
31
32          ustart = chemPot(Phi);
33          Phi = exp(-tau*(0.5*(r-r0).^2+g*Phi.*conj(Phi))).*Phi;
34          Phi = fftshift(fft2(Phi));
35          Phi = exp(-tau*(0.5*px.^2+0.5*py.^2)).*Phi;
36          Phi = ifft2(ifftshift(Phi));
37          Phi = Normalise(Phi);
38          %Calculate chemical potential of new wavefunction
39          ustop = chemPot(Phi);
40          Δu = abs((ustop-ustart)/ustart);
41
42      end
43      %=========================================================%
44
45      %=================Normalise Wavefunction===============%
46      function p = Normalise(Phi)
47
48          if (sum(sum(Phi.*conj(Phi))) ≠0)
49              p = Phi*sqrt(1/sum(sum(Phi.*conj(Phi)*(Δx^2))));
50          else
51              p = Phi;
52          end
```

```
53
54      end
55      %=========================================================%
56
57      %==============Calculate chemical potential=============%
58      function u = chemPot(Phi)
59
60          if (sum(sum(Phi.*conj(Phi))) ≠0)
61              %Real space energy
62              V = (Δxˆ2)*sum(sum(conj(Phi).*((0.5*(r-r0).ˆ2).*Phi...
63                  +g*(Phi.*conj(Phi)).*Phi)));
64              %Kinetic energy
65              K = (Δxˆ2)*sum(sum(conj(Phi).*ifft2(ifftshift((0.5*px.ˆ2+...
66                  0.5*py.ˆ2).*fftshift(fft2(Phi))))));
67              u = (V+K)/((Δxˆ2)*sum(sum(conj(Phi).*Phi)));
68          else
69              u = 0;
70          end
71      end
72          %=========================================================%
73
74
75  end
```

MATLAB code for calculating the excitation spectrum:

```
1   function Phi = CalculateExcitationSpectrum(Phi)
2
3       %Angular wavenumber of excitations to consider
4       m_values = 0:60;
5
6       %Get Phi as a function of radial variable
7       PhiR = Phi(Ngrid/2+1,:);
8       R = x(Ngrid/2+1,:);
9       %Crop R and PhiR to exclude zero
10      PhiR = PhiR(logical(R>0));
11      R = R(logical(R>0));
12      ΔR = L/Ngrid;
13      n = size(R,2);
14
15      %=================Find the excitation spectrum===============%
16
17      for i = 1:size(m_values,2)
18          m = m_values(i);
19
20          %Generate sparse matrix for diagonalising
21          %Create on diagonal terms relating to angular kinetic energy,
22          % trapping potential, mean field interactions, and chemical
23          % potenial
24          OnDiag = [(((m)ˆ2)./(2*R.ˆ2)+0.5*(R-r0).ˆ2+...
```

```
25              2*g*(PhiR.*conj(PhiR))-u)...
26              (-((m)^2)./(2*R.^2)-0.5*(R-r0).^2-...
27              2*g*(PhiR.*conj(PhiR))+u)];
28
29          %Create terms corresponding to double derivative term in the
30          %kinetic energy, d^2/dr^2.
31          OnDiagKineticSecond = -0.5*[-1/(ΔR^2) -2*ones(1,n-2)/(ΔR^2)...
32              -1/(ΔR^2) 1/(ΔR^2) 2*ones(1,n-2)/(ΔR^2) 1/(ΔR^2)];
33          OneUpDiagSecond = -0.5*[ones(1,n-1)/(ΔR^2) 0 ...
                -ones(1,n-1)/(ΔR^2)];
34          OneDownDiagSecond = -0.5*[ones(1,n-1)/(ΔR^2) 0 ...
                -ones(1,n-1)/(ΔR^2)];
35
36          %Create terms corresponding to single derivative term in the
37          %kinetic energy d/dr.
38          OnDiagKineticFirst = -0.5*[-1./(R(1:n-1)*ΔR) 1/(R(n)*ΔR)...
39              1./(R(1:n-1)*ΔR) -1/(R(n)*ΔR)];
40          OneUpDiagKineticFirst = -0.5*[1./(R(1:n-1)*ΔR) 0 ...
                -1./(R(1:n-1)*ΔR)];
41          OneDownDiagKineticFirst = -0.5*[zeros(1,n-2) -1/(R(n-1)*ΔR)...
42              zeros(1,n-1) 1/(R(n-1)*ΔR)];
43
44          OnDiagKinetic = OnDiagKineticSecond+OnDiagKineticFirst;
45          OneUpDiag = OneUpDiagSecond+OneUpDiagKineticFirst;
46          OneDownDiag = OneDownDiagSecond+OneDownDiagKineticFirst;
47
48          %Create the cross terms between the u(r) and v(r) equations
49          NOffDiag = g*PhiR.^2;
50
51          %Build matrix from individual vectors created so far. All ...
                elements
52          %not specified are set to zero
53          M = diag(OnDiag)+diag(OnDiagKinetic)+diag(OneUpDiag,1)+...
54              diag(OneDownDiag,-1)+diag(NOffDiag,size(R,2))+...
55              diag(-conj(NOffDiag),-(size(R,2)));
56
57
58          %Calculate eigenvectors and eignevalues of matirx M
59          [V,D] = eig(M,'nobalance');
60          W = diag(D);
61          %Extract lowest energy eigenvalue and the corresponding ...
                eigenvector
62          [W,index] = sort(W);
63          Omega(i) = W(1);
64          Vector = V(:,index(1));
65          Vectors{i} = Vector;
66
67      end
68
69      %Anglin surface mode vc
70      w_surface = abs(m_values)*(sqrt(2)*(u^(1/6))/(r0+sqrt(2*u)));
```

```
71      %Local speed of sound vc
72      w_sound = abs(m_values)*(2*sqrt(u*hbar*wr/(3*mass))/(r0))/(ar*wr);
73      %vc from excitation spectrum
74      [CritW,mcrit] = ...
            min(abs(Omega(abs(m_values)>0)./m_values(abs(m_values)>0)));
75      w_spectrum = abs(m_values)*CritW;
76
77  end
```

Bibliography

[1] A. Einstein. Quantentheorie des einatomigen idealen gases. *Sitzungsber. Preuss. Akad. Wiss.* **1925**, 3 (1925).

[2] S. N. Bose. Plancks gesetz und lichtquantenhypothese. *Z. Phys.* **26**, 178 (1924).

[3] H. K. Onnes. The resistance of pure mercury at helium temperatures. *Coomun. Phys. Lab. Univ. Leiden* **12** (1911).

[4] J. Bardeen, L. N. Cooper & J. R. Schrieffer. Theory of superconductivity. *Phys. Rev.* **108**, 1175–1204 (1957).

[5] P. Kapitza. Viscosity of liquid helium below the λ-point. *Nature* **141**, 74 (1938).

[6] J. F. Allen & A. D. Misener. Flow of liquid helium II. *Nature* **141**, 75 (1938).

[7] F. London. The lambda-phenomenon of liquid helium and the Bose-Einstein degeneracy. *Nature* **141**, 643 (1938).

[8] L. Tisza. Transport phenomena in helium II. *Nature* **141**, 913 (1938).

[9] L. Tisza. The theory of liquid helium. *Phys. Rev.* **72**, 838–854 (1947).

[10] M. H. Anderson, J. R. Ensher, M. R. Matthews, C. E. Wieman & E. A. Cornell. Observation of Bose-Einstein condensation in a dilute atomic vapor. *Science* **269**, 198 (1995).

[11] K. B. Davis, M. O. Mewes, M. R. Andrews, N. J. van Druten, D. S. Durfee, D. M. Kurn & W. Ketterle. Bose-Einstein condensation in a gas of sodium atoms. *Phys. Rev. Lett.* **75**, 3969 (1995).

[12] D. W. S. A. Griffin & S. Stringari. *Bose-Einstein Condensation* (Cambridge University Press, 1995).

[13] A. J. Leggett. Bose-Einstein condensation in the alkali gases: Some fundamental concepts. *Rev. Mod. Phys.* **73**, 307–356 (2001).

[14] S. Moulder, S. Beattie, R. P. Smith, N. Tammuz & Z. Hadzibabic. Quantized supercurrent decay in an annular Bose-Einstein condensate. *Phys. Rev. A* **86**, 013629 (2012).

[15] S. Beattie, S. Moulder, R. J. Fletcher & Z. Hadzibabic. Persistent currents in spinor condensates. *Phys. Rev. Lett.* **110**, 025301 (2013).

[16] F. Dalfovo, S. Giorgini, L. P. Pitaevskii & S. Stringari. Theory of Bose-Einstein condensation in trapped gases. *Rev. Mod. Phys.* **71**, 463 (1999).

[17] V. Bagnato, D. E. Pritchard & D. Kleppner. Bose-Einstein condensation in an external potential. *Phys. Rev. A* **35**, 4354 (1987).

[18] J. Dalibard. Collisional dynamics of ultra-cold atomic gases. In M. Inguscio, S. Stringari & C. Wieman (eds.) *Proceedings of the International School of Physics Enrico Fermi, Course CXL: Bose-Einstein condensation in gases, Varena 1998* (Addison-Wesley, 1998).

[19] C. J. Pethick & H. Smith. *Bose-Einstein Condensation in Dilute Gases* (Cambridge University Press, 2008), second edn.

[20] B. D. Simons. Cambridge university lecture series (2009).

[21] N. N. Bogoliubov. On the theory of superfluidity. *J. Phys. (USSR)* **11**, 23 (1947).

[22] L. D. Landau & E. M. Lifshitz. *Statistical Physics, Part 1* (Elsevier, 1980), third edn.

[23] O. Penrose & L. Onsager. Bose-Einstein condensation and liquid helium. *Phys. Rev.* **104**, 576–584 (1956).

[24] R. J. Glauber. The quantum theory of optical coherence. *Phys. Rev.* **130**, 2529–2539 (1963).

[25] L. D. Landau. The theory of superfluidity in helium II. *J. Phys. (USSR)* **5**, 71 (1941).

[26] P. W. Anderson. Considerations on the flow of superfluid helium. *Rev. Mod. Phys.* **38**, 298–310 (1966).

[27] O. Avenel & E. Varoquaux. Observation of singly quantized dissipation events obeying the Josephson frequency relation in the critical flow of superfluid ^{4}He through an aperture. *Phys. Rev. Lett.* **55**, 2704–2707 (1985).

[28] Z. Hadzibabic & J. Dalibard. Two-dimensional Bose fluids: An atomic physics perspective. In R. Kaiser, D. Wiersma & L. Fallani (eds.) *Proceedings of the International School of Physics Enrico Fermi, Course CLXXIII: Nano optics and atomics: transport of light and matter waves, Varena 2009* (IOS Press, Amsterdam and SIF, Bologna, 2011).

[29] A. L. Fetter. Rotating trapped Bose-Einstein condensates. *Rev. Mod. Phys.* **81**, 647–691 (2009).

[30] M. R. Matthews, B. P. Anderson, P. C. Haljan, D. S. Hall, C. E. Wieman & E. A. Cornell. Vortices in a Bose-Einstein condensate. *Phys. Rev. Lett.* **83**, 2498–2501 (1999).

[31] K. W. Madison, F. Chevy, W. Wohlleben & J. Dalibard. Vortex formation in a stirred Bose-Einstein condensate. *Phys. Rev. Lett.* **84**, 806–809 (2000).

[32] J. R. Abo-Shaeer, C. Raman, J. M. Vogels & W. Ketterle. Observation of vortex lattices in Bose-Einstein condensates. *Science* **292**, 476–479 (2001). `http://www.sciencemag.org/content/292/5516/476.full.pdf`.

[33] F. Chevy, K. W. Madison, V. Bretin & J. Dalibard. Interferometric detection of a single vortex in a dilute Bose-Einstein condensate. *Phys. Rev. A* **64**, 031601 (2001).

[34] S. Inouye, S. Gupta, T. Rosenband, A. P. Chikkatur, A. Görlitz, T. L. Gustavson, A. E. Leanhardt, D. E. Pritchard & W. Ketterle. Observation of vortex phase singularities in Bose-Einstein condensates. *Phys. Rev. Lett.* **87**, 080402 (2001).

[35] L. Onsager. Statistical hydrodynamics. *Nuovo Cimento* **6**, 249 (1949).

[36] R. P. Feynman. Atomic theory of the two-fluid model of liquid helium. *Phys. Rev.* **94**, 262–277 (1954).

[37] H. E. Hall & W. F. Vinen. The rotation of liquid helium II. I. Experiments on the propagation of second sound in uniformly rotating helium II. *Proceedings of the Royal Society of London. Series A. Mathematical and Physical Sciences* **238**, 204–214 (1956). `http://rspa.royalsocietypublishing.org/content/238/1213/204.full.pdf+html`.

[38] F. Chevy, K. W. Madison & J. Dalibard. Measurement of the angular momentum of a rotating Bose-Einstein condensate. *Phys. Rev. Lett.* **85**, 2223–2227 (2000).

[39] R. P. Feynman. Application of quantum mechanics to liquid helium. In C. J. Gorter (ed.) *Progress in Low Temperature Physics*, vol. 1, chap. 2 (Amsterdam: North-Holland Publishing Company, 1955).

[40] F. Piazza, L. A. Collins & A. Smerzi. Instability and vortex ring dynamics in a three-dimensional superfluid flow through a constriction. *New Journal of Physics* **13**, 043008 (2011).

[41] W. F. Vinen. Vortex lines in liquid helium II. In C. J. Gorter (ed.) *Progress in Low Temperature Physics*, vol. 3, chap. 1 (Amsterdam: North-Holland Publishing Company, 1961).

[42] A. L. Fetter. Vortices in an imperfect Bose gas. I. The condensate. *Phys. Rev.* **138**, A429–A437 (1965).

[43] D. Pines & P. Noziéres. *The Theory of Quantum Liquids*, vol. 2 (Perseus Books, 1999).

[44] R. L. D. Campbell, R. P. Smith, N. Tammuz, S. Beattie, S. Moulder & Z. Hadzibabic. Efficient production of large ^{39}K Bose-Einstein condensates. *Phys. Rev. A* **82**, 063611 (2010).

[45] R. L. D. Campbell. *Thermodynamic Properties of a Bose Gas with Tuneable Interactions*. Ph.D. thesis, University of Cambridge (2011).

[46] N. Tammuz. *Thermodynamics of Ultracold* ^{39}K *Atomic Bose Gases with Tuneable Interactions*. Ph.D. thesis, University of Cambridge (2011).

[47] N. Tammuz, R. P. Smith, R. L. D. Campbell, S. Beattie, S. Moulder, J. Dalibard & Z. Hadzibabic. Can a Bose gas be saturated? *Phys. Rev. Lett.* **106**, 230401 (2011).

[48] R. P. Smith, R. L. D. Campbell, N. Tammuz & Z. Hadzibabic. Effects of interactions on the critical temperature of a trapped Bose gas. *Phys. Rev. Lett.* **106**, 250403 (2011).

[49] R. P. Smith, N. Tammuz, R. L. D. Campbell, M. Holzmann & Z. Hadzibabic. Condensed fraction of an atomic Bose gas induced by critical correlations. *Phys. Rev. Lett.* **107**, 190403 (2011).

[50] R. P. Smith, S. Beattie, S. Moulder, R. L. D. Campbell & Z. Hadzibabic. Condensation dynamics in a quantum-quenched Bose gas. *Phys. Rev. Lett.* **109**, 105301 (2012).

[51] A. L. Gaunt, R. J. Fletcher, R. P. Smith & Z. Hadzibabic. A superheated Bose-condensed gas (2012). `arXiv:1212.5833`.

[52] C. C. Tannoudji, G. Grynberg & J. Dupont-Roe. *Atom-photon interactions* (John Wiley and Sons, 1992).

[53] M. Kasevich & S. Chu. Laser cooling below a photon recoil with three-level atoms. *Phys. Rev. Lett.* **69**, 1741–1744 (1992).

[54] S. E. Harris. Electromagnetically induced transparency. *Physics Today* **50**, 36–42 (1997).

[55] C. J. Foot. *Atomic Physics* (Oxford University Press, 2005).

[56] K. Bergmann, H. Theuer & B. W. Shore. Coherent population transfer among quantum states of atoms and molecules. *Rev. Mod. Phys.* **70**, 1003–1025 (1998).

[57] C. Zener. Non-adiabatic crossing of energy levels. *Proceedings of the Royal Society of London. Series A* **137**, 696–702 (1932). `http://rspa.royalsocietypublishing.org/content/137/833/696.full.pdf+html`.

[58] R. Grimm, Weidemüller & Y. B. Ovchinnikov. Optical dipole traps for neutral atoms. *Adv. At. Mol. Opt. Phys.* **42**, 95 (2000).

[59] E. L. Raab, M. Prentiss, A. Cable, S. Chu & D. E. Pritchard. Trapping of neutral sodium atoms with radiation pressure. *Phys. Rev. Lett.* **59**, 2631 (1987).

[60] P. D. Lett, R. N. Watts, C. I. Westbrook, W. D. Phillips, P. L. Gould & H. J. Metcalf. Observation of atoms laser cooled below the Doppler limit. *Phys. Rev. Lett.* **61**, 169 (1988).

[61] J. Dalibard & C. Cohen-Tannoudji. Laser cooling below the Doppler limit by polarization gradients: simple theoretical models. *J. Opt. Soc. Am. B* **6**, 2023 (1989).

[62] G. Breit & I. I. Rabi. Measurement of nuclear spin. *Phys. Rev.* **38**, 2082 (1931).

[63] E. Majorana. Atomi orientati in campo magnetico variabile. *Nuovo Cimento* **9**, 43 (1932).

[64] T. H. Bergeman, P. McNicholl, J. Kycia, H. Metcalf & N. L. Balazs. Quantized motion of atoms in a quadrupole magnetostatic trap. *J. Opt. Soc. Am. B* **6**, 2249–2256 (1989).

[65] W. Petrich, M. H. Anderson, J. R. Ensher & E. A. Cornell. Stable, tightly confining magnetic trap for evaporative cooling of neutral atoms. *Phys. Rev. Lett.* **74**, 3352 (1995).

[66] Y.-J. Lin, R. L. Compton, A. R. Perry, W. D. Phillips, J. V. Porto & I. B. Spielman. Bose-Einstein condensate in a uniform light-induced vector potential. *Phys. Rev. Lett.* **102**, 130401 (2009).

[67] F. Ferlaino, C. D'Errico, G. Roati, M. Zaccanti, M. Inguscio, G. Modugno & A. Simoni. Feshbach spectroscopy of a K-Rb atomic mixture. *Phys. Rev. A* **73**, 040702 (2006).

[68] E. G. M. van Kempen, S. J. J. M. F. Kokkelmans, D. J. Heinzen & B. J. Verhaar. Interisotope determination of ultracold rubidium interactions from three high-precision experiments. *Phys. Rev. Lett.* **88**, 093201 (2002).

[69] T. Esslinger, I. Bloch & T. W. Hänsch. Bose-Einstein condensation in a quadrupole-Ioffe-configuration trap. *Phys. Rev. A* **58**, R2664 (1998).

[70] J. Dalibard & C. Cohen-Tannoudji. Dressed-atom approach to atomic motion in laser light: the dipole force revisited. *J. Opt. Soc. Am. B* **2**, 1707–1720 (1985).

[71] I. Gotlibovych. *Microwave manipulation of ultra-cold atoms.* Master's thesis, University of Cambridge (2010).

[72] F. W. Grover. *Inductance calculations, working formulas and tables* (Dover Publications, 1962).

[73] A. Haase *et al.* Nmr probeheads for in vivo applications. *Concepts in Magnetic Resonance* **12**, 361–388 (2000).

[74] A. Dareau. *Optical devices for imaging, trapping and manipulating cold atoms.* Master's thesis, University of Cambridge (2010).

[75] W. Alt. An objective lens for efficient fluorescence detection of single atoms. *Optik* **113**, 142 (2002).

[76] D. A. Steck. Rubidium 87 D line data. `http://steck.us/alkalidata/` (23^{rd} December 2010).

[77] B. Gao. Effects of Zeeman degeneracy on the steady-state properties of an atom interacting with a near-resonant laser field: Analytic results. *Phys. Rev. A* **48**, 2443–2448 (1993).

[78] H. J. Metcalf & P. Van Der Straten. *Laser Cooling and Trapping* (Springer, 1999).

[79] A. Ramanathan, S. R. Muniz, K. C. Wright, R. P. Anderson, W. D. Phillips, K. Helmerson & G. K. Campbell. Partial-transfer absorption imaging: A versatile technique for optimal imaging of ultracold gases. *Review of Scientific Instruments* **83**, 083119 (2012).

[80] W. Ketterle, D. Durfee & D. Stamper-Kurn. Making, probing and understanding Bose-Einstein condensates. In *Proceedings of the International School of Physics - Enrico Fermi* (IOS Press, 1999).

[81] W. A. Little. Decay of persistent currents in small superconductors. *Phys. Rev.* **156**, 396–403 (1967).

[82] J. S. Langer & V. Ambegaokar. Intrinsic resistive transition in narrow superconducting channels. *Phys. Rev.* **164**, 498–510 (1967).

[83] D. E. McCumber & B. I. Halperin. Time scale of intrinsic resistive fluctuations in thin superconducting wires. *Phys. Rev. B* **1**, 1054–1070 (1970).

[84] M. Sahu, M.-H. Bae, A. Rogachev, D. Pekker, T.-C. Wei, N. Shah, P. M. Goldbart & A. Bezryadin. Individual topological tunnelling events of a quantum field probed through their macroscopic consequences. *Nature Physics* **5**, 503–508 (2009).

[85] P. Li, P. M. Wu, Y. Bomze, I. V. Borzenets, G. Finkelstein & A. M. Chang. Switching currents limited by single phase slips in one-dimensional superconducting Al nanowires. *Phys. Rev. Lett.* **107**, 137004 (2011).

[86] J. D. Reppy. Application of a superfluid gyroscope to the study of critical velocities in liquid helium near the λ transition. *Phys. Rev. Lett.* **14**, 733–735 (1965).

[87] E. Varoquaux, M. W. Meisel & O. Avenel. Onset of the critical velocity regime in superfluid ^{4}He at low temperature. *Phys. Rev. Lett.* **57**, 2291–2294 (1986).

[88] J. C. Davis, J. Steinhauer, K. Schwab, Y. M. Mukharsky, A. Amar, Y. Sasaki & R. E. Packard. Evidence for quantum tunneling of phase-slip vortices in superfluid ^{4}He. *Phys. Rev. Lett.* **69**, 323–326 (1992).

[89] Y. Shin, M. Saba, M. Vengalattore, T. A. Pasquini, C. Sanner, A. E. Leanhardt, M. Prentiss, D. E. Pritchard & W. Ketterle. Dynamical instability of a doubly quantized vortex in a Bose-Einstein condensate. *Phys. Rev. Lett.* **93**, 160406 (2004).

[90] T. P. Simula, S. M. M. Virtanen & M. M. Salomaa. Stability of multiquantum vortices in dilute Bose-Einstein condensates. *Phys. Rev. A* **65**, 033614 (2002).

[91] S. Tung, V. Schweikhard & E. A. Cornell. Observation of vortex pinning in Bose-Einstein condensates. *Phys. Rev. Lett.* **97**, 240402 (2006).

[92] J. A. Sauer, M. D. Barrett & M. S. Chapman. Storage ring for neutral atoms. *Phys. Rev. Lett.* **87**, 270401 (2001).

[93] A. S. Arnold, C. S. Garvie & E. Riis. Large magnetic storage ring for Bose-Einstein condensates. *Phys. Rev. A* **73**, 041606 (2006).

[94] S. Gupta, K. W. Murch, K. L. Moore, T. P. Purdy & D. M. Stamper-Kurn. Bose-Einstein condensation in a circular waveguide. *Phys. Rev. Lett.* **95**, 143201 (2005).

[95] T. Fernholz, R. Gerritsma, P. Krüger & R. J. C. Spreeuw. Dynamically controlled toroidal and ring-shaped magnetic traps. *Phys. Rev. A* **75**, 063406 (2007).

[96] I. Lesanovsky & W. von Klitzing. Time-averaged adiabatic potentials: Versatile matter-wave guides and atom traps. *Phys. Rev. Lett.* **99**, 083001 (2007).

[97] B. E. Sherlock, M. Gildemeister, E. Owen, E. Nugent & C. J. Foot. Time-averaged adiabatic ring potential for ultracold atoms. *Phys. Rev. A* **83**, 043408 (2011).

[98] D. S. Naik & C. Raman. Optically plugged quadrupole trap for bose-einstein condensates. *Phys. Rev. A* **71**, 033617 (2005).

[99] C. Ryu, M. F. Andersen, P. Cladé, V. Natarajan, K. Helmerson & W. D. Phillips. Observation of persistent flow of a Bose-Einstein condensate in a toroidal trap. *Phys. Rev. Lett.* **99**, 260401 (2007).

[100] A. Ramanathan, K. C. Wright, S. R. Muniz, M. Zelan, W. T. Hill, C. J. Lobb, K. Helmerson, W. D. Phillips & G. K. Campbell. Superflow in a toroidal Bose-Einstein condensate: An atom circuit with a tunable weak link. *Phys. Rev. Lett.* **106**, 130401 (2011).

[101] K. Henderson, C. Ryu, C. MacCormick & M. G. Boshier. Experimental demonstration of painting arbitrary and dynamic potentials for Bose-Einstein condensates. *New Journal of Physics* **11**, 043030 (2009).

[102] K. C. Wright, R. B. Blakestad, C. J. Lobb, W. D. Phillips & G. K. Campbell. Driving phase slips in a superfluid atom circuit with a rotating weak link. *Phys. Rev. Lett.* **110**, 025302 (2013).

[103] A. Das & J. Sabbatini. Winding up superfluid in a torus via Bose-Einstein condensation. *Scientific Reports* **2** (2012).

[104] N. R. Cooper & Z. Hadzibabic. Measuring the superfluid fraction of an ultracold atomic gas. *Phys. Rev. Lett.* **104**, 030401 (2010).

[105] T. L. Gustavson, P. Bouyer & M. A. Kasevich. Precision rotation measurements with an atom interferometer gyroscope. *Phys. Rev. Lett.* **78**, 2046–2049 (1997).

[106] A. Lenef, T. D. Hammond, E. T. Smith, M. S. Chapman, R. A. Rubenstein & D. E. Pritchard. Rotation sensing with an atom interferometer. *Phys. Rev. Lett.* **78**, 760–763 (1997).

[107] S. Wu, E. Su & M. Prentiss. Demonstration of an area-enclosing guided-atom interferometer for rotation sensing. *Phys. Rev. Lett.* **99**, 173201 (2007).

[108] B. Canuel *et al.* Six-axis inertial sensor using cold-atom interferometry. *Phys. Rev. Lett.* **97**, 010402 (2006).

[109] Y.-J. Wang, D. Z. Anderson, V. M. Bright, E. A. Cornell, Q. Diot, T. Kishimoto, M. Prentiss, R. A. Saravanan, S. R. Segal & S. Wu. Atom Michelson interferometer on a chip using a Bose-Einstein condensate. *Phys. Rev. Lett.* **94**, 090405 (2005).

[110] S. Gupta, K. Dieckmann, Z. Hadzibabic & D. E. Pritchard. Contrast interferometry using Bose-Einstein condensates to measure h/m and α. *Phys. Rev. Lett.* **89**, 140401 (2002).

[111] P. L. Halkyard, M. P. A. Jones & S. A. Gardiner. Rotational response of two-component Bose-Einstein condensates in ring traps. *Phys. Rev. A* **81**, 061602 (2010).

[112] G. E. Marti, R. Olf & D. M. Stamper-Kurn. A Collective Excitation Interferometer for Rotation Sensing with a Trapped Bose-Einstein Condensate. *ArXiv e-prints* (2012). `1210.0033`.

[113] B. T. Seaman, M. Krämer, D. Z. Anderson & M. J. Holland. Atomtronics: Ultracold-atom analogs of electronic devices. *Phys. Rev. A* **75**, 023615 (2007).

[114] J. Vaughan & D. Willetts. Interference properties of a light beam having a helical wave surface. *Optics Communications* **30**, 263 – 267 (1979).

[115] M. Clifford, J. Arlt, J. Courtial & K. Dholakia. High-order Laguerre-Gaussian laser modes for studies of cold atoms. *Optics Communications* **156**, 300 – 306 (1998).

[116] L. Allen, M. W. Beijersbergen, R. J. C. Spreeuw & J. P. Woerdman. Orbital angular momentum of light and the transformation of Laguerre-Gaussian laser modes. *Phys. Rev. A* **45**, 8185–8189 (1992).

[117] A. Gaunt. *Unconventional Bose-Einstein Condensates*. CPGS report, University of Cambridge (2012).

[118] A. L. Gaunt & Z. Hadzibabic. Robust digital holography for ultracold atom trapping. *Scientific Reports* **2** (2012).

[119] A. L. Gaunt, T. F. Schmidutz, I. Gotlibovych, R. P. Smith & Z. Hadzibabic. Bose-Einstein condensation of atoms in a uniform potential. *ArXiv e-prints* (2012). `1212.4453`.

[120] K. T. Gahagan & J. G. A. Swartzlander. Optical vortex trapping of particles. *Opt. Lett.* **21**, 827–829 (1996).

[121] H. He, N. Heckenberg & H. Rubinsztein-Dunlop. Optical particle trapping with higher-order doughnut beams produced using high efficiency computer generated holograms. *Journal of Modern Optics* **42**, 217–223 (1995). `http://www.tandfonline.com/doi/pdf/10.1080/09500349514550171`.

[122] F. Tamburini, E. Mari, A. Sponselli, B. Thid, A. Bianchini & F. Romanato. Encoding many channels on the same frequency through radio vorticity: First experimental test. *New Journal of Physics* **14**, 033001 (2012).

[123] G. Foo, D. M. Palacios & J. Grover A. Swartzlander. Optical vortex coronagraph. *Opt. Lett.* **30**, 3308–3310 (2005).

[124] S. Fürhapter, A. Jesacher, S. Bernet & M. Ritsch-Marte. Spiral interferometry. *Opt. Lett.* **30**, 1953–1955 (2005).

[125] G. Gibson, J. Courtial, M. Padgett, M. Vasnetsov, V. Pas'ko, S. Barnett & S. Franke-Arnold. Free-space information transfer using light beams carrying orbital angular momentum. *Opt. Express* **12**, 5448–5456 (2004).

[126] C. Tamm. Frequency locking of two transverse optical modes of a laser. *Phys. Rev. A* **38**, 5960–5963 (1988).

[127] M. Beijersbergen, L. Allen, H. van der Veen & J. Woerdman. Astigmatic laser mode converters and transfer of orbital angular momentum. *Optics Communications* **96**, 123 – 132 (1993).

[128] J. Courtial & M. Padgett. Performance of a cylindrical lens mode converter for producing Laguerre-Gaussian laser modes. *Optics Communications* **159**, 13 – 18 (1999).

[129] G. Turnbull, D. Robertson, G. Smith, L. Allen & M. Padgett. The generation of free-space Laguerre-Gaussian modes at millimetre-wave frequencies by use of a spiral phaseplate. *Optics Communications* **127**, 183 – 188 (1996).

[130] M. Beijersbergen, R. Coerwinkel, M. Kristensen & J. Woerdman. Helical-wavefront laser beams produced with a spiral phaseplate. *Optics Communications* **112**, 321 – 327 (1994).

[131] N. R. Heckenberg, R. McDuff, C. P. Smith & A. G. White. Generation of optical phase singularities by computer-generated holograms. *Opt. Lett.* **17**, 221–223 (1992).

[132] J. F. S. Brachmann, W. S. Bakr, J. Gillen, A. Peng & M. Greiner. Inducing vortices in a Bose-Einstein condensate using holographically produced light beams. *Opt. Express* **19**, 12984–12991 (2011).

[133] J. E. Curtis & D. G. Grier. Structure of optical vortices. *Phys. Rev. Lett.* **90**, 133901 (2003).

[134] R. Bowman, A. Wright & M. Padgett. An SLM-based Shack-Hartmann wavefront sensor for aberration correction in optical tweezers. *Journal of Optics* **12**, 124004 (2010).

[135] G. D. Bruce, J. Mayoh, G. Smirne, L. Torralbo-Campo & D. Cassettari. A smooth, holographically generated ring trap for the investigation of superfluidity in ultracold atoms. *Physica Scripta* **2011**, 014008 (2011).

[136] G. D. Bruce, S. L. Bromley, G. Smirne, L. Torralbo-Campo & D. Cassettari. Holographic power-law traps for the efficient production of Bose-Einstein condensates. *Phys. Rev. A* **84**, 053410 (2011).

[137] A. Jesacher, A. Schwaighofer, S. Fürhapter, C. Maurer, S. Bernet & M. Ritsch-Marte. Wavefront correction of spatial light modulators using an optical vortex image. *Opt. Express* **15**, 5801–5808 (2007).

[138] C. Raman, M. Köhl, R. Onofrio, D. S. Durfee, C. E. Kuklewicz, Z. Hadzibabic & W. Ketterle. Evidence for a critical velocity in a Bose-Einstein condensed gas. *Phys. Rev. Lett.* **83**, 2502–2505 (1999).

[139] R. Onofrio, C. Raman, J. M. Vogels, J. R. Abo-Shaeer, A. P. Chikkatur & W. Ketterle. Observation of superfluid flow in a Bose-Einstein condensed gas. *Phys. Rev. Lett.* **85**, 2228 (2000).

[140] R. Desbuquois, L. Chomaz, T. Yefsah, J. Leonard, J. Beugnon, C. Weitenberg & J. Dalibard. Superfluid behaviour of a two-dimensional Bose gas. *Nature Physics* **8**, 645–648 (2012).

[141] T. W. Neely, E. C. Samson, A. S. Bradley, M. J. Davis & B. P. Anderson. Observation of vortex dipoles in an oblate Bose-Einstein condensate. *Phys. Rev. Lett.* **104**, 160401 (2010).

[142] A. E. Leanhardt, A. Görlitz, A. P. Chikkatur, D. Kielpinski, Y. Shin, D. E. Pritchard & W. Ketterle. Imprinting vortices in a Bose-Einstein condensate using topological phases. *Phys. Rev. Lett.* **89**, 190403 (2002).

[143] S.-I. Ogawa, M. Möttönen, M. Nakahara, T. Ohmi & H. Shimada. Method to create a vortex in a Bose-Einstein condensate. *Phys. Rev. A* **66**, 013617 (2002).

[144] A. E. Leanhardt, Y. Shin, D. Kielpinski, D. E. Pritchard & W. Ketterle. Coreless vortex formation in a spinor Bose-Einstein condensate. *Phys. Rev. Lett.* **90**, 140403 (2003).

[145] L. S. Leslie, A. Hansen, K. C. Wright, B. M. Deutsch & N. P. Bigelow. Creation and detection of skyrmions in a Bose-Einstein condensate. *Phys. Rev. Lett.* **103**, 250401 (2009).

[146] M. F. Andersen, C. Ryu, P. Cladé, V. Natarajan, A. Vaziri, K. Helmerson & W. D. Phillips. Quantized rotation of atoms from photons with orbital angular momentum. *Phys. Rev. Lett.* **97**, 170406 (2006).

[147] K. C. Wright, L. S. Leslie & N. P. Bigelow. Optical control of the internal and external angular momentum of a Bose-Einstein condensate. *Phys. Rev. A* **77**, 041601 (2008).

[148] A. Widera, S. Trotzky, P. Cheinet, S. Fölling, F. Gerbier, I. Bloch, V. Gritsev, M. D. Lukin & E. Demler. Quantum spin dynamics of mode-squeezed Luttinger liquids in two-component atomic gases. *Phys. Rev. Lett.* **100**, 140401 (2008).

[149] M. Cozzini, B. Jackson & S. Stringari. Vortex signatures in annular Bose-Einstein condensates. *Phys. Rev. A* **73**, 013603 (2006).

[150] E. Lundh. Multiply quantized vortices in trapped Bose-Einstein condensates. *Phys. Rev. A* **65**, 043604 (2002).

[151] H. Pu, C. K. Law, J. H. Eberly & N. P. Bigelow. Coherent disintegration and stability of vortices in trapped Bose condensates. *Phys. Rev. A* **59**, 1533–1537 (1999).

[152] A. L. Fetter & A. A. Svidzinsky. Vortices in a trapped dilute Bose-Einstein condensate. *Journal of Physics: Condensed Matter* **13**, R135 (2001).

[153] M. Baert, V. V. Metlushko, R. Jonckheere, V. V. Moshchalkov & Y. Bruynseraede. Composite flux-line lattices stabilized in superconducting films by a regular array of artificial defects. *Phys. Rev. Lett.* **74**, 3269–3272 (1995).

[154] P. Engels, I. Coddington, P. C. Haljan, V. Schweikhard & E. A. Cornell. Observation of long-lived vortex aggregates in rapidly rotating Bose-Einstein condensates. *Phys. Rev. Lett.* **90**, 170405 (2003).

[155] P. O. Fedichev & G. V. Shlyapnikov. Dissipative dynamics of a vortex state in a trapped Bose-condensed gas. *Phys. Rev. A* **60**, R1779–R1782 (1999).

[156] D. V. Freilich, D. M. Bianchi, A. M. Kaufman, T. K. Langin & D. S. Hall. Real-time dynamics of single vortex lines and vortex dipoles in a Bose-Einstein condensate. *Science* **329**, 1182–1185 (2010). `http://www.sciencemag.org/content/329/5996/1182.full.pdf`.

[157] J. A. Seman *et al.* Three-vortex configurations in trapped Bose-Einstein condensates. *Phys. Rev. A* **82**, 033616 (2010).

[158] R. Navarro, R. Carretero-Gonzalez, P. J. Torres, P. G. Kevrekidis, D. J. Frantzeskakis, M. W. Ray, E. Altunta & D. S. Hall. Dynamics of Few Co-rotating Vortices in Bose-Einstein Condensates. *ArXiv e-prints* (2013). `1302.6612`.

[159] Z. Hadzibabic, P. Kruger, M. Cheneau, B. Battelier & J. Dalibard. Berezinskii-Kosterlitz-Thouless crossover in a trapped atomic gas. *Nature* **441**, 1118–1121 (2006).

[160] K. Kärkkäinen, J. Christensson, G. Reinisch, G. M. Kavoulakis & S. M. Reimann. Metastability of persistent currents in trapped gases of atoms. *Phys. Rev. A* **76**, 043627 (2007).

[161] S. Baharian & G. Baym. Bose-Einstein condensates in toroidal traps: Instabilities, swallow-tail loops, and self-trapping. *Phys. Rev. A* **87**, 013619 (2013).

[162] R. Kanamoto, L. D. Carr & M. Ueda. Topological winding and unwinding in metastable Bose-Einstein condensates. *Phys. Rev. Lett.* **100**, 060401 (2008).

[163] G. L. Pollack. Experimental superfluidity. r. j. donnelly. chicago lectures in physics. *Science* **158**, 1442–1443 (1967). `http://www.sciencemag.org/content/158/3807/1442.2.full.pdf`.

[164] A. Amar, Y. Sasaki, R. L. Lozes, J. C. Davis & R. E. Packard. Quantized phase slippage in superfluid ^{4}He. *Phys. Rev. Lett.* **68**, 2624–2627 (1992).

[165] O. Avenel, G. Ihas & E. Varoquaux. The nucleation of vortices in superfluid ^{4}He: Answers and questions. *Journal of Low Temperature Physics* **93**, 1031–1057 (1993).

[166] E. Varoquaux, O. Avenel, Y. Mukharsky & P. Hakonen. The Experimental Evidence for Vortex Nucleation in ^{4}He. In C. F. Barenghi, R. J. Donnelly & W. F. Vinen (eds.) *Quantized Vortex Dynamics and Superfluid Turbulence*, vol. 571 of *Lecture Notes in Physics, Berlin Springer Verlag*, 36 (2001).

[167] E. Varoquaux & O. Avenel. Vortex nucleation in phase-slippage experiments in ultrapure superfluid ^{4}He below 0.5 K. *Phys. Rev. B* **68**, 054515 (2003).

[168] J. E. Mooij & C. J. P. M. Harmans. Phase-slip flux qubits. *New Journal of Physics* **7**, 219 (2005).

[169] J. E. Mooij & Y. V. Nazarov. Superconducting nanowires as quantum phase-slip junctions. *Nature Physics* **2**, 169–172 (2006).

[170] L. D. Landau & E. M. Lifshitz. *Fluid Mechanics* (Pergamon, New York, 1987), second edn.

[171] A. K. Ramanathan. *A Ring with a Spin: Superfluidity in a toroidal Bose-Einstein condensate*. Ph.D. thesis, University of Maryland (2011).

[172] A. L. Fetter, B. Jackson & S. Stringari. Rapid rotation of a Bose-Einstein condensate in a harmonic plus quartic trap. *Phys. Rev. A* **71**, 013605 (2005).

[173] F. Piazza, L. A. Collins & A. Smerzi. Critical velocity for a toroidal Bose-Einstein condensate flowing through a barrier. *ArXiv e-prints* (2012). `1208.0734`.

[174] F. Piazza, L. A. Collins & A. Smerzi. Vortex-induced phase-slip dissipation in a toroidal Bose-Einstein condensate flowing through a barrier. *Phys. Rev. A* **80**, 021601 (2009).

[175] A. C. Mathey, C. W. Clark & L. Mathey. Decay of a superfluid current of ultra-cold atoms in a toroidal trap. *ArXiv e-prints* (2012). `1207.0501`.

[176] E. Zaremba. Sound propagation in a cylindrical Bose-condensed gas. *Phys. Rev. A* **57**, 518–521 (1998).

[177] C. Raman, J. R. Abo-Shaeer, J. M. Vogels, K. Xu & W. Ketterle. Vortex nucleation in a stirred Bose-Einstein condensate. *Phys. Rev. Lett.* **87**, 210402 (2001).

[178] M. W. Zwierlein, J. R. Abo-Shaeer, A. Schirotzek, C. H. Schunck & W. Ketterle. Vortices and superfluidity in a strongly interacting Fermi gas. *Nature* **435**, 1047–1051 (2005).

[179] P. O. Fedichev & G. V. Shlyapnikov. Critical velocity in cylindrical Bose-Einstein condensates. *Phys. Rev. A* **63**, 045601 (2001).

[180] J. R. Anglin. Local vortex generation and the surface mode spectrum of large Bose-Einstein condensates. *Phys. Rev. Lett.* **87**, 240401 (2001).

[181] R. Dubessy, T. Liennard, P. Pedri & H. Perrin. Critical rotation of an annular superfluid Bose-Einstein condensate. *Phys. Rev. A* **86**, 011602 (2012).

[182] D. S. Petrov, M. Holzmann & G. V. Shlyapnikov. Bose-Einstein condensation in quasi-2d trapped gases. *Phys. Rev. Lett.* **84**, 2551–2555 (2000).

[183] P. Bhattacharyya, T. L. Ho & N. D. Mermin. Stability of superflow in ^{3}He-A. *Phys. Rev. Lett.* **39**, 1290–1293 (1977).

[184] T.-L. Ho. Superfluidity of a spin-$\frac{1}{2}$ Bose fluid: Spin-polarized hydrogen. *Phys. Rev. Lett.* **49**, 1837–1840 (1982).

[185] J. Smyrnakis, S. Bargi, G. M. Kavoulakis, M. Magiropoulos, K. Kärkkäinen & S. M. Reimann. Mixtures of Bose gases confined in a ring potential. *Phys. Rev. Lett.* **103**, 100404 (2009).

[186] S. Bargi, F. Malet, G. M. Kavoulakis & S. M. Reimann. Persistent currents in Bose gases confined in annular traps. *Phys. Rev. A* **82**, 043631 (2010).

[187] K. Anoshkin, Z. Wu & E. Zaremba. Persistent currents in a bosonic mixture in the ring geometry. *ArXiv e-prints* (2012). `1207.3449`.

[188] J. Stenger, S. Inouye, D. M. Stamper-Kurn, H.-J. Miesner, A. P. Chikkatur & W. Ketterle. Spin domains in ground-state Bose-Einstein condensates. *Nature* **396**, 345–348 (1998).

[189] M. D. Barrett, J. A. Sauer & M. S. Chapman. All-optical formation of an atomic Bose-Einstein condensate. *Phys. Rev. Lett.* **87**, 010404 (2001).

[190] M.-S. Chang, C. D. Hamley, M. D. Barrett, J. A. Sauer, K. M. Fortier, W. Zhang, L. You & M. S. Chapman. Observation of spinor dynamics in optically trapped ^{87}Rb Bose-Einstein condensates. *Phys. Rev. Lett.* **92**, 140403 (2004).

[191] T.-L. Ho. Spinor Bose condensates in optical traps. *Phys. Rev. Lett.* **81**, 742–745 (1998).

[192] T. Ohmi & K. Machida. Bose-Einstein condensation with internal degrees of freedom in alkali atom gases. *Journal of the Physical Society of Japan* **67**, 1822–1825 (1998).

[193] M.-S. Chang, Q. Qin, W. Zhang, L. You & M. S. Chapman. Coherent spinor dynamics in a spin-1 Bose condensate. *Nature Physics* **1**, 111–116 (2005).

[194] A. Widera, F. Gerbier, S. Fölling, T. Gericke, O. Mandel & I. Bloch. Coherent collisional spin dynamics in optical lattices. *Phys. Rev. Lett.* **95**, 190405 (2005).

[195] A. Griesmaier, J. Werner, S. Hensler, J. Stuhler & T. Pfau. Bose-Einstein condensation of chromium. *Phys. Rev. Lett.* **94**, 160401 (2005).

[196] M. Lu, N. Q. Burdick, S. H. Youn & B. L. Lev. Strongly dipolar Bose-Einstein condensate of dysprosium. *Phys. Rev. Lett.* **107**, 190401 (2011).

[197] S. Yi, L. You & H. Pu. Quantum phases of dipolar spinor condensates. *Phys. Rev. Lett.* **93**, 040403 (2004).

[198] S. Yi & H. Pu. Spontaneous spin textures in dipolar spinor condensates. *Phys. Rev. Lett.* **97**, 020401 (2006).

[199] M. Vengalattore, S. R. Leslie, J. Guzman & D. M. Stamper-Kurn. Spontaneously modulated spin textures in a dipolar spinor Bose-Einstein condensate. *Phys. Rev. Lett.* **100**, 170403 (2008).

[200] D. M. Stamper-Kurn & M. Ueda. Spinor Bose gases: Explorations of symmetries, magnetism and quantum dynamics. *ArXiv e-prints* (2012). 1205.1888.

[201] Y. Kawaguchi & M. Ueda. Spinor Bose-Einstein condensates. *ArXiv e-prints* (2010). 1001.2072.

[202] A. Widera, F. Gerbier, S. Fölling, T. Gericke, O. Mandel & I. Bloch. Precision measurement of spin-dependent interaction strengths for spin-1 and spin-2 ^{87}Rb atoms. *New Journal of Physics* **8**, 152 (2006). arXiv:cond-mat/0604038.

[203] K. Kasamatsu, M. Tsubota & M. Ueda. Spin textures in rotating two-component Bose-Einstein condensates **71**, 043611 (2005). arXiv:cond-mat/0411544.

[204] D. S. Hall, M. R. Matthews, J. R. Ensher, C. E. Wieman & E. A. Cornell. Dynamics of component separation in a binary mixture of Bose-Einstein condensates. *Phys. Rev. Lett.* **81**, 1539–1542 (1998).

[205] K. M. Mertes, J. W. Merrill, R. Carretero-González, D. J. Frantzeskakis, P. G. Kevrekidis & D. S. Hall. Nonequilibrium dynamics and superfluid ring excitations in binary Bose-Einstein condensates. *Phys. Rev. Lett.* **99**, 190402 (2007).

[206] S. De, D. L. Campbell, R. M. Price, A. Putra, B. M. Anderson & I. B. Spielman. Quenched binary Bose-Einstein condensates: spin domain formation and coarsening. *ArXiv e-prints* (2012). 1211.3127.

[207] H.-J. Miesner, D. M. Stamper-Kurn, J. Stenger, S. Inouye, A. P. Chikkatur & W. Ketterle. Observation of metastable states in spinor Bose-Einstein condensates. *Phys. Rev. Lett.* **82**, 2228–2231 (1999).

[208] S. Hofferberth, I. Lesanovsky, T. Schumm, A. Imambekov, V. Gritsev, E. Demler & J. Schmiedmayer. Probing quantum and thermal noise in an interacting many-body system. *Nature Physics* **4**, 489–495 (2008).

[209] C. K. Law, C. M. Chan, P. T. Leung & M.-C. Chu. Critical velocity in a binary mixture of moving Bose condensates. *Phys. Rev. A* **63**, 063612 (2001).

[210] S. Ishino, M. Tsubota & H. Takeuchi. Countersuperflow instability in miscible two-component Bose-Einstein condensates. *Phys. Rev. A* **83**, 063602 (2011).

[211] K. Fujimoto & M. Tsubota. Counterflow instability and turbulence in a spin-1 spinor Bose-Einstein condensate. *Phys. Rev. A* **85**, 033642 (2012).

[212] A. Sinatra & Y. Castin. Binary mixtures of Bose-Einstein condensates: Phase dynamics and spatial dynamics. *The European Physical Journal D* **8**, 319–332 (2000).

[213] A. S. Sørensen, E. Demler & M. D. Lukin. Fractional quantum hall states of atoms in optical lattices. *Phys. Rev. Lett.* **94**, 086803 (2005).

[214] F. Gerbier & J. Dalibard. Gauge fields for ultracold atoms in optical superlattices. *New Journal of Physics* **12**, 033007 (2010).

[215] M. Aidelsburger, M. Atala, S. Nascimbène, S. Trotzky, Y.-A. Chen & I. Bloch. Experimental realization of strong effective magnetic fields in an optical lattice. *Phys. Rev. Lett.* **107**, 255301 (2011).

[216] J. Dalibard, F. Gerbier, G. Juzeliūnas & P. Öhberg. *Colloquium* : Artificial gauge potentials for neutral atoms. *Rev. Mod. Phys.* **83**, 1523–1543 (2011).

[217] I. B. Spielman. Raman processes and effective gauge potentials. *Phys. Rev. A* **79**, 063613 (2009).

[218] Y.-J. Lin, R. L. Compton, K. Jimenez-Garcia, J. V. Porto & I. B. Spielman. Synthetic magnetic fields for ultracold neutral atoms. *Nature* **462**, 628–632 (2009).

[219] Y.-J. Lin, R. L. Compton, K. Jimenez-Garcia, W. D. Phillips, J. V. Porto & I. B. Spielman. A synthetic electric force acting on neutral atoms. *Nature Physics* **7**, 531–534 (2011).

[220] Y.-J. Lin, K. Jimenez-Garcia & I. B. Spielman. Spin-orbit-coupled Bose-Einstein condensates. *Nature* **471**, 83–86 (2011).

[221] D. R. Nelson & J. M. Kosterlitz. Universal jump in the superfluid density of two-dimensional superfluids. *Phys. Rev. Lett.* **39**, 1201–1205 (1977).

[222] D. J. Bishop & J. D. Reppy. Study of the superfluid transition in two-dimensional ^{4}He films. *Phys. Rev. Lett.* **40**, 1727–1730 (1978).

[223] L. A. Sidorenkov, M. Khoon Tey, R. Grimm, Y.-H. Hou, L. Pitaevskii & S. Stringari. Second sound and the superfluid fraction in a resonantly interacting Fermi gas. *ArXiv e-prints* (2013). 1302.2871.

[224] C. N. Weiler, T. W. Neely, D. R. Scherer, A. S. Bradley, M. J. Davis & B. P. Anderson. Spontaneous vortices in the formation of Bose-Einstein condensates. *Nature* **455**, 948–951 (2008).

[225] NIST Digital Library of Mathematical Functions. http://dlmf.nist.gov/, Release 1.0.5 of 2012-10-01. Online companion to [226].

[226] F. W. J. Olver, D. W. Lozier, R. F. Boisvert & C. W. Clark (eds.) *NIST Handbook of Mathematical Functions* (Cambridge University Press, New York, NY, 2010). Print companion to [225].